From Synthesis to Battery Cell Integration of Al-doped $Li_7La_3Zr_2O_{12}$ Solid Electrolyte

TECHNISCHE
UNIVERSITÄT
DARMSTADT

Vom Fachbereich Material- und Geowissenschaften
der Technischen Universität Darmstadt

zur Erlangung des akademischen Titels
Doktor-Ingenieur (Dr.-Ing.)

genehmigte Dissertation von
Dipl.-Ing. Miriam Botros
geboren in Kairo

1. Gutachten: Prof. Dr. Horst Hahn

2. Gutachten: Prof. Dr. Wolfgang Ensinger

Tag der Einreichung: 17.10.2017

Tag der Prüfung: 20.12.2017

Darmstadt 2018 — D 17

Erklärung zur Dissertation

Hiermit versichere ich, dass ich meine Dissertation selbstständig und nur mit den angegebenen Quellen und Hilfsmitteln angefertigt habe. Diese Arbeit hat in gleicher oder ähnlicher Form noch keiner Prüfungsbehörde vorgelegen.

Darmstadt, den

(Miriam Botros)

Abstract

The main aim of this work is to study the capability of synthesizing a garnet type Al-doped $Li_7La_3Zr_2O_{12}$ ceramic achieving a Li-ion conductivity in the order of 0.1 mS cm^{-1} at room temperature and to integrate the material as an electrolyte in a full battery cell. Nebulized spray pyrolysis is chosen as the synthesis method resulting in nanocrystalline starting powder. Further heat treatment using conventional sintering and field assisted sintering, after powder calcination, are used to achieve the cubic garnet modification, which exhibits high ionic conductivity. The synthesis and processing temperatures can be reduced to below 1000 °C, which is an advantage compared to conventional solid state reaction routes because Li loss from the garnet structure increases with increasing temperature. The processing parameters and their influence on the Li loss during calcination, which influences the electrochemical performance, are optimized and the influence of the calcination atmosphere is studied using high temperature X-ray diffraction. The solid electrolyte is characterized by means of scanning electron microscopy and transmission electron microscopy combined with energy dispersive X-ray spectroscopy for microstructural imaging and elemental mapping of powders and ceramics. The material properties like phase composition, density, grain size and microstrain are studied and their possible influence on the electrochemical performance is determined. AC-impedance spectroscopy is utilized for temperature dependent conductivity measurements as well as the determination of the area specific resistance of the interface between the solid electrolyte and Li metal in a symmetrical cell configuration. The highest total Li-ion conductivity achieved is 0.77 mS cm^{-1} and the best area specific resistance is calculated to 30.7 Ω cm^2, both values are amongst the best reported in the literature to date. Al-doped $Li_7La_3Zr_2O_{12}$ is integrated in full battery cells using a melted Li metal anode and different cathodes, e.g., a thin film $LiCoO_2$ cathode resulting in a full all-solid-state battery operational at room temperature and a slurry-based cathode resulting in a hybrid cell containing a small amount of liquid electrolyte; both battery cells present novel approaches towards an industrially applicable solid-state battery cell.

Acknowledgements

The success of this work relied on fruitful collaborations, support by colleagues and friends as well as family members and I would like to thank everyone.

I would like to express my deepest gratitude to Prof. Dr.-Ing. Horst Hahn for giving me the opportunity to work in his group providing the best research conditions. I appreciate his support and trust throughout my work and his sincere advice in addition to the opportunity to attend several international conferences, which enriched my experience as a doctoral candidate.

I also would like to acknowledge Prof. Dr. Wolfgang Ensinger for acting as co-examiner and Prof. Dr. Wolfgang Donner and Prof. Dr. Jürgen Janek for serving on the examination committee.

Dr. Ruzica Djenadic is gratefully acknowledged for her supervision especially in the initial phase and continuous support and fruitful discussions. I would like to thank her for proof reading parts of the thesis even after she was no longer member of our group.

Prof. Dr. Oliver Clemens is gratefully acknowledged for many constructive discussions throughout my work and for his sincere support and help concerning X-ray diffraction experiments and Rietveld refinements. Additionally, I would like to express my gratitude for proof reading the thesis.

Parts of the thesis would not have been possible without valuable collaborations. In this respect, I would like to thank Prof. Dr. Olivier Guillon and his group at Forschungszentrum Jülich, Institute of Energy and Climate Research (IEK-1). Extensive discussions regarding field assisted sintering with Dr. Martin Finsterbusch and Dr. Jesus Gonzales are highly appreciated as well as providing the possibility for DTA-TGA and ICP-OES measurements.

Additionally, I would like to acknowledge Dr. Christian Kübel and his group especially Dr. Torsten Scherer and Dr. C.V.S. Kiran at the Institute of Nanotechnology (INT) and Helmholtz Institute Ulm (HIU) for their support concerning FIB cross-section preparation, SEM and STEM imaging. Further imaging techniques (HAADF/EDXS) were performed at the Laboratory for Electron Microscopy (LEM) by Dr. Radian Popescu also as a part of the Karlsruhe Nano Micro Facility (KNMF) for which I would like to express my gratitude.

I sincerely thank Prof. Dr. Barbara Albert and her group members at the Eduard-Zintl-Institut für Anorganische und Physikalische Chemie, Technische Universität Darmstadt (TUD) for providing access to the field assisted sintering equipment and their support.

Prof. Ralf Riedel and his group members are acknowledged for providing the know-how for slurry-based electrodes and access to necessary laboratory equipment.

I am thankful for the members of Nichtmetallische-Anorganische Werkstoffe (NAW), TUD for constructive discussions and providing access to a furnace during break down of my own equipment.

The workshop team at Materials Science Department, TUD, and especially Mr. Jochen Rank and Mr. Michael Weber are acknowledged for manufacturing and repairing crucial metal parts, e.g., for the NSP setup and electrical devices, respectively. I am grateful for their support and high quality work. For the processing of ceramic parts Mr. Michael Heyse (NAW) is acknowledged.

The density measurements using laser confocal microscopy were conducted by Dr. Askar Kilmametov at the Institute of Nanotechnology (INT). In addition, high pressure torsion experiments that are not included in the thesis but I am thankful for his efforts and support. Hot pressing was performed by

Dr. Simon Sawatzki at Functional Materials Department, TUD. Despite the fact that the data is not incorporated into the thesis, I am very thankful for his efforts and helpfulness.

I am grateful for Mrs. Renate Hernichel for all the administrative work and her kind support.

I would like to thank Helmholtz Association (Germany) for financial support through the Helmholtz Portfolio Project “Electrochemical Storage in Systems - Reliability and Integration”.

My thanks also go to all my colleagues at the Joint Research Laboratory Nanomaterials (NM), TUD, and Institute of Nanotechnology, KIT, for their constant motivation and support.

My parents, sister and husband have a crucial impact on my achievements. I would not be where I am today without their ongoing encouragement and support.

Table of content

1 Introduction

Volta discovered in 1800 that a continuous flow of electrical current was generated when using certain fluids as conductors to promote a chemical reaction between the metals or electrodes. This led to the invention of the first voltaic cell, better known as the battery. Volta discovered further that the voltage would increase when voltaic cells were connected in series. All the batteries had been composed of primary cells, meaning that they could not be recharged. In 1859, the French physicist Gaston Planté invented the first rechargeable battery. This secondary battery was based on lead acid chemistry, a system that is still used today [1]. In 1991, the tremendous success of the lightweight Li-ion battery started by its commercial release through Sony Energytech [2]. The Li-ion rechargeable battery has enabled the integration of numerous wireless devices, such as cell phones, laptop computers, digital cameras and tablets, which have revolutionized global communication. Furthermore, this technology could enable modern civilization to secure a sustainable, distributed energy supply for all people and reduce the imprint on air pollution of the internal combustion engine and coal-fired power plants. A portable rechargeable battery and the electrochemical capacitor can, together, displace the internal combustion engine by powering electric vehicles and a stationary rechargeable battery can efficiently store electrical energy generated by solar and/or wind power, thus providing a distributed or a centralized energy storage. Reduction of production costs, safety, reliability, high energy density and high capacity are crucial factors for the final market success [3]. The arrival of electric vehicle manufacturing is expected to cause the massive scale up of battery manufacture, dropping its costs and making even home energy storage systems affordable. The Li-ion battery shows many advantages including high cell voltage and energy density, low self-discharge, and excellent rate capabilities, therefore, it is the most considered for practical application. But it also has major shortcomings like high cost, low temperature tolerance, and the need for protective circuitry to prevent cell degradation and thermal runaway [4], that have to be addressed.

1.1 Motivation

For large scale battery applications, the safety of the battery packs is of increasing importance. The replacement of the flammable liquid electrolyte with a solid electrolyte is an approach to eliminate the safety issue that originates from the dendrite formation on the anode side and their penetration reaching the cathode leading to short circuiting of the cells and potentially ignition of the liquid electrolyte. Solid electrolytes that have attracted a lot of attention, mainly due to their high room temperature Li-ion conductivity and chemical stability against Li metal [5,6], are the garnet type solid electrolytes.

1.2 Objectives

In this work Al-doped $Li_7La_3Zr_2O_{12}$ is chosen amongst the garnet type electrolytes. Novel synthesis and processing methods are employed, that might be suitable for large scale synthesis of the solid electrolyte powder as well as sintered ceramics, while considering cost effectiveness of both the synthesis route, concerning the required temperatures and time, and precursor materials. Achieving a solid electrolyte with a high room temperature ionic conductivity comparable to the conductivity of the liquid electrolyte is the main objective allowing for its integration in symmetrical cells with Li metal electrodes and eventually in full battery cells. To ensure a high ionic conductivity the phase composition is characterized and optimized by several means, e.g., the calcination atmosphere, temperature and Li-content. The Al doping level and mechanism is of high importance to stabilize the desired garnet structure as well as for the ionic conduction, therefore, the Al content is optimized and its coordination and thereby the defect mechanism is identified. Additionally, the influence of the microstructure on the electrochemical performance including the area specific resistance against Li electrodes is determined. The density, grain size and microstrain of the ceramic electrolyte have a significant impact on its performance and consequently on the cell performance. An optimization of the microstructure is attempted by optimizing the density and grain size. Additionally, the enhancement of the electrochemical performance due to microstrain is studied. Manufacturing symmetrical cells with Li metal electrodes is undertaken and the interfacial resistance is determined. Finally, efforts are made to integrate Al-doped $Li_7La_3Zr_2O_{12}$ in different full battery cells: an all-solid-state battery cell with a thin film $LiCoO_2$ cathode, a bulk all-solid-state battery cell with a composite cathode and a hybrid cell containing a small amount of liquid electrolyte on the slurry-based cathode side.

1.3 Outline of the thesis

Chapter 2: An introduction to the basic principle of Li-ion batteries and the advantages of all-solid-state Li-ion batteries are given. Additionally, an overview of the literature about garnet type solid electrolytes is presented. The characterization methods applied throughout this work are introduced and the experimental procedures are presented.

Chapter 3: The synthesis method of nebulized spray pyrolysis and the basics of ceramic processing through conventional sintering and field assisted sintering with a detailed experimental setup and procedures are presented.

Chapter 4: The fabrication of phase pure solid electrolyte ceramics by means of conventional sintering is presented. The electrochemical performance as well as the Al coordination are determined and the incorporation into the lattice are confirmed establishing nebulized spray pyrolysis as a promising synthesis method. The biggest challenge that remains is the achievement of high densities.

Chapter 5: To achieve higher densities the optimization of powder processing is crucial to obtain the desired garnet structure already prior to ceramic processing. The influence of the calcination atmosphere on the phase composition as well as the temperature, time and Li excess during synthesis are optimized.

Chapter 6: The combination of nebulized spray pyrolysis and field assisted sintering is presented for the first time. The successful fabrication of dense, fine grained ceramics is achieved with good electrochemical performance and their integration in symmetrical cells with Li electrodes allows for the determination of the area specific resistance against Li metal.

Chapter 7: From previous observations it is evident that the processing technique and conditions have a significant impact on the electrochemical performance, which is presented here in detail. The impact of an additional ball milling step, the pressure variation during field assisted sintering, an additional thermal treatment of the sintered ceramics and storage conditions is determined.

Chapter 8: Three approaches for the integration of the garnet-type solid electrolyte in full all-solid-state battery cells are presented and their performance is evaluated and correlated to the microstructure.

Chapter 9: Concluding remarks and an outlook for further research possibilities are given to further understand the parameters by which the performance of the garnet solid electrolytes can be enhanced.

2 Basics of Li-ion batteries

A battery is a device that converts the chemical energy contained in its active materials directly into electric energy by means of an electrochemical redox-reaction. While the term *battery* is often used, the basic electrochemical unit is referred to as the *cell* [7]. A battery is constructed by connecting basic cells in parallel to increase current, in series to increase voltage or combined configurations [8]. There are primary and secondary battery cells. While primary cells are for single use only, the secondary cells are rechargeable due to the reversibility of the redox-reaction taking place during discharge. Rechargeable Li-ion cells are already mass produced for the application in portable electronic devices, medical equipment and electric tools. A conventionally produced battery cell is depicted in Figure 2-1. A battery cell consists of three components, the cathode (positive electrode), the anode (negative electrode) and the electrolyte containing Li-ions. The electrodes are isolated from each other by a separator, typically a microporous polymer membrane. The separator allows the exchange of Li-ions between the two electrodes but not electrons [8]. During the charging process, the two electrodes are connected to an external electrical supply. The electrons are forced to be released at the cathode material and move externally to the anode. Simultaneously the Li-ions move in the same direction, but internally, from cathode material to anode material through the electrolyte. During discharge electrons move from anode to the cathode through an external load and Li-ions move from anode to the cathode through the electrolyte [8]. The cathode material most commonly integrated in commercial cells is $LiCoO_2$ (LCO). This is due to its long cycle life (>500 cycles) and stability against the liquid electrolyte. Furthermore, it is an intercalation compound, which shows small structural changes during charge and discharge compared to conversion materials. LCO can be easily manufactured in a large scale and is stable in air [8]. The anode material commonly used is graphite (LiC_6), i.e., lithiated graphite, since its chemical potential is close to that of Li metal. It can also be reversibly lithiated and delithiated (Li:C = 1:6) without a strong impact on its mechanical and electronic properties [7]. The electrode reactions during discharge are as follows [9]:

$$\mathrm{Li}_y\mathrm{C}_{6(s)} \rightarrow y\mathrm{Li}^+ + 6\mathrm{C}_{(s)} + y\mathrm{e}^- \qquad [\ 2\text{-}1\ ]$$

$$\mathrm{Li}_{1-y}\mathrm{CoO}_{2(s)} + y\mathrm{Li}^+ + y\mathrm{e}^- \rightarrow \mathrm{LiCoO}_{2(s)} \qquad [\ 2\text{-}2\ ]$$

During the first lithiation process of the anode a solid electrolyte interphase (SEI) is formed and Li is consumed irreversibly. The SEI formation is presumed to be due to the reduction of the liquid electrolyte at the electrolyte-anode interface. When the SEI reaches a thickness where the electron tunneling can be suppressed, no further reduction takes place and the anode is cycled reversibly. The liquid electrolyte commonly used, which ensures the ionic transport between the two electrodes is $LiPF_6$ salt dissolved in non-aqueous solvents. Despite its sensitivity towards moisture, leading to the formation of HF, it provides a high ionic conductivity. This chapter provides information about the general concept of batteries. An introduction to all-solid-state Li-ion batteries and their advantages as well as challenges are presented. Additionally, different solid electrolyte materials are presented and their application is discussed and compared to the garnet solid electrolyte. Finally, the characterization techniques that are utilized to characterize the solid electrolyte, half and full battery cells are briefly introduced.

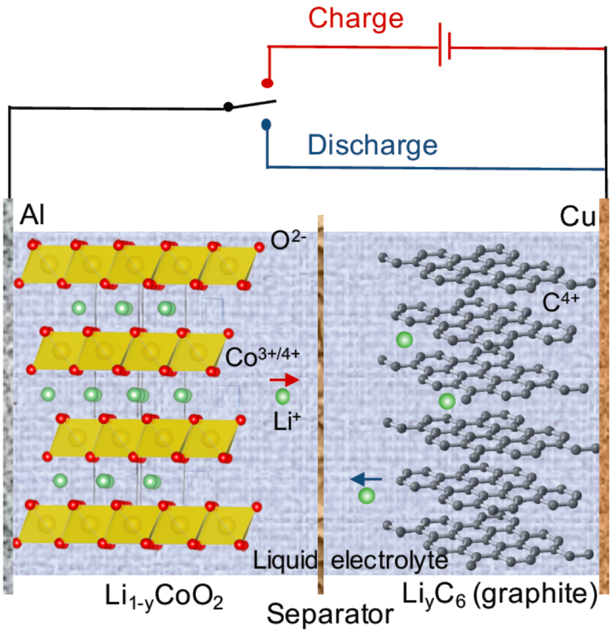

Figure 2-1: Conventional battery cell with a LCO cathode and graphite anode.

2.1 Electrochemical principles

The amount of energy the battery cell can deliver is related to the electrochemical reaction taking place during discharge. The following electrode reaction is considered [10]:

$$pA + qB \rightarrow rC + sD \qquad [\ 2\text{-}3\ ]$$

Where p, q, r and s are the stoichiometric coefficients of the involved chemical species A, B, C and D. The maximum possible electric energy (W_{max}) is correlated to the change in Gibbs free energy (ΔG) of the electrochemical reaction:

$$-W_{max} = \Delta G = -nFE \qquad [\ 2\text{-}4\ ]$$

This shows the relation between the Gibbs free energy during equilibrium and the electromotive force (E), F the Faraday constant and n the number of moles of electrons participating in the reaction, leading to the Nernst equation:

$$E = E^0 - \frac{R\mathrm{T}}{nF} \ln \frac{a_C^r a_D^s}{a_A^p a_B^q} \qquad [\ 2\text{-}5\ ]$$

Here a_C^r is the activity of product C with the stoichiometric coefficient r, E^0 is the standard potential, R the universal gas constant and T is the temperature. The electric potential is therefore affected by the concentration, which is proportional to the activity, of the species involved in the electrochemical reaction. When there is no current and the circuit is not closed the open circuit voltage (V_{oc}) of a Li-ion battery cell, which is equivalent to the electromotive force, is determined by the difference of the Li electrochemical potential of the cathode (μ_c(Li)) and the anode (μ_a(Li)) as follows [3]:

$$V_{oc} = \frac{\mu_c(\text{Li}) - \mu_a(\text{Li})}{e} \qquad [\,2\text{-}6\,]$$

The energies involved in both the electron and Li-ion transfer determine the open circuit voltage. The first is related to the work function of the cathode and anode, respectively, while the latter is determined by the crystal structure and the coordination geometry of the site where the Li-ion is inserted and extracted [11]. The energy diagrams for a Li-ion battery cell with both liquid and solid electrolyte are depicted in Figure 2-2. To ensure the electrochemical stability of the electrolyte against the electrode materials, the electrochemical potentials of the cathode and anode have to lie within the band gap (E_g) of the electrolyte. This stability requirement imposes a limitation on the cell open circuit voltage:

$$eV_{oc} = \mu_c(Li) - \mu_a(Li) < E_g \qquad [\,2\text{-}7\,]$$

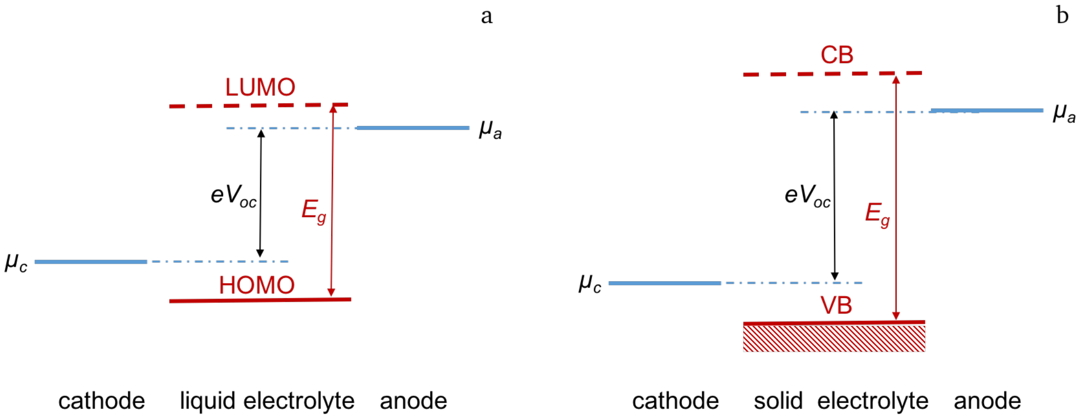

Figure 2-2: Schematic energy diagram of the lithium cell at open circuit showing the highest occupied molecular orbital (HOMO) and lowest unoccupied molecular orbital (LUMO) for a liquid electrolyte (a), the valence band (VB) and conduction band (CB) for a solid electrolyte.

The application of an electrolyte material with a large band gap, i.e., a large electrochemical window can increase the maximum open circuit voltage and thereby increase the energy density of the Li-ion battery cell, provided suitable electrode materials. Therefore, solid electrolytes can provide an advantage over liquid electrolytes, focusing the attention on all-solid-state battery cells introduced in section 2.2. When the battery is in an equilibrium state with little or no current flow, it can provide electric energy equal to the amount of ΔG. Since current continues to flow in the battery during discharge, it is considered to be in a nonequilibrium state according to thermodynamics. The actual voltage in this case is always less than the open circuit voltage and therefore the maximum possible energy cannot be used [10]. The ideal open circuit voltage is reduced by several effects in a practical battery cell. Figure 2-3 shows the dependence of the cell voltage on the current drawn from the cell indicating three different regions, one related to resistive voltage drop (ohmic region) and the others due to the rate at which the reaction can proceed kinetically (activation and mass transport regions).

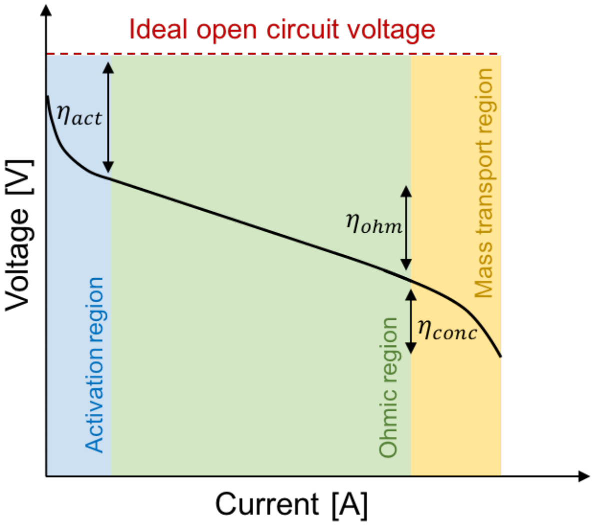

Figure 2-3: Dependence of the cell voltage on the current schematically showing the different polarization and ohmic regions. Indicated are the activation polarization (η_{act}), the ohmic polarization (η_{ohm}) and the concentration polarization (η_{conc}).

The polarization (η_{dis}) refers to the difference between the actual potential V_a and the equilibrium potential V_{oc}, during discharge where the actual potential is always smaller than the equilibrium potential, while during charge the overpotential (η_{ch}) is larger.

$$\eta_{dis} = \eta_{ohm} + \eta_{act} + \eta_{conc} \qquad [\ 2\text{-}8\ ]$$

The capacity of a battery is the product of the total amount of charge, when completely discharged under given conditions, and time. The theoretical capacity C_T is determined by the amount of active material and is calculated as follows [10]:

$$C_T = n \cdot F \qquad [\ 2\text{-}9\ ]$$

Here, F is the Faraday constant and n is the number of moles of electrons produced from the discharging process. The practical capacity, C_P, is smaller than the theoretical capacity because reactants are not completely consumed during discharge. As the rate of charging/discharging increases, the practical capacity is further reduced due to the internal resistance drop (IR drop). In general, the rate of charging/discharging is denoted by the C-rate. The battery capacity and current drawn during charging/discharging are related by the following equation:

$$t = \frac{C_P}{i} \qquad [\ 2\text{-}10\ ]$$

Here, t is the elapsed time [h] to completely discharge (or charge) a battery, i is the current drawn [A], and C_P is the battery capacity [Ah]. The reciprocal of t is given by the C-rate. In other words, as C-rate increases, the battery requires less time to be charged or discharged. Battery capacity can be measured using the gravimetric specific capacity [mAh g^{-1}] or the volumetric specific capacity [mAh cm^{-3}] [10].

Energy density, an important factor in determining battery performance, is the amount of energy stored per unit mass or volume. The maximum energy that can be obtained from 1 mol of reactant is given as follows:

$$\Delta G = -FE = \varepsilon_T \qquad [\ 2\text{-}11\ ]$$

Here, E is again the electromotive force of the battery and ε_T is the theoretical energy [Wh mol^{-1}] for the cell reaction of 1 mol. The actual energy ε_P, which varies according to the discharge method, from 1 mol of reactant is derived as follows:

$$\varepsilon_P = -\mathrm{F}\ (\mathrm{E}_{eq} - \eta_{dis}) \qquad [\ 2\text{-}12\ ]$$

As the rate of discharge increases, the electric potential of the battery departs further from the equilibrium potential. Similar to battery capacity, energy density can be expressed gravimetrically [mWh g^{-1}] or volumetrically [mWh cm^{-3}].

As for the battery capacity and energy, power per unit mass or volume is described as power density. The power of a battery refers to the energy that can be derived per unit time. The power P is the product of current i and electric potential E.

$$P = i \cdot E \qquad [\ 2\text{-}13\ ]$$

Electric power is a measure of the amount of current flowing at a given electric potential. When the current increases, the power rises to a peak and declines when the current goes beyond a certain limit, since the battery potential drops. This phenomenon of polarization is related to the diffusion of lithium ions and the internal resistance of the battery, see Figure 2-3. An enhancement of the diffusion rate of Li-ions and the electrical conductivity leads to power improvement [10].

2.2 All-solid-state Li-ion battery

All-solid-state batteries have been studied since the 1950s [12]. In addition to the possibly larger electrochemical window of the solid-electrolyte compared to the liquid counterpart, they provide many advantages like the absence of electrolyte leakage, absence of problems related to vaporization of liquid electrolytes, absence of phase transitions at low temperatures improving low-temperature performance and ease of miniaturization [13]. Additionally, Li-ion batteries are on the verge of being used on a large scale, e.g., in electric vehicles where the safety issue concerning the flammability of the liquid electrolyte has a larger proportion. Therefore, the application of all-solid-state Li-ion batteries could give a solution [14]. Figure 2-4 shows an exemplary all-solid-state battery cell with $LiCoO_2$ as the cathode, Li metal as the anode and a solid electrolyte, additionally acting as a separator between the electrodes due to its negligible electronic conductivity. This cell design could reduce the cell volume as well as the cell mass leading to an increase in energy density. The possibility of using high voltage cathode materials would also benefit the energy density.

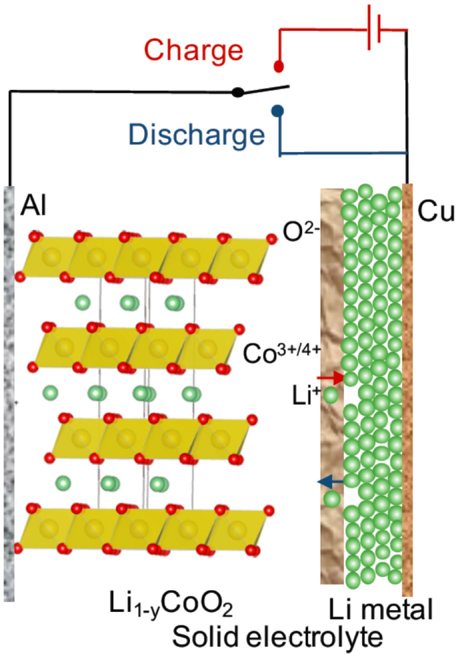

Figure 2-4: All-solid-state battery cell with $LiCoO_2$ cathode and Li metal anode.

The biggest challenge facing all-solid-state Li-ion batteries is the low power density. This is due to the impeded ionic transport. The first hindrance is the low conductivity of the solid electrolyte compared to the liquid electrolyte with a conductivity in the order of 10 mS cm^{-1}. While cations and anions of the liquid electrolyte contribute to the total conductivity, the solid electrolyte provides only Li-ions as charge carries leading to a required room temperature conductivity of 1 mS cm^{-1}. This value has been achieved for several solid electrolytes, yet the increase of power density remains challenged by the interfacial resistances [14]. Although sulfide-based solid electrolytes achieve ionic conductivities of 10 mS cm^{-1}, their contact with 4 V cathode materials, e.g., $LiCoO_2$ depletes the Li-ions in the sulfide solid electrolyte causing high interfacial resistance [15]. Oxide-based solid electrolytes on the other hand provide a good interface with high voltage cathode materials [14]. Perovskite-type $Li_{3x}La_{2/3-x}TiO_3$ solid electrolyte for example exhibits a total Li-ion conductivity of 0.07 mS cm^{-1} at room temperature [16]. Despite the good electrochemical properties, the material reacts chemically with Li reducing Ti^{4+} to Ti^{3+} limiting its application as a solid electrolyte. Garnet-type solid electrolytes exhibit good chemical stability against Li [5,6], in addition to their good electrochemical performance and presumed wide electrochemical window up to 6 V vs. Li/Li^+ [17].

2.3 Garnet-type solid electrolytes

The garnet structure has a general formula $A_3B_3C_2O_{12}$ with a space group $Ia\bar{3}d$, where A is eight-fold coordinated, B is tetrahedrally coordinated and C is in an octahedral site, therefore, it can accommodate a large range of cations [18]. There has been a great interest in this structure due to the observation of fast Li-ion conduction in a number of phases containing an excess of Li that surpasses the above stoichiometry [5]. The first to explore novel garnet-type Li containing transition metal oxides with the nominal chemical compositions $Li_5La_3M_2O_{12}$ (M = Nb, Ta) and $Li_6ALa_2M_2O_{12}$ (A = Ca, Sr, Ba; M = Nb, Ta) for fast Li-ion conduction were Thangadurai and Weppner [19]. Among the materials investigated is $Li_6BaLa_2Ta_2O_{12}$, which exhibits the highest Li-ion conductivity of 0.04 mS cm^{-1} and an activation energy of 0.40 eV [20]. The performance was not sufficient to develop a bulk all-solid-state Li-ion rechargeable battery, therefore, further Li-stuffed garnets were explored by Murugan et al. [5] that house the Li cations in some of the usual tetrahedral garnet sites as well as in octahedral oxide environments that are unoccupied in conventional garnets [21]. In $Li_7La_3Zr_2O_{12}$ lanthanum occupies the A site, while zirconium resides on the C site. There are two main polymorphs of the $Li_7La_3Zr_2O_{12}$ garnet structure, namely the low temperature tetragonal structure ($I4_1/acd$) and the high temperature cubic structure ($Ia\bar{3}d$) that mainly differ in the arrangement of Li-ions [22,23]. Three different Li sites have been identified for the tetragonal $Li_7La_3Zr_2O_{12}$ [24]: a tetrahedral Li(1) (8a) site and two different distorted octahedral sites Li(2) (16f) and Li(3) (32g). On the other hand, in the cubic $Li_7La_3Zr_2O_{12}$ only two different types of Li sites can be differentiated: a tetrahedral site Li(1) (24d) and a distorted octahedral site Li(2) [22], which can be interpreted as the result of a splitting of the octahedral 48g into two energetically equivalent displaced octahedral 96h sites as illustrated in Figure 2-5. While the crystallographic Li sites in tetragonal $Li_7La_3Zr_2O_{12}$ are fully occupied, a considerably reduced site occupancy (g = 0.35) of the Li(2) site and an occupancy of almost one (g = 0.94) for the Li(1) site was found in cubic $Li_7La_3Zr_2O_{12}$ [22,24]. Lower Li site occupancies in cubic $Li_7La_3Zr_2O_{12}$ have also been observed in neutron diffraction studies but with a different ratio of Li(1)/Li(2) occupancy (g(Li(1)) = 0.56, g(Li(2)) = 0.44) [25]. Occupational disorder in the Li sublattice is considered a requirement for ionic conductivity of garnet solid electrolytes [22,23,26], which explains the one to two orders of magnitude higher ionic conductivity of the cubic garnet structure (0.3 mS cm^{-1}) compared to its tetragonal counterpart (0.02 mS cm^{-1}) [5,24,27]. Therefore, one of the objectives while synthesizing $Li_7La_3Zr_2O_{12}$ is stabilizing the high temperature cubic structure at room temperature. The stabilization can be achieved by the introduction of supervalent dopants, e.g., Al^{3+}, Ga^{3+}, Ta^{4+} and Nb^{4+} [5,28,29]. When Al^{3+}, for instance, is used as a dopant, charge compensation takes place through substitution of 3 Li^{+} by one Al^{3+} and creation of two Li vacancies, which reduces the free energy advantage of complete ordering on the Li sublattice, and eventually, with increasing vacancy concentration, leading to disorder and a stabilization of the cubic symmetry at room temperature [28]. Additionally, the finding that the total and bulk conductivities are of the same order of magnitude is a most attractive feature of the $Li_7La_3Zr_2O_{12}$ garnet-type oxide compared to other ceramic Li-ion conductors [5].

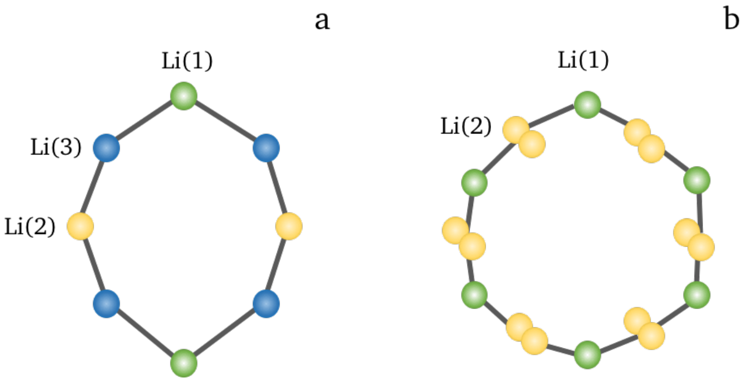

Figure 2-5: Loop arrangement of different Li sites; tetrahedral Li(1) site (green), octahedral Li(2) (orange) and Li(3) (blue) sites for the tetragonal (a) and cubic (b) modification (redrawn after [21]).

2.4 Characterization techniques

This section gives a short description of the characterization methods used in this work and the corresponding experimental procedures. The methods include electrochemical techniques, electron microscopy, X-ray diffraction both at room temperature and at elevated temperatures and chemical analysis techniques.

2.4.1 AC-impedance spectroscopy

An ideal resistor follows Ohm's law at all current, voltage, and AC frequency levels. The characteristic resistance value R [Ω] is independent of AC frequency, while AC current and voltage signals do not exhibit any phase shift:

$$\mathrm{R} = \rho \frac{d}{A} \qquad [\ 2\text{-}14\ ]$$

where ρ [Ω cm] is the characteristic electrical resistivity of a material. The conductivity σ [S cm^{-1}] is the inverse of the resistivity and reflects the ability of the material to conduct electrical current between two bounding electrodes. Another ideal element that completely rejects any flow of current can replace an ideal resistor in the circuit. This element is referred to as an ideal capacitor, which stores energy created by an electric field, which is formed when two bounding electrodes are separated by a non-conducting or dielectric medium. The AC current and voltage signals of the ideal capacitor for instance show a phase shift, with the current following voltage. The value of the capacitance, C [F], depends on the area of the electrodes *A*, the distance between the electrodes *d*, and the properties of the dielectric reflected in a relative permittivity parameter ε_r:

$$\mathrm{C} = \frac{\varepsilon_0 \, \varepsilon_r \, A}{d} \qquad [\ 2\text{-}15\ ]$$

here ε_0 is the constant electrical permittivity of a vacuum ($8.85 \cdot 10^{14}$ F cm^{-1}). The ability of the material to store electrical energy is represented by the relative permittivity value. The impedance represents neither a pure resistance or pure capacitance and it takes the phase differences between the input voltage and output current into account. Like resistance, impedance is the ratio between voltage and current. The real impedance term represents the ability of a circuit to resist the flow of electrical current, while the imaginary impedance term reflects the ability of a circuit to store electrical energy. Impedance can be defined as a complex resistance encountered when current flows through a circuit composed of various resistors, capacitors, and inductors [30].

Experimentally the electrochemical impedance is usually measured using an AC voltage signal V with a small amplitude V_A, which is applied at a certain frequency. The voltage signal *V(t)* as a function of time is expressed as:

$$V(t) = V_A \, \sin(2\pi f t) = V_A \sin{(\omega t)} \qquad [\ 2\text{-}16\ ]$$

In this notation the radial frequency, ω, is related to the applied AC frequency as $\omega = 2\pi f$. In a linear system, the response current signal *I(t)* is shifted by φ and has an amplitude, I_A:

$$I(t) = I_A \sin{(\omega t + \varphi)} \qquad [\ 2\text{-}17\ ]$$

The calculation of the complex impedance of the system as the ratio of input voltage *V(t)* and output measured current *I(t)* can be expressed analogous to Ohm's law:

$$Z^* = \frac{V(t)}{I(t)} = \frac{V_A \sin{(\omega t)}}{I_A \sin{(\omega t + \varphi)}} = Z_A \frac{\sin{(\omega t)}}{\sin{(\omega t + \varphi)}} \qquad [\ 2\text{-}18\ ]$$

The impedance is therefore expressed in terms of a magnitude, $Z_A = |Z|$, and a phase shift, φ.
Euler’s relationship:

$$e^{\mathrm{i}\varphi} = cos\varphi + \mathrm{i}\, sin\varphi \qquad [\ 2\text{-}19\ ]$$

allows for the expression of the impedance as a complex function with the voltage as:

$$V(t) = V_A\, e^{\mathrm{i}\omega t} \qquad [\ 2\text{-}20\ ]$$

and the current expressed as:

$$I(t) = I_A\, e^{\mathrm{i}(\omega t - \mathrm{i}\varphi)} \qquad [\ 2\text{-}21\ ]$$

The impedance is then represented as a complex number as a combination of real, or in-phase ($\mathrm{Re}(Z')$), and imaginary, or phase shifted ($\mathrm{Im}(Z'')$) parts as follows:

$$Z^* = \frac{V(t)}{I(t)} = Z_A e^{\mathrm{i}\varphi} = Z_A(\cos(\varphi) + \mathrm{i}\sin(\varphi)) = \mathrm{Re}(Z') + \mathrm{i}\,\mathrm{Im}(Z'') \qquad [\ 2\text{-}22\ ]$$

Frequency response analyzers allow for the automation of the sinusoidal voltage input applied with variable frequencies and the collection of the output current responses as the frequency is scanned from high (MHz-GHz) to low frequency values (μHz). An equivalent circuit model that corresponds to the setup and materials investigated is used to fit the collected data. The Randles circuit R(R CPE) is the model most commonly used, which is depicted in the inset of Figure 2-6a. It contains a parallel circuit of a resistance R and a constant phase element, CPE, to simulate both the real and the imaginary part of the impedance, respectively. The CPE is a non-ideal capacitor and it is characterized by two parameters Q and n. The experimental impedance data are typically displayed in the forms of Cole-Cole (Nyquist) and Bode plots, which are presented in Figure 2-6. In the first, the negative imaginary part of the impedance ($-\mathrm{Im}(Z'')$) is plotted versus the real part of the impedance ($\mathrm{Re}(Z')$). The Nyquist plot is a very convenient data representation, since it shows an ideal semi-circle ($n = 1$) as an indication of an activation energy controlled charge transfer process. A depressed semi-circle ($0.5 < n < 1$) in the Nyquist plot is an indication of multiple processes with similar relaxation time constants:

$$\tau = \frac{1}{2\pi f_c} = \frac{1}{2\pi RC} \qquad [\ 2\text{-}23\ ]$$

with f_c being the critical relaxation frequency, or distributed non-ideal kinetics [30]. The major disadvantage of this representation is the incomplete information about the frequency data. In the Bode plot, the absolute impedance, $|Z|$, and phase angle, φ, are complementarily plotted versus the frequency, f.

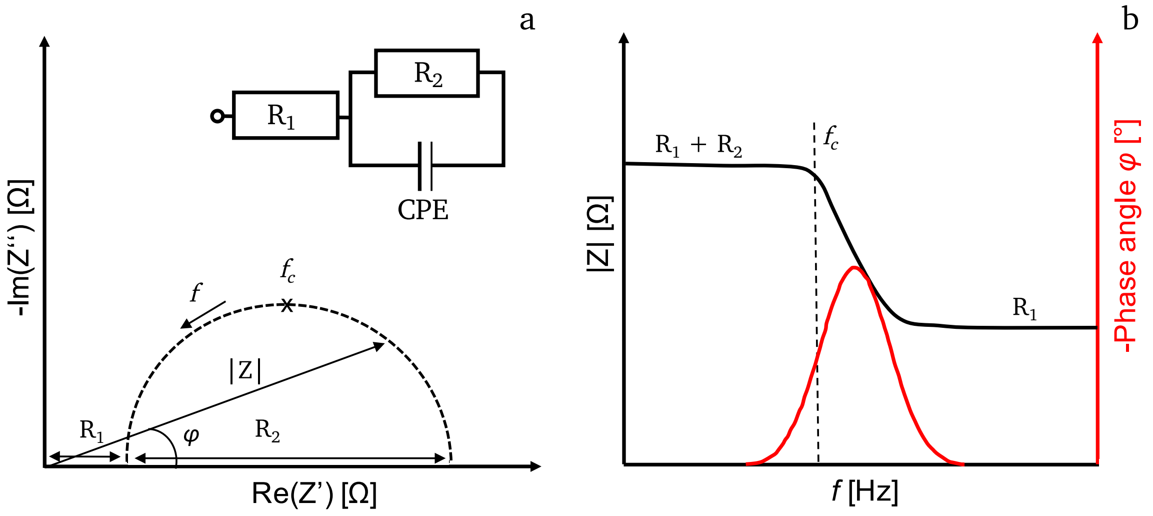

Figure 2-6: Nyquist plot or Cole-Cole plot showing the real impedance on the x-axis and the imaginary part on the y-axis and the phase shift represented in the angle φ, inset represents the equivalent circuit (R: resistance, CPE: constant phase element) (a) and the Bode plot combining the absolute impedance value |Z| and the phase angle φ plotted against the frequency (b).

Each charge transfer process has a characteristic relaxation time constant and thereby a characteristic capacitance, C. Table 2-1 gives an overview of the capacitance values and the corresponding phenomenon for a sample with an A to d ratio of approximately unity, allowing for data interpretation. The capacitance, C, can also be calculated using the fit results of the CPE element as follows:

$$\mathrm{C} = \sqrt[n]{R^{1-n}\,Q} \qquad [\ 2\text{-}24\ ]$$

Table 2-1: Overview of the capacitance values and their corresponding phenomenon [31].

Capacitance [F]	Phenomenon responsible
10^{-12}	bulk
10^{-11}	minor, second phase
10^{-11}-10^{-8}	grain boundary
10^{-10}-10^{-9}	bulk ferroelectric
10^{-9}-10^{-7}	surface layer
10^{-7}-10^{-5}	sample-electrode interface
10^{-4}	electrochemical reactions

In most cases the phenomena taking place during the impedance measurement have a different temperature dependence of their time constants and therefore can be identified separately by conducting temperature dependent measurements that are also necessary for the determination of the activation energy E_a, using the Arrhenius relation:

$$\sigma = \frac{\sigma_0}{\mathrm{T}}\, e^{-\frac{E_a}{RT}} \qquad [\ 2\text{-}25\ ]$$

with σ being the conductivity, T the temperature [K] and R the gas constant. The development of a series of assumptions about the chemical, physical and mechanical characteristics of the analyzed system is highly recommended. An anticipation of the influence of the experimental setup on the impedance data and possible data interpretation is needed. A successful characterization of a studied system is typically based on the comparison of the obtained experimental impedance data with these expectations, that are typically based on previously published examples for similar systems [30].

During this work, AC-impedance measurements are performed with two different setups. For both setups the pellets are coated with gold electrodes on both sides using a sputter coater, Quorum Q300T D, (thickness approximately 100 nm). For contacting the first setup, copper wires are connected to the electrodes using silver paste. To insure complete drying of the silver paste, the pellet is placed under vacuum for several hours. The wires (two wires on each side of the pellet) are then connected to the frequency response analyzer (Solartron 1260) using clamps, while the sample is heated up to 338 K using a heating tape wrapped around an alumina tube where the sample is placed. The data collected using the first setup is presented in Chapter 4. All further impedance data are collected using the second setup where the coated pellets are placed in a cryostat (Janis STVP-200-XG) with brass connection plates directly contacted to the gold electrodes. An image with further details is shown in Figure 2-7. The cryostat allowed for measurements in the temperature range between 200 K and 393 K. The frequency range used for all measurements was 1 MHz down to 0.1 Hz with a collection rate of 50 points per decade and a potential amplitude V_A of 20 mV.

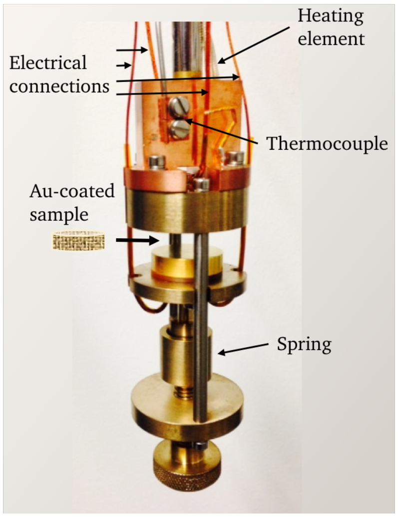

Figure 2-7: Image of the sample holder of the cryostat (Janis STVP-200-XG) showing the sample position and the wiring for electrical connection and temperature control.

2.4.2 Cell testing

Two standard testing methods are utilized during this study namely cyclic voltammetry and galvanostatic cycling. During cyclic voltammetry the potential is varied with a defined rate in the potential range suitable for the cell components and the current is detected. A triangular potential sweeps the potential of the working electrode between the starting potential to the switching potential and back again [32]. The reversibility of the redox reaction can be evaluated by the difference between the maximum current peaks, ΔE, indicated in Figure 2-8a. If the positions of the maximum current peaks with regard to their potential do not change as a function of the scan rate, and the heights of the anodic and cathodic peaks appear to be equal, then the process occurring is reversible. This is also true if the peaks are about 59 mV apart and a one-electron transfer ($z = 1$) takes place [32]:

$$\Delta E = E_{anodic} - E_{cathodic} = \frac{0.059}{z} \qquad [\ 2\text{-}26\ ]$$

For the second testing method, galvanostatic cycling, the current is kept constant at a value in accordance with the capacity of the cathode, usually rates between 0.2C and 1C are utilized on a laboratory scale, while the potential is detected within a defined potential range. Galvanostatic conditions can be realized by connecting an external power source in series to the cell, which has a much higher voltage than the V_{oc} of the cell. The current in the circuit is adjusted with the aid of a high resistance rheostat. Small fluctuations in cell voltage under transitory conditions have little effect compared to the large value of the external voltage, so that there is little change in current during the transition period [33]. Typical charge and discharge cycles are shown in Figure 2-8b.

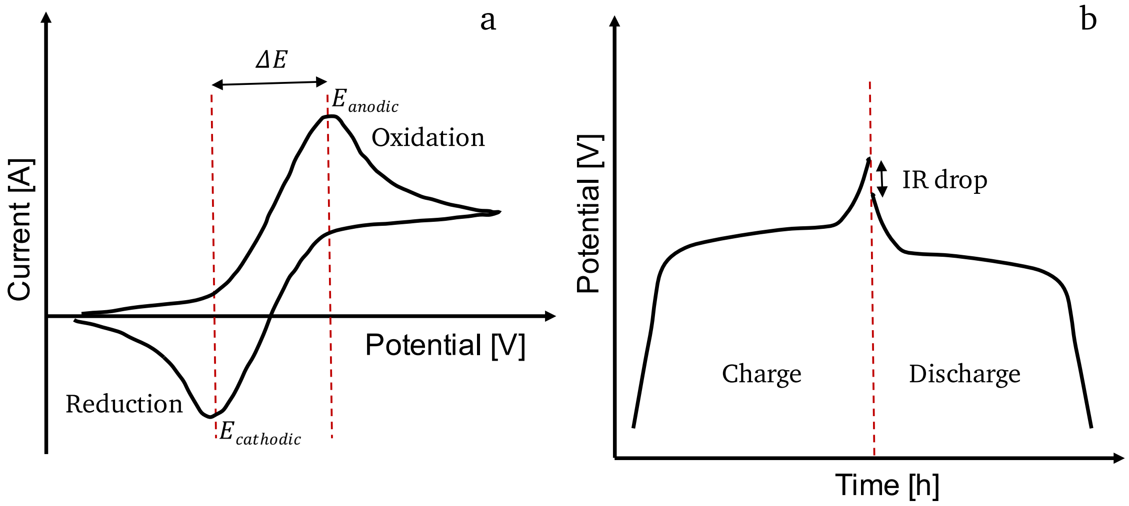

Figure 2-8: Exemplary cyclic voltammogram indicating one redox-reaction (a), typical galvanostatic charge and discharge curves (b).

Cyclic voltammetry and galvanostatic cycling (Solartron Analytical 1470E/1455) are performed on cells mounted inside Swagelok type connections containing a spring for the application of a constant pressure to ensure good electrical and thermal contact during cycling. A temperature cabinet (Memmert IPP 260) is used to ensure stable temperatures.

2.4.3 Electron microscopy

The morphology of the as-synthesized powders is studied using high-resolution scanning electron microscopy, SEM (Philips XL30 FEG). Prior to imaging all samples are coated with Au using a sputter coater (30 s, 30 mA) to prevent electrical charging. The pellets are contacted using silver paste, in addition to the carbon tape, to the sample holder. Focused ion beam (FIB Strata 400 STEM) is used to prepare and to study cross sections of the sintered samples.

High angle annular dark field scanning transmission electron microscopy (HAADF STEM) combined with energy dispersive X-ray spectroscopy (EDXS) is used to investigate the chemical composition. The experiments are performed on an FEI Osiris ChemiSTEM microscope at 200 kV acceleration tension, which is equipped with a Bruker Quantax system (XFlash detector) for EDXS. EDXS elemental maps are recorded and used to investigate the elemental distribution within grains and along the grain boundaries. The maps are quantified by the ESPRIT software (version 1.9) from Bruker. Using ESPRIT, element concentrations are calculated on the basis of a refined Kramers' law model [34], which includes corrections for detector absorption and background subtraction. For this purpose, standardless quantification, i.e., by means of theoretical sensitivity factors is applied, without thickness correction.

2.4.4 X-ray diffraction

X-ray diffraction is used to determine the phase composition, lattice parameters as well as the microstrain, ε, of the analyzed samples (powders and pellets). The patterns are recorded using a Bruker D8 diffractometer with Bragg-Brentano geometry equipped with an X-ray tube with Cu anode, and a Ni filter for the removal of the K_β radiation. A VANTEC detector and a fixed divergence slit (0.3°) are used. The measurements are performed with a step size of 0.015° with a collection time of 1 s at 30 kV and 40 mA over the 2θ angular range between 10° and 120°, while the high temperature X-ray diffraction patters are recorded in the range between 10° and 60° up to a temperature of 1000 °C. The phase quantifications are performed by Rietveld analysis using the program TOPAS 4.2 (Bruker AXS, Karlsruhe, Germany). The quality of the Rietveld fit is measured by the weighted profile R-factor (R_{wp}), while the best possible R_{wp} is determined as the expected R-factor (R_{exp}). The squared goodness of fit χ^2 is thereby defined as $(R_{wp}/R_{exp})^2$ and in an ideal scenario it is unity, but mostly it is larger [35,36]. The instrumental intensity distribution for the X-ray data is determined empirically from a fundamental parameters set, using a reference scan of LaB_6 (NIST 660a).

2.4.5 Inductively coupled plasma optical emission spectrometry

The concentration of main elements Li, La, Zr and Al was determined by inductively coupled plasma optical emission spectrometry (ICP-OES, OPTIMA 4300 DV, PerkinElmer). The samples (2-3 mg) are dissolved in a mixture of 5 ml nitric acid and 5 ml sulfuric acid at 235 °C for 3 h with the pressure digestion system DAB 2 (Berghof). Every sample has been digested three times. The acid solution was filled up to 50 ml and diluted in a ratio of 1:50 for the analysis of Li, La and Zr and 1:2.5 for the analysis of Al. The analyses were accomplished with four different calibration solutions and two internal standards (Na and Sc).

2.4.6 Differential thermal analysis and thermogravimetric analysis

Differential thermal analysis and thermogravimetric analysis (DTA-TGA) is performed on both as-synthesized powders (STA 449C Jupiter), section 5.1, and ceramic pellets (STA 449F1), section 7.3. The measurements are performed up to a temperature of 1000 °C and 700 °C, respectively, with a heating rate of 5 °C min^{-1}. Further information is provided in the respective sections.

2.4.7 Nuclear magnetic resonance

In order to determine the Al^{3+} coordination ^{27}Al magic angle spinning nuclear magnetic resonance (MAS NMR) measurements of the sintered sample are performed on a Bruker Avance III spectrometer at a magnetic field of 11.7 T, corresponding to a Larmor frequency of 130.3 MHz. Sample spinning was done in 2.5 mm rotors at a spinning speed of 30 kHz. Spectra were acquired with a one-pulse sequence with a π/2 pulse length of 2.3 μs and a repetition delay of 5 s. The chemical shifts are referenced to an aqueous solution of 1M $Al(NO_3)_3$ at 0 ppm.

3 Introduction to synthesis procedure and ceramic processing

3.1 Nebulized spray pyrolysis

Nebulized spray pyrolysis (NSP) is an aerosol based synthesis method that allows for the synthesis of nanocrystalline materials. The principle of NSP is depicted in Figure 3-1. The precursors, usually water-soluble nitrates, are dissolved to prepare a stable solution. This is then injected into a glass nebulizer by means of a syringe pump. Underneath the solution a membrane performing periodic mechanical vibration of ultrasound frequency destabilizes the liquid to a point of break-up and the formation of droplets (aerosol) takes place [37]. The droplets are carried through the hot-wall reactor by means of the carrier and/or reaction gas, where the synthesis temperature can be controlled. The pressure of the system as well as the gas flow can be controlled using a pump and a mass flow controller allowing for the variation of the residence time in the reactor. The processes occurring in the reactor are presented in Figure 3-1. The aerosol droplets first undergo solvent evaporation and precursor precipitation upon heating. The individual droplets of the aerosol can act as segregated, micron scale reaction vessels for synthesis. As the aerosol droplets proceed further into the heated reaction zone, precursor decomposition or solid state reactions occur to produce particles of the synthesized material [37]. The crystallization process takes place depending on the solubility of each material system, and nanocrystallites are synthesized forming spherical agglomerates according to the droplet size at the solubility limit. In the subsequent step sintering of the nanocrystallites takes place. The nanocrystalline powder is then collected using a glass fiber filter (Sartorius, Germany) collector, which is moderately heated (120 °C) to eliminate residual moisture using a heating tape (HBS 450, Horst, Germany).

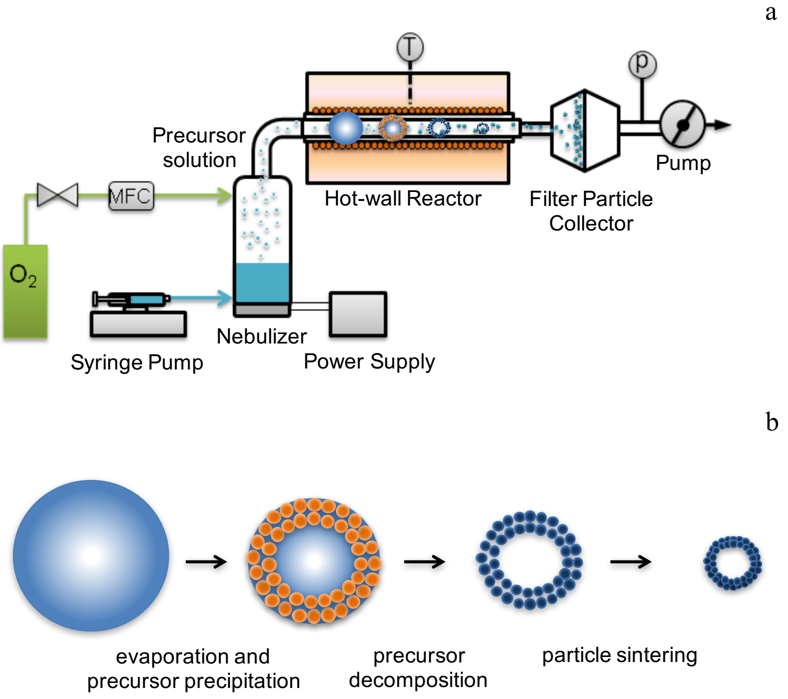

Figure 3-1: Nebulized spray pyrolysis synthesis setup (a), illustrated stages of particle formation during the NSP process (b).

Garnet type solid electrolytes as many other oxide materials are commonly synthesized using solid-state reactions, which typically require high temperatures above 1200 °C and long sintering times. The method of choice in this work is NSP because of its many advantages. NSP allows the production of nanocrystalline powders either directly in the desired crystal structure and phase composition [38] or as a precursor for further heat treatments. In the present work the latter applies and the as-synthesized powders are used for a further heat treatment (Chapter 5) to obtain the desired phase composition, i.e., cubic garnet type $Li_{7-3x}La_3Al_xZr_2O_{12}$. The nanocrystalline as-synthesized powder allows for the formation of the garnet structure at relatively low temperatures compared to solid-state reaction and requiring much shorter times. Additionally, NSP provides a very high yield up to 99% and it is scalable, since it allows for a continuous precursor solution delivery and continuous powder collection. The precise and reproducible adjustment of the concentration of the desired product phase by control of the precursor solution allows even the accurate control and homogeneous distribution of the desired Al-doping in the NSP process. A further advantage of NSP is the possibility to adjust the precursor amounts beforehand taking the loss of volatile elements into account. In the present work it is known that during heat treatment of the Li-containing compounds Li loss occurs especially in atmospheres containing moisture and CO_2 [39]. Therefore, the Li-excess, which is needed to compensate for these losses can be adjusted and added to the precursor solution.

The water-based precursor solution (total cation concentration 0.05 mol l^{-1}) is prepared in three steps. First, the Zr precursor ($Zr(C_5H_7O_2)_4$, ABCR, 98%) is dissolved in a small volume of methanol. Subsequently, the nitrate based precursors of Li, La and Al ($LiNO_3$, Sigma Aldrich, 99.99%, $La(NO_3)_3{\cdot}6H_2O$, Alfa Aesar, 99.9%, and $Al(NO_3)_3{\cdot}9H_2O$, Merck, 98.5%) are added to the methanol solution. Finally, deionized water is added to the precursor solution to maintain the desired concentration. A water to methanol volume ratio of 30:1 is used. The as-prepared mixture is then stirred for 1 h to produce a homogeneous transparent solution. The as-prepared precursor solution is nebulized inside the glass chamber using an ultrasonic generator (TDK, NB series, Japan) with an operating frequency between 1.6 and 1.75 MHz. The mist of the precursor solution is transported into the hot-wall reactor by flowing oxygen (5 SLM) regulated by a mass flow controller (MKS Instruments 1179A). A syringe pump (TSI) is used for continuous precursor delivery at a rate of 100 ml h^{-1} to maintain a constant level of precursor solution inside the nebulizer. The process pressure is held constant at 900 mbar using a Baratron absolute pressure gauge (MKS Instrument 628A) and a butterfly valve connected to a backing pump. The synthesis temperature is set to 900 °C and an oxygen gas flow of 5 SLM is adjusted. The reaction zone is approximately 400 mm long and the diameter of the alumina tube (Degussit AL23, Friatec, Germany) is approximately 20 mm.

3.2 Conventional sintering

For the application as a solid electrolyte, the as-synthesized nanocrystalline powders have to be processed into bulk structures with high density using sintering. During sintering the microstructure is substantially altered, i.e., extensive grain growth typically occurs depending on the processing conditions such as temperature, time and pressure. The final properties depend crucially on the microstructure. During sintering, controlling the densification and the grain growth separately presents the biggest challenge. An intergranular position of the pores is optimal for successful densification, since the matter movement at moderate temperatures is dominated by the grain boundary diffusion. Rapid grain growth by grain boundary migration and separation of the pores from the grain boundaries resulting in intragranular trapping of the pores and further densification becomes more difficult, because these pores can only be eliminated by volume diffusion [40]. Consequently, to achieve high densities the grain growth has to be limited.

Solid state sintering takes place in three successive stages. The initial stage consists of neck formation between spherical particles. The radius of the neck is dependent on the radius of the particle, the diffusion coefficient and two parameters depending on the diffusion process taking place [40]. Followed by the intermediate stage, where the polyhedral grains are interconnected at their common facets. The pores build a canal system along the edges common to three grains. The interconnection of the open porosity remains present, as long as the density does not exceed 92% of the theoretical density. In the final stage of solid state sintering the porosity is closed, while isolated pores remain at quadruple points between the grains or are trapped intragranularly [40].

On the other hand, when a melt is formed during the sintering process, it is considered liquid phase sintering. Liquid phase sintering also takes place in three stages. The first is viscous flow and grain rearrangement. When the liquid is formed the viscous flow allows for the rearrangement of the grains, by dissolving the surface roughness and small particles. If the liquid phase is present in sufficient quantity complete densification is possible. The second stage is solution and reprecipitation, where the solid is increasingly soluble in the liquid at contact points between the particles. The matter transport to low energy surfaces leads to densification. The development of the solid skeleton is the third stage of liquid phase sintering, where the liquid phase is gradually eliminated by the formation of new crystals or a solid solution, starting at this point the elimination of residual porosity is similar to the last stage of the solid state sintering process [40]. The main parameters that control the liquid phase sintering are: i. quantity of the liquid phase, ii. the viscosity of the liquid, iii. its wettability in respect to the solid, iv. the solubility of the liquid in the solid and the solid in the liquid. The optimal case would be having a liquid phase that fills all the open pores surrounding the particles, allowing for grain rearrangement. The viscosity should not be too high hindering the grain rearrangement, nor too low allowing deformation of the sintered ceramic. The wetting of the particles needs to be present and the solubility in the solid in the liquid phase is imperative for densification, while a high solubility of the liquid in the solid might lead to swelling accompanying the densification [40].

Conventional sintering during this work is performed at 1000 °C for a dwell time of 1 h in an air-filled chamber furnace (Nabertherm).

3.3 Field assisted sintering

In recent years, field assisted sintering technology (FAST) also known as spark plasma sintering (SPS) is widely applied for material synthesis as well as sintering. It is a low voltage, pulsed direct current activated, pressure assisted process [41]. The mechanical loading system, which also acts as high-power electrical circuit, is placed in a controlled atmosphere. The voltage used is typically below 10 V, due to the good electrical conductivity of the tooling materials, typically graphite. The current is typically in the range of 1 kA to 10 kA [41]. Depending on the hardware the pulse pattern can be adjusted. Heating rates as high as 1000 °C min^{-1} are possible, which reduces the process duration and cost [42]. The standard cooling rate is usually 150 °C min^{-1}, active cooling using gas flow enables quenching rates of 400 °C min^{-1}. The process is conducted under vacuum or under protective gas. The processing cycle is usually controlled by temperature measurement, which occurs through either a pyrometer or a thermocouple, depending on the temperature range. The maximum temperature using graphite tools is 2400 °C [41]. The resistance of the tool assembly, influenced by the tool dimensions and material, has a significant impact on the temperature distribution within the sample and tool [43]. During this study FAST (Dr. Sinter Lab 211-Lx) graphite foils were used to isolate the specimen from the carbon die (final diameter 7 mm). The foils are coated with boron nitride spray to prevent any carbon diffusion into the sample and to minimize possible reduction processes. A temperature of 950 °C is set, after an extensive optimization procedure. During heating at a rate of 100 °C min^{-1} an initial pressure of 15 MPa is set to provide good contact between the tool parts. A pressure between 20 MPa and 50 MPa is applied during the dwell time which ranges between 3 min and 10 min. A vacuum sintering atmosphere at 10^{-2} mbar is used as well as a protective Ar atmosphere, which is introduced at 500 °C during heating to ensure a comparable adsorbate evaporation rate to the samples sintered under vacuum. Since cool down under Ar atmosphere is faster than cooling under vacuum, a cooling rate is set to 100 °C min^{-1} for the sintering process performed under Ar also to provide good comparability.

4 LLZO ceramics by conventional sintering

The majority of the results presented in this chapter have already been published in Solid State Ionics [44].

Nebulized spray pyrolysis (NSP) can produce nanocrystalline powders, which is advantageous for further processing of the material at lower temperatures and shorter times compared to microcrystalline powders, e.g., produced by solid state reaction [5,45]. After consolidation and sintering times as short as 1 h at a moderate temperature of 1000 °C, compared to temperatures above 1200 °C as commonly used for conventional solid state routes [5], ion conducting ceramics are obtained. The Al-doped $Li_7La_3Zr_2O_{12}$ (LLZO) pellets are characterized using X-ray diffraction (XRD) to determine the phase composition, lattice parameters and crystallite size. The theoretical densities (TD) are determined using the crystallite densities of the different phases and their phase fractions obtained from Rietveld analysis and compared to the measured geometrical densities. As there have been different statements in literature concerning the Al coordination and whether the dopant resides on a Li site [23,46–48] or on a La site and/or Zr site [49,50], ^{27}Al MAS NMR is utilized to determine the oxygen coordination of the dopant and therefore its position in the garnet structure. Furthermore, inductively coupled plasma optical emission spectroscopy (ICP-OES) is employed to determine the actual stoichiometry of the sintered ceramics. A microstructural analysis is performed for all powder samples. Ceramic samples are characterized using scanning electron microscopy (SEM) on cross sections prepared by focused ion beam (FIB). The Li-ion conductivity is determined using alternating current impedance spectroscopy (AC-IS).

4.1 Material properties

The as-synthesized powders directly after the NSP procedure (synthesis temperature 900 °C) do not contain the desired garnet phase, but consist of the CaF_2-type phase $La_{0.5+\delta}Zr_{0.5\text{-}\delta}O_{1.75\text{-}\delta/2}$ ($Fm\bar{3}m$), Li_2CO_3 and La_2O_3. A direct synthesis of the garnet type structure was attempted using higher temperatures up to 1300 °C and a longer reaction zone, still resulting in the formation of mainly the CaF_2-type phase and no indication of a garnet structure. During the conventional sintering process, the as-synthesized powders not only undergo a liquid phase sintering process (melting point of Li_2CO_3 723 °C) but also a chemical reaction is taking place, simultaneously. The $Li_{7\text{-}3x}La_3Zr_2Al_xO_{12}$ ceramics obtained after sintering are synthesized using a wide range of Al-doping from $x = 0$ up to 0.25.

4.1.1 Structure and composition

The X-ray diffraction patterns for the as-synthesized powders ($x =$ 0, 0.07, 0.10, 0.15, 0.17, 0.20 and 0.25) powders are shown in Figure 4-1. All samples exhibit a similar phase composition with a main phase fraction of the CaF_2 type structure $La_{0.5+\partial}$ $Zr_{0.5\text{-}\partial}$ $O_{1.75\text{-}\partial/2}$ ($Fm\bar{3}m$) with a crystallite size in the range between 7 and 9 nm. Li_2CO_3 ($C2/c$) and a small amount of La_2O_3 ($P\bar{3}m$) are present as secondary phases. A similar phase composition is also reported for samples synthesized using the sol-gel Pechini method [51]. An overview of phase compositions and crystallite sizes for all studied as-synthesized samples obtained from Rietveld refinement of the diffraction data is given in Table 4-1.

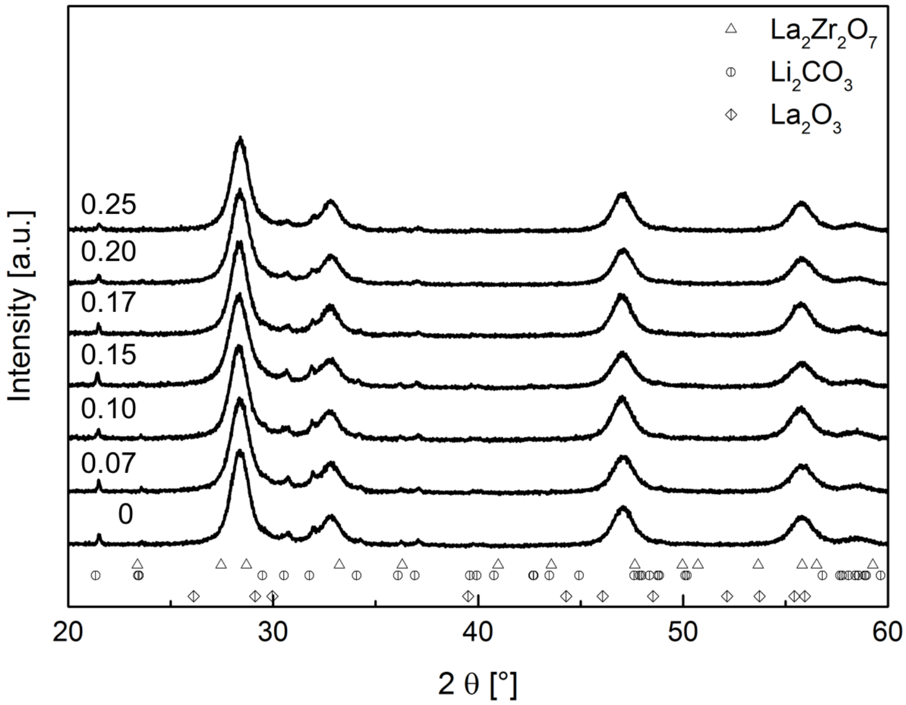

Figure 4-1: X-ray diffraction patterns of the as-synthesized powders with different Al-contents. The symbols represent Bragg's positions of each phase present.

Table 4-1: Overview of phase compositions (standard deviation < 1 wt.%) and crystallite sizes (standard deviation 1 nm) for all as-synthesized powders obtained from Rietveld refinement of X-ray diffraction data.

Nominal content	$La_{0.5+\partial}Zr_{0.5-\partial}O_{1.75-\partial/2}$ $(Fm\overline{3}m)$		Li_2CO_3 $(C2/c)$		La_2O_3 $(P\overline{3}m)$	
x	Phase fraction [wt.%]	Cryst. size [nm]	Phase fraction [wt.%]	Cryst. size [nm]	Phase fraction [wt.%]	Cryst. size [nm]
0	59	7	38	14	3	1
0.07	62	8	34	19	4	1
0.10	65	8	31	32	4	1
0.15	62	8	34	22	4	1
0.17	66	8	30	21	4	1
0.20	63	8	32	16	5	1
0.25	64	9	32	15	4	1

To obtain bulk ceramics, the as-synthesized powders were consolidated using a uniaxial press and sintered at 1000 °C for 1 hour in air. Al diffusion from the alumina crucible can be excluded, since the pellets were imbedded in their mother powder during sintering. The phase composition of the sintered ceramics is highly dependent on the Al-doping. Corresponding diffraction patterns are shown in Figure 4-2. The sample without Al exhibits, as expected, the tetragonal garnet structure ($I4_1/acd$) with a small La_2O_3 impurity. With increasing Al-content the cubic modification starts to form, presumably stabilized at ambient conditions by the heterovalent substitution of 3 Li^+ by Al^{3+} [23]. Reaching an Al-content of $x = 0.15$ a pure cubic garnet structure ($Ia\bar{3}d$) is present. Further increase of the Al-doping leads to the formation of the impurity phase $La_{0.5+\partial}Zr_{0.5-\partial}O_{1.75-\partial/2}$ and at an Al-content of $x = 0.25$ an additional $LaAlO_3$ phase is present. An overview of phase compositions obtained from the Rietveld refinement is presented in Table 4-2.

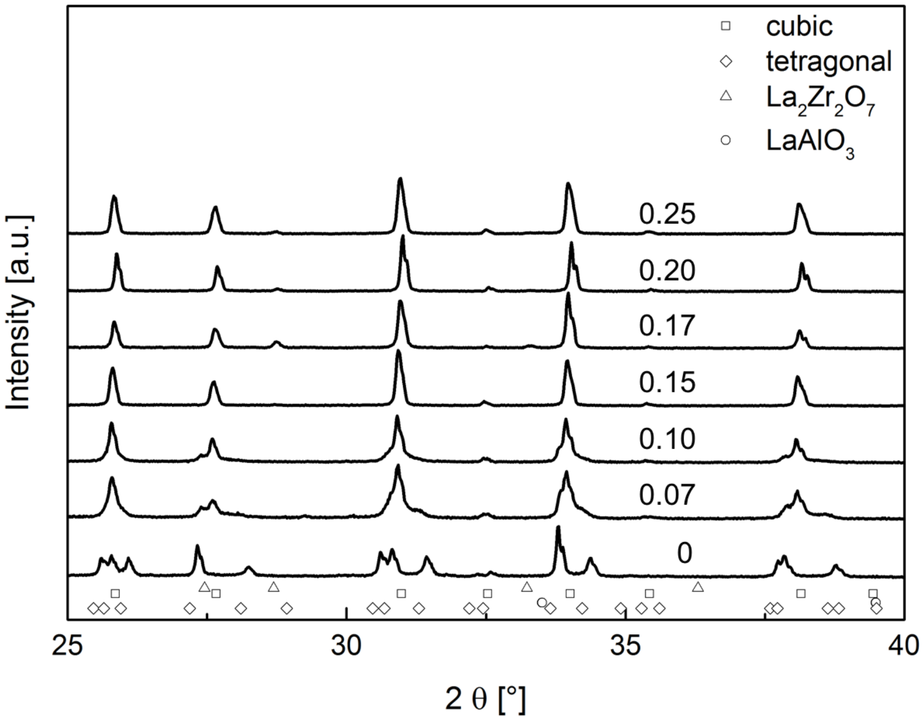

Figure 4-2: X-ray diffraction patterns of $Li_{7-3x}La_3Zr_2Al_xO_{12}$ sintered ceramics with different Al-contents at 1000 °C for 1 hour in air. The symbols represent Bragg's positions of each phase present.

Table 4-2: Rietveld refinement data for sintered ceramics with different nominal Al-contents.

x	cubic [wt.%]	tetragonal [wt.%]	$La_{0.5+\partial}Zr_{0.5-\partial}O_{1.75-\partial/2}$ [wt.%]	La_2O_3 [wt.%]	$LaAlO_3$ [wt.%]
0	0	99.4(1)	0	0.6(1)	0
0.07	31.8(4)	67.4(4)	0	0.8(5)	0
0.10	87.6(2)	11.7(2)	0	0.7(1)	0
0.15	100.0(1)	0	0	0	0
0.17	94.4(1)	0	5.6(1)	0	0
0.20	98.4(1)	0	1.6(1)	0	0
0.25	97.9(1)	0	1.3(1)	0	0.8(1)

A first indication for the Al^{3+} incorporation into the garnet lattice is the change in lattice parameter. The evolution of the lattice parameters of the cubic and tetragonal structures are presented in Figure 4-3. In the tetragonal phase, lattice parameter a decreases with increasing Al-content from $x = 0$ to 0.10, while c increases. The lattice parameter of the cubic garnet structure decreases with increasing Al-content from 12.9798(8) Å ($x = 0.07$) to 12.9705(1) Å ($x = 0.25$). This can be explained by the smaller ionic radius of Al^{3+} compared to Li^+ [52]. On the other hand a substitution of Zr^{4+} was also reported by Raskovalov et al. in $Li_7La_3Zr_{2-0.75x}Al_xO_{12}$, which would lead to a decrease in the lattice parameter according to the smaller Al^{3+} ionic radius [50].

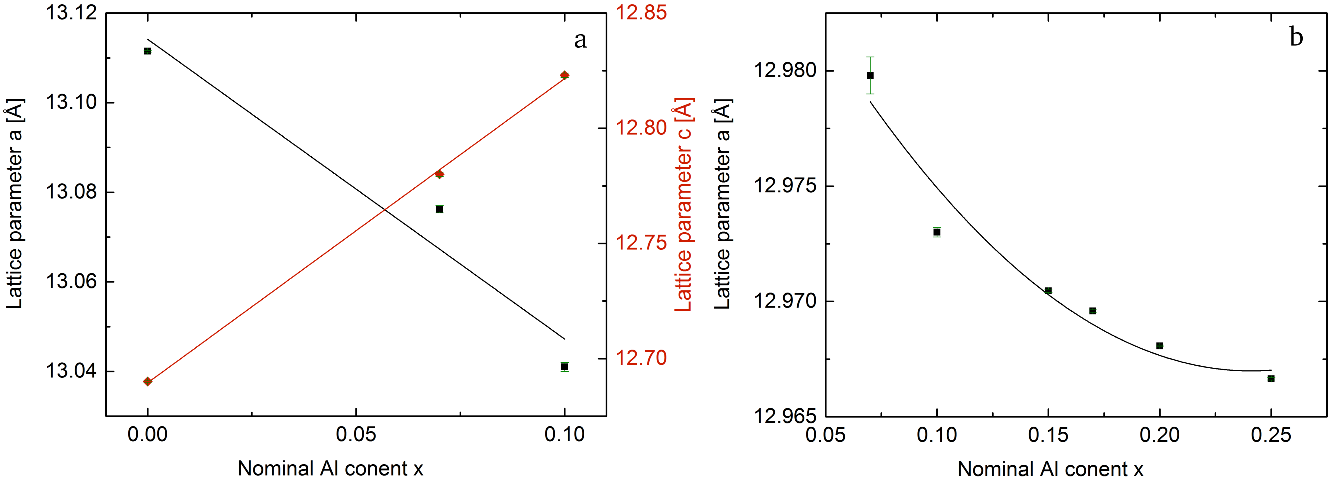

Figure 4-3: Dependence of the lattice parameters on the nominal Al-content of the tetragonal phase (a) and cubic phase (b) obtained by Rietveld refinement.

To determine whether the Al is incorporated on the Li site with tetrahedral coordination or on the Zr site that has an octahedral coordination, ^{27}Al MAS NMR was performed on a crushed pellet with pure cubic structure ($x = 0.15$). The spectrum is depicted in Figure 4-4. Only one peak is observed with a chemical shift of 65 ppm similar to what has been found by Hubaud et al. [48], which corresponds to a tetrahedral coordination. This proves the heterovalent substitution of 3 Li^+ by Al^{3+} and that the Al^{3+} ions are incorporated into the garnet structure.

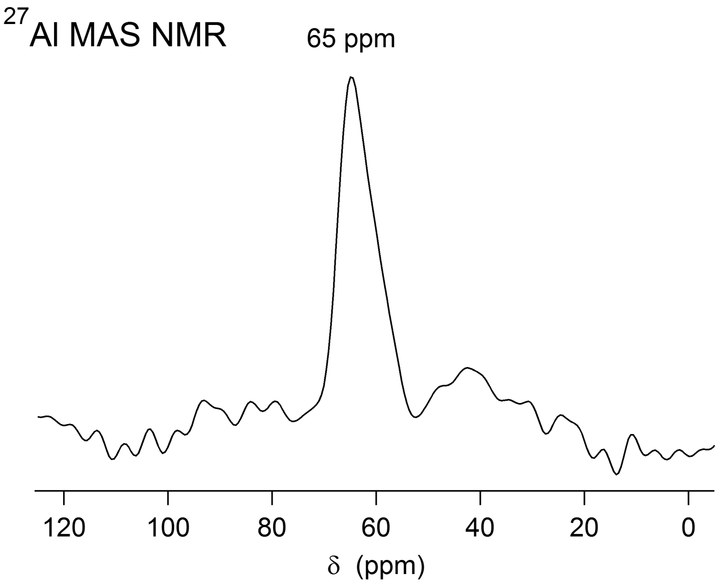

Figure 4-4: ^{27}Al MAS NMR spectrum of the purely cubic $Li_{7-3x}La_3Zr_2Al_xO_{12}$ sample with $x = 0.15$.

As it was previously mentioned, starting from an Al-content of $x = 0.17$ a $La_2Zr_2O_7$ impurity phase starts to arise. This phase is formed due to Li loss from the garnet structure, an interplay between excessive Al substitution and the Li loss mechanism related to the presence of moisture and CO_2 (see section 5.1). Although the sintering temperature did not exceed 1000 °C, opposed to sintering temperatures reported in the literature [39,47,53], Li loss could still occur. The green ceramic bodies in this work are formed by consolidating a nanocrystalline powder, in contrast to microcrystalline powders used for solid state reaction routes. This microstructure increases the surface area exposed to the surrounding atmosphere and consequently promotes the Li loss, in the form of volatile Li containing compounds. Since the ionic conductivity, which is a measure for the successful preparation of the solid electrolyte, is strongly dependent on the actual Li-content acting as a charge carrier, ICP-OES was performed to determine the actual composition of the sintered ceramics. As depicted in Figure 4-5 the actual Li-content is in good agreement with the nominal Li-content, due to the 30 wt.% Li excess used during synthesis and conventional sintering performed in a sealed crucible. Furthermore, the actual and nominal Al-contents are in very good agreement, leading to the conclusion that the synthesis using NSP allows for precise doping. Detailed ICP-OES results are presented in Table 4-3.

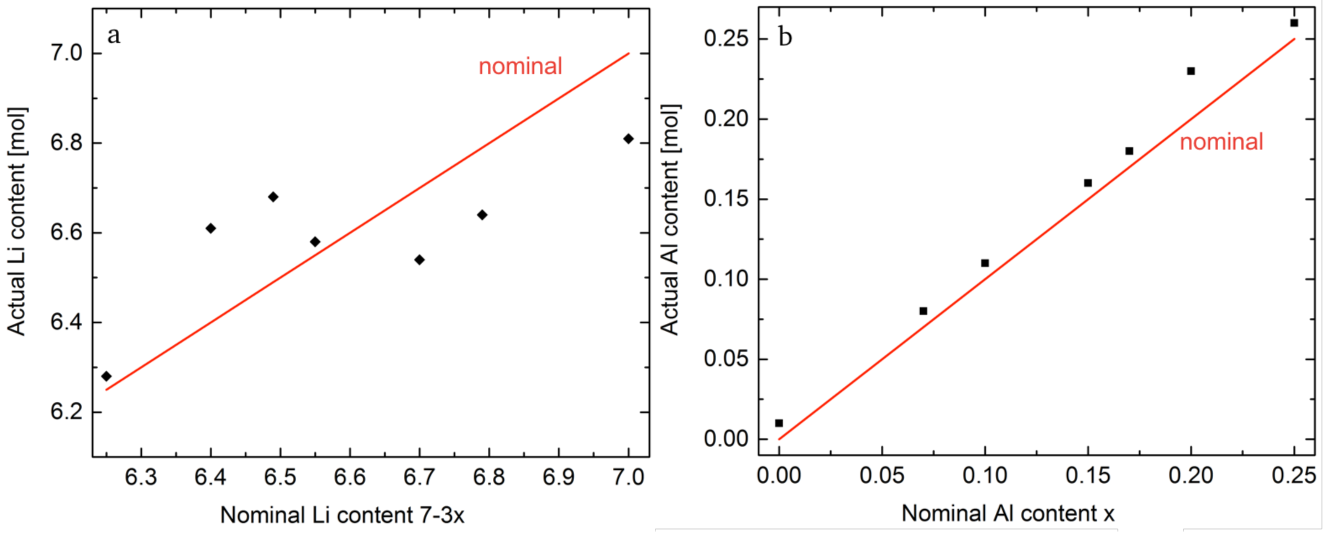

Figure 4-5: The actual Li (a) and Al (b) contents determined by ICP-OES analysis, compared to the nominal Li and Al contents.

Table 4-3: ICP-OES results for $Li_{7-3x}La_3Zr_2Al_xO_{12}$ sintered ceramics. Nominal values are given in parenthesis (standard deviation: ±1.5%).

Al	Li	Li:La	Li:Zr	Zr:La	Al:La
0.006(0)	6.81 (7.00)	2.27 (2.33)	3.50 (3.50)	0.65 (0.67)	0.002 (0.0)
0.08(0.07)	6.64 (6.79)	2.21 (2.26)	3.41 (3.40)	0.65 (0.67)	0.03 (0.02)
0.11(0.10)	6.54 (6.70)	2.18 (2.23)	3.30 (3.35)	0.66 (0.67)	0.04 (0.03)
0.16(0.15)	6.58 (6.55)	2.19 (2.18)	3.27 (3.28)	0.67 (0.67)	0.05 (0.05)
0.18(0.17)	6.68 (6.49)	2.23 (2.16)	3.35 (3.25)	0.67 (0.67)	0.06 (0.06)
0.23(0.20)	6.61 (6.40)	2.20 (2.13)	3.21 (3.20)	0.69 (0.67)	0.07 (0.07)
0.26(0.25)	6.28 (6.25)	2.09 (2.08)	3.09 (3.13)	0.68 (0.67)	0.09 (0.08)

4.1.2 Microstructure

The microstructure of the as-synthesized powders, which do not contain the garnet type phase, is typical for samples synthesized by NSP and is shown in Figure 4-6. The powder consists of spherical particles with diameters up to 5 μm. The particles are hollow with a thin shell composed of nanoparticles of about 10 nm in size as shown in Figure 4-6 b, which is in good agreement with the crystallite size obtained by X-ray diffraction. Around the hollow particle a shell of a phase that is translucent to the electron beam is visible, and most probably corresponds to Li_2CO_3.

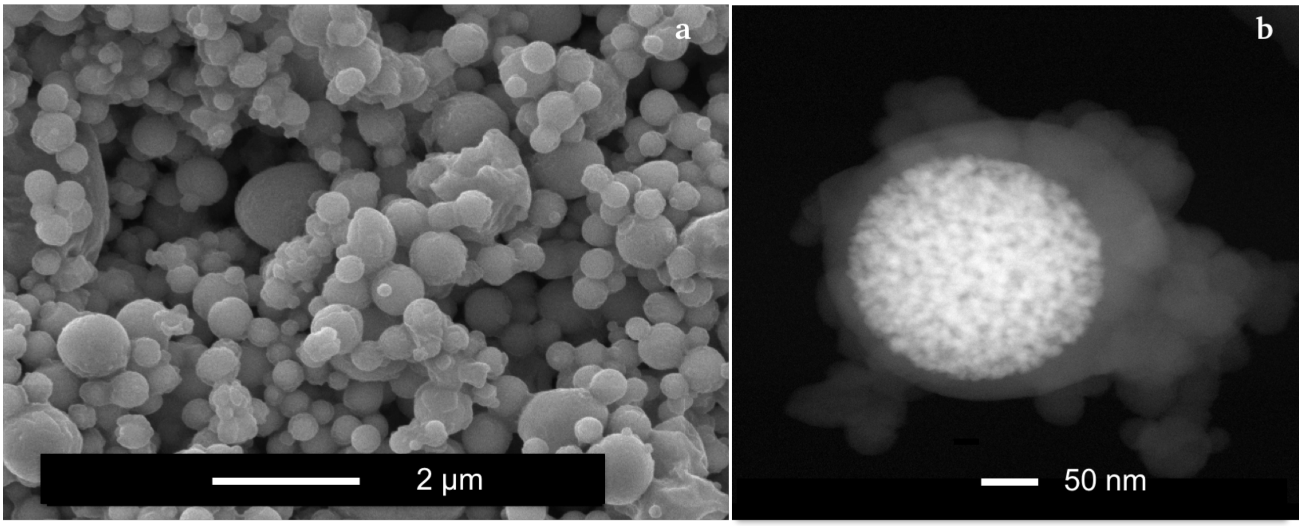

Figure 4-6: SEM image of the as-synthesized powder ($x = 0$) (a) and STEM image of one particle containing nanocrystals (b).

The micrographs of FIB cross sections of the sintered ceramics are shown in Figure 4-7. All samples exhibit high porosity throughout the whole Al range. It has been reported that an increase of the Al-doping would increase the sinterability and therefore decrease porosity of the ceramics [54,55], but in this work this observation is not made. The densities, which are determined geometrically and related to the theoretical density (TD) obtained by Rietveld refinement, range between 43% TD and 56% TD. All samples exhibit two types of microstructures, one representing the bulk of the material and the second surrounding the large pores. During imaging with an acceleration voltage of only 5 kV the second microstructure dissolves indicating a decomposition process due to the electron beam. Since the material is sintered in air it can be assumed that this second microstructure most probably represents the Li_2CO_3 phase, for which beam sensitivity has been reported [56]. Li_2CO_3 is formed at the surface of the material due to exposure to moisture and CO_2. Due to open porosity, these surface effects extend into the interior of the ceramic.

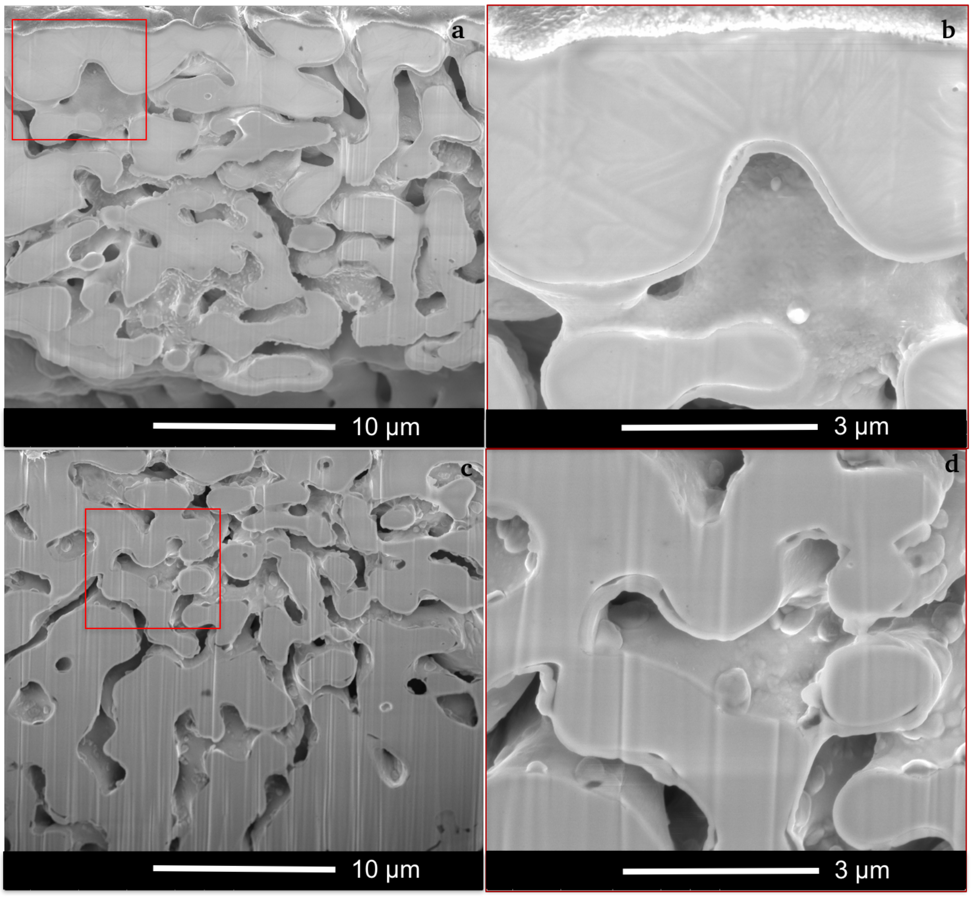

Figure 4-7: Cross sectional SEM micrographs prepared by FIB of sintered $Li_{7-3x}La_3Zr_2Al_xO_{12}$ ceramics at 1000 °C for 1 hour with $x = 0$ (a,b) and $x = 0.15$ (c,d).

4.2 Electrochemical performance

Despite the low density obtained after conventional sintering at 1000 °C for 1 hour, the Li-ion conductivity was determined using AC-impedance spectroscopy. The Nyquist plots for the different Al-contents and the equivalent circuits are shown in Figure 4-8, while the fit results are presented in Table 4-4. While all the spectra show three distinctive semi-circles, the capacitance of the third semi-circle is in the order of 10^{-8} F and 10^{-9} F for the samples with $x = 0$ and 0.07, respectively, which corresponds to a grain boundary contribution to the spectrum. For samples with higher Al-contents the capacitance is in the order of 10^{-7} F corresponding to a surface layer between the pellet and the Au electrodes. A blocking behavior, as seen in Figure 4-8, is observed for all spectra. The Li-ion conductivity of the sample with $x = 0$ composed of mostly the tetragonal garnet structure is 1.18 μS cm^{-1}, while in the sample with $x = 0.15$, which is purely cubic, the conductivity is 4.4 μS cm^{-1}. The highest reported conductivity value for the tetragonal garnet structure is 23 μS cm^{-1} for a sample with 98% TD [27], while the best Li-ion conductivity reported for a cubic garnet structure with 99.8% TD is 570 μS cm^{-1} [57]. Furthermore, Takano et al. reported one order of magnitude enhancement of the conductivity from 1.6 μS cm^{-1} to 19 μS cm^{-1} with increase of the relative density from 58% TD to 78% TD for a $Li_{7-3x}La_3Zr_2Al_xO_{12}$ ($x = 0.3$) ceramic prepared by a sol-gel process. The increase of density is achieved by introducing a sintering additive, Li_3BO_3 [58]. Therefore, the one order of magnitude lower conductivity for the tetragonal structure and two orders of magnitude lower conductivity values for the cubic structure reported here are most likely related to the low density of the pellets.

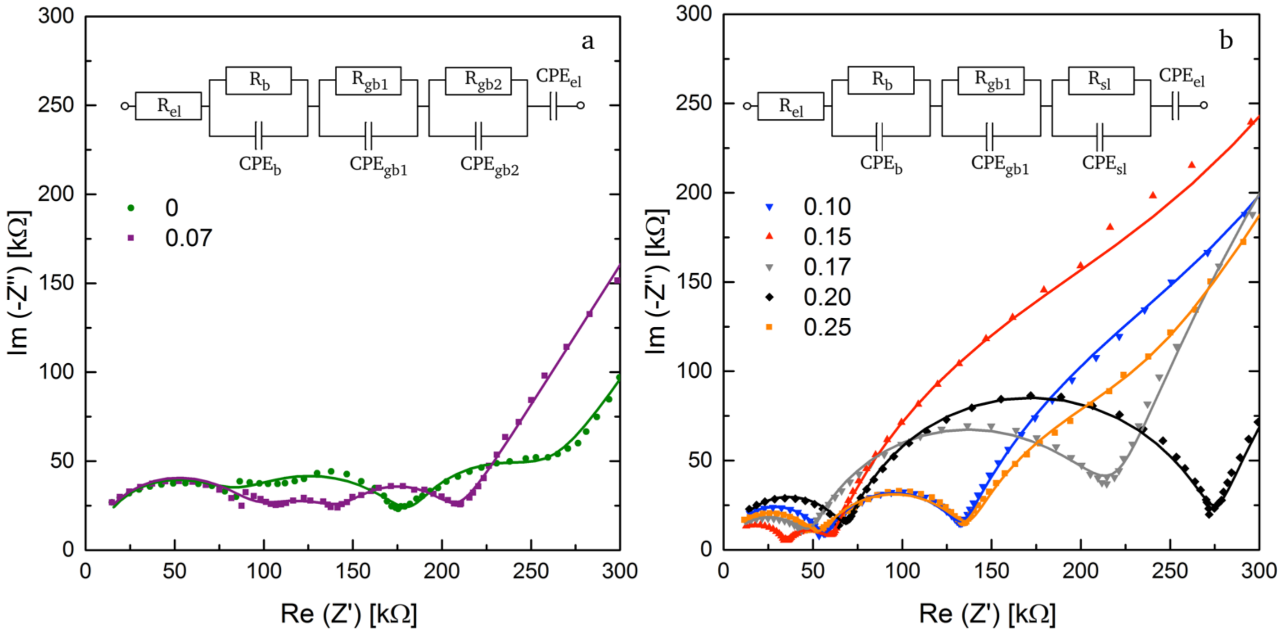

Figure 4-8: Nyquist plots and corresponding fits for $Li_{7-3x}La_3Zr_2Al_xO_{12}$ samples with $x = 0$ and 0.07 (a) and $x = 0.10$, 0.15, 0.17, 0.20 and 0.25 (b) using blocking Au electrodes at room temperature.

Table 4-4: AC-IS fit results and goodness of fit χ^2 for the measurement of the solid electrolyte with Au electrodes. R: resistance, Q and n: CPE fit parameters and C: capacitance.

x	R_b [kΩ]	Q_b [pF]	n_b	C_b [pF]	R_{gb1} [kΩ]	Q_{gb1} [nF]	n_{gb1}	C_{gb1} [nF]	R_{gb2} [kΩ]	Q_{gb2} [nF]	n_{gb2}	C_{gb2} [nF]	χ^2 10^{-4}
0	80	31	0.89	6.0	108	2.2	0.75	0.14	66	31	0.98	27	8
0.07	93	42	0.86	5.9	53	2.4	0.83	0.34	52	6.9	1	6.0	9
0.10	56	28	0.89	5.7	743	5.4	0.87	1.6	-	-	-	-	6
0.15	35	73	0.84	6.4	223	6.2	0.91	2.4	-	-	-	-	3
0.17	48	150	0.80	7.9	169	5.9	0.83	1.4	-	-	-	-	6
0.20	66	23	0.91	6.4	207	2.4	0.87	9.3	-	-	-	-	6
0.25	52	87	0.83	7.9	84	13	0.79	2.0	-	-	-	-	6

Temperature dependent measurements are conducted between 22 °C and 65 °C for all samples and the corresponding Arrhenius plots are presented in Figure 4-9. The resulting activation energies of both samples with $x = 0$ and $x = 0.15$ are 0.55 eV and 0.49 eV, respectively. Table 4-5 summarizes the results for the total ionic conductivity, activation energies and their corresponding densities. There is no direct correlation between the relative density and the activation energies for the different samples, nevertheless the values for the activation energies throughout the whole Al-doping range are higher than the reported values for the tetragonal as well as the cubic garnet structures. These values usually are between 0.31 eV [5] and 0.36 eV [59] for the cubic structure and from 0.41 eV [27] to 0.49 eV [47] for the tetragonal modification. Again, the higher activation energies reported in this study are most likely due to the low relative densities of the pellets, which leads to an increased grain boundary resistance, thus increasing the activation energy for total conductivity.

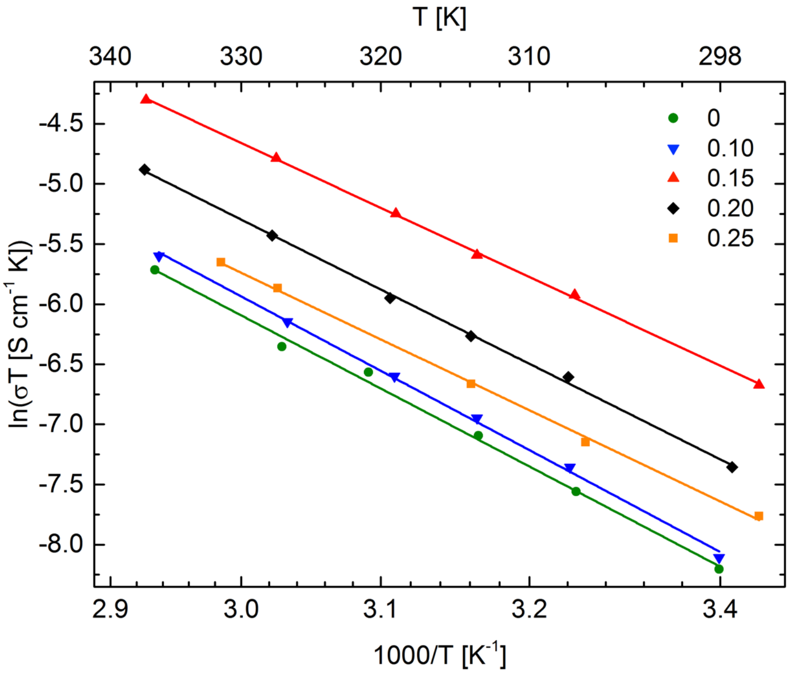

Figure 4-9: Arrhenius plot presenting the temperature dependence of the Li-ion conductivity between 295 K and 338 K for different Al-contents.

Table 4-5: Overview of room temperature total Li-ion conductivity and activation energy in relation to the Al-content *x* and relative density.

x	Total conductivity [μS cm^{-1}]	Activation energy [eV]	Relative density [% TD]
0	1.18	0.55	47
0.07	1.40	-	52
0.10	2.01	0.53	54
0.15	4.39	0.49	51
0.17	1.05	-	56
0.20	1.04	0.56	43
0.25	1.54	0.50	52

4.3 Conclusion and summary

While nebulized spray pyrolysis as a novel synthesis method for garnet Li-ion conductors is successfully combined with simple consolidation and conventional sintering at relatively low temperatures and short times to obtain LLZO ceramics, the main challenge using this method lies in the achievement of a high density, which is crucial for reaching high ionic conductivity and a reduction of the activation energy. The sintering temperature is one of the main parameters that could be increased to achieve higher densities. Higher temperatures, however, might lead to an increase in Li loss from the garnet structure, especially since the starting material is nanocrystalline and shows higher reactivity than the microcrystalline material usually used in the literature [60,61]. Since a higher sintering temperature cannot be used, other sintering methods were explored as alternatives, e.g., hot pressing (HP) and field assisted sintering technology (FAST) to achieve higher densities. In Chapter 5, the optimization of LLZO powder properties is reported with special emphasis on obtaining the desired phase composition to allow for the application of these techniques. The 4-fold increase of ionic conductivity of the purely cubic ceramic compared to the tetragonal counterpart contradicts the expected difference of one to two orders of magnitude. According to recent findings the presence of moisture and CO_2 influences the ionic conductivity through proton exchange reactions and formation of Li_2CO_3, especially at elevated temperatures [62,63]. The proton exchange leads to an overestimation of the ionic conductivity, since not only the Li^+ ions are investigated as charge carriers but also H^+ ions. Although the samples are stored under an argon atmosphere, the impedance measurements are performed in air atmosphere. Therefore, a partial proton conductivity cannot be excluded.

5 Optimization of LLZO powder properties

One of the main challenges facing the preparation of a LLZO solid electrolytes lies in the achievement of a high density [44]. It is expected that the use of FAST can overcome these issues leading to high ionic conductivities. While the field assisted sintering process allows for reactive sintering [57], unpublished data show that a phase transformation of the powder as-synthesized using NSP to the desired cubic LLZO phase is not achievable at moderate temperatures (<1100 °C), where Li loss can be minimized. Therefore, the as-synthesized powder requires a further calcination step to achieve the desired cubic garnet structure, which exhibits superior ionic conductivity compared to its tetragonal counterpart [5,23]. During calcination not only the phase transformation occurs but also a change of the microstructure. The parameters of the calcination process are optimized according to the phase composition of the calcined powder. NSP allows for the synthesis of powders with precise Al-doping, which enables the optimization of not only the calcination temperature and time but also of the Al-content. The Li/Al ratio has a significant influence on the calcination behavior of the powder and the resulting phase composition. The influence of the calcination atmosphere on the phase composition of the powder is also studied using high temperature X-ray diffraction and is correlated to differential thermal analysis and thermogravimetric analysis (DTA-TGA). There are no high temperature diffraction data in the literature that provide information about the reaction process from the as-synthesized powder, i.e., $La_{0.5+\partial}Zr_{0.5-\partial}O_{1.75-\partial/2}$ and Li_2CO_3 to the cubic garnet phase. In this study NSP provides the advantage of producing a nanocrystalline powder as a starting material, leading to significantly shorter reaction times at relatively low temperatures. The composition of the starting powder needs to be taken into consideration when comparing this work to the work reported, e.g., by Matsui et al. [64], where the starting material is the tetragonal garnet structure.

5.1 Influence of the calcination atmosphere

The calcination atmosphere has an immense impact on the phase composition and subsequently on the electrochemical performance of the solid electrolyte. It has been reported that the observed Li loss during heat treatment originates in reactions involving H_2O and CO_2 from the air atmosphere. Cheng et al. suggests the following reactions [39]:

$$Li_{56}La_{24}Zr_{16}O_{96}\,(s) + H_2O\,(g) \;=\; Li_{54}La_{24}Zr_{16}O_{95}\,(s) + 2LiOH\,(s) \qquad [\,5\text{-}1\,]$$

$$Li_{56}La_{24}Zr_{16}O_{96}\,(s) + CO_2\,(g) \;=\; Li_{54}La_{24}Zr_{16}O_{95}\,(s) + Li_2CO_3\,(s) \qquad [\,5\text{-}2\,]$$

Since these reactions occur under the presence of moisture there are two approaches utilized during this work to prevent moisture adsorption. For the calcination of the as-synthesized powder under air, the powder is removed from the furnace at 300 °C and placed in an Ar atmosphere during further cooling to room temperature. In the second approach to eliminate these reactions flowing inert Ar atmosphere is used during the whole calcination process.

High temperature X-ray diffraction is performed during the calcination of as-synthesized powders under different atmospheres, namely static air and flowing Ar. The powder samples are filled into a 0.4 mm deep Al_2O_3 sample holder for the high temperature measurements. Although interaction with the sample holder might occur, it is assumed that the X-ray penetration depth does not exceed 100 μm and therefore the measurement of the powder in direct contact with the sample holder can be eliminated. The as-synthesized powder is heated in the first cycle between 30 °C to 1000 °C. A dwell time of approximately 90 min is set at the highest temperature during which two diffractograms are collected. The heating and cooling rates are 5 °C min^{-1} and 10 °C min^{-1}, respectively. The heating and cooling of the sample is repeated and diffraction patterns are collected with a collection time of 30 min. Even though the samples experience different time-temperature history during the high temperature X-ray diffraction than during furnace calcinations, the resulting data can provide good insight into the influence of the calcination atmosphere on the phase composition.

The calcination process of as-synthesized powder with a doping level of $x = 0.22$ and a 30 wt.% Li excess during synthesis is investigated using high temperature X-ray diffraction and the patterns collected under static air are shown in Figure 5-1. No change of the phase composition is observed starting at 30 °C up to 600 °C. The main CaF_2-type phase $La_{0.5+\partial}\,Zr_{0.5-\partial}\,O_{1.75-\partial/2}$ ($Fm\bar{3}m$), Li_2CO_3 as well as a small amount of La_2O_3 are detected. Between 600 °C and 700 °C the formation of the cubic garnet structure (33 wt.%) sets in alongside the formation of a $LaAlO_3$ phase (5 wt.%) and the persistent CaF_2-type phase (62 wt.%). Li_2CO_3 is no longer detectable at 700 °C. Between 770 °C and 800 °C the CaF_2-type phase completely disappears. The cubic phase composition obtained at 800 °C remains unchanged up to 1000 °C. After a holding time of 60 min, where the second pattern at 1000 °C is recorded for 30 min, a $La_2Zr_2O_7$ impurity phase with a pyrochlore type structure ($Fd\bar{3}m$), with double the lattice parameter of the starting material, starts to emerge once again with a phase fraction of approximately 0.5 wt.% according to Rietveld refinement and persists with gradual increase throughout further cooling reaching 1 wt.%. The second heating step is carried out without delay, during which the cubic garnet structure is stable with a detectable increase of the $La_2Zr_2O_7$ phase fraction starting at approximately 900 °C reaching 2.4 wt.% at 1000 °C. The pyrochlore impurity phase increases upon heating to 1000 °C and cooling down to 30 °C. This result gives a clear indication, that the formation of the pyrochlore impurity phase takes place at temperatures higher than 900 °C, due to the increased Li loss under air. The cubic garnet structure is known not only to be stabilized by a heterovalent doping, e.g., Al^{3+} and Ga^{3+}, but also by CO_2 adsorption [65]. The CO_2 stabilized cubic structure exhibits a low ionic conductivity and is referred to as the low temperature cubic phase, as opposed to the superior ionically conductive high temperature cubic phase. The second heating step under air does not show a formation of a tetragonal structure at temperatures ranging from 450 °C to 600 °C, which is the expected range for CO_2 desorption [64]. This leads to the conclusion, that the high temperature cubic garnet structure is stabilized through Al-doping, which is incorporated into the lattice in the first heating cycle between 600 °C and 800 °C creating Li vacancies. Since CO_2 adsorption cannot be excluded during air calcination, the fact that a CO_2 stabilization did not take place indicates that a CO_2 incorporation is necessary to stabilize the low temperature cubic phase [64]. For a fully Al-stabilized cubic structure it seems that a CO_2 incorporation into the garnet lattice is not observed in the present work.

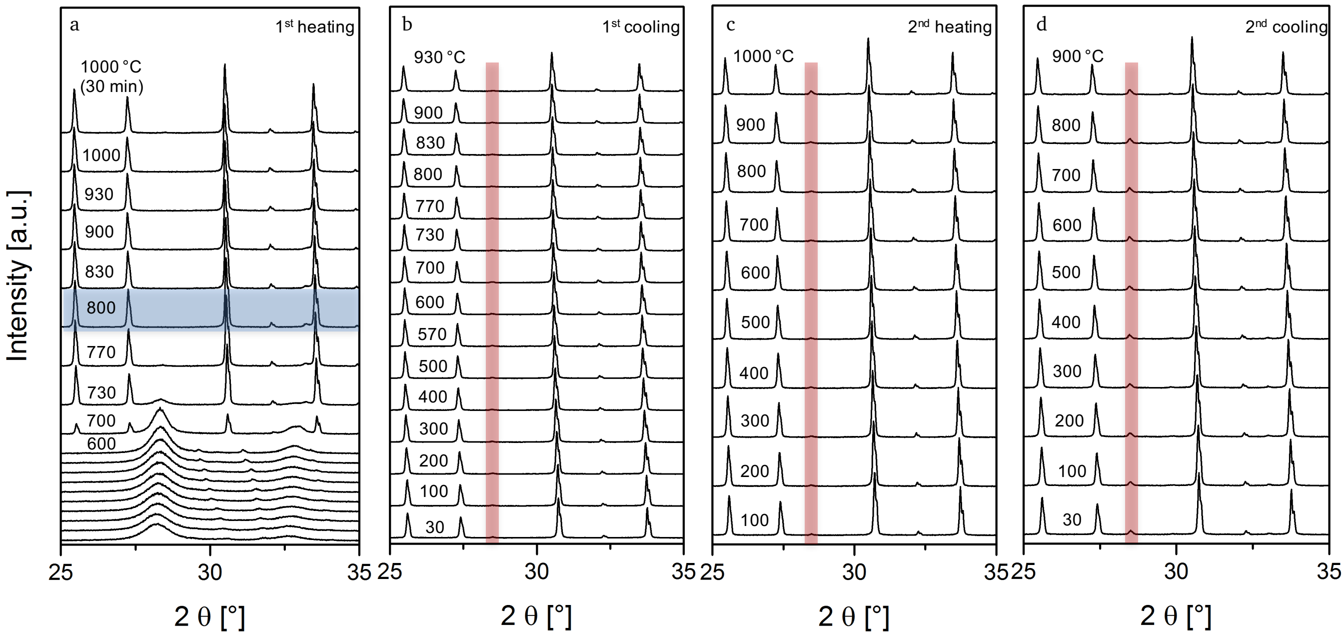

Figure 5-1: High temperature X-ray diffraction of as-synthesized powder ($x = 0.22$, 30 wt.% Li-excess) in static air atmosphere, first heating step with additional data collection after 30 min delay at 1000 °C (a), first cooling (b), second heating step up to 1000 °C (c), second cooling step (d). The highlighted pattern (blue) indicates the formation of the pure cubic structure and vertical stripes (red) mark the main reflection of the $La_2Zr_2O_7$ impurity phase.

The same procedure is carried out for the same as-synthesized powder batch under a flowing Ar atmosphere. The X-ray diffraction patterns are shown in Figure 5-2. The phase transformation to the cubic garnet structure takes place already between 600 °C and 700 °C. The pattern recorded at 700 °C does not exhibit any impurity phases, except for a small amount of Li_2CO_3 (2 wt.%) that is no longer detectable at 730 °C. A pure stable cubic structure is maintained up to 1000 °C and over a holding time of 90 min. During cool down no impurity phases are formed reaching 500 °C, where the cubic structure is no longer stable and a tetragonal garnet phase fraction (22 wt.%) starts to emerge. The phase transformation from the tetragonal to the cubic garnet structure is reversible between 500 °C and 600 °C upon repeated heating. A purely cubic structure is once again observed with no impurity phases at 600 °C. After heating up to 1000 °C, with no observable changes, the sample is cooled down to room temperature. During cool down the tetragonal modification (36 wt.%) starts to form once again between 400 °C and 300 °C, which is approximately 200 °C lower than during the first cooling step. The Al doping is expected to stabilize the high temperature cubic structure down to room temperature and thereby suppressing the formation of the tetragonal structure. The destabilization of the Li ordering in the tetragonal garnet structure is presumed to support this process [64]. The lower temperature, where the tetragonal structure starts to emerge during the second cool down indicates an enhanced stabilization of the cubic modification upon repeated heating due to Al^{3+} substitution of 3 Li^{+} supported by the increased Li disorder at high temperatures.

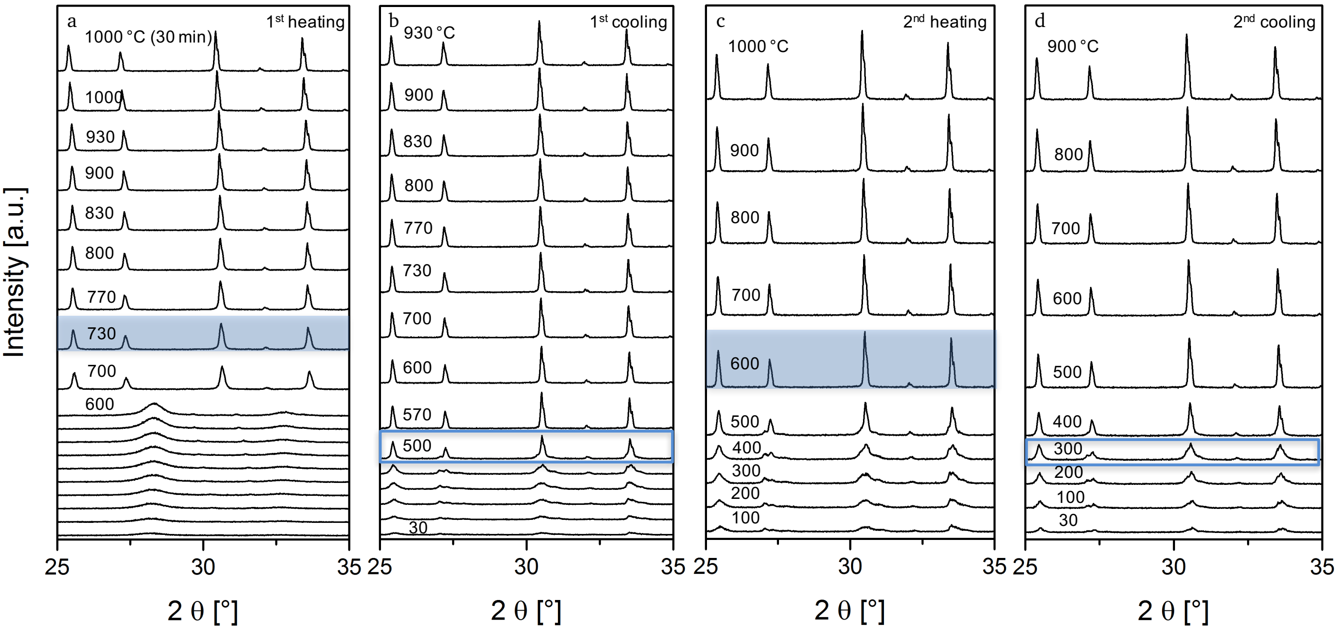

Figure 5-2: High temperature X-ray diffraction of as-synthesized powder (*x* = 0.22, 30 wt.% Li-excess) under flowing Ar atmosphere, first heating step up to 1000 °C with additional data collection after 30 min delay at 1000 °C (a), first cooling step(b), second heating cycle up to 1000 °C (c), second cooling cycle (d). Highlighted patterns indicate the formation of the pure cubic structure and framed patterns indicate the formation of the tetragonal structure upon cooling.

As the intensity of the diffraction patterns measured using the high temperature chamber at 30 °C are low due to the experimental setup, the powder is collected after the high temperature X-ray diffraction measurements and is measured again with the standard experimental setup after storage in an Ar-filled glovebox and a short air exposure. The Al diffusion from the Al_2O_3 sample holder has to be taken into consideration, when comparing the phase compositions to the high temperature X-ray diffraction data. The X-ray diffraction patterns are shown in Figure 5-3. The powder calcined under air contains a significant amount of the pyrochlore impurity phase as well as a small phase fraction of La_2O_3. The pyrochlore phase fraction of 11.9 wt.% is much higher than the phase fraction detected during high temperature X-ray diffraction. The reason for this increase might be the storage time in an Ar-filled glovebox, where moisture residues are present and might extract Li from the garnet structure forming LiOH and increasing the Li-free phase fraction or it might be due to the excess Al^{3+} incorporation from the Al_2O_3 sample holder during calcination. The main phase fraction is the Al-doped cubic garnet structure. On the other hand, the sample calcined under an Ar atmosphere is a mixture of the cubic and tetragonal garnet modifications, in addition to a small fraction of Li_2ZrO_3. The tetragonal phase fraction is lower than the one calculated from high temperature X-ray diffraction, which might indicate the increased Al-stabilization of the cubic garnet structure due to interaction with the Al_2O_3 sample holder during calcination. The phase composition of both samples obtained from Rietveld refinement is given in Table 5-1. While both samples have a comparable amount of cubic phase, Li-free and Li-rich phases are observed in the sample calcined in air and under Ar, respectively. Therefore, it can be assumed that Li is lost from the garnet framework during air calcination, leading to the pyrochlore and La_2O_3 impurities and resides in the garnet structure when calcined under Ar increasing the ordering and occupancy of the garnet framework, leading to the formation of the tetragonal garnet structure [28,45]. The formation of Li vacancies is a crucial step allowing for the Al incorporation into the garnet lattice and stabilization of the cubic structure [64]. In the sample calcined under Ar the Li occupancy is too high to allow for full stabilization of the high temperature cubic structure at room temperature after the first heating cycle. After the second cycle more Li vacancies are formed due to exposure to high temperature reducing the Li occupancy gradually leading to a decrease of the tetragonal phase fraction at room temperature. It is still unclear, whether the Li extracted from the garnet framework is lost from the solid to the gaseous phase, or if it persists in the solid state in the form of, e.g., Li_2O which is not detectable by X-ray diffraction.

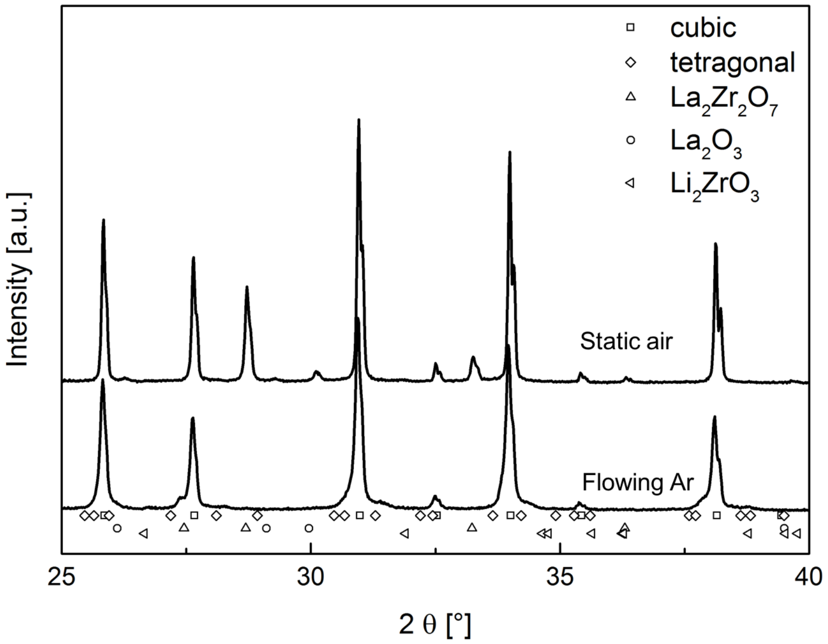

Figure 5-3: X-ray diffraction patterns of $Li_{7-3x}La_3Zr_2Al_xO_{12}$ powders ($x = 0.22$) calcined under static air and flowing Ar atmospheres, measured after performing the high temperature measurements. The symbols represent Bragg's positions of each phase present.

Table 5-1: Phase composition, obtained by Rietveld refinement of the X-ray diffraction patterns, of the powders calcined under static air and flowing argon collected at room temperature after the high temperature measurements.

Atmosphere	cubic [wt.%]	tetragonal [wt.%]	$La_2Zr_2O_7$ [wt.%]	La_2O_3 [wt.%]	Li_2ZrO_3 [wt.%]
air	87.49(9)	0	11.96(8)	0.55(4)	0
argon	88.56(26)	10.33(14)	0	0	1.11(25)

To determine whether Li is still present in the solid state after calcination under different atmospheres in the form of, e.g., Li_2O or is lost in the form of volatile Li containing compounds, e.g., LiOH, ICP-OES measurements are conducted for powders calcined under static air and flowing Ar atmosphere. The powders are collected after the high temperature diffraction experiment and stored in an Ar-filled glovebox before the quantitative ICP-OES measurement. The results are shown in Table 5-2. While the La, Zr and Al-contents are in good agreement and result in the expected Al-doping of $x = 0.22$, the Li-content of the sample calcined in static air is slightly lower than the nominal Li-content and the sample calcined under flowing Ar shows a significantly higher Li-content than the nominal value. This observation is made in addition to the presence of Li free impurity phases in the sample calcined under air, which indicates that Li is lost in the form of volatile compounds. The higher Li-content of the sample calcined under Ar might indicate the formation of additional Li containing phases that are not detectable by X-ray diffraction like, e.g., Li_2O. This claim needs to be evaluated by neutron diffraction measurements, where the Li containing phases can be identified and the Li occupancy of the cubic and tetragonal modifications can be determined.

Table 5-2: ICP-OES result for calcined powders, nominal composition $Li_{6.34}La_3Zr_2Al_{0.22}O_{12}$under static air and flowing Ar. Nominal values are given in parenthesis (standard deviation: ±0.7%).

Atmosphere	Li	Al	Li:La	Li:Zr	Zr:La
air	6.26(01)	0.206(1)	2.09	3.16	0.66
argon	6.64(02)	0.204(1)	2.21	3.35	0.66

To correlate the high temperature diffraction measurement performed under Ar with the reactions taking place DTA-TGA is performed under flowing Ar (75 ml min^{-1}). The as-synthesized powder sample (x = 0.22) is heated up to 1000 °C at a rate of 5 °C min^{-1}. After a dwell time of 1 h the sample is cooled down with a 10 °C min^{-1} rate, simulating the actual calcination process in a tube furnace. The resulting DTA-TGA curves for the heating process are shown in Figure 5-4. During dwell time and cooling no significant changes are observed, indicating the formation of stable structures. The observed phase transformation between the cubic and tetragonal garnet modification during cool down using high temperature X-ray diffraction is therefore not accompanied by a significant heat transfer. There is a continuous mass loss (5%) up to 400 °C, which can be correlated to the evaporation of adsorbed and crystalline water. In the DTA curve, three endothermic peaks are observed. The first broad peak with an onset at 465 °C and a maximum at 560 °C is correlated to a 4% weight loss. Since the high temperature diffraction under flowing Ar atmosphere shows the presence of all three phases $La_2Zr_2O_7$, Li_2CO_3 and the cubic garnet structure forming between 600 °C and 700 °C, this peak is most likely correlated to the initial phase formation of the garnet structure, i.e., the decomposition of the pyrochlore phase. The second peak with an onset at 704 °C and a maximum at 727 °C, is related to the melting of Li_2CO_3 [66] and corresponds to the temperature range where it is no longer detected using X-ray diffraction. This process is only accompanied by a weight loss of 1%, which indicates that Li_2CO_3 still persists as a melt up to its decomposition temperature. The Li_2CO_3 decomposition starts at 810 °C, with a maximum at 919 °C, and is accompanied by a weight loss of 12.4% up to the final temperature of 1000 °C. During Li_2CO_3 decomposition, Li_2O and CO_2 are formed [66]. The evaporation of Li containing species, e.g., LiOH may also occur in this temperature range. The calcined LLZO powder is collected after DTA-TGA for the determination of the phase composition using X-ray diffraction. A mostly cubic garnet structure is observed in addition to 5 wt.% of the $La_2Zr_2O_7$ impurity phase according to Rietveld refinement. This result indicates a high Li loss from the garnet structure during the DTA-TGA measurement, which can be caused by the small powder amount used for the measurement (17 mg) and the flowing Ar atmosphere reducing the LiOH partial pressure in the atmosphere surrounding the powder. This is an indication that the third observed endothermic peak also corresponds to the evaporation of Li containing species in addition to the Li_2CO_3 decomposition, which is no longer detected using X-ray diffraction. Over a holding time of 60 min a weight loss of only

0.3% is detected. The total weight loss during DTA-TGA of approximately 22% is in good agreement with the weight loss observed during actual calcination processed by weighing the powder before and after calcination.

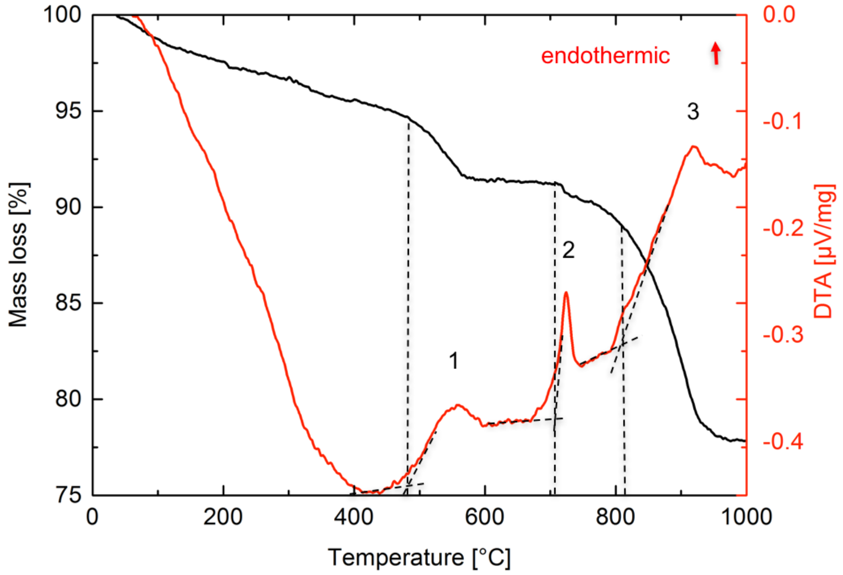

Figure 5-4: DTA-TGA curves of the calcination process of $Li_{7-3x}La_3Zr_2Al_xO_{12}$ powders (x = 0.22, 30 wt.% Li-excess) under flowing Ar atmosphere, heating to 1000 °C at 5 °C min^{-1}, onset points of three significant endothermic peaks are marked.

5.2 Optimization of further calcination parameters

The main external calcination parameters like temperature and time are optimized for achieving a pure garnet structure. Since the as-synthesized powder used for calcination is nanocrystalline, slight changes in the calcination parameters already show significant changes in the phase composition. Additionally, not only the external parameters are of great importance but also internal parameters like the Al-content and the Li-excess during synthesis. From several calcination processes under air and Ar atmospheres it becomes clear, that for each Li/Al ratio there is a need for new, separate determination of the optimal temperature and time to achieve a pure garnet structure. The phase composition of calcined powders is prawn to changes dependent on additional parameters, e.g., the quality of the zirconia crucible, the temperature at which the sample is quenched for powders calcined under air, the temperature stability of the furnace and the amount of powder. Therefore, the data presented in the following section are for samples calcined under a flowing Ar atmosphere, since it is a more controlled atmosphere leading to representative results. The first internal parameter optimized is the Li-excess used during synthesis. NSP requires the adjustment of the Li-content of the material already during preparation of the water based precursor solution. According to literature data as well as previous experiments it is expected to achieve an optimum Li-content at 10 wt.% [67,68] to 30 wt.% [44] Li-excess during synthesis. Therefore, three powder batches are synthesized with $x = 0.22$ and a Li-excess of 20 wt.%, 25 wt.% and 30 wt.%. The nanocrystalline powders are then calcined at 1000 °C for 1 h. The X-ray diffraction patterns are presented in Figure 5-5. For the sample with 20 wt.% Li-excess two impurity phases are identified, $La_2Zr_2O_7$ as the main Li-free phase and a small La_2O_3 phase. The garnet phase fraction consists of a purely cubic structure. Increasing the Li-content by only 5 wt.%, leads to the formation of an additional Li_2ZrO_3 impurity, while the $La_2Zr_2O_7$ phase increases slightly. The amount of La_2O_3 phase remains similar. The slight increase of the $La_2Zr_2O_7$ phase is unexpected for a sample with a higher Li-content, but the simultaneous formation of a Li_2ZrO_3 phase might explain this increase. Further Li containing compounds like Li_2O might be present but are not detected using X-ray diffraction. The Li-content is therefore not high enough to ensure its incorporation into the garnet structure. Synthesizing a powder with 30 wt.% Li-excess again leads to a drastic change in the phase composition. The main garnet phase fraction contains both the cubic and the tetragonal modification in comparable ratios, while the Li_2ZrO_3 phase slightly increases and the $La_2Zr_2O_7$ phase decreases reaching its lowest value. The La_2O_3 phase is no longer detected. The formation of the tetragonal structure is presumed not to be due to a lack of Al, which is crucial for the stabilization of the cubic structure, since the Al-content is kept constant for all three studied samples and no Al containing impurity phases are detected. Therefore, it can be assumed that Al is incorporated into the garnet lattice but the Li occupancy is high, leading to the formation of the favorable tetragonal structure. The main focus for the optimization of the Li-excess during synthesis is to minimize the formation of the $La_2Zr_2O_7$ phase, which is achieved using a 30 wt.% Li excess. The Rietveld data for all three samples are shown in Table 5-3.

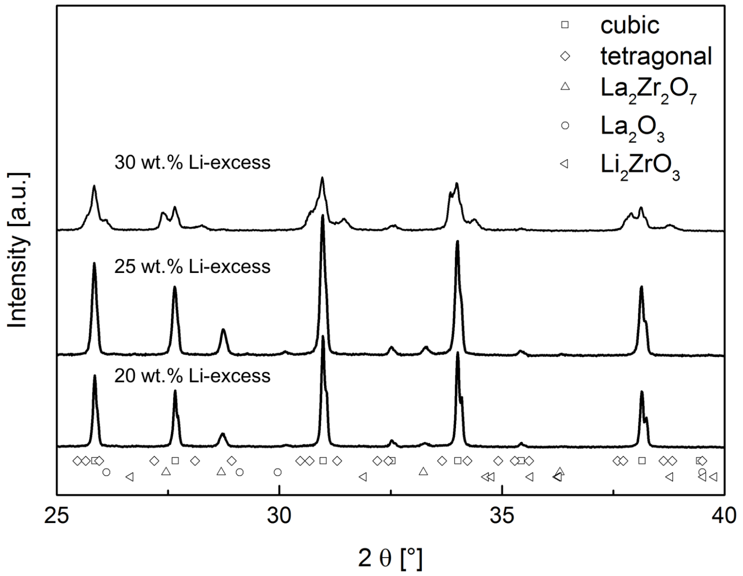

Figure 5-5: X-ray diffraction patterns of powder ($x = 0.22$) calcined at 1000 °C for 1 h under flowing Ar atmosphere with different Li-excess during synthesis.

Table 5-3: Rietveld data for calcined powders at 1000 °C for 1 h under flowing Ar with a constant Al-content of $x = 0.22$, while varying the Li-excess during synthesis.

Li-excess [wt.%]	cubic [wt.%]	tetragonal [wt.%]	$La_2Zr_2O_7$ [wt.%]	La_2O_3 [wt.%]	Li_2ZrO_3 [wt.%]	$LaAlO_3$ [wt.%]
20	93.86(6)	0	5.90(6)	0.24(3)	0	0
25	91.03(37)	0	7.51(6)	0.23(2)	1.23(40)	0
30	48.51(17)	49.66(17)	0.52(5)	0	1.31(31)	0

Influence of the Al-content on the powder phase composition during the calcination process at 900 °C and 950 °C is studied by using the powders with nominal Li-excess of 30 wt.%. The Al-content is set to $x = 0.15$, 0.22 and 0.25. A small well-defined amount of powder is used for each process (40 mg). Additionally, to avoid temperature fluctuations, all three compositions are calcined simultaneously at each temperature using three zirconia crucibles from the same manufacturer (GTS, Germany). During this optimization a thermocouple is attached to the alumina support for the three crucibles to ensure accurate temperature reading in addition to the furnace control system. The advantage of nanocrystalline powders synthesized by NSP is the ability to use lower calcination temperatures to achieve the fully stabilized garnet cubic structure. As it is shown by high temperature X-ray diffraction measurements the cubic phase is formed already at 730 °C, while the DTA data show an endothermic peak at 900 °C indicating a reaction still taking place. Therefore, the temperatures used for the optimization are 900 °C and 950 °C with a holding time of only 1 h under a flowing Ar atmosphere. The diffraction patterns are shown in Figure 5-6. At the first parameter set three different compositions are calcined. Starting from $x = 0.15$ the main phase fraction is the cubic garnet structure. Additionally, a tetragonal garnet structure is observed. Not only does this tetragonal modification exhibit a high Li occupancy according to literature [23], possibly leading to the formation of $La_2Zr_2O_7$ impurity phase but it might also indicate that the Al stabilization is not complete due to the small doping level. At an Al-content of $x = 0.22$ a larger cubic phase fraction is observed with a corresponding decrease in both the tetragonal and $La_2Zr_2O_7$ phases. An additional peak is observed for this composition at $2\theta = 31.7°$, which could only be ascribed to a La_2O_3 phase ($P\bar{3}m$) with a smaller unit cell volume of 70.7 $Å^3$, instead of the regular 82.3 $Å^3$. While the presumed La_2O_3 phase content remains low for all following samples, increasing the Al-content further to $x = 0.25$ leads to the formation of a $LaAlO_3$ phase. The tetragonal phase is no longer detected and the $La_2Zr_2O_7$ impurity increases significantly. It is evident that $x = 0.25$ is too high at the applied calcination conditions, since an Al containing impurity phase is formed in addition to the increase of the Li-free phase supporting the assumption that Li is lost from the garnet structure also due to increased Al-content. The optimal Al-content at a calcination temperature of 900 °C is $x = 0.22$, since the least amount of impurity phases are detected and the presence of the tetragonal structure is expected to be eliminated during further heat treatments. Increasing the temperature to 950 °C in fact supports this expectation, since no tetragonal phase is detected for all three compositions. The $La_2Zr_2O_7$ impurity phase increases for all samples with a minimum amount for the powder with an Al-content of $x = 0.22$. At 50 °C higher temperature a Li_2ZrO_3 impurity phase is detected for the samples with an Al-content of $x = 0.22$ and $x = 0.25$, in addition to a $LaAlO_3$ phase for the latter. The optimal Al-content for the calcination at 950 °C is also $x = 0.22$, since it presents the least amount of $La_2Zr_2O_7$ impurity phase. Nevertheless, the phase composition of the same powder calcined at 900 °C for 1 h shows a smaller amount of impurity phase of only 3 wt.% calculated using Rietveld refinement. An overview of the refinement data is presented in Table 5-4.

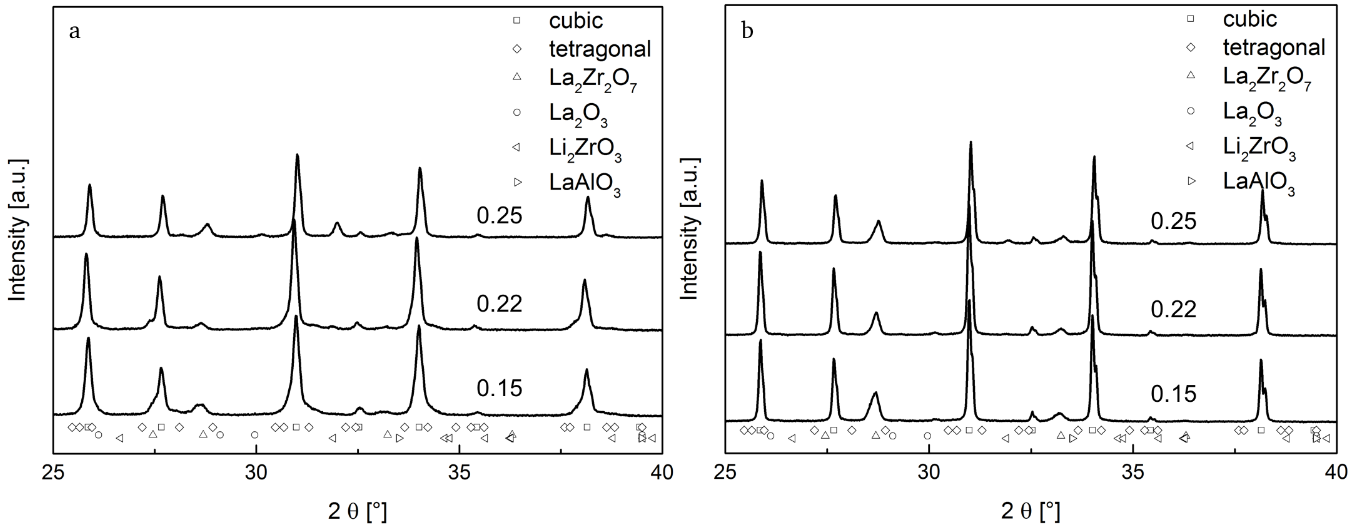

Figure 5-6: X-ray diffraction patterns of powders calcined at 900 °C for 1 h (a) and 950 °C for 1 h (b) ($x = 0.15$, 0.22 and 0.25) under flowing Ar atmosphere with 30 wt.% Li-excess.

Table 5-4: Rietveld data for calcined powders at different temperatures for 1 h under flowing Ar with a Li-excess of 30 wt.% during synthesis and varying Al-content.

Temperature [°C]	Al [mol]	cubic [wt.%]	tetragonal [wt.%]	$La_2Zr_2O_2$ [wt.%]	La_2O_3 [wt.%]	Li_2ZrO_3 [wt.%]	$LaAlO_3$ [wt.%]
900	0.15	73.6(2)	21.1(2)	5.3(1)	0	0	0
900	0.22	85.63(16)	11.11(16)	2.85(7)	0.41(3)	0	0
900	0.25	88.63(26)	0	8.97(9)	0.65(7)	0	1.75(26)
950	0.15	86.12(10)	0	13.64(9)	0.24(3)	0	0
950	0.22	89.85(30)	0	8.76(9)	0.29(4)	1.1(3)	0
950	0.25	85.3(3)	0	12.41(9)	0.64(7)	1.1(3)	0.55(5)

An optimization of a second external calcination parameter is carried out, namely the dwell time. Using a temperature of 900 °C the dwell time is increased from 1 h to 3 h. The X-ray diffraction patterns are presented in Figure 5-7. While the cubic phase fraction remains the main phase in both samples and its amount is comparable, the tetragonal phase fraction is no longer detected after calcination for a longer dwell time. Additionally, the Li-free $La_2Zr_2O_7$ phase increases drastically. The La_2O_3 impurity phase remains small but increases with increasing calcination time. This experiment shows how sensitive the resulting phase composition is to external process parameters. A prolonged time presumably leads to increased Li loss from the garnet structure indicated through the absence of the tetragonal structure and the presence of a larger phase fraction of the $La_2Zr_2O_7$ phase. Additionally, the lattice parameter of the cubic phase decreases from 12.9854(1) Å to 12.9831(1) Å with increasing calcination time, which might also indicate Li loss from the garnet structure. An overview of the Rietveld data is shown in Table 5-5.

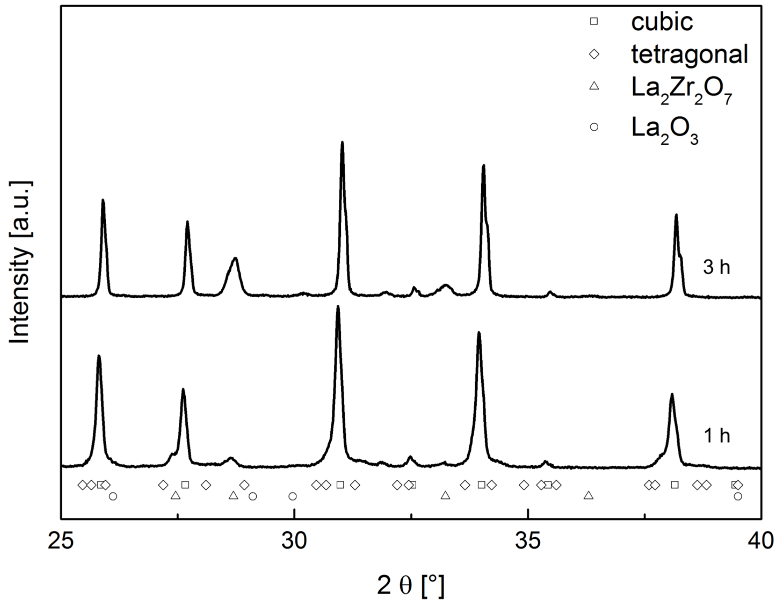

Figure 5-7: X-ray diffraction patterns of powder ($x = 0.22$) calcined at 900 °C for 1 h and 3 h under flowing Ar atmosphere with 30 wt.% Li-excess during synthesis.

Table 5-5: Phase composition obtained from Rietveld refinement of the powders calcined at 900 °C with different calcination time under flowing Ar with a constant Al-content of $x = 0.22$ and 30 wt.% Li-excess during synthesis.

Temperature [°C]	Time [h]	cubic [wt.%]	tetragonal [wt.%]	$La_2Zr_2O_2$ [wt.%]	La_2O_3 [wt.%]	Li_2ZrO_3 [wt.%]	$LaAlO_3$ [wt.%]
900	1	85.6(1)	11.1(1)	2.9(1)	0.41(3)	0	0
900	3	84.2(1)	0	14.8(1)	1.0(1)	0	0

Based on all the observations concerning the external calcination parameters it is evident that there is an interplay between the formation of a tetragonal Li-rich garnet structure and a $La_2Zr_2O_7$ Li-free structure. The phase fractions can be used as an indicator for Li loss from the garnet structure. The optimal calcination temperature is 900 °C with a dwell time of 1 h under flowing Ar. In addition to calcination temperature, time and calcination atmosphere it is observed that the amount of powder also plays an important role in the resulting phase composition. The volatility of Li containing compounds, e.g., LiOH is strongly dependent on their partial pressure surrounding the powder in the gas phase, therefore, in order to achieve this partial pressure during calcination more losses in the form of volatile species are expected for smaller amounts of powder. Additionally, the loss of volatile species is more pronounced at the surface of the powder, since they are continuously carried away by the flowing Ar atmosphere. In addition to the powder amount the sensitivity of the phase transformation to the temperature also leads to different optimum calcination parameters depending on the temperature accuracy and profile of the furnace used. In the following chapters powders are calcined under different conditions and different powder compositions are used. This is a result of a renewed optimization of the calcination parameters (Al-content, temperature and time), when using, e.g., air as a calcination atmosphere instead of Ar or when changing the furnace. The optimal calcination parameters are achieved when the calcined powder exhibits a garnet structure, preferably the cubic garnet structure. Any amorphous phase fractions have to be eliminated, therefore, the calcination temperature is chosen above 900 °C and the formation of Li-free impurity phases, e.g., $La_2Zr_2O_7$ needs to be minimized, which is influenced not only through the temperature but also the calcination time.

6 LLZO ceramics by field assisted sintering technology

The majority of the results presented in this chapter have been published in Journal of Power Sources [69].

Nebulized spray pyrolysis (NSP) and field assisted sintering technology (FAST) are combined for the first time to obtain dense LLZO ceramics. As it was mentioned earlier, FAST limits the grain growth and results in grain sizes in the order of a few microns. The highest reported Li-ion conductivity of LLZO samples produced by FAST is 0.57 mS cm^{-1}, where the mean grain size was 10 μm and the relative density was 99.8% of the theoretical density (TD) [57]. For electrolytes prepared by conventional sintering of powder synthesized by solid state reactions, where the typical grain sizes range from 100 μm to 200 μm and densities around 92% TD, Li-ion conductivity values of 0.2 mS cm^{-1} are reported [70]. Ceramics obtained by conventional sintering of sol-gel powders with a density of 96% TD and grain size of 260 nm, show Li-ion conductivity of 0.4 mS cm^{-1} [71], which is twice the value obtained by solid state reaction [70]. The reduction of the grain size in ceramics synthesized by solid state reaction to 4 μm and the increase of the density (98% TD) leads to a higher Li-ion conductivity [45], approaching the values reported for nano-grained ceramics (0.4 mS cm^{-1}). According to the literature decreasing the grain size of the sintered ceramics from 100 μm to a few microns results in higher Li-ion conductivity, while a further reduction of the grain sizes does not necessarily lead to higher Li-ion conductivities. A grain size of a few microns, in turn, not only enhances the Li-ion conductivity but also lowers the interfacial resistance between the electrolyte and the Li metal anode [70]. In the following a new ceramic processing route is introduced to produce dense, fine grained LLZO solid electrolyte. Furthermore, a symmetrical cell assembling process with Li metal electrodes is presented. The electrochemical performance is studied using AC-IS and galvanostatic cycling. The influence of the sintering technique on the phase composition, microstructure and microstrain is discussed and related to the electrochemical performance of the solid electrolyte.

6.1 Material properties and FAST processing

The samples used for this study have the nominal composition $Li_{7-3x}La_3Zr_2Al_xO_{12}$ with x = 0.15, 0.17 and 0.20. The standard NSP procedure (900 °C) is employed to synthesize the nanocrystalline powders, composed of the CaF_2-type phase $La_{0.5+\delta}Zr_{0.5-\delta}O_{1.75-\delta/2}$ ($Fm\bar{3}m$), Li_2CO_3 ($C2/c$) and La_2O_3 ($P\bar{3}m$) (Table 4-1). The as-synthesized powders are calcined to achieve the desired garnet structure. The calcination process takes place at 900 °C for 3 h in static air. The powders are removed from the furnace at 300 °C and cooled down under argon to minimize the water uptake. After calcination field assisted sintering is used for consolidation and sintering of the powders. The process parameters are chosen to achieve a high density, while limiting the Li loss, which occurs at high temperatures. Therefore, the temperature is set to 950 °C, the holding time to 10 min and the pressure to 50 MPa under vacuum (10^{-2} mbar). The pellets are polished using grinding paper with grit sizes from 800 to

1200 consecutively. No solvents are used during polishing. The polished pellets are 7 mm in diameter with a thickness of approximately 1 mm. The density is determined geometrically, including the phase fractions and the corresponding crystallite densities obtained from the Rietveld refinement of the X-ray diffraction patterns.

6.1.1 Phase composition and microstrain

The X-ray diffraction patterns and the respective refinements of the calcined $Li_{7-3x}La_3Zr_2Al_xO_{12}$ powders ($x = 0.15$, 0.17, 0.20 and 0.25) are presented in Figure 6-1. All powders exhibit a predominant cubic garnet structure ($Ia\bar{3}d$), with a varying amount of the pyrochlore impurity phase, $La_2Zr_2O_7$. The pyrochlore phase is mostly an indication for Li loss occurring during heat treatment. Since the powders are calcined in air, the presence of moisture as well as the carbon dioxide lead to increased Li losses from the garnet structure as mentioned in detail in section 5.1. The amount of the impurity phase does not show a consistent relation to the nominal Al-content of the samples. The Li loss is influenced by many parameters like for instance the amount of powder used during calcination, which alters the surface area exposed to the surrounding atmosphere and leads to the formation of the Li-free $La_2Zr_2O_7$ phase. Nevertheless, the powder with a nominal Al-content of $x = 0.17$ exhibits the least amount of impurity phase of 0.62 wt.%. The phase fractions together with the unit cell volumes and corresponding microstrain are listed in Table 6-1. The powder with a nominal Al-content of $x = 0.25$ exhibits an additional phase fraction of a $LaAlO_3$ impurity, setting an upper limit for the Al-doping under the employed calcination conditions.

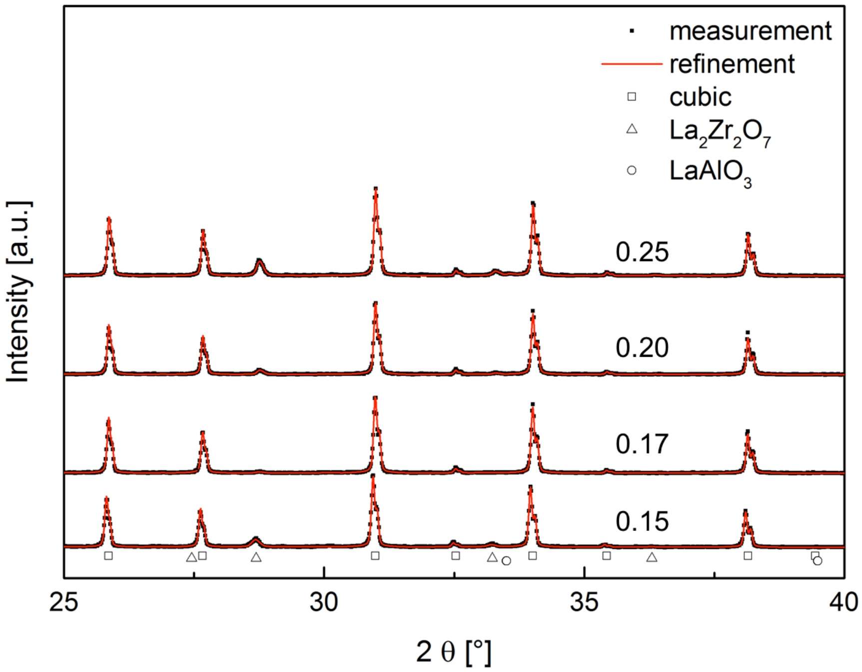

Figure 6-1: X-ray diffraction patterns and corresponding Rietveld refinements of calcined $Li_{7-3x}La_3Zr_2Al_xO_{12}$ powders with different Al-content ($x = 0.15$, 0.17, 0.20 and 0.25). Splitting of the reflections is due to $K_{\alpha1}$ and $K_{\alpha2}$ Cu radiation. The symbols represent Bragg's positions of each phase present.

Table 6-1: Rietveld refinement data for calcined $Li_{7-3x}La_3Zr_2Al_xO_{12}$ powders.

x	Phase	Phase fraction [wt.%]	Unit cell volume [Å^3]	Microstrain
0.15	cubic garnet	94.85(3)	2182.278(48)	0.018(1)
	$La_2Zr_2O_7$	5.15(3)	1269.83(18)	-
0.17	cubic garnet	99.38(3)	2183.041(44)	0.019(1)
	$La_2Zr_2O_7$	0.62(3)	1265.53(77)	-
0.20	cubic garnet	97.44(3)	2181.799(41)	0.014(1)
	$La_2Zr_2O_7$	2.56(3)	1264.09(20)	-
0.25	cubic garnet	91.7(1)	2181.889(41)	0.017(1)
	$La_2Zr_2O_7$	7.24(3)	1265.570(93)	-
	$LaAlO_3$	1.1(1)	109.2(12)	-

After sintering using FAST and subsequent polishing, both sides of the pellets are characterized using X-ray diffraction in a large angular range (2θ = 10 to 120°) to obtain information related to the microstrain present in the different phases. Exemplary diffraction patterns of the sample with $x = 0.17$ and the corresponding refinements are shown in Figure 6-2. It is found that the patterns cannot be fitted satisfactorily using a single cubic or tetragonal garnet type phase. Therefore, fitting of the patterns is attempted comparing a model with one cubic and one tetragonal garnet type phase to a model with two cubic garnet type phases. According to Hamilton's significance test [72], the patterns are more accurately described (>97%) using the first model. The phase fraction of the tetragonal phase exceeded the cubic one reaching up to 64 wt.%. The tetragonal phase, which is observed after sintering has a significantly larger cell volume compared to the cubic garnet phase. Furthermore, compared to the Li-rich tetragonal garnet phase $Li_{7-3x}La_3Zr_2Al_xO_{12}$ ($x = 0$) with a c/a ratio of 0.965 [73], it possesses a c/a ratio closer to unity indicating only small deviation from the cubic symmetry. This tetragonal phase is further referred to as distorted tetragonal phase. The tetragonal distortion also exhibits an increased microstrain compared to the cubic garnet phase. The influence of the microstrain is presented in detail in section 7.2.2. Additionally, it is observed that the two sides of the pellets slightly differ regarding the cubic/tetragonal phase ratio as well as with respect to the amount of the pyrochlore type phase. A possible explanation for this observation might lie in the uniaxial load applied during sintering, bearing in mind that the stress field is different for each side of the ceramic specimen, since the upper piston is in motion for pressure application, while the lower one is static. The application of direct current on a highly insulating material during the FAST process might induce effects that are not completely understood and in need for further studies comparing different insulating materials and the influence of the electric field [41]. Table 6-2 shows the Rietveld refinement data for the sintered ceramics averaged over both sides of the pellet.

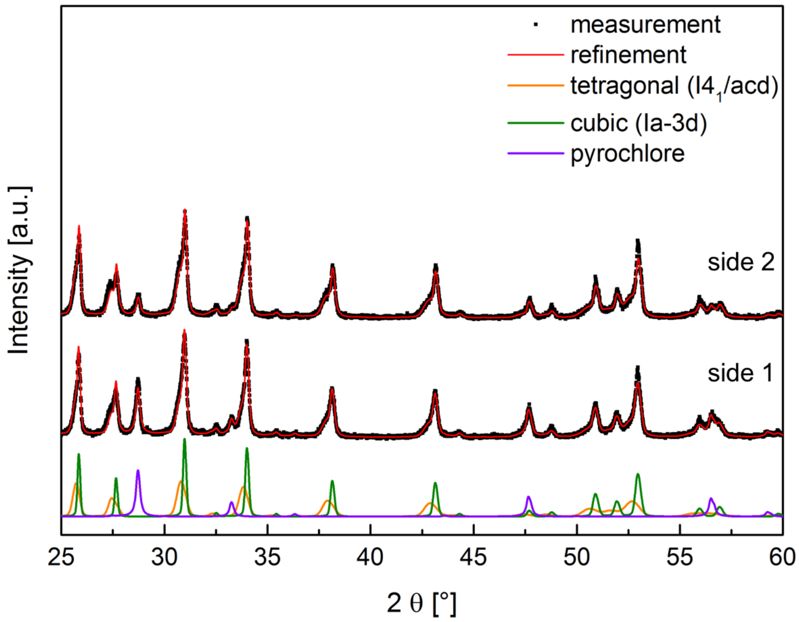

Figure 6-2: X-ray diffraction patterns and the refinements of the sintered ceramic measured on both sides of the pellet with $x = 0.17$ (side 1 and side 2).

Table 6-2: Rietveld refinement data for sintered $Li_{7-3x}La_3Zr_2Al_xO_{12}$ pellets.

x	Phase	Phase fraction [wt.%]	Unit cell volume [Å^3]	Microstrain	c/a
0.15	cubic garnet	26.41(6)	2176.50(71)	0.195(6)	1
	tetragonal g.	64.03(6)	2200.81(91)	0.314(5)	0.980
	$La_2Zr_2O_7$	9.56(3)	1264.69(36)	-	1
0.17	cubic garnet	34.54(4)	2178.18(20)	0.102(1)	1
	tetragonal g.	58.07(5)	2213.50(78)	0.339(4)	0.988
	$La_2Zr_2O_7$	7.39(3)	1266.00(24)	-	1
0.20	cubic	34.00(4)	2176.90(18)	0.089(1)	1
	tetragonal	59.23(4)	2215.98(59)	0.334(4)	0.988
	$La_2Zr_2O_7$	6.77(2)	1266.25(20)	-	1

The formation of the distorted tetragonal phase during field assisted sintering could have two different reasons. The first is Al^{3+} segregation during the sintering process. According to literature electromigration of ionic species can take place due to the presence of a direct current electric field during sintering [74]. This would lead to the formation of the tetragonal structure due to insufficient Al stabilization of the garnet structure. The second reason is merely mechanical originating in the simultaneous application of a uniaxial pressure and high temperature. The synthesis of Al^{3+} containing compounds by, e.g., solid state reaction, is well known to require very high synthesis temperatures [75]. Al^{3+} segregation during FAST appears unlikely based on the following observation: the sintered pellet is crushed manually using a mortar under ambient conditions, where the redistribution of Al^{3+} species would be impossible, due to their immobility. X-ray diffraction is performed on both the sintered pellet and the powder of the crushed pellet. The resulting diffraction patterns are presented in

Figure 6-3. The reflections corresponding to the crushed pellet are sharp and can be fitted with mainly a cubic phase, consistent with the refinement of the patterns for the sintered ceramics. The distorted tetragonal phase fraction decreases considerably, while the cubic phase fraction increases after crushing the pellet. Crushing the pellet seems to release internal stresses by changing the particle interconnections, resulting in restoration of the cubic structure and the release of the microstrain indicated by the sharpening of the reflections. This proves that no electromigration of Al^{3+} species takes place during field assisted sintering and that the tetragonal distortion accompanied by a higher microstrain are due to the mechanical stresses the specimen is exposed to during the sintering process.

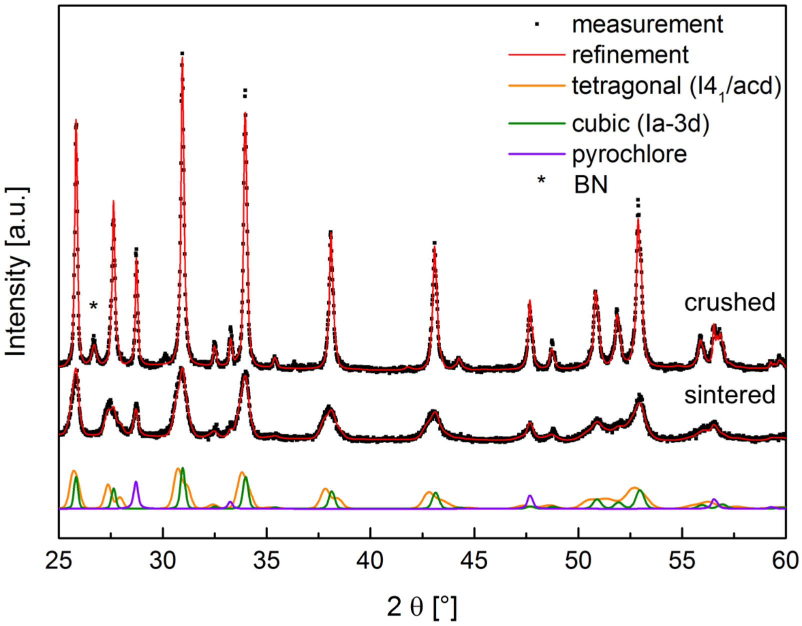

Figure 6-3: X-ray diffraction patterns and the corresponding Rietveld refinements of the sintered and crushed $Li_{7-3x}La_3Zr_2Al_xO_{12}$ ceramics ($x = 0.15$). BN: residue of boron nitride that is used in the sample preparation for FAST.

6.1.2 Microstructure

The microstructure is characterized after each processing step, and the corresponding micrographs are shown in Figure 6-4. After the NSP synthesis the powder consists of spherical particles with a diameter between 0.3 μm and 5 μm. The spheres are hollow and the shells are composed of nanocrystallites with sizes ranging from 7 nm to 9 nm. During the subsequent calcination step neck formation between the particles occurs forming particle agglomerates. A determination of the particle size is not possible. Sintering of calcined powder using FAST leads to high densities (93% TD), which can be deduced from presence of only closed pores in the cross section of a sintered pellet. The grain size is in the range between 0.5 μm and 3 μm.

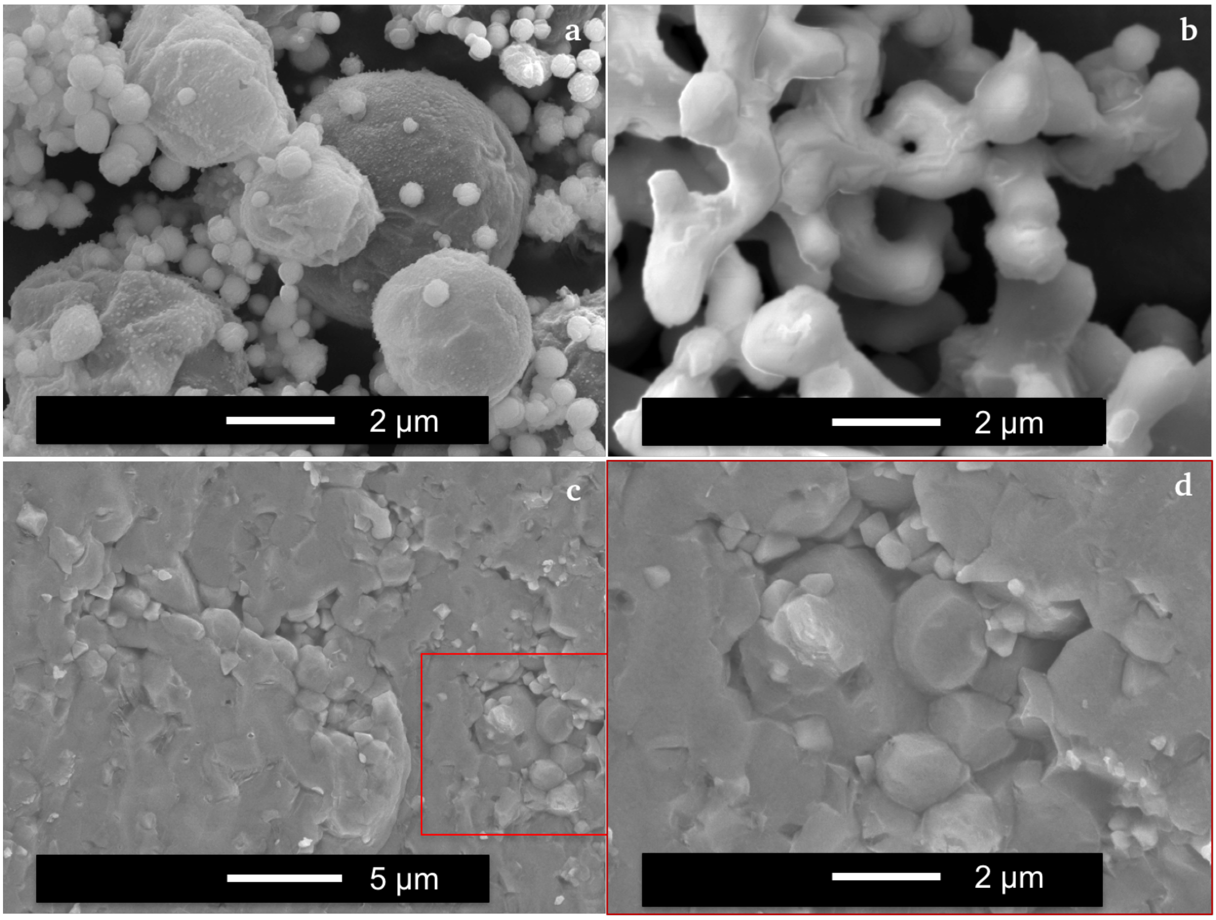

Figure 6-4: SEM images of the as-synthesized powder (a), calcined powder (b), the sintered ceramic $Li_{7-3x}La_3Zr_2Al_xO_{12}$ ($x = 0.17$) (c) and in higher magnification as in c (d).

To achieve a high ionic conductivity in the final $Li_{7-3x}La_3Zr_2Al_xO_{12}$ ceramic, which is the main objective of this study, a homogeneous distribution of the elements needs to be provided throughout the material. Impurity segregation at the grain boundaries as reported in the literature for samples produced using solid state reaction are detrimental for the electrochemical performance [76]. Therefore, energy dispersive X-ray spectroscopy (EDXS) is carried out to map the elemental distribution throughout a particle agglomerate of the calcined powder. The micrograph and the corresponding elemental maps of Al, La and Zr are shown in Figure 6-5. All elements show a homogeneous distribution within one particle and also along the sintering necks between the particles. Therefore, an impurity segregation can be ruled out presenting a good starting point for achieving a homogeneous sintered ceramic and a good electrochemical performance.

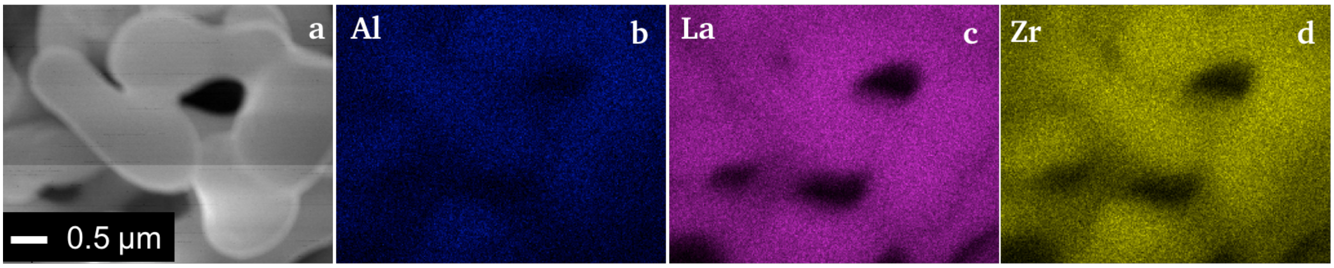

Figure 6-5: Scanning electron micrograph (a) and corresponding elemental distribution of Al (b), La(c) and Zr (d) of $Li_{7-3x}La_3Zr_2Al_xO_{12}$ calcined powder ($x = 0.17$, 30 wt.% Li-excess) at 900 °C for 3 h in air.

6.2 Electrochemical performance

The electrochemical performance is mainly characterized through the Li-ion conductivity as well as by the charge transfer resistance also referred to as area specific resistance (ASR) at the interface between the $Li_{7-3x}La_3Zr_2Al_xO_{12}$ solid electrolyte and the Li metal electrode. The charge transfer resistance is a limiting factor for the development of an all-solid-state Li-ion battery. Furthermore, the symmetrical cell is cycled galvanostatically at different current densities and the influence of cycling on the ASR is determined.

6.2.1 Li-ion conductivity

The room temperature AC-impedance spectrum shows only a single semi-circle presumably corresponding to the grain boundary contribution to the spectrum based on the calculated capacitance of 10^{-9} F. Consequently, AC-impedance spectroscopy measurements are conducted over a wide temperature range from 220 K to 298 K. Measuring at lower temperatures increases the resistance of both the bulk and grain boundary semi-circles, thus reaching resistance values in the detection range of the device. Hence, the grain boundary contribution to the spectrum can be resolved at room temperature, while the bulk contribution to the spectrum can be identified through the first intercept of the grain boundary semi-circle with the real Z'-axis. The data is collected during cool down after drying the samples at 393 K under He atmosphere inside the cryostat to eliminate residual adsorbed moisture, which would lead to lower resistances, i.e., higher conductivity. The spectra are fitted using R(R CPE)(R CPE)(R CPE)CPE equivalent circuit model, where R is the resistance and CPE represents the constant phase element. Each (R CPE) unit corresponds to the bulk, grain boundary and surface layer contribution, respectively. The measured spectra as well as their fits are presented exemplary for the sample with $x = 0.17$ in Figure 6-6. The Li-ion conductivity at room temperature (298 K) is calculated for the samples with Al-contents of $x = 0.15$, 0.17 and 0.20 to 0.30 mS cm^{-1}, 0.33 mS cm^{-1} and 0.31 mS cm^{-1}, respectively. All samples contain a certain amount of the pyrochlore phase in addition to the previously described distorted tetragonal phase (Table 6-2), nevertheless the conductivity values are in very good agreement with literature values for the pure cubic garnet structure of 0.35 mS cm^{-1} [77]. The presence of a pyrochlore impurity phase is expected to decrease the Li-ion conductivity since it does not exhibit any Li-ion conductivity, yet the influence of a high density and an optimized grain size (<3 μm) is more pronounced in enhancing the conductivity. The good agreement with values from literature further supports the assumption that the appearance of the tetragonal distortion (c/a = 0.988) from external stress fields does not have strong ramifications on the Li-ion conductivity, compared to what would be expected from the presence of a tetragonal phase resulting from Li ordering (c/a = 0.965).

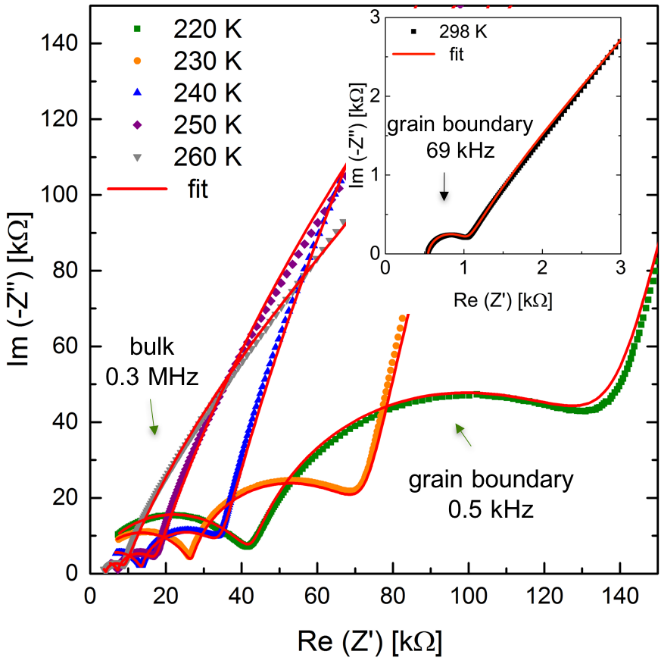

Figure 6-6: Nyquist plots and corresponding fits for a representative $Li_{7-3x}La_3Zr_2Al_xO_{12}$ (x = 0.17) ceramic obtained at room temperature (inset) and at 220 K up to 260 K using blocking Au electrodes.

The temperature dependent impedance measurements are performed for all three samples with x = 0.15, 0.17 and 0.20. The corresponding Arrhenius plots are shown in Figure 6-7 along with their linear fits. The activation energies calculated from the slopes are 0.39 eV, 0.38 eV and 0.37 eV for the samples with x = 0.15, 0.17 and 0.20, respectively. These values are in good agreement with literature values for the pure cubic structure ranging from 0.34 eV to 0.36 eV [47,77] and reports for a mixture of cubic and tetragonal phases with an activation energy of 0.38 eV [78].

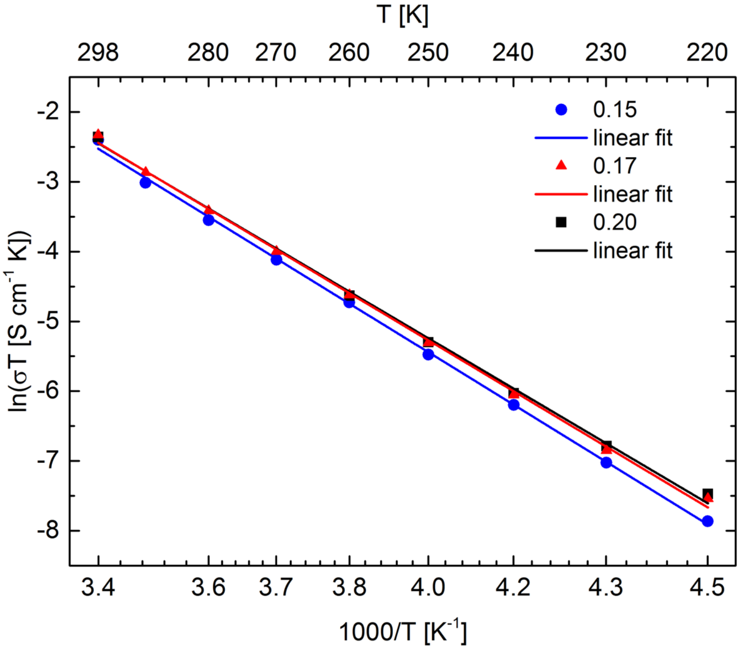

Figure 6-7: Arrhenius plot presenting the temperature dependence of the Li-ion conductivity of $Li_{7-3x}La_3Zr_2Al_xO_{12}$ with x = 0.15, 0.17 and 0.20.

6.2.2 Interfacial resistance

AC-impedance spectroscopy is performed on symmetrical cells with Li metal melted on both sides of the pellets, which is achieved by using a heating plate (180 °C) to heat up the pellet before applying the Li foil and spreading it using a soldering iron (200 °C). Figure 6-8 shows the Nyquist plots measured at room temperature for the samples with two different Al-contents (x = 0.17 and 0.20). The impedance spectra recorded with blocking Au-electrodes are included for clarity in the determination of the interfacial resistance and the area specific resistance (ASR). The first observation is that the first intercept with the real Z'-axis corresponding to the bulk contribution to the spectrum is shifted to higher resistance values for both samples. The shift varies for each sample, which excludes additional setup or connection resistances. Additionally, the shift in the range of 0.1 kΩ to 0.2 kΩ is too large to be attributed to such effects. The most plausible explanation is a variation in the surface of the Li-electrodes from the sputtered Au-electrodes. The Li-electrodes are melted on the pellet manually allowing for pores and inclusions at the interface to block the Li-ion transfer locally. This reduces the actual area (A_a) of the electrodes compared to the measurement with Au-electrodes. The difference between the actual area of the electrode and the theoretical maximum area of the pellet (A_t) can be determined from the observed difference Δ in the bulk resistance (R_b). The following equation can be used to determine the actual area, $A_a = A_t \cdot R_b \cdot (R_b + \Delta)^{-1}$. The resulting actual electrode area is found to be only 77% of the theoretical area of the pellet for the sample with x = 0.17 and 96% for the sample with x = 0.20. In the following discussion the corrected values using the actual electrode area are placed in parenthesis.

A comparison between the spectra with blocking and non-blocking electrodes allows for a determination of the interfacial resistance, even in the case of a strong overlap of the grain boundary and charge transfer contributions. The resistance values provided by the fit for the grain boundary contribution to the spectrum with blocking electrodes are kept constant for the fitting of the spectrum with non-blocking Li-electrodes, where the capacitance values for the overlapping high and low frequency semi-circles are calculated to be 10^{-9} F and 10^{-8} F, respectively. Therefore, the low frequency semi-circle represents the charge transfer of Li-ions between the solid electrolyte and both Li-electrodes [70]. In order to determine the ASR, the obtained resistance value is divided by two and multiplied by the area of the electrode. The ASR value for the sample with $x = 0.17$ is found to be 76 Ω cm^2 (59 Ω cm^2), while for the sample with $x = 0.20$ the ASR is 75 Ω cm^2 (72 Ω cm^2). These values compete with the best values reported in literature, which range from 109 Ω cm^2 [39] to 37 Ω cm^2 [70].

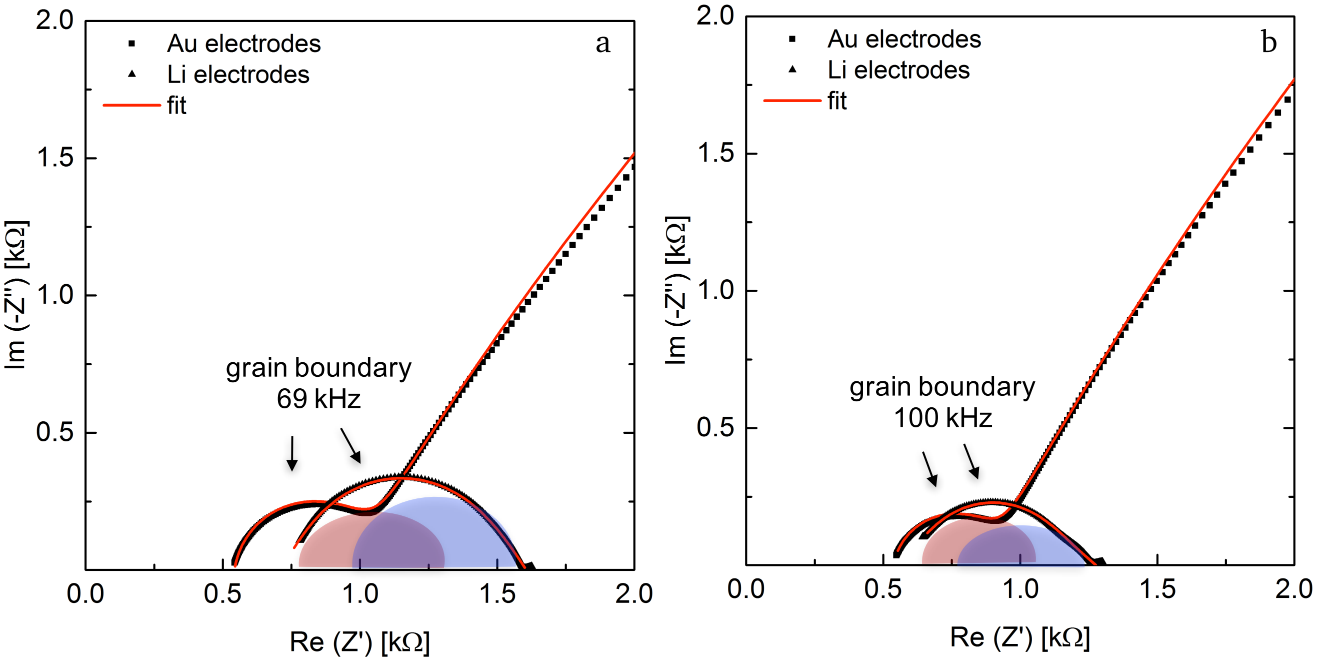

Figure 6-8: AC-impedance spectra collected at 298 K with blocking Au-electrodes and non-blocking Li-electrodes for $Li_{7-3x}La_3Zr_2Al_xO_{12}$ samples with $x = 0.17$ (a) and $x = 0.20$ (b), the semi-circles corresponding to grain boundary (red) and electrode (blue) contributions are indicated schematically.

A comparison of ASR values for different samples can only be accurate, when the surface roughness of the pellets before Li-deposition is taken into account. A relatively high surface roughness, which is reported by Cheng et al. is expected to enhance the calculated ASR values compared to a smooth surface, assuming that the rough surface is completely covered with Li metal. This is dependent on the wetting behavior of liquid Li.

As it is reported in literature the cycling of the cells influences the ASR [79]. An important aspect to bear in mind is that the current density chosen for cycling is a crucial parameter for the determination and comparison of the changes in the ASR. Additionally, the critical current density leading to short circuiting of the cell is temperature dependent [80]. Therefore, the cells presented here are cycled at room temperature (298 K) at low current densities. These conditions allow for the use of AC-impedance spectroscopy to monitor the changes in ASR after each cycling step. The cycling regime and the cell performance are presented in section 6.2.3. The AC-impedance spectra of the samples with

$x = 0.17$ and 0.20, collected at room temperature after cycling of the symmetrical cells with Li-electrodes at different current densities, are depicted in Figure 6-9. Starting with the sample with $x = 0.17$ the ASR drops from 76 Ω cm^2 (59 Ω cm^2) to 70 Ω cm^2 (54 Ω cm^2) after cycling for 10 cycles at a current density of 31 μA cm^{-2} ($j_{corr} = j{\cdot}A_a/A_t$) then decreases further after cycling for 5 more cycles at 39 μA cm^{-2} to 63 Ω cm^2 (49 Ω cm^2). After additional 5 cycles at a current density of 49 μA cm^{-2} the ASR increases to 69 Ω cm^2 (53 Ω cm^2). The sample with $x = 0.20$ also exhibits a change in the ASR, where it initially increases from 75 Ω cm^2 (72 Ω cm^2) to 92 Ω cm^2 (89 Ω cm^2) after the first 15 cycles and then it decreases to 70 Ω cm^2 (67 Ω cm^2) after cycling at the highest current density of 49 μA cm^{-2}. With the decrease of the ASR value an additional low frequency semi-circle is observed. Spectra showing an increase in the initial ASR do not exhibit this semi-circle at low frequencies. This leads to the assumption that the decrease of the ASR after cycling is accompanied by a formation of an interlayer with different electrical properties. At the interface between the solid electrolyte and the Li-electrode there is a constant dissolution and deposition of Li, which leads to a microstructural change, e.g., pore formation on the side of the reversible electrode, while the electrolyte lattice remains intact [81]. Therefore, the changes in the ASR at different current densities are unpredictable. The results presented in this study show good stability of the interface at room temperature and at the reported current densities, without showing ramifications of the change of the interface on the cell performance.

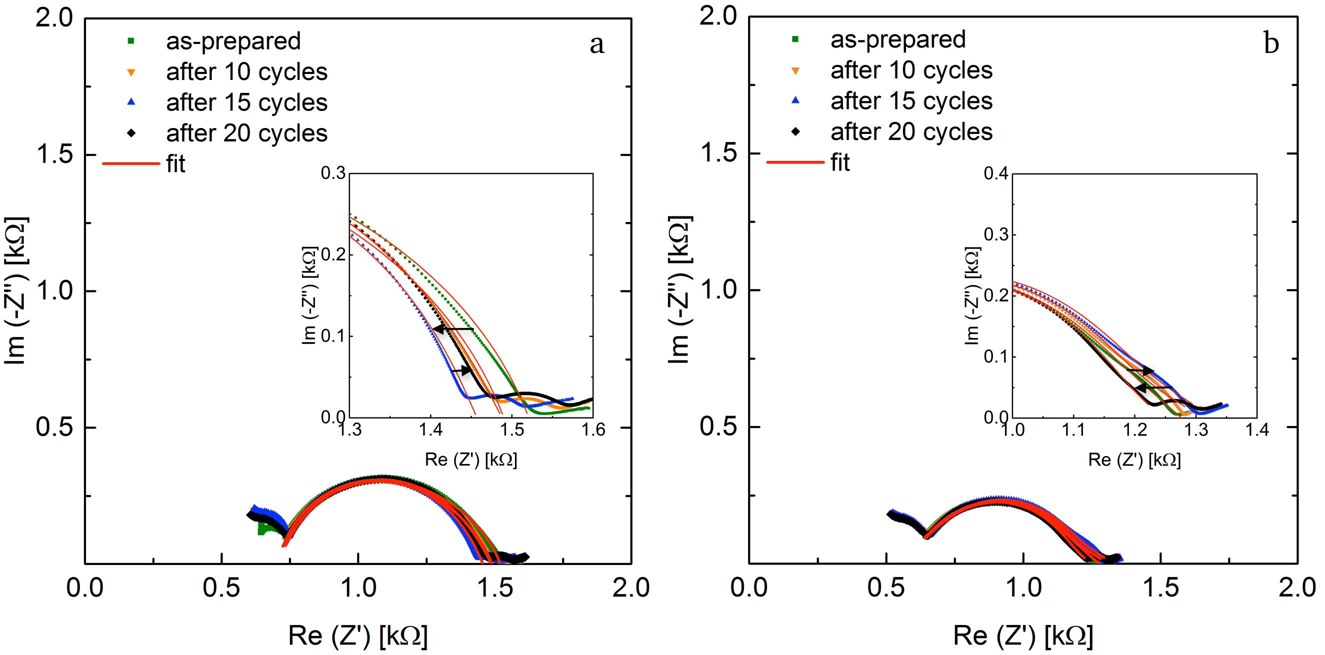

Figure 6-9: AC-impedance spectra collected at 298 K with non-blocking Li-electrodes before and after cycling at different current densities for $Li_{7-3x}La_3Zr_2Al_xO_{12}$ samples with $x = 0.17$ (a) and $x = 0.20$ (b), insets show the magnified low frequency regions.

6.2.3 Cycling behavior

Chemical and electrochemical stability of the solid electrolyte against Li metal are required for an all-solid-state Li-ion battery using Li metal as an anode, which is needed to achieve a high energy density. Galvanostatic cycling is performed at different current densities (31 μA cm^{-2}, 39 μA cm^{-2} and 49 μA cm^{-2}), calculated from the currents (12 μA, 15 μA and 19 μA) and the theoretical area A_t of the pellet not considering the surface roughness. All measurements are conducted in a temperature cabinet that is set to room temperature (298 K). The result for both symmetrical cells containing samples with $x = 0.17$ and $x = 0.20$ are presented in Figure 6-10. Both cells show stable cycling for up to 100 hours, corresponding to 25 cycles. The increase of cell potential observed during each cycling step slightly increases, but does not exceed 2 mV. Asymmetrical buildup of cell potential during charging and discharging can be explained through the presence of an impurity directly at one of the interfaces between the solid electrolyte and the molten Li metal. The amount of Li, which is transported through the electrolyte, and the active electrode volume during charge and discharge are 2.4 10^{-8} mol and 3.1 10^{-22} m^{3}, respectively.

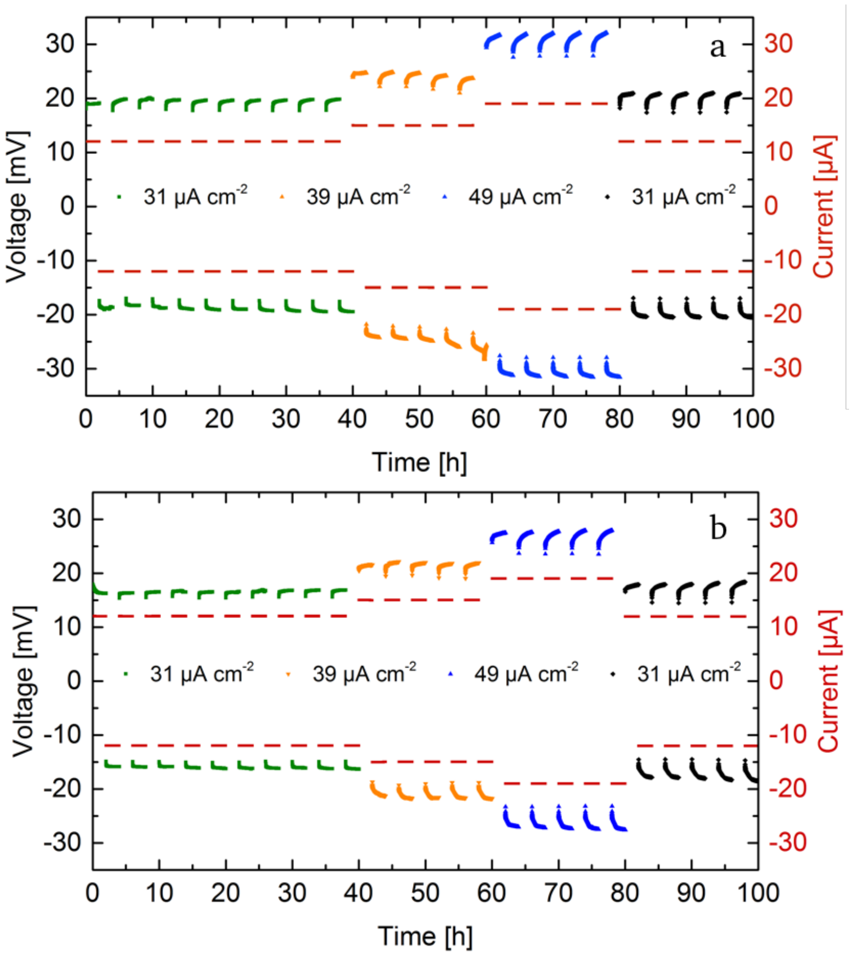

Figure 6-10: Galvanostatic cycling of symmetrical cells Li|LLZO|Li at different current densities for $Li_{7-3x}La_3Zr_2Al_xO_{12}$ (LLZO) samples with $x = 0.17$ (a) and $x = 0.20$ (b). Stable cycling is observed for 100 h.

6.3 Conclusion and summary

The main requirements for the synthesis and processing of a solid electrolyte for an all-solid-state Li-ion cell are to obtain an optimized microstructure. A high density and an optimized grain size have a more pronounced influence on the electrochemical performance than the phase composition. In this study dense, fine-grained $Li_{7-3x}La_3Zr_2Al_xO_{12}$ ceramics were synthesized for the first time by a combination of NSP and FAST. The Li-ion conductivity for the compound with $x = 0.17$ was found to be 0.33 mS cm^{-1} with an activation energy of 0.38 eV, which is in very good agreement with reported values. Therefore, it can be concluded that FAST can indeed be used for the preparation of LLZO ceramics with good electrochemical performance. The sintering technique preserved the small grain size, while achieving high densities, which were two crucial factors for achieving high Li-ion conductivities. High conductivities were found despite the presence of an impurity phase ($La_2Zr_2O_7$) as well as a distorted tetragonal garnet type phase as the main phase. The formation of the tetragonal phase was best explained by the introduction of microstrain, arising from the application of a uniaxial pressure during the sintering process. Internal ordering of the Li ions due to segregation of Al^{3+} resulting in the formation of a tetragonal phase with poor ionic conductivity could be ruled out due to the high conductivity of the ceramics and by the investigation of a crushed pellet. The increased microstrain observed for the distorted tetragonal phase might even play a role in enhancing the conductivity taking into account the presence of a non-conducting pyrochlore type impurity phase. The ASR of the Li|LLZO interface is 76 Ω cm^2 (59 Ω cm^2), which is among the best values reported to date. This value corresponds to a relatively smooth surface of the solid electrolyte consisting of grains with an average size in the range from 0.5 μm to 3 μm. Galvanostatic cycling is performed at different current densities and the cell is stably operated for over 100 hours. The change of the ASR during cycling at different current densities shows the unpredictability of the processes occurring at the Li-solid electrolyte interface. These processes especially relate to many factors starting at the manual application of the Li-electrodes, which needs to be standardized. Novel in-situ characterization techniques, e.g., X-ray diffraction and STEM need to be employed to correlate the observed change in the impedance spectra with structural, compositional and microstructural evolution of the interface during cycling, bearing in mind that the reactions and processes at this interface are crucial for the battery performance.

7 Impact of processing conditions on ceramic properties and electrochemical performance

In addition to the phase purity of the material, it has been reported that the microstructure, i.e., ceramic density and grain size, can have a significant influence on the electrochemical performance of the garnet solid electrolyte [70]. The influence of microstrain on the electrochemical performance, however, has not been studied for garnet Li-ion conductors. In a different material system, for thin film oxygen-ion conductors, it has been shown that the microstrain at the interface between two materials with different lattice parameters has an influence on the conductivity, and depending on the strain type and conduction mechanism of the ionic species the interfacial conductivity either increases or decreases. Compressive strain between yttrium stabilized zirconia (YSZ) and Sc_2O_3 layers, for instance, leads to a decrease in the ionic conductivity, while dilative strain at the interface between YSZ and Y_2O_3 results in an increase of the ionic conductivity [82]. There are several process parameters during powder synthesis and processing, during sintering using FAST and post treatments of the ceramic that can alter the microstructure and hence influence the electrochemical performance of the LLZO solid electrolyte. In the following study the microstructure of the LLZO ceramics is altered to gain insight to how the process influences its electrochemical behavior. Ball milling of the powder before sintering can have a great impact on the grain size of the respective ceramics and on the structural defect concentration near the powder particle surface, which is accompanied by a reduction of potential barriers for the nucleation of a new phase in addition to the increased surface area of the particles [83]. The influence of an additional ball milling step before conventional sintering of the as-synthesized powder and field assisted sintering of the calcined powder and the accompanying effects on the Li-ion conductivity are presented and discussed.

The uniaxial pressure during FAST is the only process parameter during the sintering process that would not have a significant influence on the grain coarsening in contrast to temperature and dwell time. Therefore, it is varied for its proposed influence on the microstrain, which is present mainly in the distorted tetragonal phase observed after sintering. The influence of the microstrain on the Li-ion conductivity is discussed and a potential strain induced enhancement of the Li-ion conductivity and thereby the cycling behavior is proposed.

After FAST the ceramics are exposed to relatively low annealing temperatures under an oxygen containing atmosphere, which might result in the release of the microstrain and a redistribution of Li-ions, thereby influencing the local structure of the solid electrolyte [84]. During field assisted sintering the specimen is exposed to simultaneous heating, at high heating and cooling rates, mechanical pressure and an electric field. The three components result in a fast sintering process at relatively low temperatures compared to conventional solid state reaction methods, while the grain growth is suppressed. Additional effects during FAST are observed for LLZO ceramics, which can result in cracking of the specimen. Underlying mechanisms for this challenging aspect of field assisted sintering are presented and possible solutions are discussed. The aim of this section, in addition to the impact of annealing on the electrochemical performance, is to present guidelines for field assisted sintering of electronically insulating oxide materials with a high ionic conductivity.

The storage conditions like time and atmosphere can possibly lead to changes in the microstructure of the ceramic. The ceramic is characterized before and after storage under an Ar atmosphere for a prolonged period of time and the resulting influence on the ionic conductivity is determined and discussed.

7.1 Conventional sintering

Although the conventional sintering of the as-synthesized NSP powder only delivers porous ceramics, resulting in low Li-ion conductivities, the following experiments are designed to determine the influence of an additional ball milling step before sintering on the ionic conductivity decoupled from any significant compositional and structural differences. The low density of the ceramics eliminates density dependent enhancement of the electrochemical performance.

7.1.1 Influence of the particle size of the starting powder

The nominal composition of the conventionally sintered ceramics is $Li_{7\text{-}3x}La_3Zr_2Al_xO_{12}$ with $x = 0.22$ and 30 wt.% Li-excess during synthesis. As it is previously reported in Chapter 4, the optimal Al-content for the conventional sintering procedure to obtain a pure cubic structure is determined to be $x = 0.15$, nevertheless a higher Al-content is chosen for this study to obtain a comparable composition to the ceramics processed by field assisted sintering (see section 7.2). The as-synthesized powder is ball milled at 500 rpm for 2 h, with rotation inversion every 30 min to obtain a finer microstructure of the starting material as well as the sintered ceramic. Ball milling is carried out under Ar. Conventional sintering at 1000 °C for 1 hour is carried out under air in a sealed alumina crucible to minimize Li loss. The pellets are imbedded in their mother powder to avoid interaction with the crucible.

7.1.1.1 Phase composition

After synthesis using NSP the as-synthesized powder is composed of $La_{0.5+\partial}Zr_{0.5\text{-}\partial}O_{1.75\text{-}\partial/2}$ ($Fm\bar{3}m$) and Li_2CO_3. The diffraction patterns for the as-synthesized powder before and after ball milling are shown in Figure 7-1a. After sintering the pellets show a mostly cubic garnet structure ($Ia\bar{3}d$) accompanied by a $La_2Zr_2O_7$ ($Fd\bar{3}m$) impurity phase indicating Li loss from the garnet structure during sintering. The ceramic with finer particles in the starting material shows a larger amount of $La_2Zr_2O_7$ impurity phase, which is expected on account to the higher surface area of the powder. This possibly leads to a higher adsorption of moisture and CO_2 leading to increased formation of volatile Li containing species, e.g., LiOH. Additionally, the ceramic with a finer microstructure shows a La_2O_3 impurity phase, while a small amount Li_2CO_3 is detected in both samples. The X-ray diffraction patterns of the sintered ceramics are presented in Figure 7-1 b.

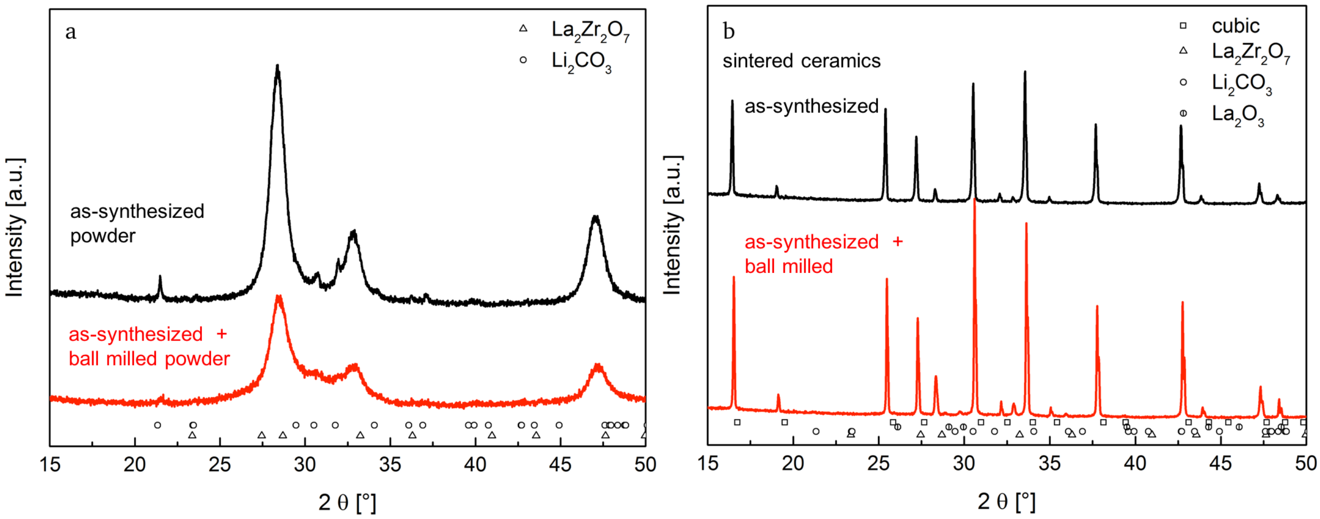

Figure 7-1: X-ray diffraction patterns of as-synthesized powder with $x = 0.22$ before and after ball milling (a) and respective conventionally sintered ceramics (b).

Rietveld refinements are carried out for all diffraction patterns and an overview of the results is presented in Table 7-1. The crystallite size of the as-synthesized powder for the main CaF_2-type phase before and after ball milling is calculated to 8.5 nm and 5.1 nm, respectively. The Li_2CO_3 phase fraction increases from 34 wt.% to 50 wt.% after ball milling. This could be due to a reaction of undetected Li_2O or LiOH in the as-synthesized powder and adsorbed CO_2 from the air exposure after synthesis. The crystallite size of the sintered ceramics lies in the range of a few hundred nanometers. Therefore, the determination of the crystallite size with high accuracy using Rietveld refinement is difficult and it is fixed to approximately 300 nm. The cubic phase fraction of both ceramics is the main phase, while the pyrochlore impurity phase is doubled when using the ball milled powder as starting material instead of the as-synthesized powder. The amount of Li_2CO_3 is comparable for both ceramics and is probably due to air exposure of the ceramics during cool down. The reason for the presence of La_2O_3 is not identified, yet the amount is negligible.

Table 7-1: Rietveld refinement results of as-synthesized powders before and after ball milling and the corresponding sintered ceramics with $x = 0.22$.

Sample	Phase	Phase fraction [wt.%]	Crystallite size [nm]
As-synthesized	$La_2Zr_2O_7$	66.0(6)	8.5(3)
	Li_2CO_3	33.9(6)	15.8(6)
Ball milled	$La_2Zr_2O_7$	49.9(4)	5.1(3)
	Li_2CO_3	50.1(4)	3.4(6)
Sintered ceramic (as-synthesized)	cubic	96.0(2)	-
	$La_2Zr_2O_7$	2.8(2)	-
	Li_2CO_3	1.16(0)	-
Sintered ceramic (as-synthesized + ball milled)	cubic	92.0(9)	-
	$La_2Zr_2O_7$	6.9(1)	-
	Li_2CO_3	0.80(0)	-
	La_2O_3	0.28(3)	-

7.1.1.2 Microstructure

The microstructures of the as-synthesized powder before and after ball milling at 500 rpm for 2 h, as well as the corresponding conventionally sintered ceramics with a composition $Li_{7-3x}La_3Zr_2Al_xO_{12}$ ($x = 0.22$) are shown in Figure 7-2. The as-synthesized powder shows a hollow spherical microstructure. The shells of the hollow spheres are composed of nanocrystallites, as previously reported in section 4.1.2. After ball milling the powder shows large agglomerates of solid particles. The spherical microstructure is no longer observed. The particle size ranges between 0.2 μm and 1.6 μm, with a mean value of 0.7 μm. The conventionally sintered ceramics using the as-synthesized powder before and after ball milling show a similar microstructure with interconnected open porosity and cracks. It is evident that the ball milling procedure significantly alters the microstructure of the starting powder. However, the microstructure of the sintered ceramic does not show a significant modification. It is possible that the modification is on a smaller scale and can only be observed at higher magnifications for example using TEM.

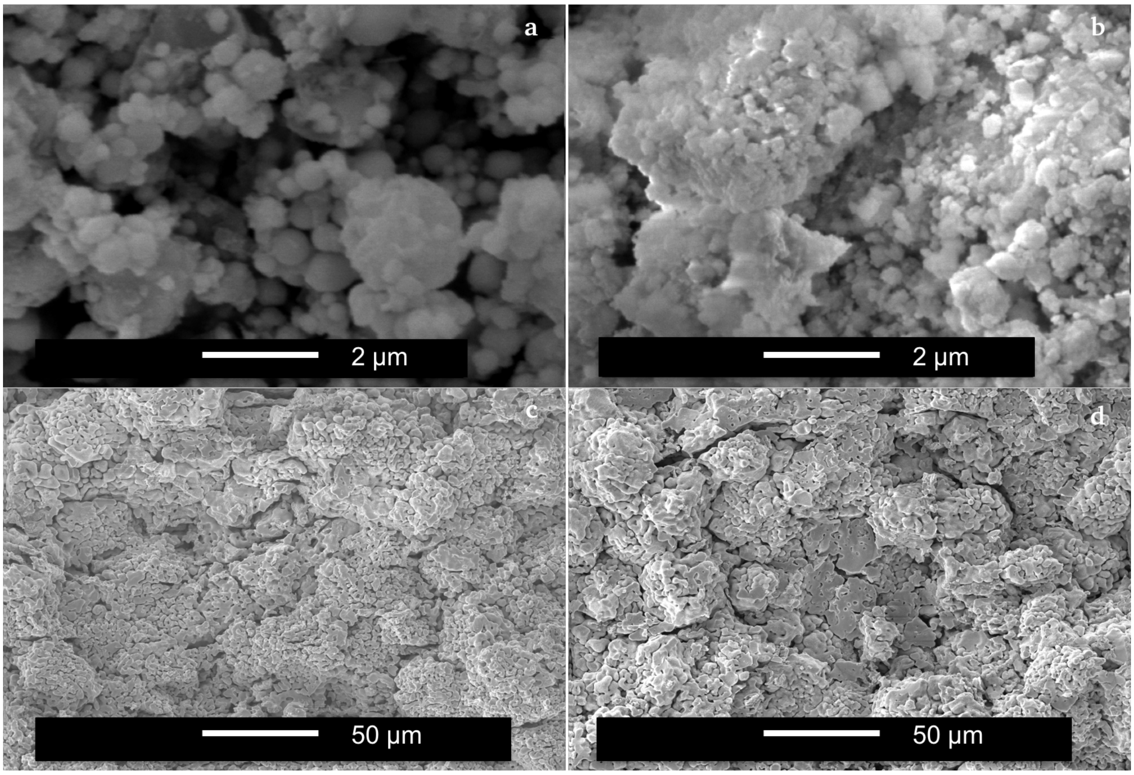

Figure 7-2: SEM images of as-synthesized powder with an Al-content $x = 0.22$ and 30 wt.% Li-excess during synthesis (a), as-synthesized powder after ball milling (b) and conventionally sintered pellet using as-synthesized powder (c) and sintered pellet using an additional ball milling step of the starting powder (d).

The main difference observed after conventional sintering is the geometrically determined density of 55% TD for the ceramic with the as-synthesized starting powder and 60% TD for the ceramic sintered after an additional ball milling step. The slightly higher density is a most likely result of the breaking of the hollow spheres during ball milling and the activation of the particle surfaces leading to higher reactivity [83]. The slight increase in density after ball milling of the starting powder shows that the limiting factor for achieving a high density is not the spherical microstructure of the powder synthesized using NSP but most probably the temperature limitation during the sintering process due to the expected Li volatility at higher temperatures.

7.1.1.3 Li-ion conductivity

AC-impedance spectroscopy is carried out in a wide temperature range from 298 K to 393 K for both ceramics coated with blocking Au-electrodes, while the resistance of the ceramic with as-synthesized starting powder is too high to be measured at room temperature up to 317 K. The coated samples are kept to dry under vacuum at 100 °C for 24 hours. The cryostat is filled with He gas during all measurements to eliminate any proton exchange reactions while heating the sample. The impedance spectra are recorded while cooling down the sample to eliminate any possible overestimation of the ionic conductivity due to residual moisture. Representative temperature dependent Nyquist pots of both large grained (as-synthesized starting powder) and small grained ceramics (ball milled starting powder) are presented in Figure 7-3. The frequencies at the maxima of the bulk and grain boundary contributions to the spectra are indicated with arrows. The magnification at low resistance values shows in the case of the large grained ceramic overlapping of the bulk and grain boundary contributions to the spectrum with a capacitance of 10^{-12} F and 10^{-11} F, respectively. For the small grained ceramic, the semi-circles are separated more clearly with a capacitance of 10^{-11} F and 10^{-9} F for the bulk and grain boundary contribution to the spectrum, respectively.

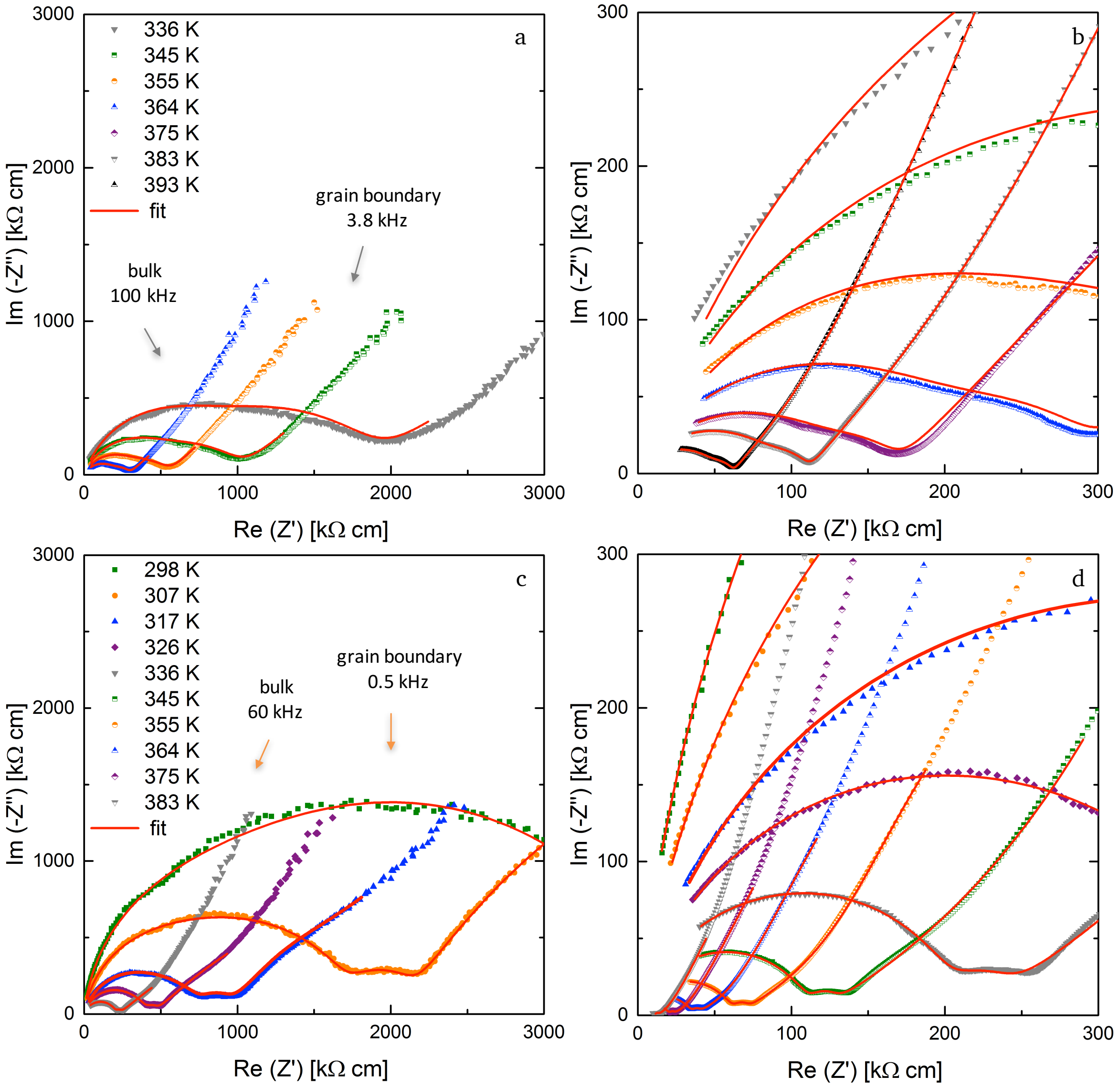

Figure 7-3: Nyquist plots and corresponding fits for sintered ceramics ($x = 0.22$) with blocking Al-electrodes between 336 K up to 393 K with as-synthesized starting powder (a), its magnification (b) and between 298 K and 383 K with ball milled starting powder (b), its magnification (d).

The temperature dependence of the ionic conductivity for both ceramics with different particle sizes of the starting powder is presented in Figure 7-4. The ceramic with a ball milled starting material has higher conductivities throughout the measured temperature range with a room temperature conductivity of 0.20 μS cm^{-1}, while the ceramic with as-prepared starting powder shows an extrapolated room temperature conductivity of 0.024 μS cm^{-1}. The one order of magnitude higher room temperature conductivity of the small grained ceramic is accompanied by a lower activation energy of 0.70 eV compared to the 0.72 eV found for the large grained ceramic.

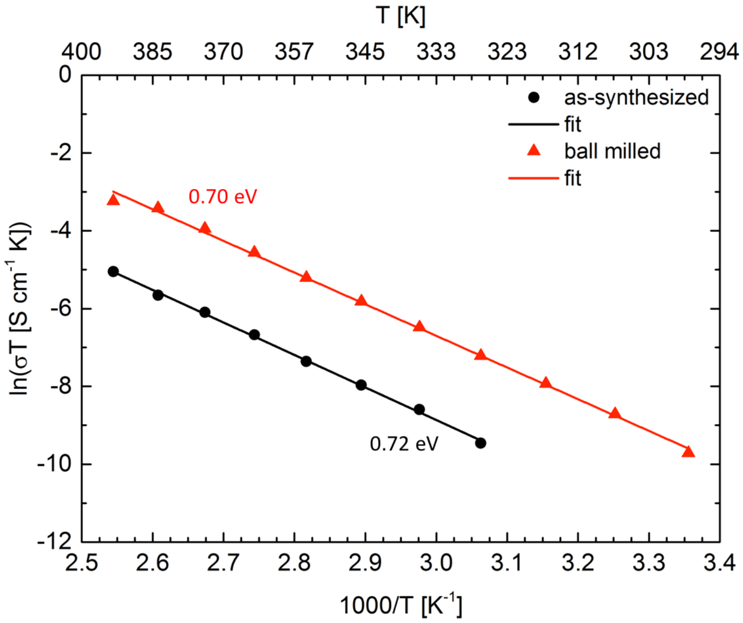

Figure 7-4: Arrhenius plot presenting the temperature dependence of the Li-ion conductivity for two different grain sizes achieved by ball milling of the as-synthesized starting powder.

The bulk and grain boundary resistance could be separated and the corresponding conductivities are calculated using the dimensions of the pellets, which is an approximation. The temperature dependent bulk and grain boundary conductivities for each ceramic are plotted in Figure 7-5. For both ceramics the grain boundary conductivity is higher than that of the bulk, while the ceramic with a ball milled starting material shows higher bulk and grain boundary conductivities, in addition to a larger difference between both contributions to the conductivity. Additionally, the bulk activation energy increases from 0.66 eV to 0.69 eV after ball milling, while the grain boundary activation energy decreases from 0.90 eV to 0.77 eV. Despite the expected Li loss from the garnet structure the grain boundary activation energy decreases drastically implying a higher mobility of Li-ions at the grain boundary of conventionally sintered ceramics after adding a ball milling step to the starting powder processing.

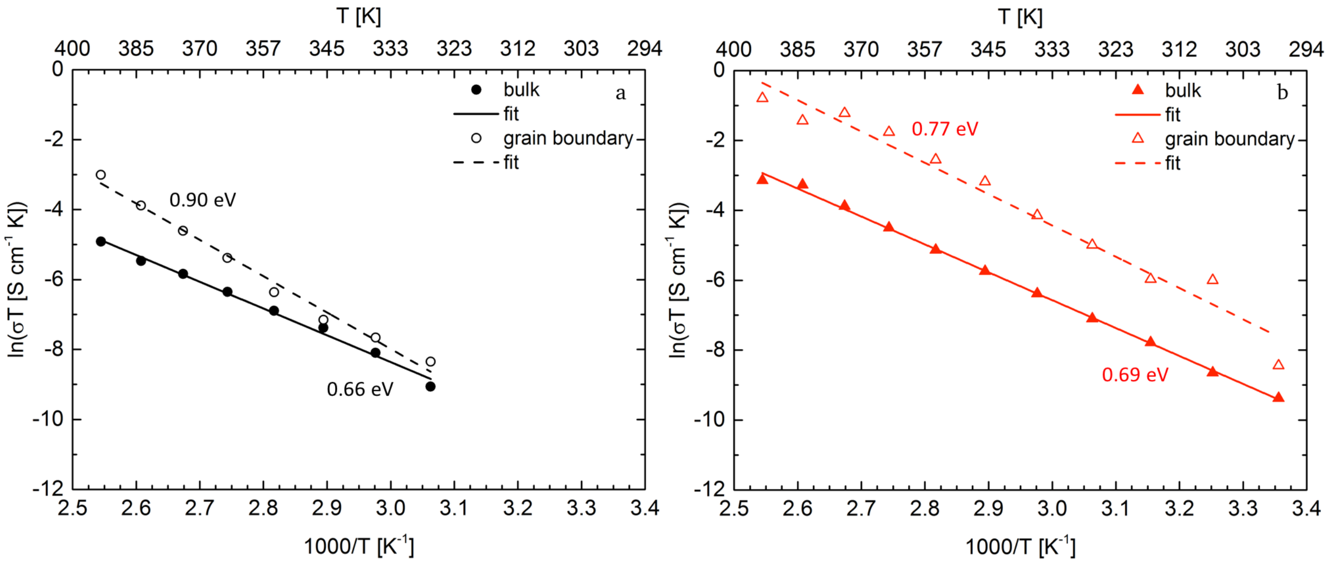

Figure 7-5: Arrhenius plots presenting the temperature dependence of the bulk and grain boundary Li-ion conductivities for two different grain sizes achieved by ball milling of the as-synthesized starting powder, large grained (a) and small grained ceramic (b).

Conventional sintering supplies ceramics with densities lower than 60% TD, regardless of the microstructure of the starting material. This is due to the limitation of the sintering temperature to 1000 °C required to minimize Li loss in the form of volatile Li containing species. Nevertheless, this study shows that the Li-ion mobility at the grain boundaries is strongly dependent on the nature, i.e., structure, microstructure and composition of the grain boundaries and therefore on the synthesis and processing methods employed. The additional ball milling step might have increased the defect concentration especially in the grain boundary region and thereby increasing the Li-ion mobility. The increase in mobility through the presumed increase of defect concentration might open the path for the synthesis of amorphous LLZO ceramics with a possible enhancement of the electrochemical performance, as it has been shown for amorphous $LiNbO_3$ compared to its microcrystalline counterpart [85].

7.2 Field assisted sintering

There are attempts reported in the literature to determine the influence of the grain size on the Li-ion conductivity by utilizing different processing methods to achieve different grain sizes, e.g., FAST followed by conventional sintering for Ga-substituted $Li_7La_3Zr_2O_{12}$ [86] or comparing ceramics synthesized using sol-gel method with ceramics synthesized using solid state reaction [71]. In the first approach it is evident that utilizing conventional sintering after field assisted sintering not only leads to grain coarsening (from 1 μm to 7 μm) but also increases the density of the ceramics leading to higher ionic conductivities. The second study suggests a similar room temperature ionic conductivity for ceramics with a grain size of 3.3 μm compared to those with a grain size of 260 nm. For small grained ceramics an activation energy of 0.41 eV is calculated, while it is determined to 0.26 eV for large grained ceramics [71]. Using different synthesis routes for varying the grain size affects the phase composition and microstructure of the grain boundaries, which is crucial for determining the influence of solely the grain size on the ionic conductivity. Furthermore, work by Cheng et al. [70] suggests that reducing the grain size from 100-200 μm down to 10 μm leads to a slightly higher conductivity from 0.20 mS cm^{-1} to 0.25 mS cm^{-1} accompanied by a slight increase in activation energy from 0.32 eV to 0.34 eV. Additionally, an improvement of the area specific resistance against Li metal from 130 Ω cm^2 to 37 Ω cm^2 is observed [70]. In section 7.2.1 ball milling is utilized before field assisted sintering of the calcined powder to determine the influence of the initial particle size on the electrochemical performance of the dense LLZO ceramic. Underlying microstructural and compositional variation due to the additional ball milling step are presented and discussed.

Determining the influence of solely the density on the electrochemical performance is also challenging, since it is difficult to decouple it from other effects. This is the reason for the absence of reports on the density dependence of the ionic conductivity in the literature, without the overlaying effect of grain size or composition [86–89]. While the utilization of field assisted sintering brings many advantages, such as high densities within short sintering times, which reduces the Li loss during sintering and suppresses grain growth, it also exhibits the disadvantage of the limited knowledge of the effect of the applied electric field on electronically insulating specimens [41,90]. Therefore, only the influence of the uniaxial pressure applied during FAST on the microstructure of the LLZO ceramics, insuring a comparable electric field, is studied and presented in section 7.2.2.

7.2.1 Influence of the particle size of the starting powder

The samples used for this study have the nominal composition $Li_{7-3x}La_3Zr_2Al_xO_{12}$ with $x = 0.22$ and 30 wt.% Li-excess during synthesis via NSP. This composition is chosen since it shows the best electrochemical performance. The as-synthesized powder is calcined under an Ar atmosphere at 900 °C for 1 hour, see section 5.2 for further details about the optimization of the calcination process. After calcination a defined amount of powder (approx. 300 mg) is used for FAST, while 1 g is ball milled using Retsch PM100CM planetary ball mill. A 50 ml zirconia jar is used filled with 10 zirconia balls (diameter 10 mm). The speed is set to 500 rpm for 2 hours, with direction inversion every 30 min. The powder is filled and removed from the jar in an Ar-filled glove box. Field assisted sintering is carried out directly after ball milling, while the surfaces of the particles are activated and therefore show a higher reactivity and sinterability [83].

7.2.1.1 Phase composition

The phase composition of the calcined powder as well as after ball milling is shown in Figure 7-6a. Rietveld refinement of the pattern of the calcined powder shows a mixture of cubic and tetragonal phase of 47.48 wt.% and 51.35 wt.%, respectively. Additionally, 1 wt.% of Li_2ZrO_3 is detected. The crystallite size lies in the range of a few hundred nanometers and cannot be accurately determined and therefore is fixed to approximately 300 nm during Rietveld refinement. After ball milling a broadening of the reflections is observed indicating a decrease in crystallite size down to approximately 15 nm. The presence of impurity phases is negligible for both starting materials. After field assisted sintering the pellets are measured on both sides and the corresponding X-ray diffraction patterns are shown in

Figure 7-6b. Comparable results are observed concerning the emerging of the previously discussed strained, distorted tetragonal phase as well as the presence of a phase fraction of the $La_2Zr_2O_7$ impurity phase, which is indicative for Li loss from the garnet structure during sintering. An overview of the Rietveld refinement data for the sintered ceramics are presented in Table 7-2. The values given are mean values over both sides of the pellets. The variation of the phase fraction of the impurity phase on both sides of the ceramic sample most probably originates in electromigration of the Li-ions due to the direct current electric field applied during field assisted sintering. The most prominent difference between the sintered ceramics is the amount of $La_2Zr_2O_7$ impurity phase. The mean value of the impurity phase fraction for the ceramic sintered after ball milling of the starting powder is significantly higher than for the ceramic sintered directly after calcination. This fact has to be taken into consideration, since the electrochemical performance might suffer due to the presence of the $La_2Zr_2O_7$ phase.

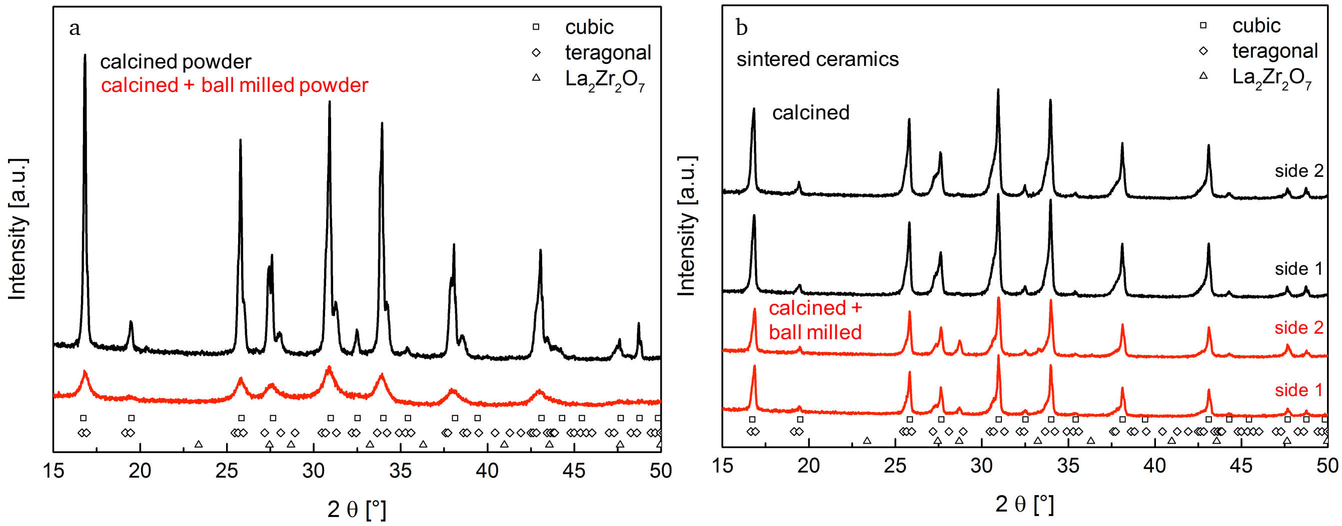

Figure 7-6: X-ray diffraction patterns of the $Li_{7-3x}La_3Zr_2Al_xO_{12}$ calcined powder with $x = 0.22$ at 900 °C for 1 h and followed by ball milling at 500 rpm for 2 h (a) and respective sintered ceramics measured on both sides of the pellets (side 1 and side 2) (b).

Table 7-2: Rietveld refinement data for sintered ceramics with calcined and additionally ball milled starting material with $x = 0.22$.

Sample	Phase	Phase fraction [wt.%]	Unit cell volume [Å^3]	Microstrain	c/a
Sintered ceramic	cubic	50.7(2)	2175.669(94)	0.036(4)	1
(calcined)	tetragonal	49.0(2)	2211.0(16)	0.333(2)	0.992
	$La_2Zr_2O_7$	0.31(2)	1260.4(14)	-	1
Sintered ceramic	cubic	57.6(1)	2176.73(14)	0.047(4)	1
(calcined+	tetragonal	38.8(1)	2216.2(13)	0.346(3)	0.992
ball milled)	$La_2Zr_2O_7$	4.6(2)	1262.43(29)	-	1

The higher amount of the $La_2Zr_2O_7$ impurity phase is an indication of Li loss from the garnet structure and thereby possibly reducing the charge carrier concentration, i.e., Li-ion concentration for ionic conductivity. To confirm the Li loss, ICP-OES measurements are carried out for ceramics sintered with a starting material directly after calcination and after an additional ball milling step. The results are shown in Table 7-3. It is evident that the Li amount in the sample showing a higher impurity phase fraction is indeed 9% lower, but the Li-content for both samples is higher than the nominal value for the garnet phase. This might be due to the Li-excess used during synthesis, which is still present in the form of Li containing compounds, e.g., Li_2CO_3 and Li_2O or occupying Li vacancies in the garnet structure. The Li-ions involved in the conduction process, that reside on tetrahedral and octahedral sites, is estimated to be only 12.3% of the total Li-ion concentration in the garnet structure [91]. Therefore, a possible Li loss from the garnet structure due to the processing route including ball milling does not necessarily mean a loss of charge carriers for the conduction process. A high Li occupancy, however, could reduce the Li-ion mobility due to the reduced number of Li vacancies.

Table 7-3: ICP-OES results for sintered ceramics, nominal composition $Li_{6.34}La_3Zr_2Al_{0.22}O_{12}$, with different grain sizes due to additional ball milling of the starting powder after calcination.

Sample	Li	Al	Li:La	Li:Zr	Zr:La
Calcined	7.14(24)	0.196(2)	2.38	3.35	0.68
Calcined+ Ball milled	6.50(06)	0.217(2)	2.17	3.16	0.68

7.2.1.2 Microstructure

For the characterization of the microstructure of the calcined powder before and after ball milling as well as the corresponding sintered ceramics, scanning electron microscopy is utilized. The micrographs for the powders with an Al-content of $x = 0.22$ and cross sections of the sintered ceramics are presented in Figure 7-7. The calcined powder shows large agglomerates consisting of solid particles. Between the particles sintering necks are formed indicating the onset of the sintering process. After ball milling the sintering necks are no longer observed and the particle size ranges from 0.2 μm to 3.3 μm, with a mean value of 0.9 μm. Nevertheless, agglomeration is still present. After field assisted sintering of the calcined powder the pellet is broken manually to investigate the cross section. The micrograph shows a high density, as expected from density measurements using a novel method employing laser confocal microscopy. A detailed description of the method is reported elsewhere [92]. The measured density is 5.11(5) g cm^{-3} (>99% TD). Grain sizes between 1.1 μm and 5.9 μm have been measured on 100 grains with a mean value of 2.2 μm. The cross sectional imaging of the ceramic sintered using an additionally ball milled powder shows a significantly smaller grain size between 0.2 μm and 1.7 μm with a mean value at 0.7 μm and a high density of 4.97(5) g cm^{-3} (97% TD) measured using laser confocal microscopy [92]. The difference in density between both large and small grained ceramics is 3%, which is negligible considering the expected larger impact of the grain size on the further characterization of the electrochemical performance.

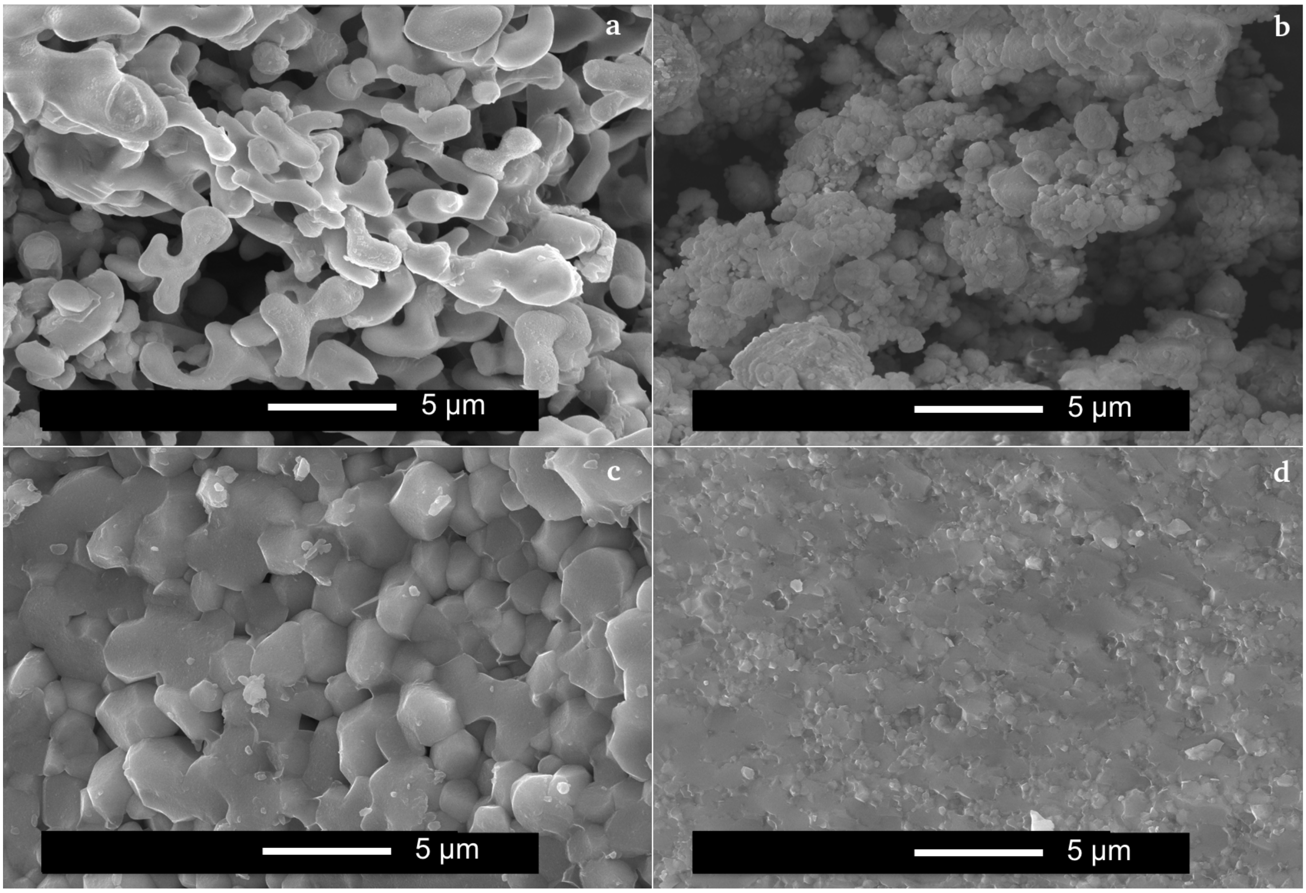

Figure 7-7: SEM images of calcined $Li_{7-3x}La_3Zr_2Al_xO_{12}$ powder ($x = 0.22$) before (a), after (b) ball milling and the corresponding large (c) and small grained ceramics (d).

A more detailed characterization of the microstructure, especially of the inter- and intragranular elemental distribution and actual composition, is carried out using HAADF STEM. Thin lamellae (50 nm) of the large and small grained ceramics are prepared using a Ga focused ion beam (FIB). A microstructural instability is observed during the FIB preparation especially around pores. This observation is most probably due to the decomposition of residual Li containing species like, e.g., Li_2CO_3 that are known for their beam sensitivity [56]. This phenomenon increases with reduced thickness of the specimen, since it becomes more vulnerable to the electron beam as well as the ion beam during final polishing of the lamellae. Nevertheless, the grains and the grain boundaries without any large pores, where the beam sensitive species presumably reside, remain stable during FIB preparation. The lamellae are transferred to the transmission electron microscope for further characterization after only a few minutes of air exposure. The EDXS elemental maps for Zr ($K_{\alpha1}$-line), La ($L_{\alpha1}$-line), Al ($K_{\alpha1}$-line), O (K-line) and C (K-line) for the large grained ceramic are shown in Figure 7-9. The EDXS elemental map of the Al distribution within the sample clearly shows that Al is not segregated at the grain boundaries and that Al is uniformly distributed within the $Li_{7-3x}La_3Zr_2Al_xO_{12}$ grains. EDXS elemental maps show also the uniform distribution of Zr and La, as well as, C contamination within the grains, with a low contamination level of approximately 2 at.% according to EDXS quantitative analysis. Additionally, the HAADF STEM image shows the formation of circular pores within some grains. EDXS indicated no segregation of Al, as well as, any other element in regions where the observed pores reside. It can be ruled out that the pores are an artefact due to sample preparation, since the second sample with a smaller grain size, prepared under the same conditions, does not exhibit intergranular pores. The agglomerated calcined powder with sintering necks between the particles might be the origin for this pore formation. The regions chosen for the quantification of the EDXS elemental distribution of the large grained ceramic are shown in Figure 7-10a and the results are given in Table 7-4. The quantitative analysis shows the formation of stoichiometric $Li_{6.1}La_3Zr_2Al_{0.3}O_{12}$ with the Li-content being calculated from the observed Al-content for the intragranular regions with and without pores. Additionally, the grain boundary region is examined resulting in a chemical composition also confirming the formation of the stoichiometric compound.

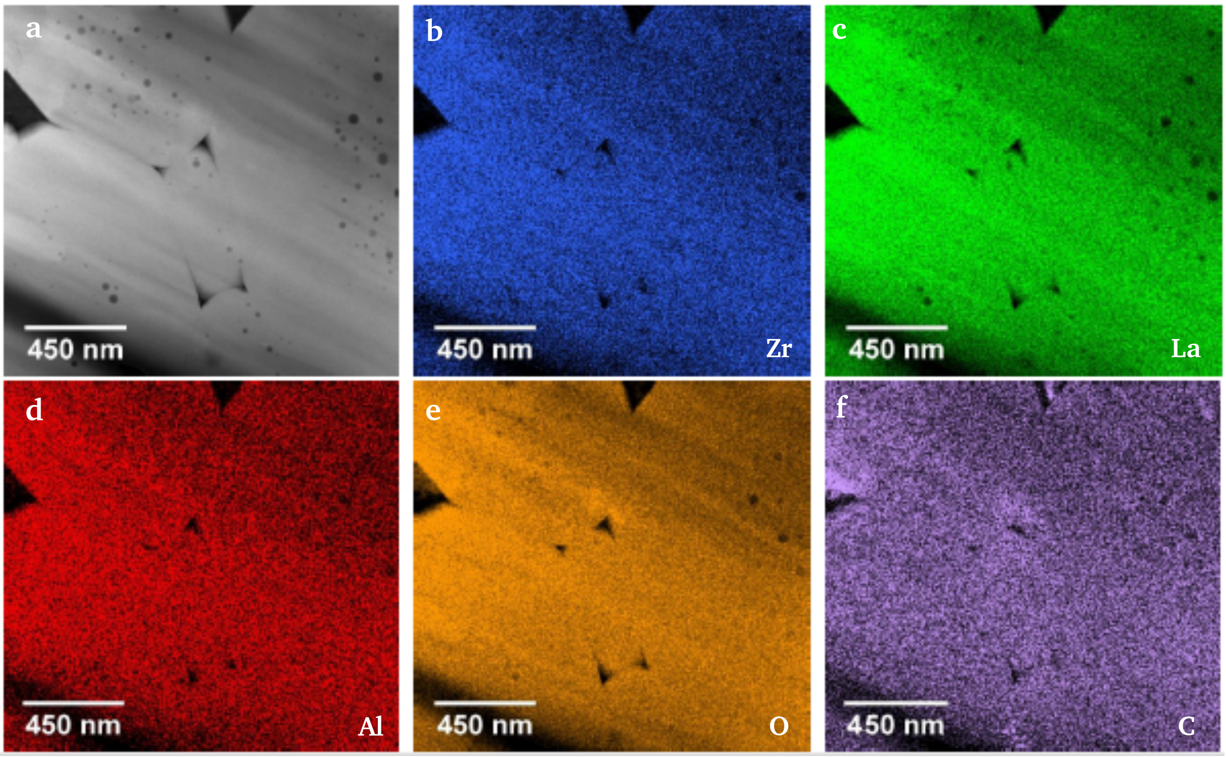

Figure 7-8: HAADF STEM image (a) and corresponding EDXS elemental distribution of Zr (b), La (c), Al (d), O (e) and C (f) of sintered $Li_{7-3x}La_3Zr_2Al_xO_{12}$ large grained ceramic ($x = 0.22$).

A second measurement presented in Figure 7-9 shows a precipitation of a secondary phase with brighter contrast compared to that of the grains. Because the contrast on HAADF STEM images is directly related to the atomic number of chemical elements contained in the material, different chemical composition of the precipitates and grains is expected. This is suggested also by EDXS elemental maps of O and C distributions, which show that the segregated material contains more O and C compared to the grain. It has to be pointed out that the O/C concentration measured by EDXS for the precipitate is a sum of the real concentration of O/C within the secondary phase and the O/C concentration of the grain. Therefore, the O/C concentration of a neighboring region of the grain must be determined and subtracted from the total composition of O/C measured for the secondary phase before calculating its real composition. For that reason, EDXS area scans on the grain in regions near the investigated precipitate, are separately recorded and quantified.

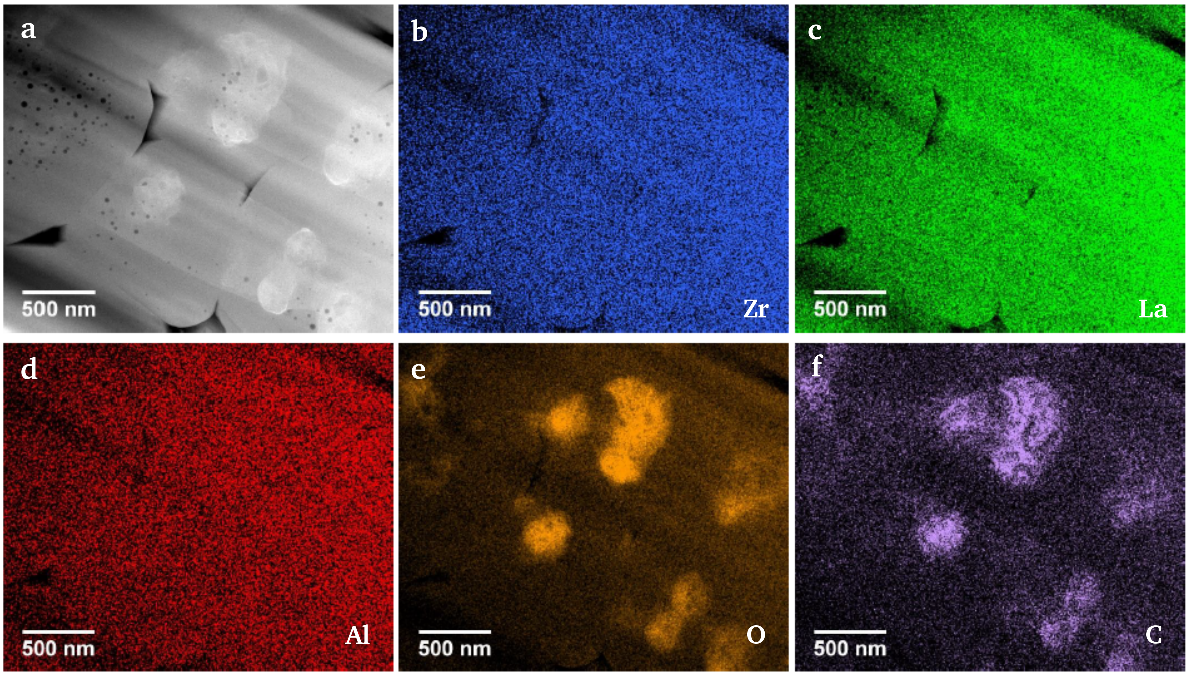

Figure 7-9: HAADF STEM image (a) and corresponding EDXS elemental distribution of Zr (b), La(c), Al (d), O (e) and C (f) of sintered $Li_{7-3x}La_3Zr_2Al_xO_{12}$ large grained ceramic ($x = 0.22$).

EDXS maps are used to determine the chemical composition of the grain and of neighboring precipitate. The chosen regions for quantification are presented in Figure 7-10b and the quantification results are presented in Table 7-4. The significantly sub-stoichiometric oxygen composition of grains containing precipitates needs to be noted in comparison to grains without a secondary phase. Considering the error for the Al-content it is comparable to the results for grains without precipitates. After subtraction the composition of the grain from the composition of the segregated material, a chemical composition of $CO_{2.9}$ is calculated and no La, Zr or Al are obtained after subtraction. This might correspond to the composition expected for Li_2CO_3 taking into account that Li cannot be quantified. This result is confirmed by a second quantification of a different grain. The oxygen deficiency of the garnet phase around the segregated material as well as the confirmation that the segregation is a carbonate containing phase, leads to the conclusion that oxygen as well as Li are extracted from the garnet structure during sintering and react with carbon contamination most probably from adsorbed CO_2 during the short transport of the powder in air. EDXS maps are further used to determine the chemical composition of regions at the grain boundaries. Here no compositional change is expected from the visual inspection of EDXS elemental maps. The quantification results are comparable considering the margin of error, with a sub-stoichiometric oxygen composition for the grains containing a secondary phase. The Al-content is between $x = 0.20$ and $x = 0.30$ throughout all measurements and no Al segregation is observed. The sub-stoichiometric oxygen content of the grain boundaries might indicate the formation of Li_2CO_3 in the corresponding grain boundary region during sintering, it is not detected using HAADF STEM due to its decomposition during field assisted sintering or FIB processing.

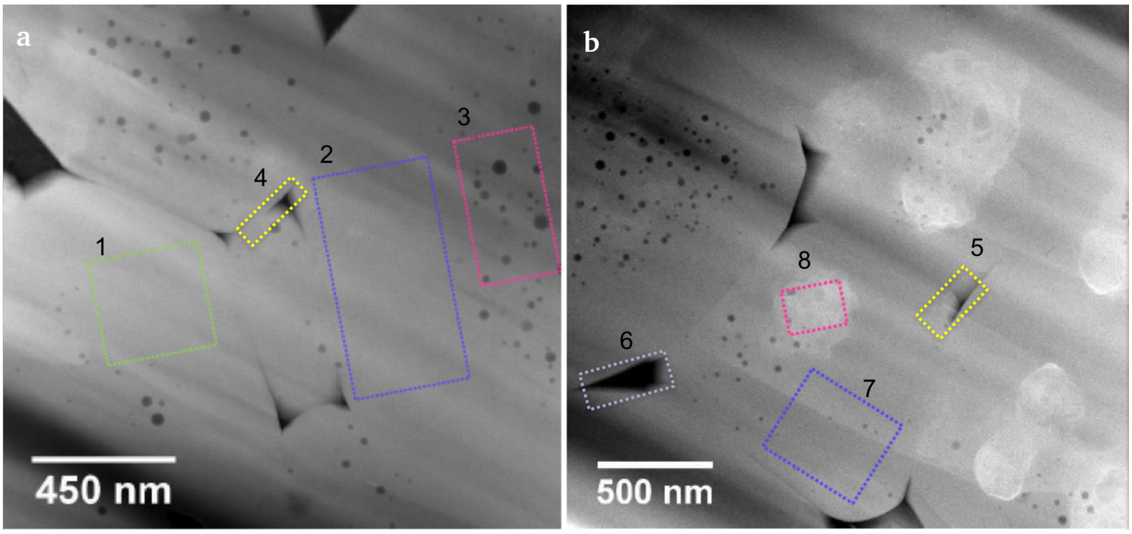

Figure 7-10: HAADF STEM images of the regions quantified by EDXS for large grained $Li_{7-3x}La_3Zr_2Al_xO_{12}$ ceramics ($x = 0.22$) without precipitates (a) with Li_2CO_3 precipitates (b).

Table 7-4: EDXS quantitative results of the selected regions of the large grained ceramic.

Region	La [mol]	Zr [mol]	Al [mol]	O [mol]	C [mol]
1	3.20(30)	2.00(20)	0.28(04)	11.5(6)	-
2	3.20(30)	2.00(20)	0.26(04)	12.0(6)	-
3	3.20(30)	2.00(20)	0.28(04)	12.3(6)	-
4	3.30(30)	2.00(20)	0.28(04)	13.3(9)	-
5	3.10(25)	2.00(20)	0.22(04)	10.6(9)	-
6	3.20(32)	2.00(20)	0.28(04)	9.1(8)	-
7	3.10(26)	2.00(20)	0.18(03)	7.6(3)	0.24(03)
8	3.22(42)	2.00(35)	0.23(06)	21.6(9)	5.16(22)

The EDXS elemental maps for Zr ($K_{\alpha1}$-line), La ($L_{\alpha1}$-line), Al ($K_{\alpha1}$-line), O (K-line) and C (K-line) for the small grained ceramic are shown in Figure 7-11. The C contamination level is low, the quantification of the EDXS data results in a level <2 at.%. The EDXS elemental map of Al distribution within the sample clearly shows that no segregation of Al at the grain boundaries takes place and Al being uniformly distributed over the $Li_{7-3x}La_3Zr_2Al_xO_{12}$ grains. The exception is the grain with higher contrast on the HAADF STEM image. Because the contrast on HAADF STEM images is directly related to the atomic number of chemical elements contained in the material, different chemical composition of this grain is expected. This is suggested also by EDXS elemental maps of Zr and Al distributions, which show that this grain contains more Zr and less Al compared to the other grains. Figure 7-13a shows the regions chosen to determine the chemical composition from the quantification of the EDXS maps and the results are shown in Table 7-5. The quantification of the grain interior shows stoichiometric composition. On the other hand, the grain with a brighter contrast shows a chemical composition, which corresponds very well to the $La_2Zr_2O_7$ phase with a similar La content as the other grains (18 at.%), but more Zr (18 at.% compared to 11 at.%) and almost no Al. The formation of grains with stoichiometric $Li_{6.1}La_3Zr_2Al_{0.3}O_{12}$ is observed. The quantification of the grain boundary region shows, as expected from the visual inspection of the elemental maps, a chemical composition, which is in very good agreement with the composition of the $Li_{6.1}La_3Zr_2Al_{0.3}O_{12}$ grains.

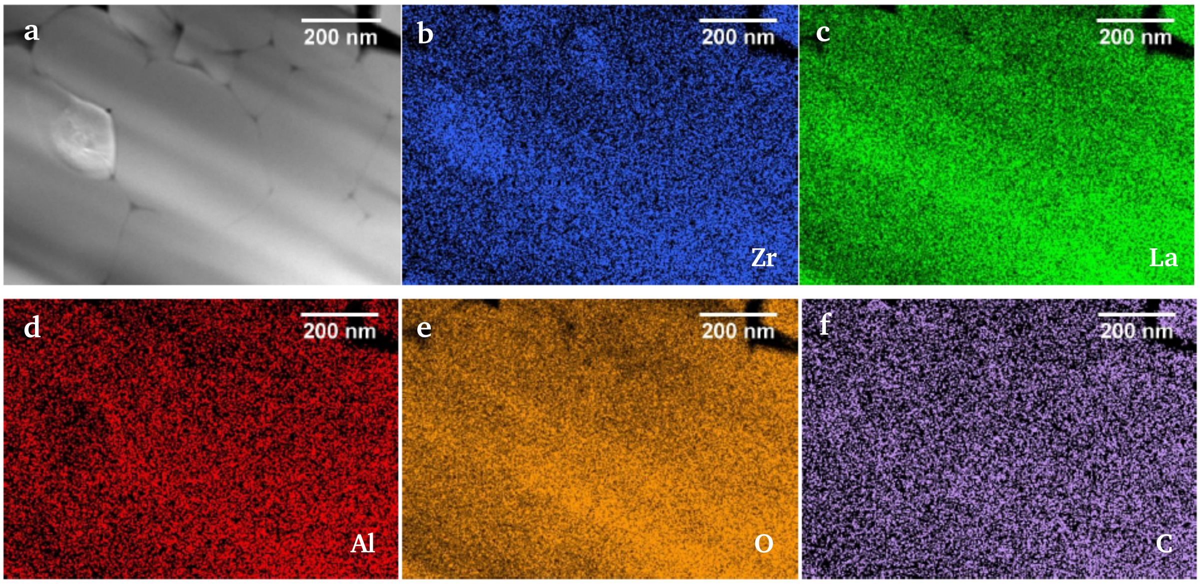

Figure 7-11: HAADF STEM image (a) and corresponding elemental distribution of Zr (b), La(c), Al (d), O (e) and C (f) of sintered $Li_{7-3x}La_3Zr_2Al_xO_{12}$ small grained ceramic ($x = 0.22$).

To confirm the obtained results a second region of the sample is characterized. The HAADF STEM image and corresponding EDXS elemental maps are shown in Figure 7-12. The EDXS elemental map of Al distribution within the sample clearly shows that no segregation of Al at the grain boundaries takes place and that Al is uniformly distributed over the $Li_{7-3x}La_3Zr_2Al_xO_{12}$ grains. The exception is again the grain with a brighter contrast on the HAADF STEM image, which has a smaller Al, but higher La and Zr content compared to the other grains. This is also confirmed by EDXS elemental maps of Al, Zr and La distributions. The quantification of the EDXS data is carried out in two regions depicted in Figure 7-13b for a grain with higher and lower contrast from the HAADF STEM micrograph and the results are presented in Table 7-5. The bright grain results in a composition, which corresponds very well to the $La_2Zr_2O_7$ phase with a larger La content (20 at.% compared to 18 at.%), Zr (19 at.% compared to 12 at.%) compared to the dark grain and almost no Al. The dark grain shows a chemical composition in very good agreement with the composition $Li_{6.1}La_3Zr_2Al_{0.3}O_{12}$.

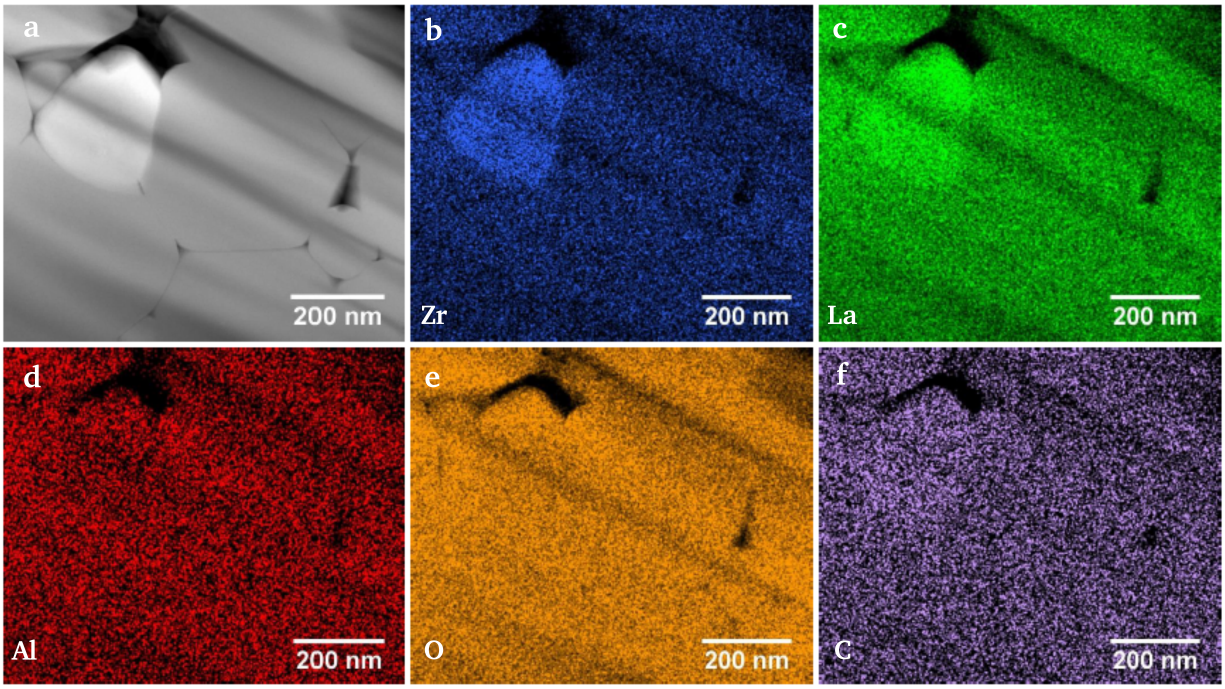

Figure 7-12: HAADF STEM image (a) and corresponding elemental distribution of Zr (b), La(c), Al (d), O (e) and C (f) of sintered $Li_{7-3x}La_3Zr_2Al_xO_{12}$ small grained ceramic ($x = 0.22$).

It is evident for the small grained ceramics that no circular pores are formed during sintering, which is due to the fine microstructure of the ball milled powder not showing any sintering necks between the particles compared to the calcined powder. This confirms that the circular, intragranular pores of the large grained ceramics, in fact, form during sintering and not during the FIB processing.

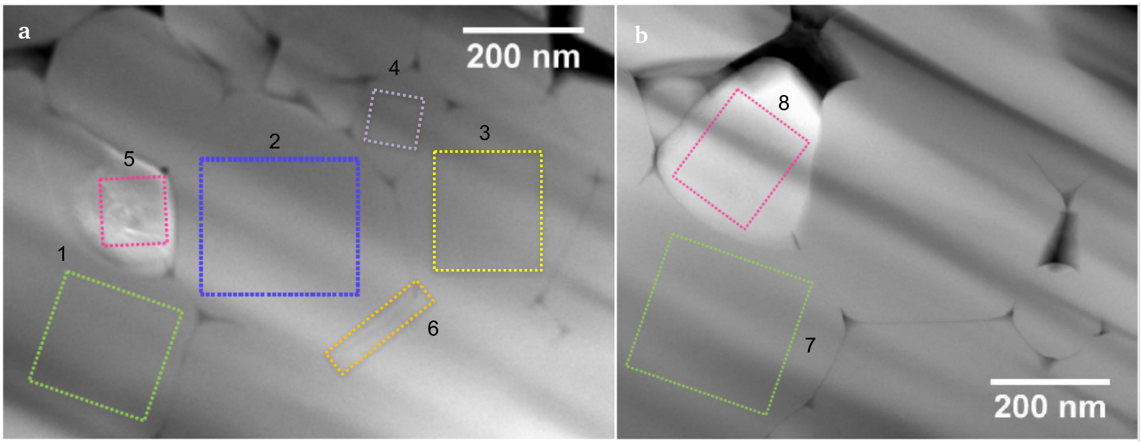

Figure 7-13: HAADF STEM images of the regions quantified by EDXS for small grained $Li_{7-3x}La_3Zr_2Al_xO_{12}$ ceramics ($x = 0.22$).

Table 7-5: EDXS quantitative results for the selected regions of the small grained ceramic.

Region	La [mol]	Zr [mol]	Al [mol]	O [mol]
1	3.20(30)	2.00(20)	0.34(04)	12.3(8)
2	3.20(30)	2.00(20)	0.32(04)	12.4(6)
3	3.20(30)	2.00(20)	0.34(04)	11.6(6)
4	3.10(30)	2.00(20)	0.28(04)	12.3(9)
5	1.97(28)	2.00(22)	0.03(2)	6.7(2)
6	3.10(32)	2.00(20)	0.28(04)	12.5(8)
7	3.00(26)	2.00(20)	0.26(03)	11.3(9)
8	2.06(27)	2.00(22)	0.06(2)	6.1(3)

Additionally, no Li_2CO_3 grain inclusions are detected, which can also be explained by the microstructure of the starting material. Li_2CO_3 grain inclusions are most probably formed due to the CO_2 adsorbed on the surface of the particles before sintering. This is supported by the sub-stoichiometric oxygen content of the grains showing Li_2CO_3 inclusions, while pure LLZO grains in the large and small grained ceramics show a stoichiometric oxygen content. Therefore, it is assumed that during the field assisted sintering process highly mobile Li reacts with the adsorbed CO_2 extracting oxygen from the garnet structure. The particle surfaces, where this reaction takes place are both intra- and intergranular in the case of the large grained ceramic. On the other hand, in the case of the small grained ceramic the particle surfaces of the ball milled powder, which are expected to exhibit a higher reactivity due to ball milling form the grain boundaries of the sintered ceramic, and thereby are only intergranular. For both ceramics no intergranular Li_2CO_3 phase is detected, which might indicate its decomposition during the sintering process at 950 °C forming gaseous CO_2.

7.2.1.3 Li-ion conductivity

To determine the influence of the grain size on the ionic conductivity AC-impedance spectroscopy is carried out with blocking Au-electrodes. The advantage of measuring at low temperatures, as low as 220 K, is the possibility to separate the bulk and the grain boundary contributions to the spectrum. This is successfully achieved for both samples with different grain sizes. The Nyquist plots are shown in Figure 7-14 with arrows indicating the frequencies at the maximum point of each semi-circle at the lowest temperature. Equivalent circuits are chosen to fit the detected semi-circles at each temperature. At low temperatures R(R CPE)(R CPE)CPE is employed since the surface layer contribution expected at low frequencies is not detected. Starting 240 K the equivalent circuit R(R CPE)(R CPE)(R CPE)CPE is used to fit the spectra. The normalized resistance values show an increase in both bulk and grain boundary contributions to the spectrum for the ceramic with smaller grain size. The increase in bulk resistance is not expected to be affected by the grain size. This increase of approximately 23% could, therefore, result from the increased Li loss from the garnet structure due to the smaller grain size and the formation of $La_2Zr_2O_7$ grains, as observed from HAADF STEM. Since the Li loss mechanism is governed by the presence of moisture and CO_2 a finer grain size and thus a larger surface area of the particles allows for the adsorption of a larger amount of these species leading to a higher reactivity with Li during the sintering process. The increase of normalized resistance is approximately 67% higher for the ceramic with a smaller grain size compared to the large grained ceramic. This much larger increase in grain boundary resistance compared to the bulk resistance increase indicates that an additional more significant phenomenon is taking place, which is the increased number of grain boundaries due to the smaller grain size, leading to a lower grain boundary conductivity. The room temperature total conductivities for large grained and small grained ceramics are 0.43 mS cm^{-1} and 0.23 mS cm^{-1}, respectively.

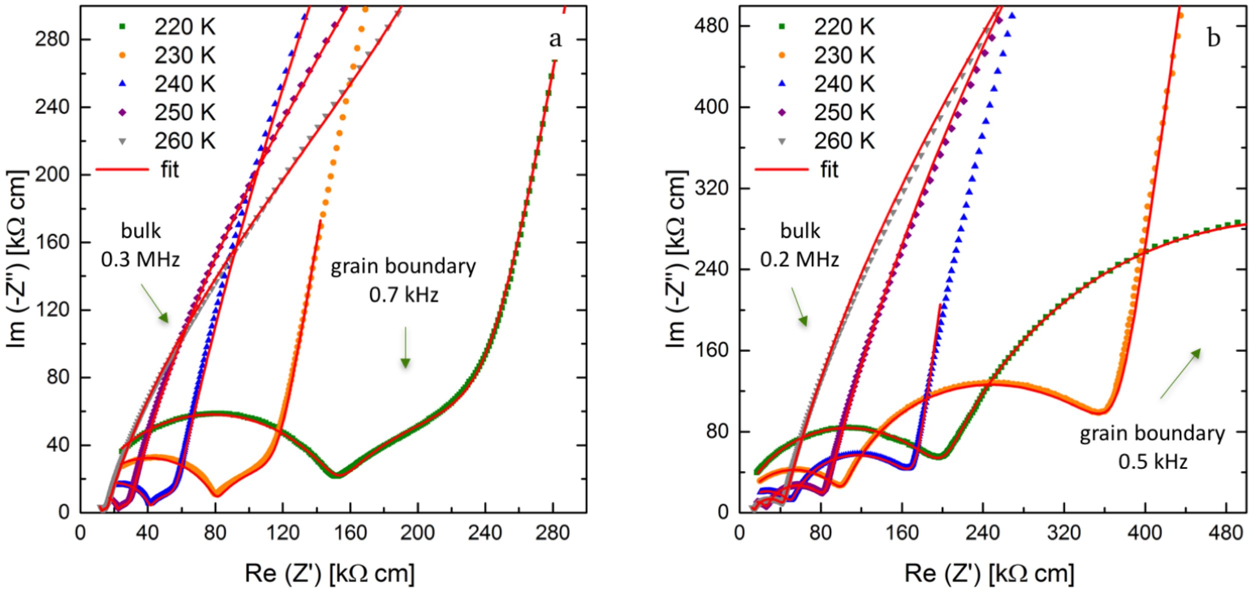

Figure 7-14: Nyquist plots and corresponding fits for sintered ceramics (x = 0.22) with blocking Au-electrodes at 220 K up to 260 K with calcined (a) and calcined then ball milled starting powder (b).

The Arrhenius plot showing the temperature dependence of the total conductivity for both samples is shown in Figure 7-15. The ceramic prepared from calcined powder shows higher conductivities throughout the whole temperature range and an activation energy of 0.36 eV. On the other hand, the ceramic with a smaller grain size due to the additional ball milling step of the starting material shows an activation energy of 0.40 eV. In addition to the decrease of the bulk and grain boundary conductivities the activation energy is significantly increased for the ceramic with a smaller grain size. This indicates that an increase in the amount of grain boundaries decreases the Li-ion mobility, which is the determining factor for the electrochemical performance [93].

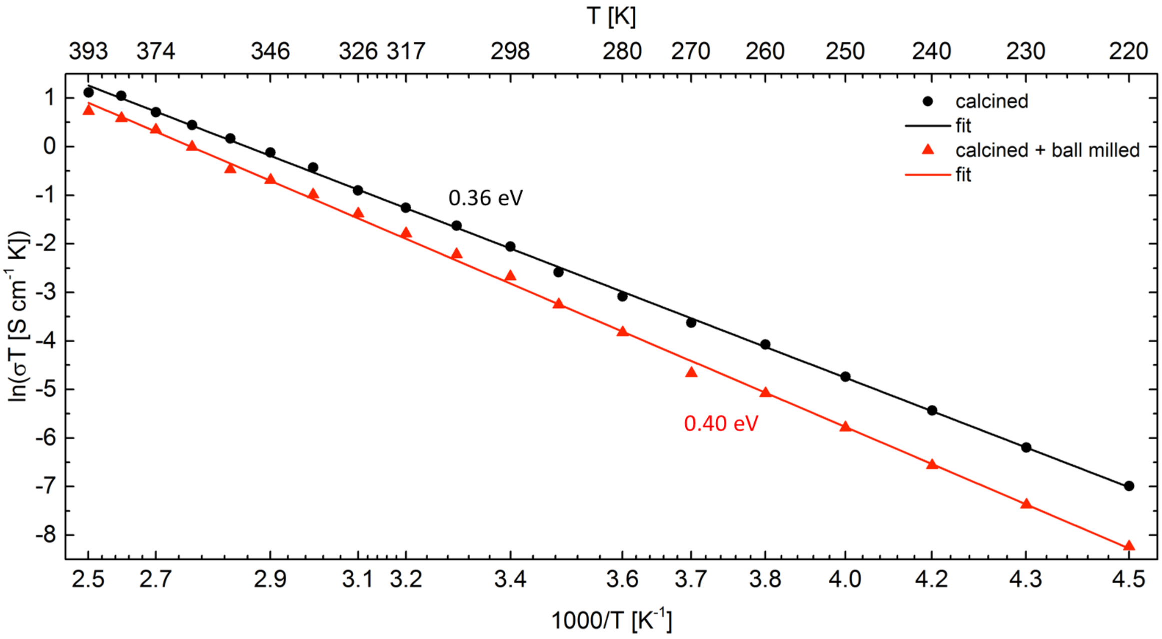

Figure 7-15: Arrhenius plot presenting the temperature dependence of the total Li-ion conductivity between 220 K and 393 K for two different grain sizes achieved by ball milling of the starting powder.

For further evaluation of both effects occurring as a result of the decreased grain size the bulk and grain boundary conductivities are calculated using the dimensions of the pellet for both values. This is only an approximation, since the real thickness to surface ratio is expected to be larger for the grain boundary conductivity than for the bulk conductivity leading to higher values for the grain boundary conductivity than reported here. A direct comparison of the temperature dependence of the bulk and grain boundary conductivities is given in Figure 7-16. The sample with a large grain size shows higher grain boundary conductivities than the bulk conductivities throughout the whole temperature range, while the bulk and grain boundary activation energies are calculated to 0.34 eV and 0.40 eV, respectively. The ceramic with a smaller grain size not only shows a decrease in grain boundary conductivity but also an increase in the grain boundary activation energy up to 0.43 eV, while the bulk activation energy only increased to 0.35 eV. This again proves that Li loss during sintering and the increased formation of the $La_2Zr_2O_7$ impurity phase has a much lower impact on the activation energy, which is observed for the bulk, while the impact of the larger amount of grain boundaries is more significant for the grain boundary conductivity as well as the activation energy, which leads to the conclusion that the ionic mobility is reduced in the ceramic with a smaller grain size (0.7 μm) compared to the large grained ceramic (2.2 μm).

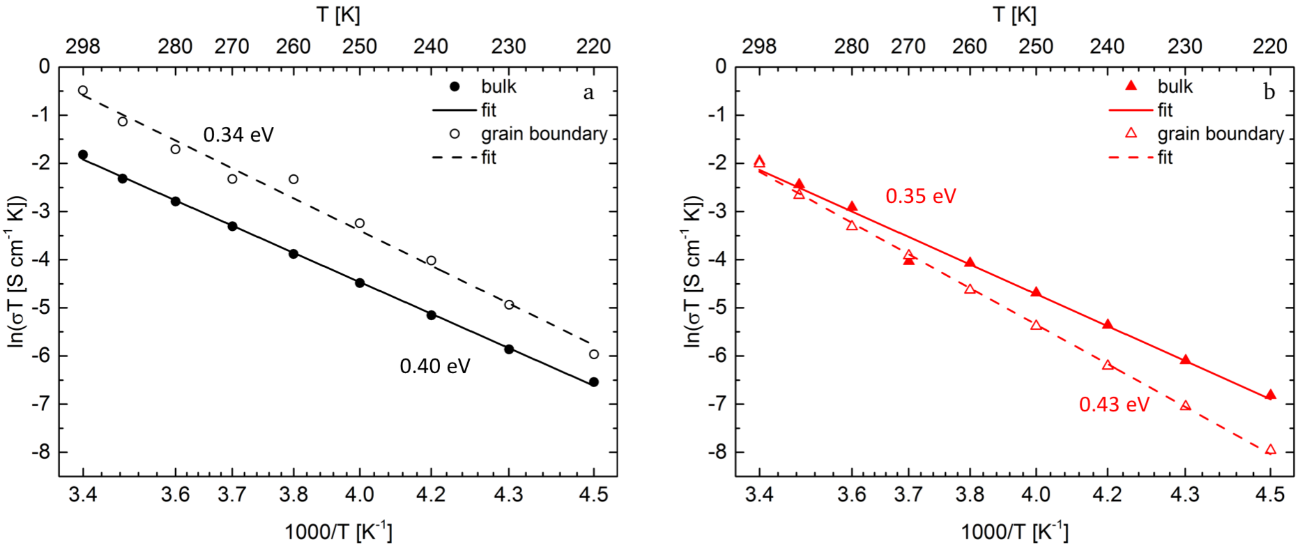

Figure 7-16: Arrhenius plots presenting the temperature dependence of the bulk and grain boundary Li-ion conductivities between 220 K and 298 K for two different grain sizes achieved by ball milling of the starting powder: large grained (a) and small grained ceramic (b).

7.2.1.4 Cycling behavior

According to the literature a decrease of the grain size from a few hundred microns to 40 μm leads to an enhancement of the cycling stability against Li metal [70]. In this study the grain size is reduced from 2.2 μm to 0.7 μm, which covers a different range than reported. For the characterization of the electrochemical stability against Li metal the large and small grained ceramics are contacted on both sides with Li metal electrodes as described in section 6.2.2. Two different current densities are used, 50 μA cm^{-2} and 75 μA cm^{-2}. Since stability has already been demonstrated in previous experiments up to 50 μA cm^{-2} the influence of higher current densities is studied. Galvanostatic cycling results are depicted in Figure 7-17. The large grained ceramic shows a very good electrochemical stability at the initial current density (50 μA cm^{-2}) for 10 cycles, while the cell potential shows a slight increase of approximately 1 mV during each cycling step upon cycling at the higher current density for 5 cycles. The following 10 cycles at the initial current density show stable cycling with no significant change compared to the first 10 cycles. On the other hand, the small grained ceramic shows great instability in the first 5 cycles at 50 μA cm^{-2}, which stabilizes starting with the sixth cycle but showing an increase in cell potential in each step of 7 mV. Increasing the current density leads to the expected increase in cell potential and an additional increase during each step of 8 mV. The subsequent cycles at the initial current density show symmetrical cell potential during charge and discharge with an increase of 7 mV during each cycling step. It is evident that the sample with larger grain size shows the better electrochemical stability against Li metal and that increasing the current density above 50 μA cm^{-2} leads to a slight degradation of the cell.

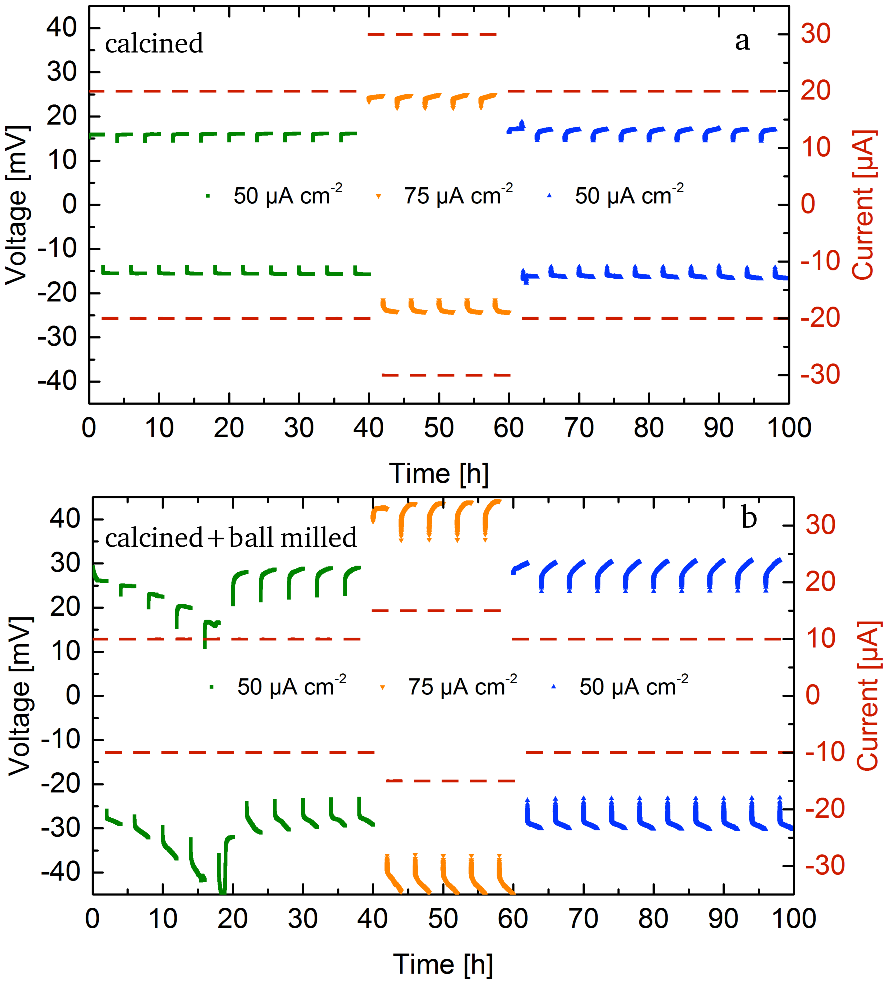

Figure 7-17: Galvanostatic cycling of symmetrical cells Li|LLZO|Li at different current densities for ceramics with $x = 0.22$ prepared from two different starting powders: calcined (a) and calcined then ball milled (b).

According to literature [70] a more stable cycling performance of the small grained ceramics is expected due to the larger number of grain boundaries with higher conductivity than the bulk. For a large grained ceramic (100-200 μm), the current pathways are limited since the current accumulates in the regions with highest conductivity creating current spikes and accelerates dendrite formation. On the other hand, when there is a larger number of high conductivity regions (grain boundaries) the current distribution is more homogeneous throughout the interface between Li and the solid electrolyte with a smaller grain size (40 μm) [70]. In the present study this argument holds true for grain sizes down to 2.2 μm, where the current is homogeneously distributed and the cell is stable during cycling for 100 hours. Whereas, reducing the grain size further to 0.7 μm the grain boundary conductivity evidently decreases and is comparable to the bulk conductivity at room temperature. This might explain the great instability of the interface during cycling in the first 5 cycles, where the current pathways are formed throughout the interface. There is no clear pathway with a higher conductivity, therefore, the current flow needs more time to stabilize and the cell exhibits higher cell potentials due to the higher resistances compared to the large grained ceramic (2.2 μm).

7.2.1.5 Interfacial resistance

AC-impedance spectroscopy is carried out to obtain a deeper understanding of the findings of the galvanostatic cycling and to determine the ASR at the interface between LLZO and Li. The Nyquist plots for measurements with blocking Au-electrodes as well as non-blocking Li-electrodes at room temperature are shown in Figure 7-18. The measurements with non-blocking Li-electrodes are conducted before cycling, after 10 cycles at 50 μA cm^{-2}, after further 5 cycles at 75 μA cm^{-2} and after 10 additional cycles at the initial current density. The total resistance of the symmetrical cell before cycling is 0.786 kΩ for the ceramic with a larger grain size, while it is 2.730 kΩ for the small grained ceramic. These values are in good agreement with the total cell resistance calculated from galvanostatic cycling. The fits of the spectra are carried out using R(R CPE)(R CPE) equivalent circuit, where the first (R CPE) element corresponds to the grain boundary contribution to the spectrum with a capacitance value in the order of 10^{-9} F for both samples, while the second (R CPE) element corresponds to the charge transfer for both electrodes and its capacitance calculates to 10^{-8} F for the large grained ceramic and 10^{-9} F for the small grained ceramic. The grain boundary resistance is fixed for all the fits to the value measured with blocking Au-electrodes.

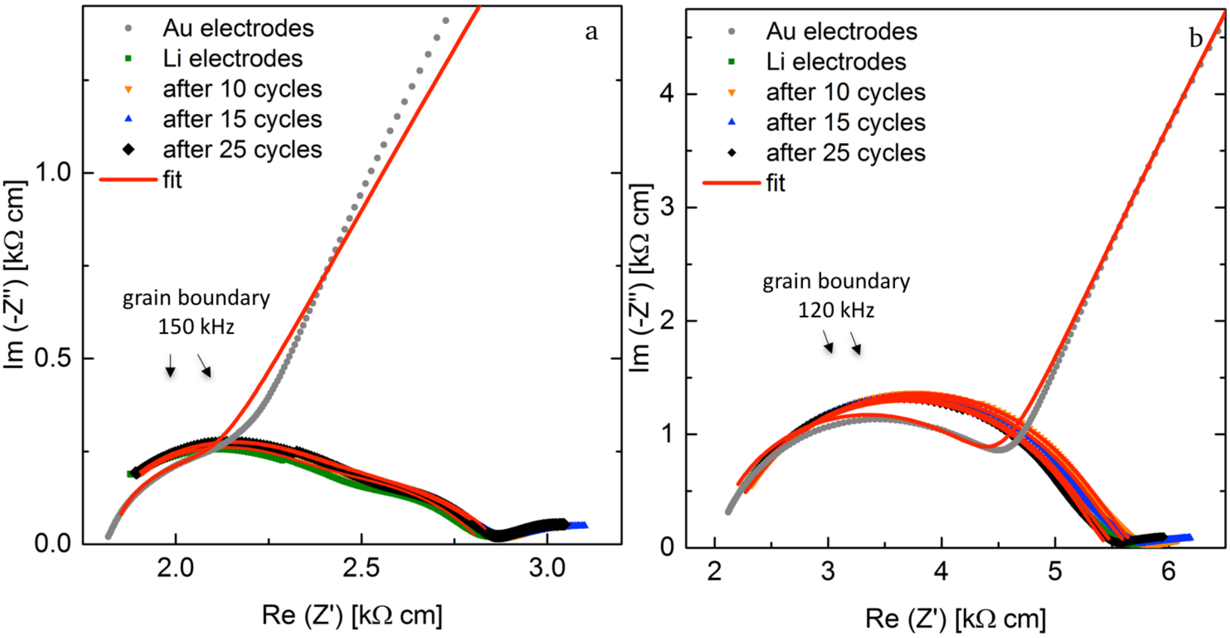

Figure 7-18: AC-impedance spectra at 298 K with blocking Au-electrodes and non-blocking Li-electrodes as-prepared and after cycling for ceramics with $x = 0.22$ with calcined (a) and calcined then ball milled starting powder (b).

The ASR values and their evolution after cycling are presented in Figure 7-19. The large grained ceramic has an ASR of 30.7 Ω cm^2 against Li metal, which is the best value reported to date. The ASR value increases after cycling at 75 μA cm^{-2} reaching 34.4 Ω cm^2 and remains stable at 34.3 Ω cm^2 after additional cycling at 50 μA cm^{-2}. The ASR values for the small grained ceramic are almost double the values measured for the ceramic with a larger grain size. Before cycling the ASR is determined to 60.9 Ω cm^2, then it increases to 67 Ω cm^2 and remains stable even at the higher current density. After additional 10 cycles at the initial current density the ASR decreases to 59.5 Ω cm^2. This decrease is significant and leads to the assumption that a fine grained ceramic might have a good long term stability of the interface towards Li metal, but it definitely results in a higher ASR.

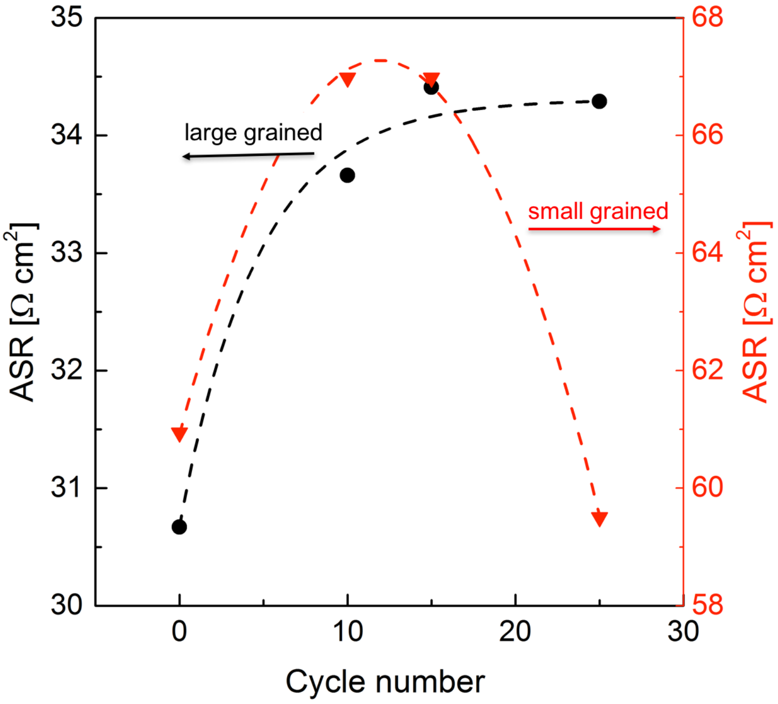

Figure 7-19: ASR values for large (2.2 µm) and small grained (0.7 µm) ceramics measured before and after cycling at different current densities (dashed lines act as visual aid only).

To determine the influence of the grain size on the electrochemical performance of $Li_{7-3x}La_3Zr_2Al_xO_{12}$ the compositional and structural differences of the grain boundaries need to be eliminated. Therefore, employing a single synthesis route for the large and small grained ceramics is a great advantage, that helps minimize such differences. In this study, it is observed that a smaller grain size of 0.7 μm leads to significantly lower conductivities across the whole measured temperature range, than for ceramics with a grain size of 2.2 μm. Additionally, the activation energy is increased. Separating the bulk and grain boundary contributions confirms that the main influence observed is due to the increased number of grain boundaries and not only due to the increased Li loss expected for ceramics with a finer starting powder. The increase in activation energy is also observed in the literature for a similar grain size region for samples produced using two different synthesis methods. It has been reported that the ceramic with a smaller grain size shows a similar room temperature conductivity and higher conductivities for temperatures above 312 K [71]. The activation energies for small and large grained ceramics are different, therefore, which ceramic shows superior Li-ion conductivity is dependent on the operating temperature of the cell assuming structural and compositional stability. Since the solid electrolyte is meant to be used mainly at room temperature, samples synthesized using the combination of NSP and FAST would have an optimal grain size of 2-3 μm, where the conductivity is double of that of the counterpart with a grain size of 0.7 μm.

7.2.2 Influence of the pressure during sintering

To achieve different microstructures with conventional sintering an increase of sintering temperature results most often in an increase of the density. However, the kinetics of FAST are more complicated, which leads to the formation of additional impurity phases due to the temperature difference and consequently the electrochemical characteristics are affected. Therefore, the sintering temperature is kept constant at 950 °C for all samples with a dwell time of 3 min, ensuring that the influence of the electric field is comparable and maintaining a comparable grain size, while the pressure is set to 20 MPa, 30 MPa and 50 MPa to achieve different microstructures. The specimens are sintered under Ar atmosphere to presumably minimize the formation and decomposition of a liquid phase during sintering (see section 7.3). This study is designed to determine the influence of the pressure variation during field assisted sintering on the ionic conductivity of $Li_{7-3x}La_3Zr_2Al_xO_{12}$ with $x = 0.22$ and 30 wt.% Li-excess during synthesis. The as-synthesized powder is calcined under an Ar atmosphere at 900 °C for 1 hour, see section 5.2 for further details about the optimization of the calcination process.

7.2.2.1 Phase composition

The diffraction patterns of the sintered ceramics, measured on both sides of the pellet, are shown in Figure 7-20. After field assisted sintering at different pressures the impurity phase $La_2Zr_2O_7$ is present for the ceramics sintered at higher pressures, while it disappears for the lowest pressure. At the higher pressures, 50 MPa and 30 MPa, the distorted tetragonal phase is formed, while at a lower pressure of 20 MPa this distortion is clearly reduced.

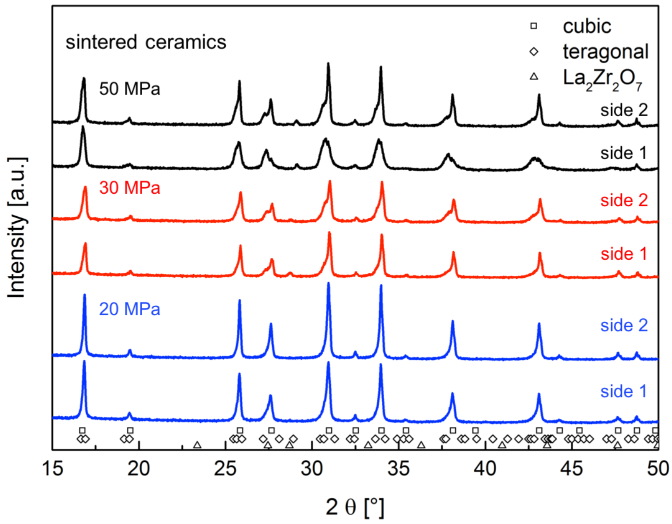

Figure 7-20: X-ray diffraction pattern of the $Li_{7-3x}La_3Zr_2Al_xO_{12}$ with $x = 0.22$ at 900 °C for sintered ceramics measured on both sides of the pellets (side 1 and side 2).

The results of the Rietveld refinement for the sintered ceramics with different densities measured on both sides of the pellet are listed in Table 7-6. After sintering the Li_2ZrO_3 impurity phase present in the calcined powder is no longer detected, while $La_2Zr_2O_7$ is still present in the ceramic sintered under

50 MPa and 30 MPa with a phase fraction calculated to 2.1 wt.% and 1.4 wt.% respectively. For the ceramic sintered under 20 MPa there is no impurity phase detected. Adding this observation to the fact that the $La_2Zr_2O_7$ impurity phase exhibits different values on each side of the ceramic specimen, leads to the assumption that the formation of the $La_2Zr_2O_7$ phase is a result of electromigration of Li-ions due to the direct current electric field applied during sintering. This effect is reduced with decreasing pressure, since there are less Li-ion pathways allowing the electromigration in addition to the reduced local electric field at grain interconnections as a result of the larger grain boundary region expected at a low pressure. In general, the amount of the impurity phase $La_2Zr_2O_7$ can be neglected for further electrochemical investigations, since the microstructure is expected to have a more significant influence. The pressure during field assisted sintering influences the microstrain, which is more pronounced in the distorted tetragonal phase with a large unit cell volume. With decreasing pressure, the microstrain decreases from 0.330, through 0.313 down to 0.204, while the c/a ratio increases approaching unity. This observation clearly links the observed microstrain to the applied pressure, that causes a structural change in the unit cell during field assisted sintering.

Table 7-6: Rietveld refinement data for $Li_{7-3x}La_3Zr_2Al_xO_{12}$ sintered pellets with $x = 0.22$. Results are mean values obtained from both sides of the pellets.

Sample	Phase	Phase fraction [wt.%]	Unit cell volume [Å^3]	Microstrain	c/a
Sintered	cubic garnet	40.6(1)	2176.92(48)	0.124(2)	1
50 MPa	tetragonal g.	57.3(1)	2200.3(6)	0.330(2)	0.983
	$La_2Zr_2O_7$	2.11(1)	1205.72(77)	-	1
30 MPa	cubic garnet	58.2(1)	2177.71(15)	0.045(1)	1
	tetragonal g.	40.5(1)	2214.3(17)	0.313(1)	0.989
	$La_2Zr_2O_7$	1.35(1)	1261.82(37)	-	1
20 MPa	cubic garnet	45.5(1)	2177.14(1)	0.043(2)	1
	tetragonal g.	54.5(1)	2191.70(99)	0.204(9)	0.994

For this study a simple microstrain model could not be fitted to the diffraction data with high accuracy especially for the ceramic sintered at 50 MPa. A preferred orientation model according to March-Dollase is applied for the distorted tetragonal phase [94]. Different choices of lattice planes, with respect to the degree of texturing, are tested. Among them a (0 0 1) lattice plane is identified and results in a significant improvement in the fit (R_{wp} value of 9.7% in contrast to an R_{wp} value of 11.2% without the preferred orientation model). The March-Dollase model refines only one preferred orientation parameter, G. This parameter is then used for the calculation of the preferred orientation function P_k, which, is a factor for the correction of the intensity calculated of each reflection k. The dependence is as follows, with α being the angle of intersection between the lattice plane of reflection k and the predefined texturing lattice plane, (0 0 1).

$$P_k = (G^2 \cdot cos^2 \alpha + (1/G \cdot sin^2 \alpha))^{-3/2} \qquad [\ 7\text{-}1\ ]$$

In the present case this means that for the intensity correction of the (0 0 1) reflection the sine squared term is zero, since α is zero and the intensity correction for the corresponding reflection becomes $1/G^3$, while for the (0 1 0) reflection the angle is π/2 resulting in an intensity correction of $G^{3/2}$. The G values for the distorted tetragonal phase with a preferred orientation are calculated to 1.35, 1.45 and 1.39 for the samples sintered at 50 MPa, 30 MPa and 20 MPa, respectively. These mean values of the G parameter are determined for both sides of the pellet. The discrepancy between the G value on both sides is 0.09, 0.05 and 0.01 for all three pellets, which decreases with decreasing pressure during sintering. This phenomenon can be explained through the experimental setup during field assisted sintering, where the upper piston is moved uniaxially compressing the specimen, while the lower piston is fixed. This leads to different stress fields on the opposite sides of the pellet leading to different G parameters as well as microstrain. The difference in microstrain between both sides of the pellet is higher for the sample sintered at 50 MPa with a value of $\Delta\varepsilon = 0.1$, than for the samples sintered at lower pressures with a difference of microstrain of 0.03. The G values calculated for the preferred orientation model for the (0 0 1) lattice plane leads to an intensity correction of 0.36 for the (0 0 4)-refection (decrease in intensity) and 1.66 for the (0 4 0)-refection (increase in intensity) of the tetragonal garnet structure. The X-ray diffraction data and the Rietveld refinement with and without the preferred orientation model are shown in Figure 7-21 for both sides of the ceramic sintered under 50 MPa. The intensity correction shows that less crystallites with parallel orientation of the (0 0 1) lattice planes in relation to the pellet surface and more crystallites with perpendicular (1 0 0) and (0 1 0) lattice planes to the pellet surface are found than to be expected for a statistical distribution of crystal orientations. Therefore, the larger lattice parameters a and b are oriented perpendicular to the surface of the pellet, i.e., parallel to the applied force during field assisted sintering.

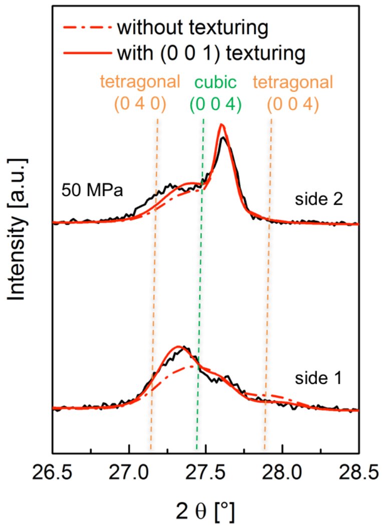

Figure 7-21: Rietveld refinement fits with (solid line) and without (dashed line) the application of the March-Dollase preferred orientation model for the (0 0 1) lattice plane. The solid line shows a better representation of the collected data. R_{wp} value decreases to 9.7% in contrast to an R_{wp} value of 11.2% without the preferred orientation model.

7.2.2.2 Microstructure

To achieve a higher accuracy for the density measurements than the geometrical density measurement, where the open porosity and surface roughness are neglected, a novel method is applied using laser confocal microscopy. A detailed description of the method is reported elsewhere [92]. For the samples sintered at 50 MPa, 30 MPa and 20 MPa the densities are calculated to 5.35(5) g cm^{-3}, 5.07(5) g cm^{-3} and 5.11(5) g cm^{-3}, respectively. These values lie within the range of 95% TD to 100% TD. Scanning electron microscopy is carried out on cross sections of all three pellets sintered at different pressures. The corresponding micrographs are presented in Figure 7-22. The grain sizes of the ceramics are mean values after measuring 100 grains. The mean values for the ceramics are 2.2 μm (min. 0.7 μm and max. 4.7 μm) for the ceramic pressed at the highest pressure, increases slightly to 2.4 μm (min. 0.6 μm and max. 5.4 μm) when reducing the pressure and calculated to 2.3 μm (min. 0.4 μm and max. 5.5 μm) when decreasing the pressure further to 20 MPa. The ceramics sintered under different pressures do not show differences in the mean value of the grain size. Additionally, all samples exhibit two different phases one which presents the smooth grains of the material and another phase consisting of much smaller particles at the grain boundaries, i.e., on the surface of the grains in cross sectional SEM images. The second is most probably a result of a liquid phase formed during sintering at 950 °C.

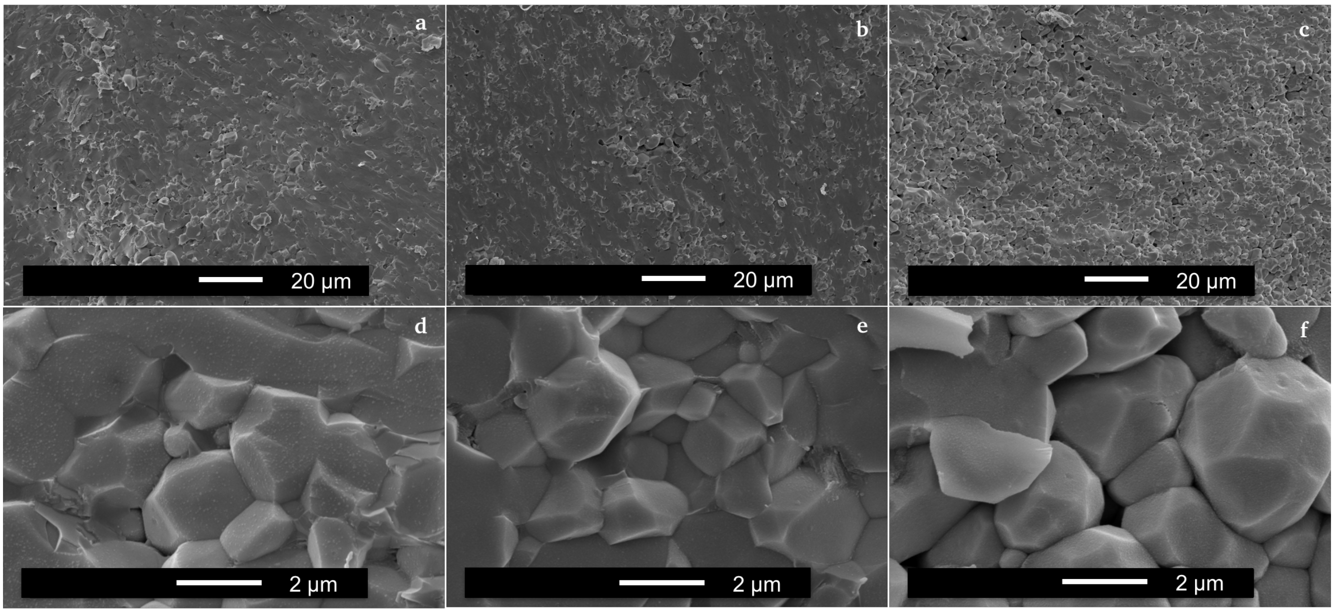

Figure 7-22: SEM images of the $Li_{7-3x}La_3Zr_2Al_xO_{12}$ sintered ceramic at 50 MPa (a,d), 30 MPa (b,e) and 20 MPa (c,f) with two different magnifications.

7.2.2.3 Li-ion conductivity

AC-impedance spectroscopy is carried out between 220 K and 298 K. Figure 7-23 shows the Nyquist plots for the low temperature measurements with arrows indicating the frequencies at the maximum of the semi-circles at 220 K. Utilizing low temperatures allows for the detection of the bulk and grain boundary contribution to the spectrum. The decreased microstrain due to the application of different pressures during sintering is correlated with an increase in both bulk and grain boundary resistances. The increase in grain boundary resistance is plausible since at lower pressures grain-grain contact surface is decreased, which might result in higher residual grain boundary porosity. The increase in bulk resistance is, however, an indication that the pressure during FAST does alter the structure of the unit cell structurally inducing a microstrain in the grain interior. This has a significant influence on the ionic conductivity. The total room temperature ionic conductivities are 0.42 mS cm^{-1} for the sample sintered under the highest pressure, decreasing the pressure it decreases to 0.36 mS cm^{-1} and a further decrease in pressure leads to a total conductivity of 0.26 mS cm^{-1}.

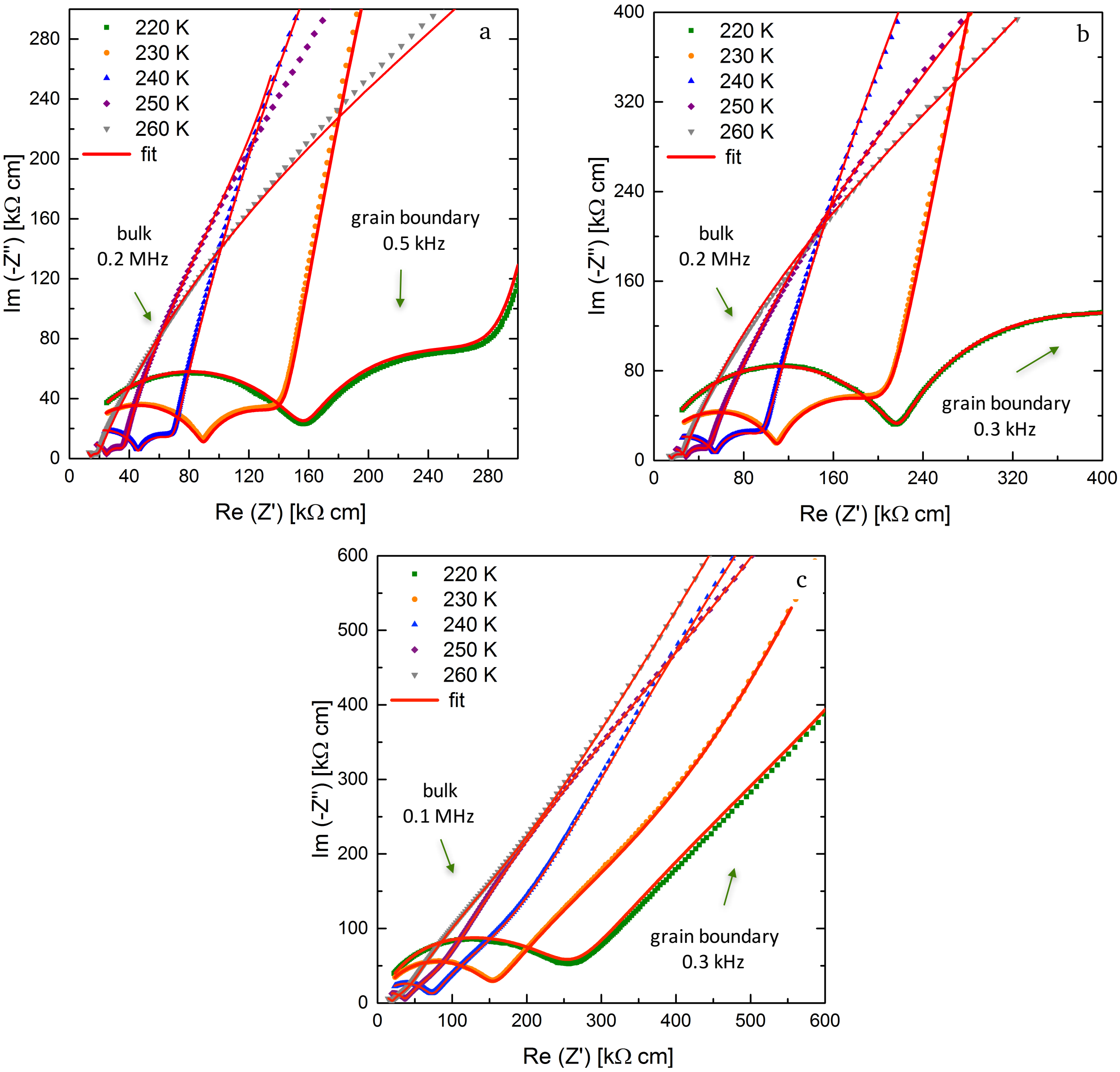

Figure 7-23: Nyquist plots and corresponding fits for $Li_{7-3x}La_3Zr_2Al_xO_{12}$ samples (x = 0.22) with blocking Au electrodes at 220 K up to 260 K sintered at a pressure of 50 MPa (a), 30 MPa (b) and 20 MPa (c).

The Arrhenius plots for all three ceramics sintered under 50 MPa, 30 MPa and 20 MPa are shown in Figure 7-24. Additionally, the bulk and grain boundary contributions to the conductivity are plotted separately. The calculation of both contributions is carried out using the pellet dimensions, which is only an approximation. The activation energies for the sample sintered under 50 MPa calculates to 0.37 eV, while it slightly increases for the sample sintered under 30 MPa to 0.38 eV. The sample exhibiting the lowest microstrain sintered at 20 MPa exhibits an activation energy of 0.41 eV. The increase in activation energy with decreasing microstrain is observed with different proportion for the bulk and grain boundary. The bulk activation energy increases from 0.35 eV through 0.36 eV to 0.37 eV for samples with decreasing microstrain. On the other hand, the grain boundary activation energy rises from 0.41 eV through 0.43 eV to 0.47 eV. A change of 5% in density could not be expected to have such drastic influence on the activation energy for Li-ion diffusion in $Li_{7-3x}La_3Zr_2Al_xO_{12}$, therefore, it is assumed that the change in bulk activation energy is attributed to the change of microstrain in correlation to the applied pressure during sintering. Furthermore, the microstrain seems to have a greater influence on the grain boundary Li-ion diffusion than it does on the bulk diffusion. With increasing microstrain, measured using X-ray diffraction, the total Li-ion conductivity increases and the activation energy decreases leading to the proposed hypothesis that an enhancement of the electrochemical performance of LLZO may be achieved by processes inducing a distortion of the cubic unit cell leading to the presence of microstrain, i.e., texture accompanied microstrain.

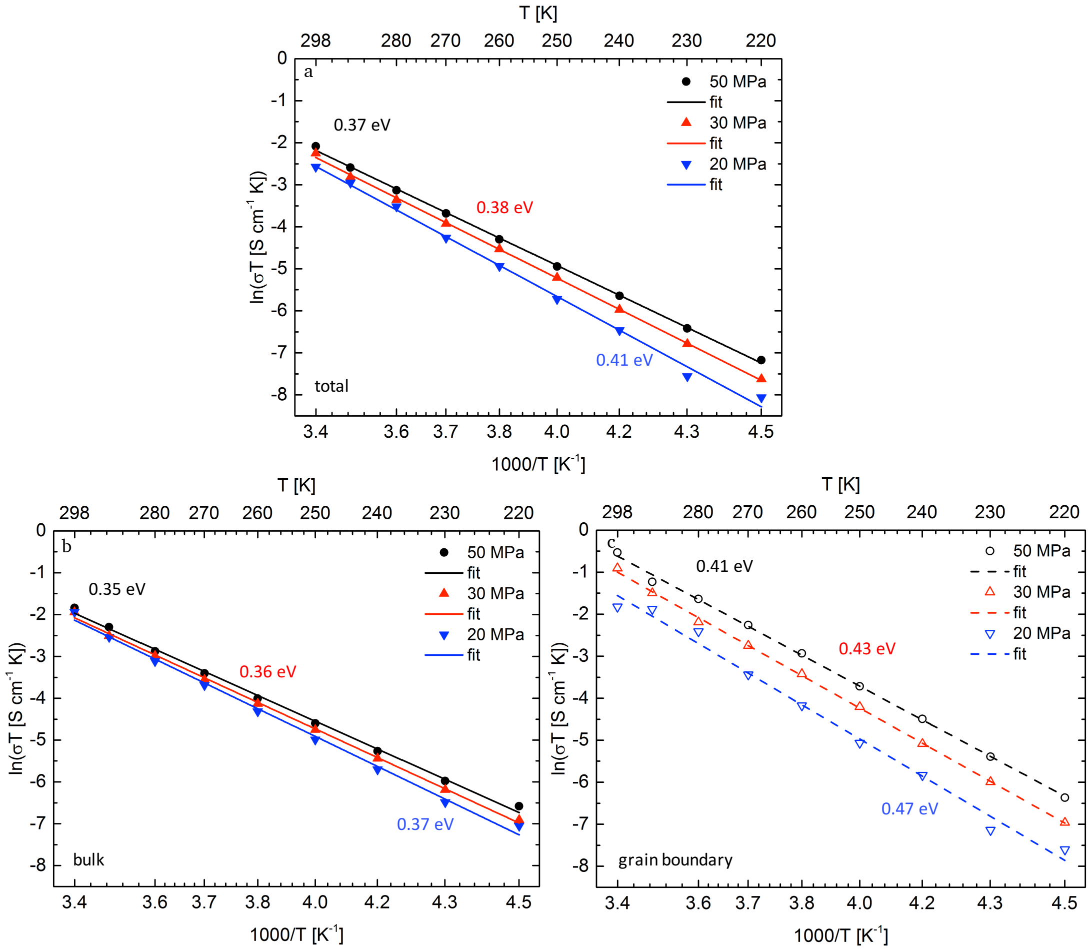

Figure 7-24: Arrhenius plots presenting the temperature dependence of the total Li-ion conductivity (a), bulk conductivity (b) and grain boundary conductivity (c) between 220 K and 298 K for three different ceramic densities achieved by different pressures.

As observed by X-ray diffraction the microstrain is directly correlated to the formation of a distorted tetragonal phase with a larger unit cell volume and a preferred orientation, i.e., texture. Since the Li-ion diffusion mechanism in the garnet structure is a vacancy hopping mechanism [95] a larger unit cell volume with a low Li occupancy, as known for the high temperature cubic LLZO structure, could be beneficial for ionic transport. This effect is observed in a larger proportion for the grain boundary than for the bulk Li-ion transport. This phenomenon can be explained by the liquid phase sintering mechanism taking place during field assisted sintering. A liquid phase, Li_2CO_3, resides at the particle interconnections during the heating segment under an initial pressure of only 15 MPa. As soon as the target temperature is reached the pressure is increased to the respective value and held during the complete dwell time (3 min). During this time the grains rearrange under the force of the uniaxial pressure and radial volume expansion takes place. After completion of the sintering process the uniaxial pressure is released before cooling of the specimen and a residual pressure between the die wall and the ceramic specimen, due to the volume expansion during sintering, leads to the compression of the lattice parameters parallel and the expansion for lattice parameters perpendicular to the pellet surface. The textured, distorted phase fraction exhibits the observed microstrain. The liquid phase residing at the grain boundaries at this point would play a significant role in accelerating this proposed process for crystallites near the grain boundaries due to enhanced diffusion processes compared to the solid bulk of the ceramic specimen. An additional indication that the distorted tetragonal phase exhibiting a higher microstrain resides near the grain boundaries is the fact that after crushing of the pellet, which usually causes intergranular separation, the distorted tetragonal phase becomes cubic and the overall microstrain strongly decreases, see section 6.1.1. The proposed mechanism for the formation of the distorted tetragonal phase during field assisted sintering is based on the findings of X-ray diffraction, see section 7.2.2.1, where the intensity corrections of the (0 4 0)-reflection and the (0 0 4)-refection indicate the presence of the larger lattice parameters perpendicular to the pellet surface. To confirm the proposed mechanism presented in Figure 7-25, additional local diffraction experiments need to be conducted at the grain boundaries and the bulk of the ceramic. This can be achieved by electron diffraction using transmission electron microscopy.

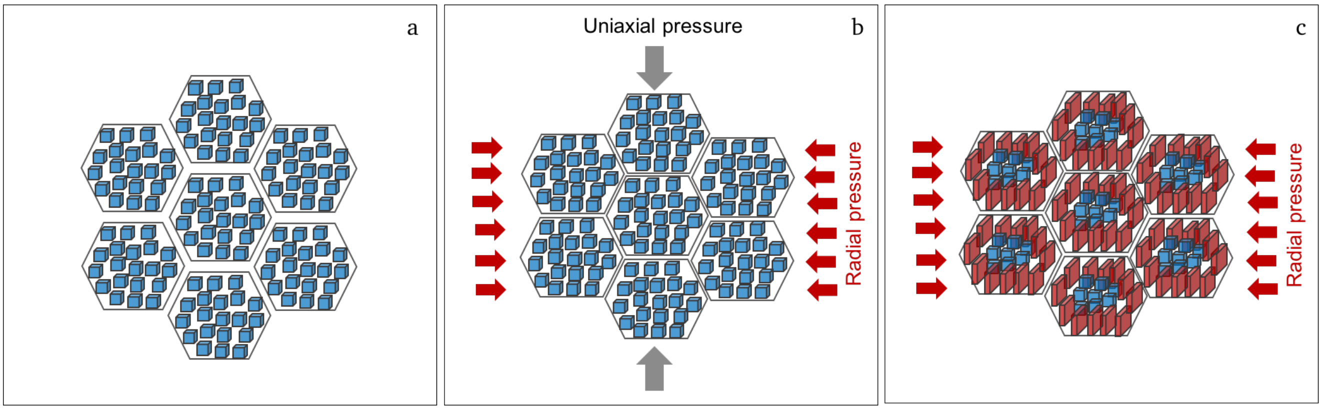

Figure 7-25: Proposed mechanism for the formation of the textured distorted tetragonal phase showing the cubic starting powder (a), the sintering process at 950 °C under uniaxial pressure, where radial volume expansion takes place (b) the formation of the textured distorted tetragonal phase near the grain boundary region (red crystallites) after release of the uniaxial pressure during cooling of the sample due to residual radial pressure (c).

7.2.2.4 Cycling behavior

The cycling behavior of two samples sintered under 50 MPa and 30 MPa is determined by attaching Li-electrodes on both sides of the pellet, as it is previously described in section 6.2.2. Two different current densities are used, 50 μA cm^{-2} and 75 μA cm^{-2}. Previous experiments show stability up to 50 μA cm^{-2}, therefore, the influence of a higher current density is studied. Galvanostatic cycling is shown in Figure 7-26 for samples exhibiting a different microstrain. The cycling is stable for both samples for 100 hours, which correspond to 25 cycles. While applied currents are identical the cell containing the ceramic with higher microstrain shows lower cell voltages, consistent with its higher ionic conductivity. Additionally, the increase in cell potential observed during each step of cycling is higher for the cell containing the sample with lower microstrain, which indicates larger losses during charge and discharge presumably at the interface between LLZO and the Li-electrodes. For the ceramic sintered under 50 MPa (highest microstrain) these potential increases are symmetrical, while they show an asymmetrical behavior starting from the 8th cycle for the cell with a ceramic exhibiting a lower microstrain. This is an indication that these losses are in fact related to the interface on each side of the solid electrolyte, showing higher losses and inhomogeneity for the solid electrolyte with a lower microstrain and therefore a lower grain boundary conductivity.

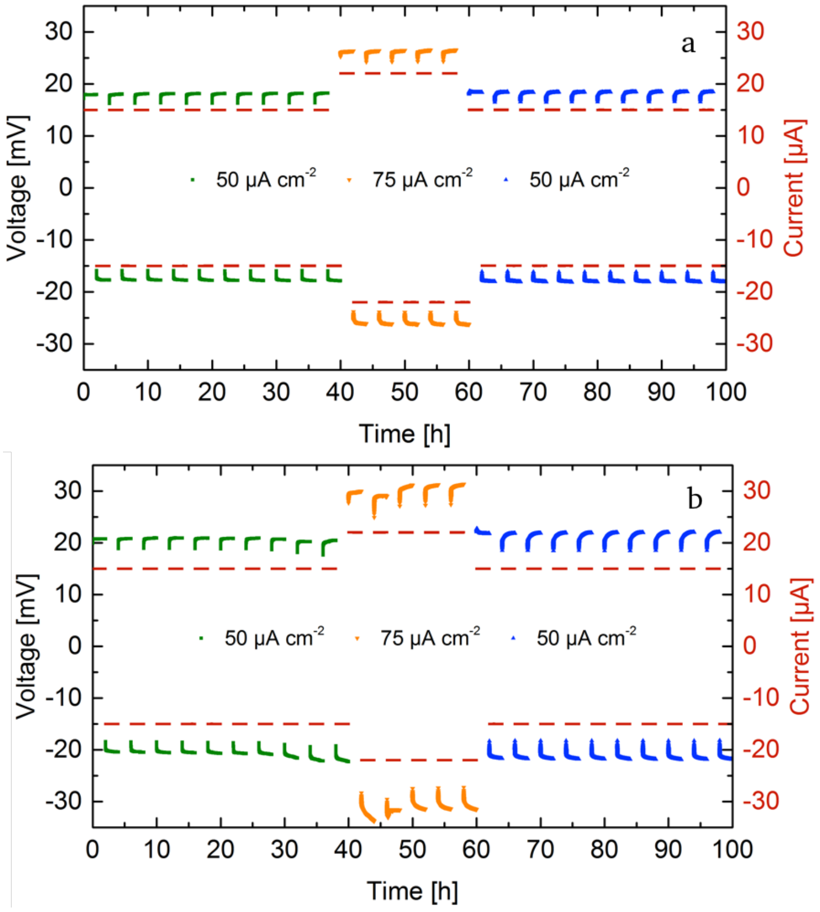

Figure 7-26: Galvanostatic cycling of symmetrical cells Li|LLZO|Li at different current densities for $Li_{7-3x}La_3Zr_2Al_xO_{12}$ (LLZO) samples with $x = 0.22$, sintered at 50 MPa (a) and 30 MPa (b).

7.2.2.5 Interfacial resistance

AC-impedance spectroscopy is conducted to determine the ASR for the samples sintered under a pressure of 50 MPa and 30 MPa. The measurements are carried out at room temperature (298 K). Figure 7-27 shows the Nyquist plots for the measurements with blocking Au-electrodes as well as non-blocking Li-electrodes before cycling and after cycling for 10 cycles at 50 μA cm^{-2}, 5 further cycles at 75 μA cm^{-2} and additional 10 cycles at the initial current density. The arrows indicate the frequency at the maximum of the grain boundary semi-circle, clearly identifiable in both spectra with blocking and non-blocking electrodes. The fit of the sample with non-blocking electrodes uses an R(R CPE)(R CPE) equivalent circuit, while the resistance of the first (R CPE) circuit is fixed to the value of the grain boundary resistance obtained with blocking electrodes. As previously reported in 6.2.2 the spectra with non-blocking electrodes are shifted to higher resistances compared to the ones with non-blocking electrodes, due to a reduced actual electrode surface area. The shift is calculated to $\Delta = 70.2\ \Omega$ for the ceramic sintered under 50 MPa and to $\Delta = 42.7\ \Omega$ for the ceramic sintered under 30 MPa. This leads to an actual surface area A_a, which is 90% and 94% of the theoretical surface area A_t for ceramics sintered under 50 MPa and 30 MPa, respectively. The corrected ASR values due to the surface area deviation are placed in parenthesis.

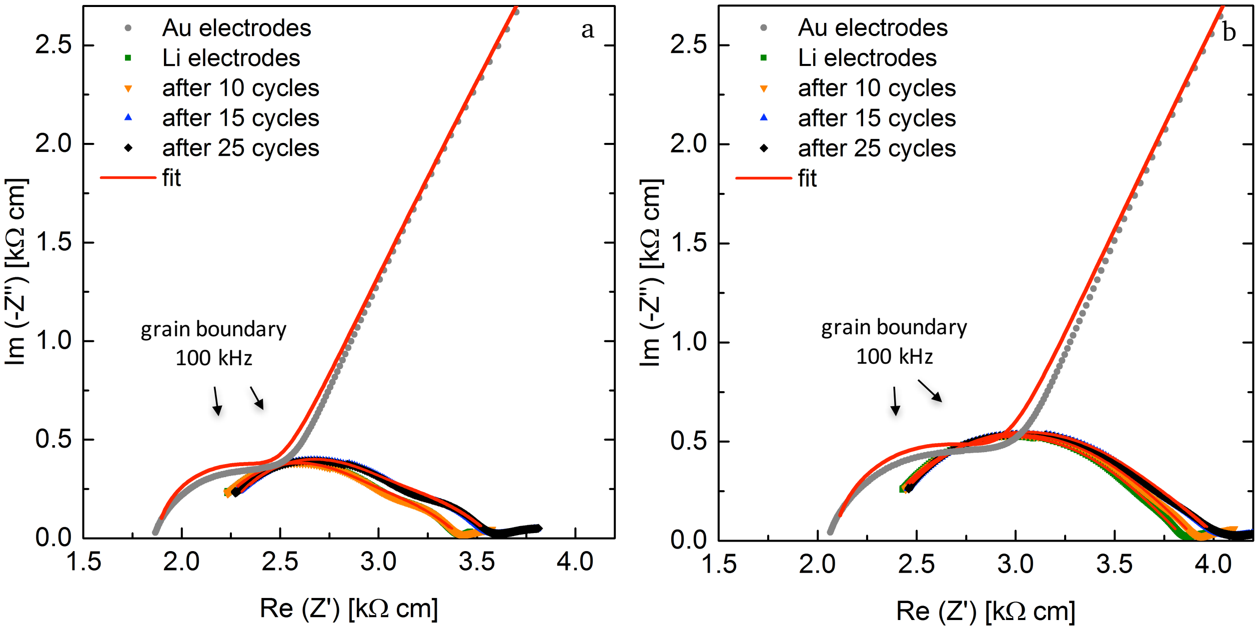

Figure 7-27: AC-impedance spectra at 298 K with blocking Au-electrodes and non-blocking Li-electrodes as-prepared and after cycling for samples with $x = 0.22$, sintered at 50 MPa (a) and 30 MPa (b).

The ASR for the sample sintered under 50 MPa is calculated to 41.2 Ω cm^2 (37.1 Ω cm^2), while the sample sintered under 30 MPa shows a slightly higher ASR of 44.3 Ω cm^2 (41.6 Ω cm^2). After cycling for the first 10 cycles the ASR of the first sample remains stable at 41.5 Ω cm^2 (37.3 Ω cm^2), while the second sample exhibits a detectable increase up to 45.8 Ω cm^2 (43.1 Ω cm^2). An increase of current density for 5 further cycles leads to a similar increase of the ASR of both symmetrical cells up to 46.3 Ω cm^2 (41.7 Ω cm^2) for the ceramic sintered under a higher pressure and 51.5 Ω cm^2 (48.4 Ω cm^2)

for the ceramic sintered under a lower pressure. Reducing the current density to the initial 50 μA cm^{-2} for 10 additional cycles does not have any impact on the ASR for both samples, showing a good stability at the lower current density. The ASR values after 25 cycles calculate to 46.5 Ω cm^2 (41.9 Ω cm^2) and 51.9 Ω cm^2 (48.8 Ω cm^2) for the sample sintered under 50 MPa and 30 MPa, respectively. These ASR values are amongst the best values reported to date for the interfacial resistance between LLZO and Li metal [70].

7.3 Influence of thermal treatment after sintering

Thermal treatment after sintering, i.e., annealing is often used to tune ceramic properties by, e.g., inducing grain growth, decomposition of residual organic components, interdiffusion between different materials and phase transformations. Furthermore, for highly strained ceramics a post annealing step might release the strain originating from intense plastic deformation [96]. The LLZO ceramic sintered using FAST exhibits a highly strained distorted tetragonal phase fraction (see section 6.1.1), which is assumed to reside near the grain boundary region. A thermal treatment might therefore reduce the fraction of the distorted phase and thereby effectively reduce the total stain in the ceramic.

In this study calcined $Li_{7-3x}La_3Zr_2Al_xO_{12}$ powder ($x = 0.22$) at 1000 °C for 1 h under flowing Ar is sintered using FAST at a temperature of 950 °C with a heating rate of 100 °C min^{-1}, a uniaxial pressure of 30 MPa and a dwell time of 3 min under vacuum. The pellet is then cut in two halves, one of which is annealed under a flowing oxygen atmosphere (5 SLM) at 500 °C for 24 h in a zirconia crucible. The electrochemical performance of the as-prepared and annealed halves of the pellet are characterized.

During the course of the study a particular cracking of the pellets is observed for ceramics sintered under the conditions mentioned above. The cracking leads to total destruction of the ceramic specimen since the cracks propagate throughout the whole pellet. Many efforts have been made to prevent the cracking but the limited knowledge about the sintering mechanism using FAST for electronically insulation materials posed a great challenge. Additionally, the garnet solid electrolyte possesses a high Li-ion mobility under the conditions used for FAST. The problem has been tackled experimentally by changing one process parameter at a time during sintering. One of the chosen parameters is the sintering atmosphere, where the vacuum (10^{-2} mbar) sintering is replaced by sintering under an Ar atmosphere, which has proven successful for obtaining more stable ceramics. The Ar atmosphere supposedly suppresses the melting as well as the decomposition of Li_2CO_3 leading to a smaller amount of liquid phase during sintering and the elimination of the CO_2 evolution during Li_2CO_3 decomposition, which presumably leads to the cracking of the ceramic specimen. The as-prepared half of the pellet, sintered under vacuum by FAST, is further characterized using DTA-TGA up to 700 °C and compared to a second ceramic sintered under an Ar atmosphere to determine the impact of the sintering atmosphere while further studying the impact of heat treatment.

7.3.1 Phase composition and microstrain

The X-ray diffraction patterns for the calcined powder, with an Al doping level of x = 0.22 and a 30 wt.% Li-excess during synthesis, and the sintered ceramic using FAST before and after annealing for the determination of the phase composition as well as the microstrain are presented in Figure 7-28.

The calcined powder is composed of mainly the cubic garnet phase, the tetragonal garnet phase known for the higher Li occupancy and a small $La_2Zr_2O_7$ impurity phase. The mixture of cubic and tetragonal garnet structures has proven to be beneficial for further processing into a solid electrolyte with a high ionic conductivity, since a certain Li loss from the garnet structure is expected during sintering transforming the observed tetragonal phase in to the cubic structure with lower Li occupancy. After sintering using FAST the $La_2Zr_2O_7$ phase is no longer detected, which confirms the redistribution of Li and the successful minimization of the Li loss from the garnet structure during sintering. Additionally, the distorted tetragonal phase is present due to the uniaxial pressure applied to the ceramic specimen at 950 °C. The sintered ceramic is then annealed under oxygen atmosphere at 500 °C for 24 h. The X-ray diffraction pattern does not show any impurity phase formation, while the distorted tetragonal phase fraction increases by only 5 wt.%, which is not significant considering the overlapping of the reflections. The more significant effects of annealing under oxygen atmosphere are the reduction of the unit cell volume of the distorted tetragonal phase as well as its c/a ratio. Additionally, the decrease in the microstrain of the distorted phase is observed with (0 0 1) preferred orientation parameters, G, of 1.33(2) and 1.38(2) before and after annealing, respectively. An overview of the Rietveld refinement results is presented in Table 7-7. The observation made after annealing of the sample at 500 °C all point to an initiation of a structural and microstructural change of the ceramic specimen. An increase in temperature is expected to result in a more significant and more accurately quantifiable change. Therefore, an annealing procedure is carried out at 700 °C while measuring DTA-TGA.

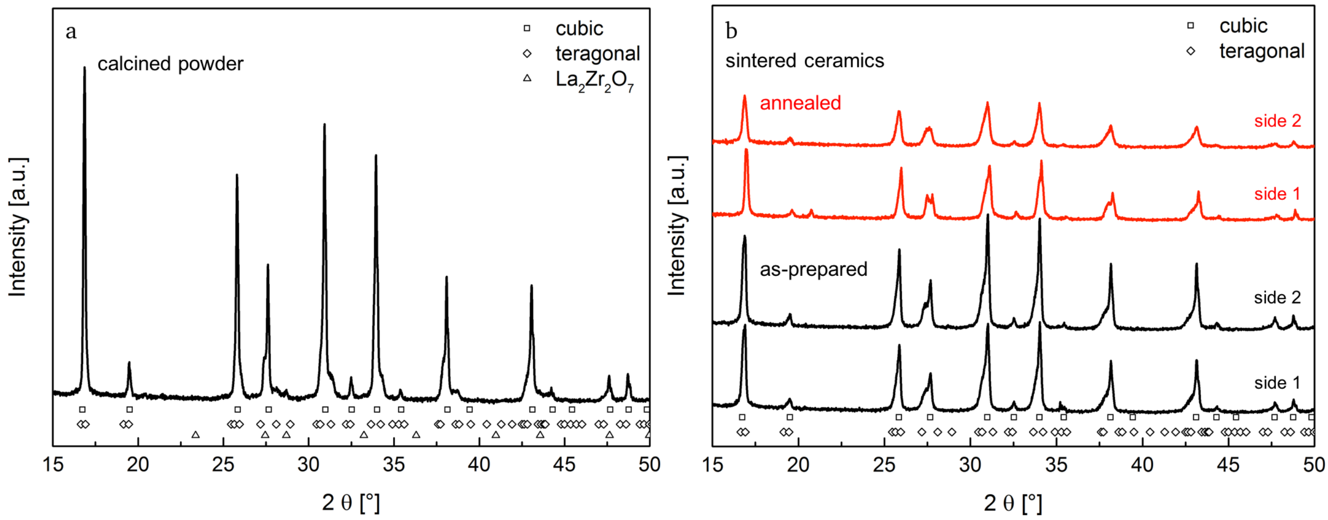

Figure 7-28: X-ray diffraction patterns of the $Li_{7-3x}La_3Zr_2Al_xO_{12}$ calcined powder ($x = 0.22$) (a) and sintered ceramic as-prepared and after annealing (b) at 500 °C for 24 h under oxygen atmosphere.

Table 7-7: Overview of the Rietveld refinement data of the calcined powder and as-prepared sintered ceramic before and after annealing at 500 °C for 24 h.

Sample	**Phase**	**Phase fraction [wt.%]**	**Unit cell volume [Å^3]**	**Microstrain**	c/a
Calcined powder	cubic garnet	71.2(1)	2187.286(86)	0.119(9)	1
	tetragonal g.	27.5(1)	2181.27(35)	0.02(21)	0.976
	$La_2Zr_2O_7$	1.3(1)	1275.3(14)	-	1
As-prepared ceramic	cubic garnet	43.9(2)	2176.92(11)	0.039(3)	1
	tetragonal g.	56.1(2)	2214.5(12)	0.310(15)	0.991
Annealed ceramic	cubic garnet	39.3(2)	2179.56(20)	0.07(13)	1
	tetragonal g.	60.7(2)	2198.88(84)	0.217(65)	0.984

For further characterization of the influence of the thermal treatment on the microstructure and thereby on the electrochemical performance, DTA-TGA measurements are carried out for ceramics sintered using FAST under vacuum and Ar atmosphere. During thermal treatment it is expected that the oxygen vacancies formed during field assisted sintering would be occupied by oxygen from the surrounding atmosphere. Differences between the two measurements could give clues to the ceramic failure observed when sintered under vacuum, opposed to the more stable ceramics obtained when sintered under Ar. The DTA-TGA measurements are shown in Figure 7-29. The first heating cycle performed under Ar atmosphere up to 600 °C results in the elimination of moisture. Although the samples are stored in an Ar-filled glovebox, a mass loss is detected starting at 100 °C and increases gradually with increasing temperature. For both samples the first two endothermic peaks correspond to the desorption of moisture, while the third peak with an onset temperature of approximately 300 °C and a maximum at 600 °C might correspond to the desorption of CO_2 from the ceramic surface. The second heating cycle is performed under synthetic air (20 vol.% O_2 and 80 vol.% N_2) up to a maximum temperature of 700 °C. Both ceramics show the same endothermic peaks observed during the first heating cycle, while no significant mass loss is observed until the maximum temperature is reached. Once the ceramics reach 700 °C a mass loss of 0.1% is detected for the sample sintered under vacuum and 0.3% for the sample sintered under Ar. It has to be noted at this point that the sample sizes are not identical, the sample masses are 31.7 mg and 53.3 mg for the ceramic sintered under Ar and vacuum, respectively. The difference in mass loss between both samples can be attributed to the different surface to volume ratio of the samples being larger for the smaller sample sintered under Ar. Therefore, the mass ratio of the adsorbed species, that are desorbed during annealing, to the total mass is larger. Furthermore, both samples show a similar mass increase of approximately 0.05% at the end of the dwell time. This increase might be related to the expected incorporation of oxygen into the garnet lattice, but it is too small to be able to draw any conclusions. The fact remains that both samples sintered under vacuum and Ar show almost identical behavior when heating up to 700 °C for 1 hour.

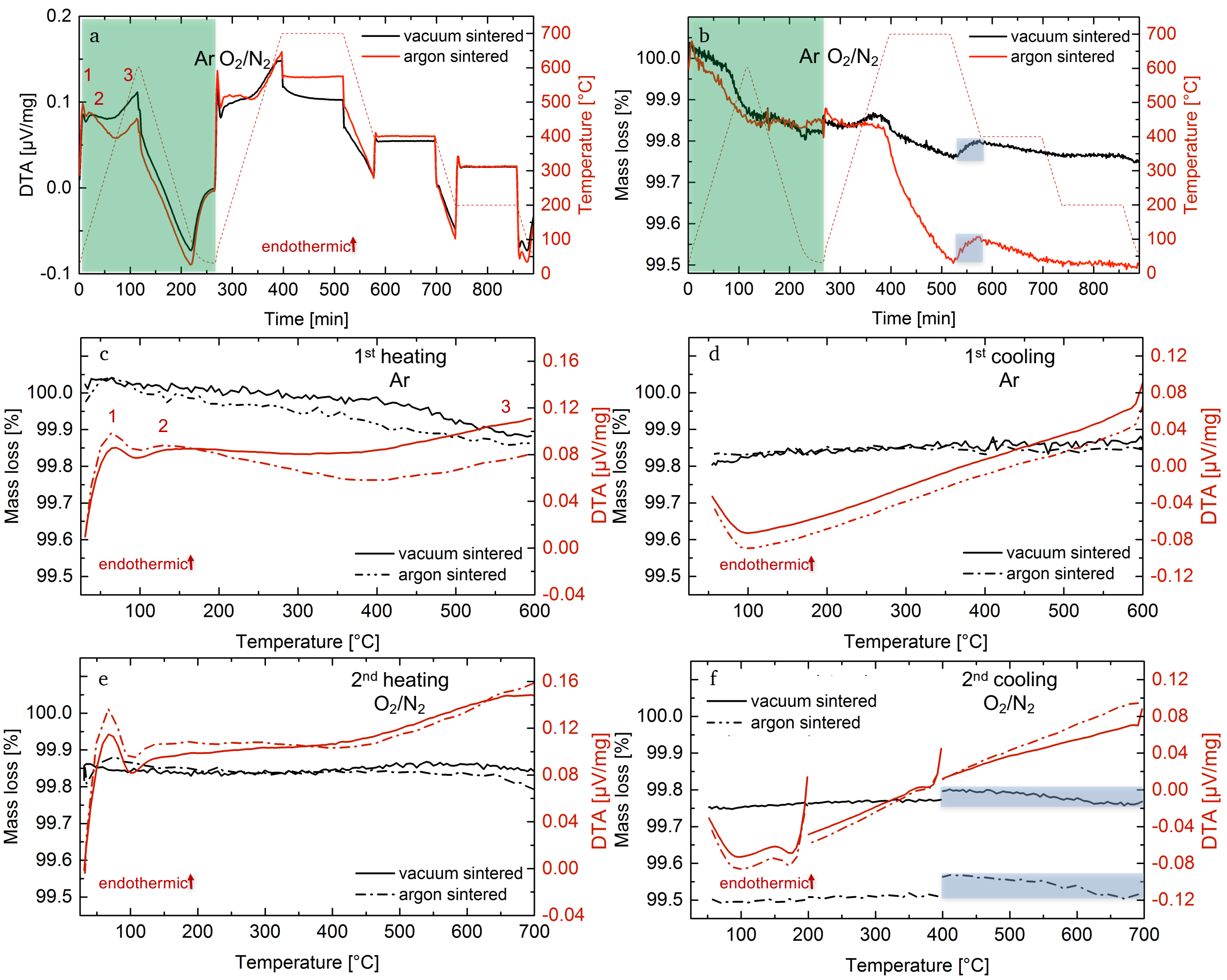

Figure 7-29: Overview of the DTA curves (a) and TGA curves (b) of sintered pellets under vacuum (10^{-2} mbar) and under Ar atmosphere. The first temperature cycle is performed under Ar, where first three peaks are marked and the second under synthetic air (O_2/N_2), where the mass increase is highlighted. Detailed graphs plotted against the temperature for the 1st heating (c), 1st cooling (d), 2nd heating (e) and 2nd heating (f).

There are two possible explanations for the cracking of the ceramic specimen during sintering under vacuum as opposed to Ar atmosphere where the cracking could be eliminated. The first is the formation of oxygen vacancies during field assisted sintering, which is supported by the sub-stoichiometric oxygen content of the grains containing Li_2CO_3, as reported in section 7.2.1.2. In contrast to sintering under vacuum where the oxygen vacancies could be reoccupied during cool down, since the FAST chamber is vented before complete cool down, which might lead to volume expansion and cracking. Under Ar atmosphere the ceramic specimen is kept under inert atmosphere until complete cool down to room temperature preventing the oxygen reincorporation. The second reason is the suppression of the Li_2CO_3 decomposition through the introduction of Ar into the chamber. The decomposition under the formation of CO_2 gas is not expected to lead to cracking of the ceramic as long as the carbonate resides at the grain boundaries, where it enhances the sintering behavior as a liquid phase. There the CO_2 is allowed to escape due to the lower density of the grain boundaries. If the carbonate phase resides within the grains as it is observed using STEM (section 7.2.1.2), its decomposition can easily lead to the failure of the ceramic. Under Ar atmosphere the local temperature of the ceramic specimen during sintering is expected to be lower than during sintering under vacuum, since the heat transfer from the die, where the temperature is measured using a thermocouple, to the surrounding atmosphere is enhanced. Therefore, local overheating, which might lead to the decomposition of the intragranular carbonate phase, is eliminated. The oxygen incorporation into oxygen vacancies formed during sintering may be present according to the DTA-TGA data, yet the ceramic samples remain intact, therefore, it seems more likely that the Ar atmosphere does in fact suppress not only the decomposition of Li_2CO_3 but also reduces the formation of a liquid phase, which is evident from the reduced adhesion of the ceramic specimen to the graphite foil after sintering.

X-ray diffraction is performed for the ceramics sintered under vacuum and under Ar atmosphere before and after the DTA-TGA measurement, i.e., after annealing at 700 °C and the diffraction patterns are shown in Figure 7-30. The as-prepared ceramic sintered under Ar exhibits a mixture of cubic and distorted tetragonal phase fractions and a small amount of $La_2Zr_2O_7$ impurity phase, which is no longer detected after annealing. The “distorted tetragonal phase” is not detected after annealing leading to a cubic garnet structure with an unknown impurity phase. The as-prepared ceramic sintered under vacuum is composed of the cubic garnet structure and the distorted tetragonal phase with a higher microstrain. After annealing the latter is no longer detected and an unknown impurity phase emerges. An overview of the Rietveld data is presented in Table 7-8.

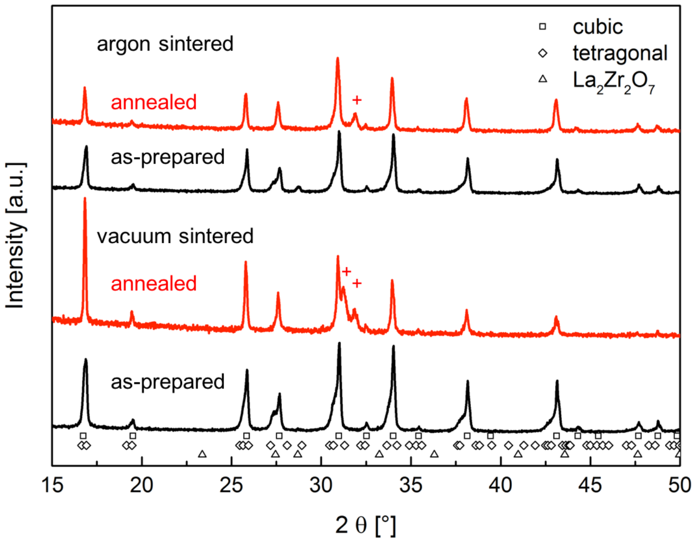

Figure 7-30: X-ray diffraction patterns of the sintered ceramic ($x = 0.22$) under vacuum (a) and under Ar atmosphere (b) as-prepared and annealed after the DTA-TG characterization performed up to 700 °C und synthetic air (O_2/N_2), + marking peaks of unknown phase.

Table 7-8: Overview of the Rietveld refinement data for ceramics before and after DTA-TG characterization.

Sample	Phase	Phase fraction [wt.%]	Unit cell volume [Å^3]	Microstrain	c/a
As-prepared (argon)	cubic garnet	58.2(1)	2177.71(15)	0.045(1)	1
	tetragonal g.	40.5(1)	2214.3(17)	0.313(1)	0.989
	$La_2Zr_2O_7$	1.35(1)	1261.82(37)	-	1
Annealed (N_2/O_2)	cubic garnet	100 (- unknown)	2179.52(20)	0.064(4)	1
As-prepared (vacuum)	cubic garnet	43.3(1)	2176.92(11)	0.039(3)	1
	tetragonal g.	56.7(1)	2214.5(12)	0.312(15)	0.991
Annealed (N_2/O_2)	cubic garnet	100 (- unkown)	2183.15(60)	0.089(34)	1

7.3.2 Li-ion conductivity

The optimization of the Li-ion conductivity of the solid electrolyte is the main objective of this work, therefore, it is measured using AC-impedance spectroscopy for as-prepared ceramic using FAST (vacuum sintered) and the annealed ceramic. The Nyquist plots showing the impedance spectra and corresponding fits for the ceramic sample with $x = 0.22$ before and after annealing are presented in Figure 7-31 where the arrows indicate the frequencies at the maxima of the respective semi-circle at the lowest temperature. The spectra are collected in the temperature range starting 220 K to be able to detect both the bulk and grain boundary contributions to the spectrum and up to 298 K where only the grain boundary semi-circle is detected and the bulk resistance is determined by its first intercept with real Z'-axis. Comparing the bulk resistance of the spectrum collected at 220 K for the as-prepared ceramic to the one of the annealed ceramic, a decrease is observed. On the other hand, when comparing the grain boundary semi-circles, a significant increase of resistance is observed after annealing at 500 °C. Although the annealing temperature is too low for significant detectable changes concerning the phase composition, yet the ionic conductivities of the bulk and grain boundary region show significantly different behavior after annealing. To exclude that the changes in bulk and grain boundary resistances are merely due to renewed polishing of the ceramic after annealing and a redistribution of the bulk and grain boundary fractions across the surface, three impedance measurements are carried out after renewed polishing of the sample on one side. The result shows no change of the bulk and grain boundary contributions due to repeated polishing. The total conductivity at 298 K remains unchanged after annealing at 0.77 mS cm^{-1}, which is the highest room temperature Li-ion conductivity reported to date for $Li_{7-3x}La_3Zr_2Al_xO_{12}$ ($x = 0.22$).

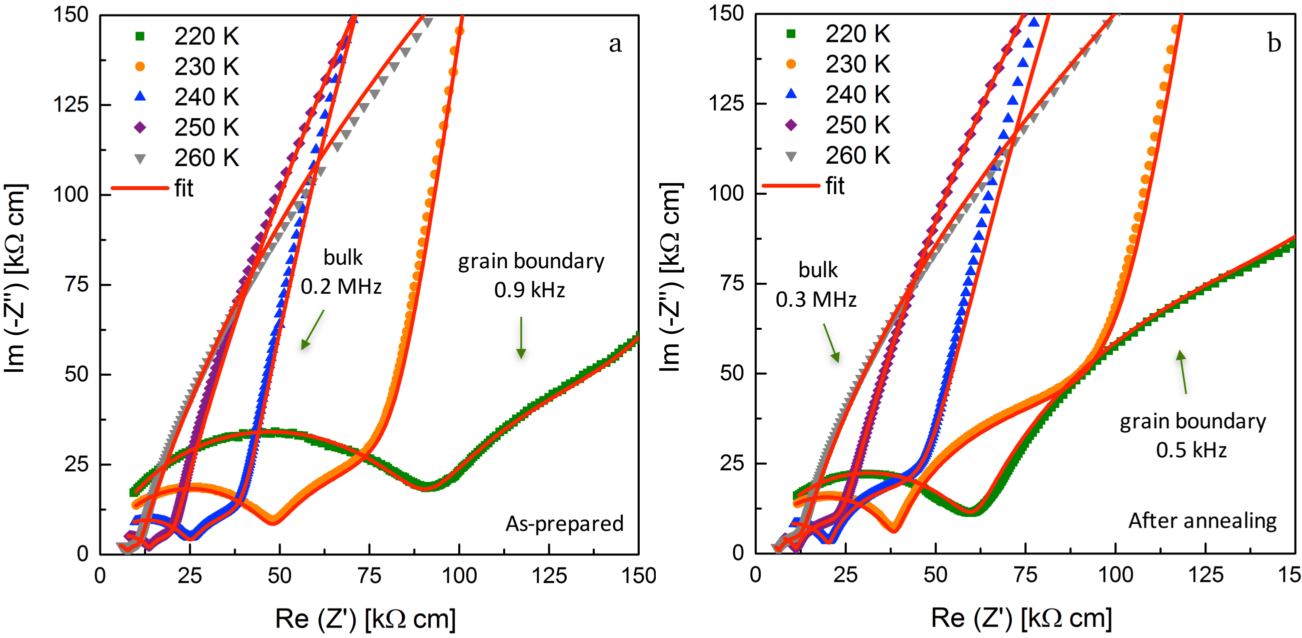

Figure 7-31: Nyquist plots and corresponding fits for $Li_{7-3x}La_3Zr_2Al_xO_{12}$ sintered ceramics ($x = 0.22$) with blocking Au-electrodes between 220 K up to 260 K as-prepared (a) and after annealing at 500 °C for 24 h under oxygen atmosphere (b).

To determine the change of the activation energy before and after annealing at 500 °C under oxygen atmosphere the Arrhenius plots of the total ionic conductivity are plotted. The temperature dependence is shown in Figure 7-32. While the room temperature total conductivity does not change after annealing, the activation energy increases from 0.36 eV for the as-prepared ceramic to 0.39 eV after annealing. This change indicates the influence of the annealing process on the Li-ion mobility. A redistribution of the Li-ions within the garnet structure might be a reason for this decrease. Additionally, for the case of an enhancement of the ionic mobility due to an increased microstrain using FAST, a release of the microstrain during annealing could be a second explanation for this observation.

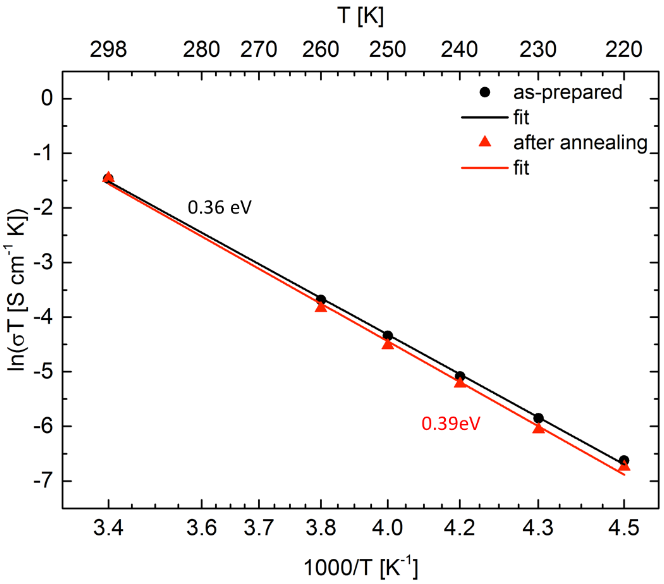

Figure 7-32: Arrhenius plot presenting the temperature dependence of the Li-ion conductivity for $Li_{7-3x}La_3Zr_2Al_xO_{12}$ sintered ceramics ($x = 0.22$) as-prepared by FAST and after annealing at 500 °C for 24 h under oxygen atmosphere.

The AC-impedance measurements at low temperatures allow for the extraction of the bulk and grain boundary activation energies, since the semi-circles are clearly detected and separated. The Arrhenius plots for the bulk and grain boundary conductivities versus temperature are shown in Figure 7-33 for the as-prepared as well as for the annealed ceramic. The conductivity values are calculated using the dimensions of the pellet, which is an approximation. The bulk activation energy decreases from 0.35 eV to 0.33 eV after annealing of the ceramic, while the grain boundary activation energy increases significantly from 0.43 eV to 0.46 eV.

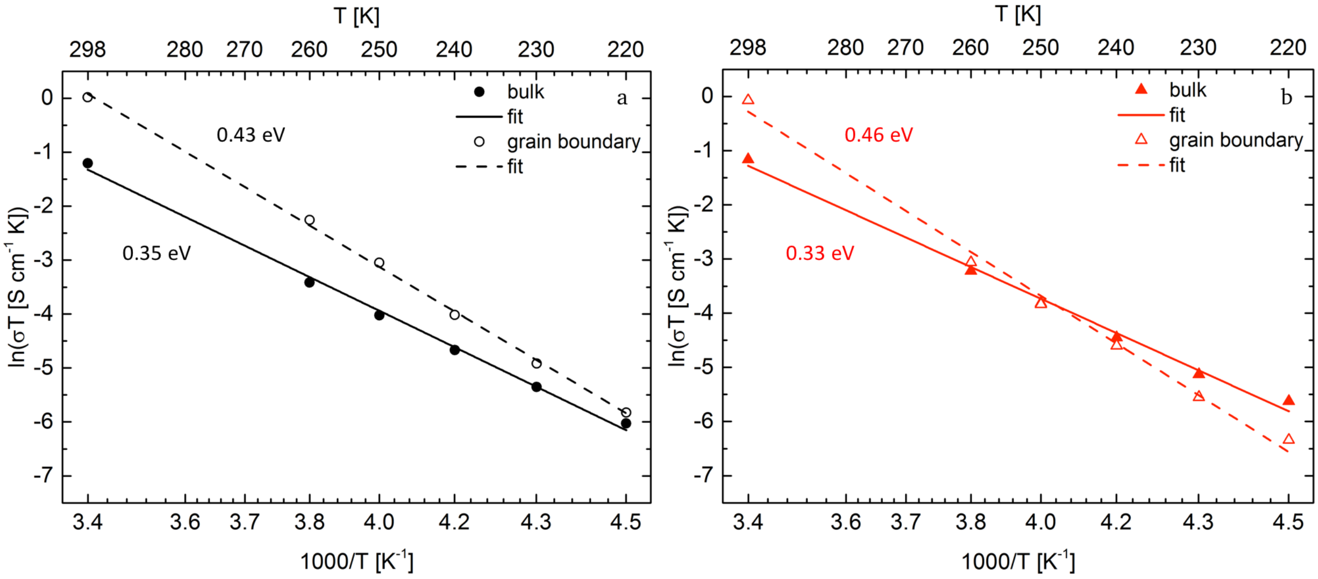

Figure 7-33: Arrhenius plots presenting the temperature dependence of the bulk and grain boundary Li-ion conductivities for as-prepared ceramic (a) and after annealing (b).

The opposite behavior of the bulk and grain boundary conductivity characteristics might be due to opposite processes taking place in each region. Considering the assumption made in section 7.2.1.3 that the distorted tetragonal structure showing a higher microstrain resides near the grain boundary region, the bulk and grain boundary characteristics observed due to annealing might be correlated to the changes in microstrain observed for the distorted tetragonal garnet structure (grain boundary region). For this specific case a decrease in microstrain of the distorted tetragonal structure is accompanied by a decrease in ionic conductivity and increase of activation energy of the grain boundary contribution. During annealing the Li-ions are expected to diffuse to energetically more favorable positions, e.g., with a lower microstrain until an equilibrium is achieved, which may lead to the increased bulk conductivity and the decrease of the activation energy. This is merely speculation based on the data presented in this study and further detailed experiments are needed to confirm these correlations. Nevertheless, a dependence of the electrochemical behavior on the observed microstrain originating from mechanical deformation during FAST is present. The thermal treatment has been successfully applied to alter the microstructural properties of the solid electrolyte by reducing the microstrain correlated with the formation of the distorted tetragonal phase, presumably residing near the grain boundary region. Opposite trends for the electrochemical changes observed for the bulk and grain boundary region suggest competing processes taking place during annealing, i.e., Li-ion diffusion and microstrain relief.

7.4 Influence of storage conditions

In addition to the thermal treatment, storage conditions, i.e., atmosphere and duration might have a significant influence on the microstructure, which might influence the electrochemical performance of the garnet solid electrolyte. Therefore, a sample, which is stored in an Ar-filled glovebox for approximately 10 months is characterized before and after storage.

7.4.1 Phase composition and microstrain

In this study calcined $Li_{7-3x}La_3Zr_2Al_xO_{12}$ powder ($x = 0.22$) is sintered using FAST under vacuum. The X-ray diffraction data for the ceramic before and after storage measured on both sides of the pellet are shown in Figure 7-34. The as-prepared ceramic exhibits a phase composition of mainly the cubic phase and the distorted tetragonal phase exhibiting a higher microstrain, and a small amount of $La_2Zr_2O_7$ impurity phase. A preferred orientation model is used for the (0 0 1) lattice plane resulting in a G value of 1.45. After storage the impurity phase is no longer detected, which might indicate a redistribution of the Li-ions. Additionally, the distorted tetragonal phase shows a significantly lower microstrain and the utilization of a preferred orientation model is no longer needed to achieve an appropriate fit. An overview of the refinement data is presented in Table 7-9. It is evident that in addition to the reduction of the microstrain of the distorted tetragonal phase the unit cell volume is reduced, while the c/a ratio approaches unity. This leads to the conclusion that the tetragonal distortion observed after field assisted sintering due to mechanical loading of the ceramic at high temperatures is no longer observed after a long period of storage time in an Ar-filled glovebox.

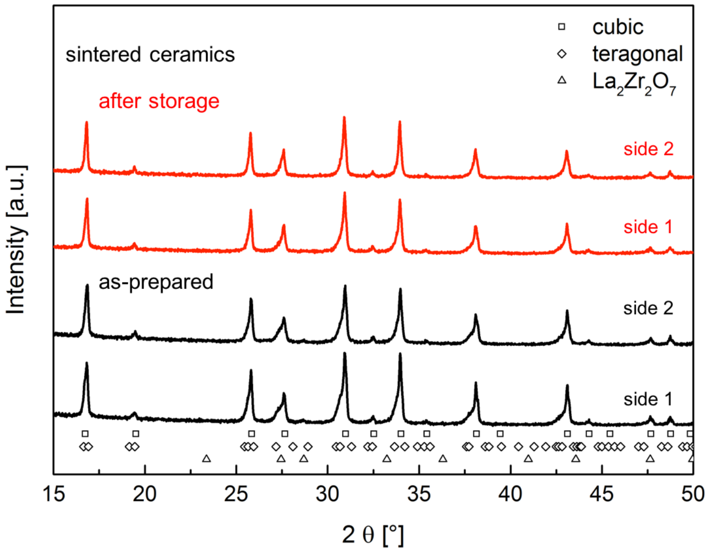

Figure 7-34: X-ray diffraction patterns of the sintered ceramic ($x = 0.22$) as-prepared and after storage for 10 months in an Ar-filled glovebox.

Table 7-9: Overview of the Rietveld refinement data of X-ray diffraction patterns of the as-prepared sintered ceramic and after storage for 10 months in an Ar-filled glovebox.

Sample	Phase	Phase fraction [wt.%]	Unit cell volume [Å^3]	Microstrain	c/a
As-prepared ceramic	cubic garnet	50.9(1)	2177.69(12)	0.039(5)	1
	tetragonal g.	48.5(1)	2213.1(20)	0.302(21)	0.992
	$La_2Zr_2O_7$	0.60(4)	1262.9(28)		
After storage	cubic garnet	57.2(2)	2181.3(5)	0.011(3)	1
	tetragonal g.	42.8(2)	2193.4(13)	0.099(9)	1

7.4.2 Li-ion conductivity

The influence of storage under an Ar atmosphere on the Li-ion conductivity of $Li_{7-3x}La_3Zr_2Al_xO_{12}$ ceramic ($x = 0.22$) is studied. The storage conditions of the solid electrolyte are crucial for optimized cell manufacturing and performance. A first step to determine the influence of storage under an Ar atmosphere is measuring the Li-ion conductivity using AC-impedance spectroscopy. The Nyquist plots and corresponding fits are shown in Figure 7-35 where the arrows indicate the frequency values at the maxima of the semi-circles. The spectra for the as-prepared and for the same sample after storage are collected starting at 220 K up to 298 K during heating. The samples are heated up to 393 K prior to the measurement to eliminate residual moisture. At low temperatures the bulk and grain boundary contributions to the spectra are clearly separated. The as-prepared ceramic shows higher bulk resistances compared to its grain boundary resistance. This has proven to be beneficial for the interfacial resistance of fine grained ceramics (2-3 μm) towards Li metal, as opposed to ceramics with similar bulk and grain boundary resistances (see section 7.2.1.5). After storage for 10 months under an Ar atmosphere both bulk and grain boundary resistance increase significantly, while the grain boundary resistance shows higher values than the bulk resistance at the lowest temperature. The room temperature total Li-ion conductivity decreases from 0.62 mS cm^{-1} to 0.48 mS cm^{-1} after storage.

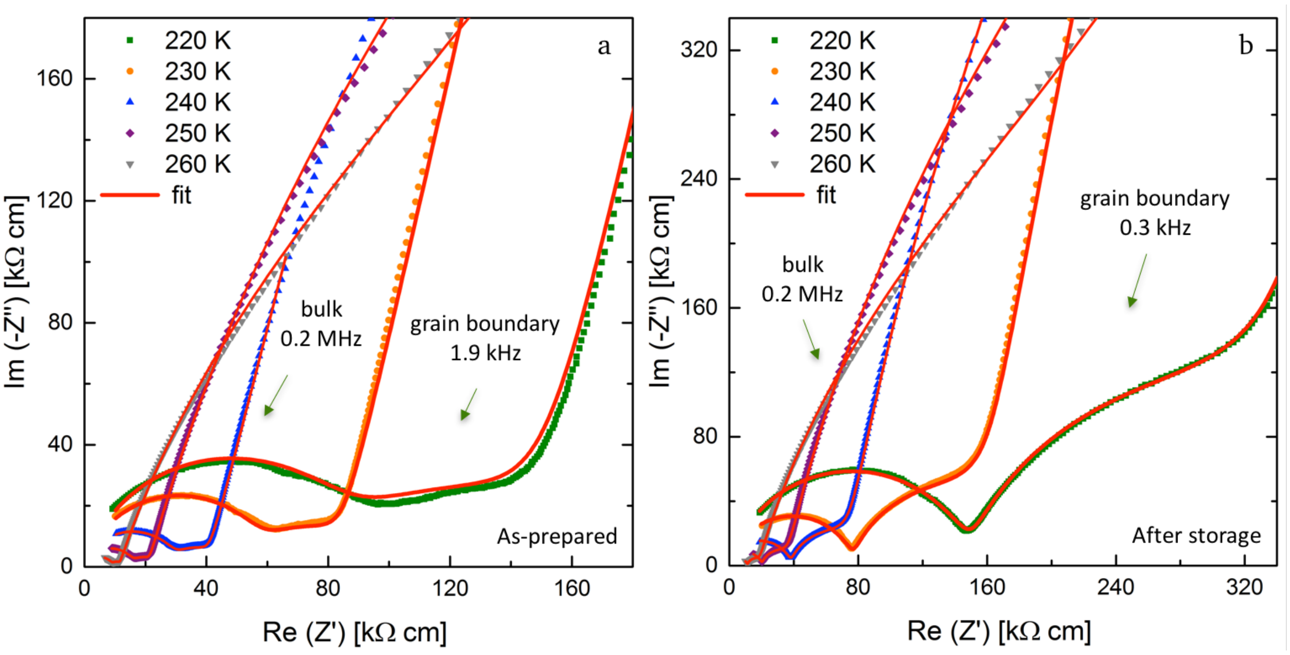

Figure 7-35: Nyquist plots and corresponding fits for $Li_{7-3x}La_3Zr_2Al_xO_{12}$ sintered ceramics (x = 0.22) with blocking Au-electrodes between 220 K up to 260 K as-prepared (a) and after storage under an Ar atmosphere (b), arrows indicate the frequency at the maxima of the corresponding semi-circle.

The Arrhenius plots showing the temperature dependence of the total Li-ion conductivity are presented in Figure 7-36. In addition to the decreased room temperature Li-ion conductivity, the activation energy increases from 0.36 eV for the as-prepared ceramic to 0.39 eV after storage for 10 months under an Ar atmosphere. This significant performance decay could be due to the release of microstrain as a result of the storage time or due to small moisture residues inside the Ar-filled glove box (<0.1 ppm) that adsorb to the sample during storage forming LiOH and extracting Li from the garnet structure and thereby possibly reducing the charge carrier concentration.

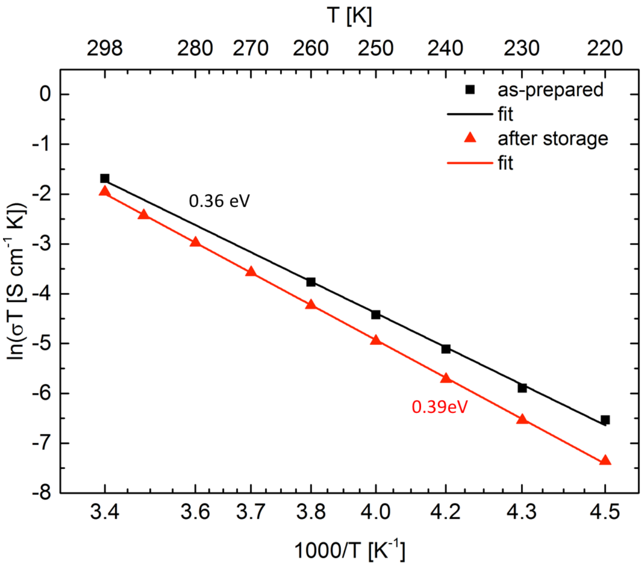

Figure 7-36: Arrhenius plot presenting the temperature dependence of the Li-ion conductivity for $Li_{7-3x}La_3Zr_2Al_xO_{12}$ sintered ceramics ($x = 0.22$) as-prepared by FAST and after storage under an Ar atmosphere.

For a more detailed investigation of the degradation of the electrochemical performance after storage the bulk and grain boundary conductivities are calculated using the pellet dimensions. The temperature dependence of both contributions are shown in Figure 7-37 for the sintered ceramic, as-prepared and after storage. The superior Li-ion conductivity of the grain boundary compared the bulk conductivity is evident, except for the ceramic after storage at low temperatures. Additionally, the bulk activation energy increases from 0.33 eV to 0.35 eV, while the grain boundary activation energy increases from 0.42 eV to 0.47 eV for the ceramic before and after storage, respectively. Both contributions show a decay in performance, while the degradation of the grain boundary contribution is more pronounced. This might be due to the higher porosity of the grain boundary, which allows for larger adsorbate amounts during storage and thereby extracting more charge carriers from the grain boundary region. An alternative explanation, if the proposed hypothesis that the distorted tetragonal phase resides near the grain boundary region is true, see section 7.2.2.3, is that the microstrain relief would have a more significant influence on the grain boundary conduction characteristics.

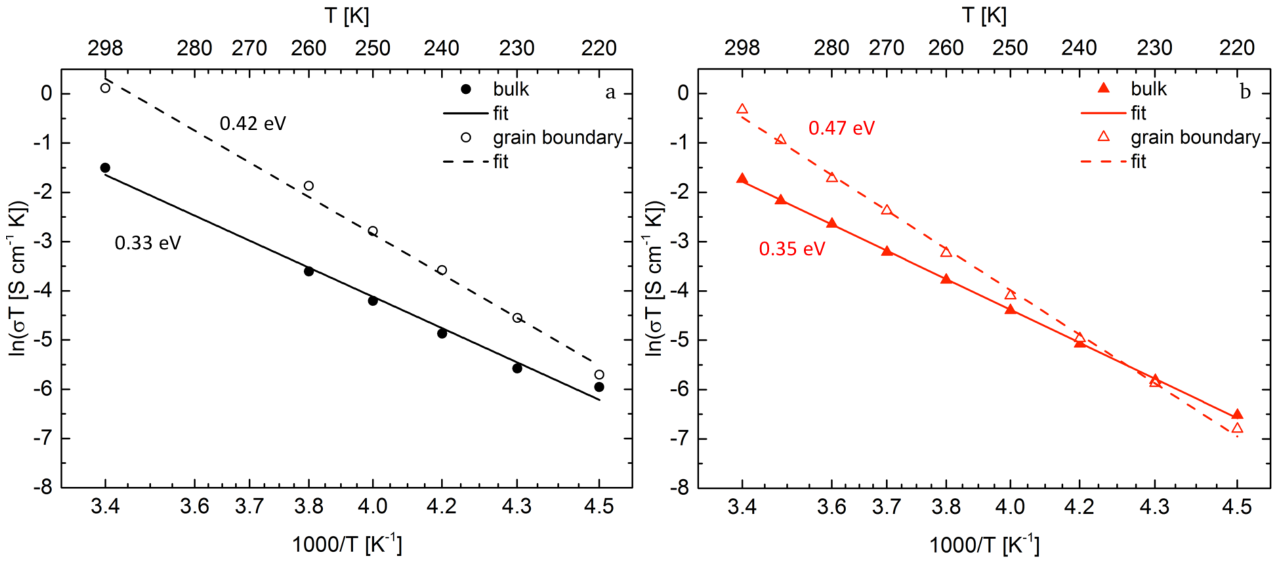

Figure 7-37: Arrhenius plots presenting the temperature dependence of the bulk and grain boundary Li-ion conductivities for as-prepared ceramic (a) and after storage under Ar (b).

The observed degradation of the solid electrolyte after storage for 10 months under Ar atmosphere is an important indication that the known moisture sensitivity of LLZO is not overcome by storage under Ar atmosphere alone. The sensitivity towards moisture remains present even at the smallest amounts (<0.1 ppm) over a long storage time. The degradation in electrochemical performance of the solid electrolyte would influence its interfacial resistance when contacted with electrode materials, as well as the total cell resistance. Therefore, it is of great importance to prepare vacuum sealed cells, when integrating LLZO into full operational cells on a large scale. Additionally, any residual moisture from the electrode materials and other cell components might lead to performance decay over long periods of time, especially at very low operating temperatures (<250 K).

7.5 Conclusion and summary

The processing step utilized to alter the grain size of the ceramics was ball milling. The as-synthesized powder was ball milled before conventional sintering and the electrochemical performance of both ceramics with ball milled and as-synthesized powder was characterized using AC-impedance spectroscopy. The ceramic with a ball milled starting powder showed a superior total ionic conductivity and a smaller activation energy. The decrease of activation energy is mainly due to increased mobility in the grain boundary region, while the bulk activation energy increased slightly. The higher mobility of the Li-ions, which is presumed to be due to the presence of a higher defect concentration after ball milling, might open the solid electrolyte field to obtaining an amorphous LLZO structure with higher Li-ion mobility due to higher defect concentration, as it was shown for amorphous $LiNbO_3$ compared to its microcrystalline structure [85]. The calcined powder, that was used for field assisted sintering, was ball milled for only 2 hours to avoid contamination due to the ball milling process, as for the as-synthesized powder. A clear change in particle microstructure was observed leading to a mean particle size of 0.7 μm. The grain size of the sintered ceramic using calcined powder with and without the ball milling processing step showed a mean value of 0.7 μm and

2.2 μm, respectively. A FIB lamella of each sample was prepared and HAADF STEM combined with EDXS was carried out. No segregation of Al or Zr was observed for both samples, which confirms the homogeneous distribution of the dopant using the combination of NSP and FAST, and additionally, it indicates that the ball milling step did not lead to any contamination of the powder. Furthermore, for the large grained ceramic circular pores were observed intragranularly, while the grains of the small grained ceramic did not show any porosity. Additionally, a Li_2CO_3 inclusion in the grains was detected for the large grained ceramic, accompanied by a sub-stoichiometric oxygen content of these grains. This is due to the different microstructure of the starting powder. The calcined powder showed necking between the particles, as a starting step of the sintering process already taking place during calcination, while the particles were separated after ball milling. Li_2CO_3 is known to reside on the surface of the powder particles during air exposure and, thereby, is found intragranularly for the large grained ceramic together with the circular pores, that are a result of the rigid necks between the particles, and expected to have been only intergranular for the small grained ceramic acting as a sintering aid due to liquid phase formation, before its decomposition. The additional $La_2Zr_2O_7$ phase, which was detected by X-ray diffraction for the small grained ceramic, was observed using EDXS as separate grains, which reduces its expected role in deteriorating the electrochemical performance compared to an impurity phase that might have resided along the grain boundaries. The compositional and microstructural observations could be correlated to the superior electrochemical performance of the large grained ceramic (2.2 μm). The conductivity decreases with decreasing grain size, while the activation energy increases. The grain boundary performance of the small grained ceramic showed a more significant decay compared to the large grained ceramic, which is an indication that the Li loss observed for the small grained ceramic does not necessarily imply a loss of charge carriers, but the larger amount of grain boundaries has a more significant role in the deterioration of the electrochemical performance. The ASR determined for the interface between the solid electrolyte and Li metal was 30.7 Ω cm^2 for the large grained ceramic and is amongst the best value reported to date for $Li_{7-3x}La_3Zr_2Al_xO_{12}$ ceramics. Due to the superior electrochemical characteristics of the large grained ceramic the cycling was, in turn, more stable than the small grained ceramic, which showed larger ASR values that exhibited a decrease after cycling for 100 hours. This might be an indication to the long term stability of the interface with a finer microstructure, yet the interfacial resistance remains high. The microstructure of the LLZO ceramic has a significant influence on its electrochemical performance, therefore, each processing step or technique used, which alters the microstructure, could possibly enhance or deteriorate the ionic conductivity as well as influence the activation energy of the material. This makes a comparison between two different synthesis routes difficult and many factors need to be taken into account. A comparison of two different sintering techniques, conventional sintering and FAST, concerning the influence of the initial particle size on the electrochemical performance lead to enhanced electrochemical performance for the conventionally sintered ceramics with smaller starting particle size and the contrary for the ceramics sintered using FAST. A more detailed investigation of the grain boundary regions of both ceramics is needed to establish the key differences controlling the electrochemical performance, e.g., the defect concentration due to ball milling and differences arising from the fact that during conventional sintering reactive sintering in addition to liquid phase sintering are taking place simultaneously, while during FAST the starting material is already in the desired garnet structure.

Another approach utilized for tuning the microstructure of the LLZO solid electrolyte and to determine its influence on the electrochemical performance was the variation of the pressure during sintering using FAST. The pressures used were 50 MPa, 30 MPa and 20 MPa for ceramics with a doping level $x = 0.22$. Results from X-ray diffraction clearly show a correlation between the microstrain observed mainly in the distorted tetragonal phase and the pressure. With decreasing pressure, the microstrain decreases and an increase of the c/a ratio of the distorted phase was observed approaching unity. This observation confirms that the formation of the distorted tetragonal phase during field assisted sintering is due to the mechanical load leading to radial volume expansion and unit cell deformation presumably after the release of the pressure at 950 °C. The electrochemical performance also showed a dependence on the applied pressure during sintering, while the differences in density and grain size between the ceramics were eliminated, for the densities being within the range of 95% TD to 100% TD and grain sizes with mean values from 2.2 μm and 2.4 μm. The total ionic conductivity was reduced from 0.42 mS cm^{-1} to 0.36 mS cm^{-1} down to 0.26 mS cm^{-1} with decreasing pressure, while the activation energy increased significantly from 0.37 eV to 0.41 eV for the highest and lowest pressure, respectively. The separation of the bulk and grain boundary contributions to the spectrum allowed for a more detailed characterization of the decay of the electrochemical performance with decreasing pressure. The grain boundary conductivity as well as activation energy show a more significant performance decay with decreasing pressure during sintering than the bulk characteristics. The proposed strain enhancement of the electrochemical performance for the ceramics sintered under high pressures seems to be localized within the grains near the grain boundary region, where the formation of the tetragonal distortion is supported by the liquid phase during sintering allowing for enhanced diffusion. This is merely a hypothesis that needs to be supported by further local characterization of the crystallographic structure of the grain center, grain edge, as well as the grain boundary region of the material using electron diffraction.

Using thermal treatment to alter the microstructure was successful in terms of changing the electrochemical behavior of the ceramic after annealing at 500 °C. The structural changes after annealing were detectable using X-ray diffraction, where the distorted tetragonal phase, presumed to reside near the grain boundary region, showed a lower microstrain. For a more pronounced detection of the structural and chemical changes during the annealing process DTA-TGA was carried out up to 700 °C. In addition to the ceramic sintered under vacuum, a ceramic sintered under Ar was characterized under the same conditions, where they both showed comparable results. The most significant observation is the mass increase at the end of the dwell time at the highest temperature, which might be related to oxygen uptake of the ceramic occupying oxygen vacancies created during field assisted sintering. Oxygen vacancies were recently observed for garnet solid electrolytes [97]. X-ray diffraction performed after the DTA-TGA measurement showed a cubic structure with no traces of the highly strained distorted tetragonal phase, while an additional unknown impurity phase emerged for both samples. The diffraction experiment confirmed the influence of heat treatment on the structure of the garnet solid electrolyte, which is the release of the microstrain induced during sintering until the distorted tetragonal phase is no longer detected. This structural alteration and the presumed oxygen uptake were not accompanied by crack formation in the ceramic specimen and can, therefore, be excluded as reasons for the failure of the ceramics observed after sintering under vacuum. The proposed reason for this failure, which was not observed for ceramics sintered under Ar, is that the Ar introduced during sintering reduces the formation of the Li_2CO_3 liquid phase and suppresses its decomposition by preventing local overheating. The suppression of the decomposition of the Li_2CO_3 phase is crucial because of the formation of CO_2 gas as a product, especially when the Li_2CO_3 phase resides intragranularly, as observed using STEM. It was shown that local overheating could be fatal for garnet solid electrolytes processed using FAST, which is probably applicable to many Li-ion conducting ceramics that are electronically insulating, where the Li_2CO_3 formation during field assisted sintering is inevitable and is accompanied by the formation of a sub-stoichiometric oxygen content. The total room temperature Li-ion conductivity of the as-prepared and annealed ceramics at 500 °C remained unchanged at the highest reported value of 0.77 mS cm^{-1}, while the activation energy increased from 0.36 eV to 0.39 eV. The bulk and grain boundary contributions were separated and the result was an enhancement of the bulk and a deterioration of the grain boundary electrochemical properties, which leads to the assumption that two competing processes are taking place. The decrease in microstrain of the distorted tetragonal structure is accompanied by a decrease in ionic conductivity and increase of activation energy of the grain boundary contribution, while during annealing the Li-ions are expected to diffuse to energetically more favorable positions, e.g., with a lower microstrain until an equilibrium is achieved which may lead to the increased bulk conductivity and the decrease of the activation energy. It can be concluded that a thermal treatment of LLZO ceramics at moderate temperatures might alter the microstructure and change the electrochemical performance. This phenomenon is important for the integration of the solid electrolyte in all-solid-state battery cells, where deposition of the electrode layers requires the exposure of the solid electrolyte to elevated temperatures.

The storage of the solid electrolyte even under an Ar atmosphere also had significant influence of the microstructure, i.e., the microstrain as well as on the electrochemical performance. The microstrain observed for the distorted tetragonal phase decreased after a storage time of 10 months. Additionally, the room temperature total Li-ion conductivity decreased significantly from 0.62 mS cm^{-1} to 0.48 mS cm^{-1}, while the activation energy increased from 0.36 eV to 0.39 eV. The electrochemical deterioration is present in both, the bulk and grain boundary characteristics, where it is more pronounced. The proposed reason for this ageing effect is the presence of a small amount of moisture (<0.1 ppm) that adsorbs to the ceramic and forms LiOH over long periods of time extracting Li from the garnet structure and thereby possibly reducing the charge carrier concentration. This observation is important for the integration of LLZO in cell and battery manufacturing, since a vacuum sealed system completely free of moisture needs to be provided to ensure long term stability of the electrochemical performance of the solid electrolyte.

8 Full all-solid-state cell assembly

Garnet solid electrolytes are promising candidates to act as a starting point for the development of an all-solid-state Li-ion battery. The Al-doped LLZO exhibits good chemical stability against Li metal [98] allowing for its application as anode material, which has great advantage towards achieving a higher energy density. Additionally, the ionic conductivity at room temperature is suitable for a bulk battery integration. Achieving a full all-solid-state battery cell, specifically a bulk Li-ion cell, is the aim of the experiments described in this chapter. Since the interfacial resistance between LLZO and Li metal was optimized and reached its best reported value of 30.7 Ω cm^2 for a smooth electrolyte pellet and melted Li foil, the main challenge to achieve an operational full all-solid-state cell is to minimize the interfacial resistance between the solid electrolyte and the cathode material. $LiCoO_2$ (LCO) is chosen as a cathode active material, since it is well studied and most commonly used in combination with LLZO [99,100]. To achieve an optimized interface between LCO and LLZO many challenges present themselves, like for instance the reactivity between LCO and LLZO at high processing temperatures starting at 600 °C [101]. Additionally, the charge transfer between the solid electrolyte and the cathode at room temperature is limited, leading to the need for composite cathode materials, including LCO, LLZO and carbon black to ensure electronic conductivity [102]. The optimization of the amounts of the components for such composites and their particle size is required to achieve a low interfacial resistance toward the solid electrolyte and to ensure the formation of percolation pathways for the conduction of Li-ions and electrons within the cathode composite [78]. A smaller particle size would be beneficial to achieve a high surface area, which would enhance the Li-ion and electron transport through the LLZO particles and carbon black, respectively, and the reduction of the Li-ions at the particle interfaces during discharge. Furthermore, the cathode density plays an important role as well. Highly dense cathodes are needed in order to ensure a large number of conductive pathways for both electrons and Li-ions.

To address all these challenges three approaches for cell design are considered in this work, and they are illustrated in Figure 8-1. The first approach towards an all-solid-state cell combines the already optimized Li metal anode and the bulk LLZO solid electrolyte with a thin film LCO cathode [103], Figure 8-1a. To avoid reaction and interdiffusion between LLZO and LCO, a Nb interlayer is deposited on the LLZO pellet before the cathode deposition. According to literature, an in-situ formation of ionically conductive, amorphous $LiNbO_3$ at the interface is expected, which would enhance the interfacial charge transfer and reduce the chemical interaction between the two materials [101]. The cell assembly procedure as well as the cycling performance are discussed in section 8.1. The second approach is based on replacing the thin film LCO cathode with a composite cathode containing LCO as an active material, LLZO electrolyte and carbon black, Figure 8-1b. The composite cathode powder is sintered together with the solid electrolyte pellet using field assisted sintering. Further details are presented in section 8.2. The third approach aims to enhance the interface between the cathode and the solid electrolyte by introducing a thin layer of liquid electrolyte only on the cathode side, eliminating its contact with the Li anode, Figure 8-1c. The cathode is produced using conventional printing of a LCO slurry using a doctor blade technique [104]. Description of the processing and electrochemical characterization is presented in section 8.3.

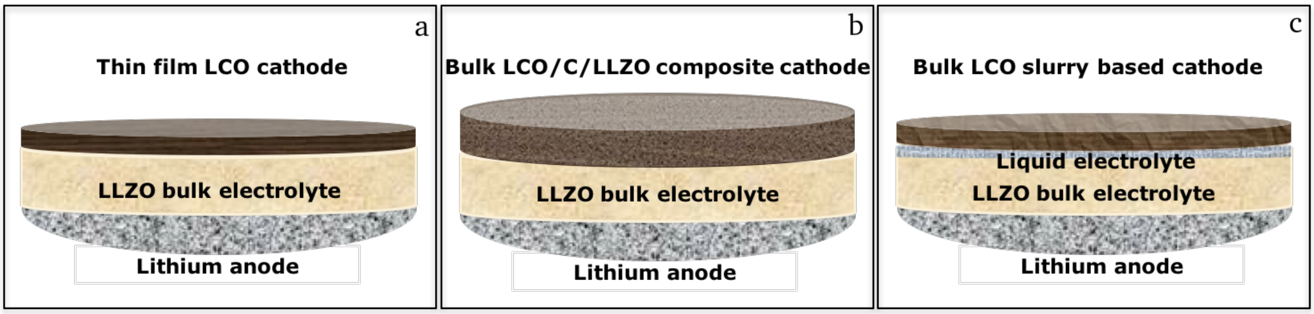

Figure 8-1: Approaches for achieving an all-solid-state cell using LLZO as bulk solid electrolyte with a LCO thin film cathode and Li anode (a), bulk composite cathode and Li anode (b) and a slurry-based LCO cathode immersed with liquid electrolyte and Li anode (c).

8.1 Thin film LCO cathode deposition by LA-CVD

The LCO thin film deposition using laser assisted chemical vapor deposition (LA-CVD) has many advantages, most prominent is the good contact between the cathode and solid electrolyte, due to the relatively high deposition temperature. Additionally, the LCO film is dense and it is phase pure [103]. Furthermore, for thin film LCO cathodes there is no need for the addition of an electronically conductive material, e.g., carbon black [105]. The $Li_{7-3x}La_3Zr_2Al_xO_{12}$ ceramic, with $x = 0.22$ and 30 wt.% Li-excess during synthesis, used for this study is synthesized combining NSP and FAST, achieving an ionic conductivity of 0.23 mS cm^{-1} and an activation energy for Li-diffusion of 0.36 eV.

8.1.1 Cathode processing

The deposition method used for the synthesis of the high temperature LCO thin film is a flash evaporation method, which relies on the non-equilibrium flash evaporation of a mixture of solid metal organic precursors of low volatility using a CO_2 laser [106]. The powder precursors, cobalt(III)acetylacetonate (98%, Sigma Aldrich), and 2,2,6,6-tetramethyl-3,5-heptanedionato lithium (98%, Sigma Aldrich), in molar ratio 1 to 3, are premixed under an inert gas atmosphere, and then transferred into a gas evaporation chamber where they are evaporated using the CO_2 laser. The precursor vapor mixture is carried to the substrate using an argon gas flow, and an oxygen gas flow is introduced shortly before the vapor reaches the heated substrate [103]. For more detailed information about the synthesis procedure and setup refer to the work of Loho et al. [103]. LA-CVD allows for the deposition of dense, homogeneous LCO films over a temperature range from 600 °C to 800 °C [103]. Since the LLZO pellet is used as a substrate and changes to its microstructure and composition need to be minimized during deposition, the temperature is set to 700 °C using an infrared laser and a pyrometer for temperature control. The relatively high temperature assures the formation of a good contact between the solid electrolyte and thin film cathode, while preventing Li loss from the substrate material. The reactivity between the two materials, which might occur at higher temperatures, is limited. Additionally, the LLZO pellet is cut into two halves. Only one half is coated with a 10 nm thick Nb layer using a sputter coater at 30 mA for 50 s, while the second is used as an uncoated reference. The two halves of the pellet are fixed in a stainless steel sample holder for simultaneous deposition of the LCO film. After deposition the samples are measured using X-ray diffraction. They then are placed in an Ar-filled glovebox for contacting with the Li anode as described in section 6.2.2. The cells are then placed in Swagelok type cells for electrochemical characterization. After galvanostatic cycling and cyclic voltammetry the samples are broken manually for cross-sectional SEM imaging.

8.1.2 Phase composition

The as-synthesized powder composed of $La_{0.5+\partial}Zr_{0.5-\partial}O_{1.75-\partial/2}$ and Li_2CO_3, synthesized using NSP at 900 °C is calcined under an Ar atmosphere at 950 °C for 1 hour. After calcination a powder composed of a mixture of the cubic and the tetragonal garnet phase is obtained. As previously described in section 5.1, the calcination atmosphere presents a great impact on the phase composition of the ceramic. The detected tetragonal phase is most probably due to a high occupancy of the Li sites, since the Ar atmosphere reduced the loss of Li from the garnet structure during calcination. No impurity phases are detected for the calcined powder, except a small amount of Li_2ZrO_3. Sintering of the ceramic is conducted using FAST at 950 °C for 3 min at a pressure of 30 MPa. The resulting relative density is approximately 93% TD, which is calculated geometrically. The sintered ceramic is measured on both sides of the pellet and the corresponding X-ray diffraction patterns are shown in Figure 8-2. A cubic garnet structure is observed in addition to the distorted tetragonal phase exhibiting a higher microstrain. A minor $La_2Zr_2O_7$ impurity phase is detected in account for the Li loss during sintering, the corresponding phase fraction calculated using Rietveld refinement is negligible. After the cathode deposition X-ray diffraction patterns are recorded for both samples with and without Nb interlayer. Both patterns show identical structure, since the Nb coating is only 10 nm thick and its influence is below the detection limit of this measurement. The (0 0 3)-reflection of the high temperature $LiCoO_2$ ($R\bar{3}mh$) thin film is clearly visible. After coating an additional reflection is detected at approximately 24°, which belongs to an unidentified phase.

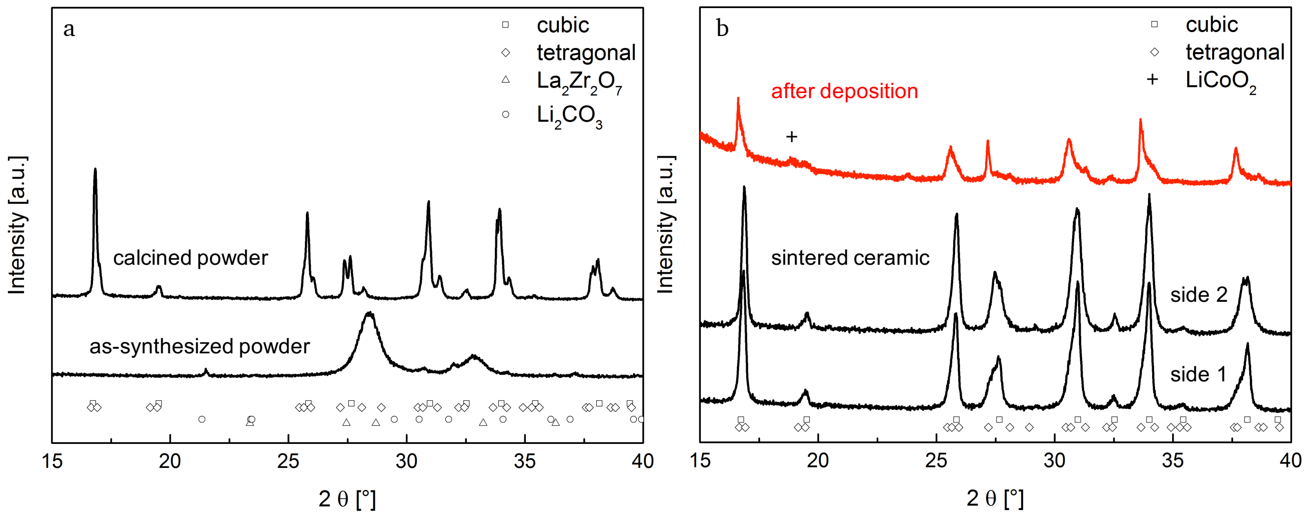

Figure 8-2: X-ray diffraction patterns of the as-synthesized and calcined powder at 950 °C for 1 hour under Ar (a) and of the sintered ceramic measured on both sides of the pellet before and after Nb/LCO films deposition (b), + marks the (0 0 3)-reflection of the textured $LiCoO_2$ film. The symbols represent Bragg's positions of each phase present.

Rietveld refinement is conducted for the patterns corresponding to the calcined powders and sintered ceramics before and after coating. The values are presented in Table 8-1. The phase fractions for the sintered ceramic are mean values calculated from the refinement of both sides of the pellet. Rietveld refinement is carried out using a preferred orientation model in (0 0 l)-direction for the distorted tetragonal phase, which is described in more detail in section 7.2.2.1. The G value increases after coating the sample with $LiCoO_2$ from 1.27 to 1.32, while the microstrain present in the distorted tetragonal phase decreases from 0.27 to 0.11. The microstrain of the cubic phase on the other hand increases after coating. Additionally, the c/a ratio of the distorted tetragonal phase after LCO deposition is reduced to 0.970, which is the value calculated for the tetragonal phase of the calcined powder. Evidently, the LA-CVD process, which involves heating the LLZO ceramic to 700 °C under an atmosphere containing a mixture of Ar and O_2 influences the microstructure and therefore has a great chance of altering the electrochemical performance of the solid electrolyte. A detailed study to understand this phenomenon is needed to be able to optimize the film deposition process, while maintaining or enhancing the performance of the solid electrolyte. This is beyond the scope of the present study.

Table 8-1: Rietveld refinement data for calcined powder and sintered ceramic before and after deposition of Nb/LCO films.

Sample	Phase	Phase fraction [wt.%]	Unit cell volume [Å^3]	Microstrain	c/a
Calcined	cubic garnet	51.5(2)	2189.62(16)	0.069(6)	1
	tetragonal g.	47.5(2)	2181.54(20)	0.062(5)	0.972
	Li_2ZrO_3	0.96(19)	-	-	-
Before deposition	cubic garnet	44.5(2)	2176.03(28)	0.136(9)	1
	tetragonal g.	55.2(2)	2195.59(90)	0.265(2)	0.982
	$La_2Zr_2O_7$	0.33(2)	1199.6(25)	-	1
After deposition	cubic garnet	28.0(2)	2178.7(16)	0.262(56)	1
	tetragonal g.	69.9(4)	2178.86(88)	0.112(22)	0.970
	$LiCoO_2$	2.06(67)	100.63(24)	-	4.909

8.1.3 Cycling behavior

The full all-solid-state cells with and without a Nb interlayer between the $LiCoO_2$ thin film cathode and the solid electrolyte are placed in Swagelok type connections, where the cells are fixed using a spring without additional pressure. After a resting step for 24 hours for the cells to reach electrochemical and thermal equilibrium, 5 cycles of galvanostatic cycling are performed at 500 nA between 3 V and 4.2 V vs. Li/Li^+. Cyclic voltammetry is performed before the current is again set to 500 nA for further 10 cycles and reduced to 250 nA for 10 additional cycles. A calculation of the C-rate would be highly inaccurate, since the volume of the cathode layer can only be roughly estimated. All cycling experiments are performed at 25 °C using a temperature cabinet to maintain a constant temperature. Figure 8-3 shows the galvanostatic cycling behavior of both LCO|LLZO|Li and LCO|Nb|LLZO|Li cells.

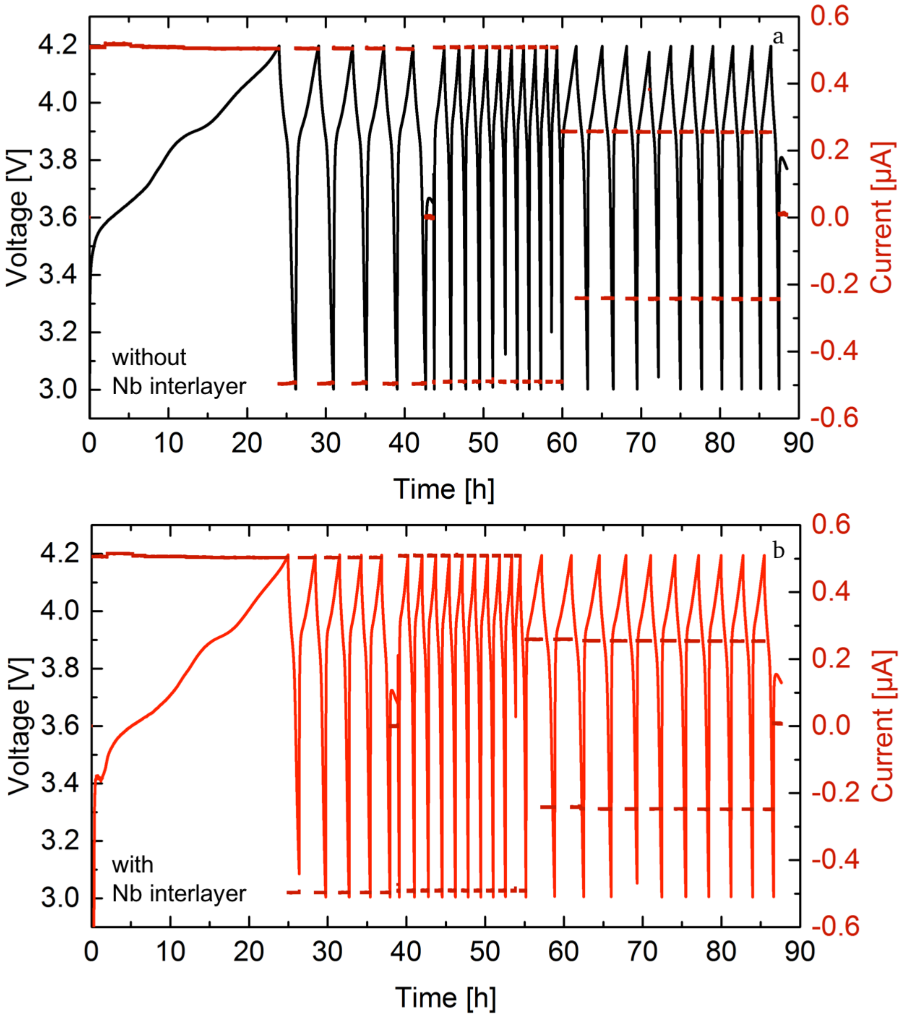

Figure 8-3: Galvanostatic cycling of LCO|LLZO|Li (a) and LCO|Nb|LLZO|Li (b) cells at 500 nA and 250 nA in the potential range between 3 V and 4.2 V vs. Li/Li^+ for a total of 25 cycles at 25 °C.

As shown in Figure 8-4, the first charging step of both all-solid-state cells shows two plateaus; the first at 3.6 V and the second at 3.9 V. The first plateau corresponds to a non-reversible reaction occurring at the interface between $LiCoO_2$ and LLZO and it is independent of the presence of a Nb interlayer. It has to be noted, that Li_2CO_3 is formed during the cathode deposition as an intermediate product due to the reaction of the carbon containing Li precursor with oxygen gas [103]. Since the deposition temperature is set to 700 °C Li_2CO_3 might have not completely decomposed, residing at the interface between $LiCoO_2$ and LLZO. It is very likely that a non-reversible decomposition is taking place at the interface creating Li_2O and CO_2 gas. This process effectively increases the cell impedance during the first charging process leading to the plateau at 3.6 V. The second plateau at 3.9 V is expected and it is related to the delithiation of the active material during the charging process [107]. During the first discharge the 3.9 V plateau is reversible and stable, yet less pronounced throughout 25 cycles, shown in Figure 8-3, while the 3.6 V plateau is not detected already during the first discharge process. The cell containing a Nb interlayer shows a voltage drop at approximately 3.4 V, which is most probably related to an additional reaction taking place at the interface involving Nb. This is also a non-reversible reaction, observed only during the first charging step and its reproducibility needs to be confirmed.

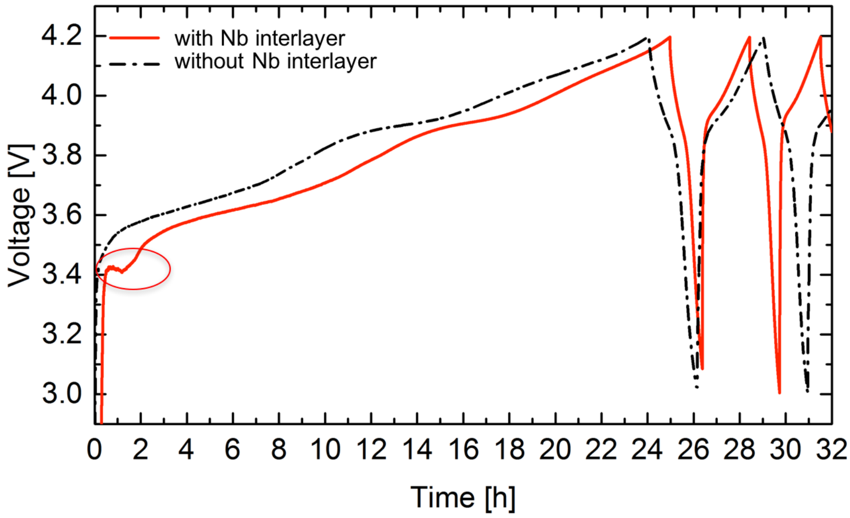

Figure 8-4: First cycles of the galvanostatic charge and discharge at 500 nA in the potential range between 3 V and 4.2 V vs. Li/Li^+ of the all-solid-state LCO|Nb|LLZO|Li (voltage drop at 3.4 V is marked) and LCO|LLZO|Li cells.

After performing stable galvanostatic cycling for approximately 40 hours, cyclic voltammetry is performed comparing both all-solid-state cells with and without the Nb interlayer. As it is shown in Figure 8-5 both cells show reversible cycling behavior for additional 5 cycles with a cycling rate of 0.1 mV s^{-1} at 25 °C. The maximum of the oxidation peak corresponding to the de-intercalation of Li from the $LiCoO_2$ layered structure is shifted to an approximately 0.2 V higher potential in the LCO|Nb|LLZO|Li cell. The reduction peak is slightly shifted to a lower potential compared to the LCO|LLZO|Li cell, which leads to a higher overpotential of 0.35 V in the LCO|Nb|LLZO|Li cell compared to an overpotential of 0.12 V for the LCO|LLZO|Li cell. This might indicate a higher interfacial resistance for the cell containing a Nb interlayer. Additionally, the current observed during the charging process is higher than the one observed during discharge. A possible reason for this asymmetry of the cyclic voltammograms is the reduced kinetics during lithiation of the cathode compared to its delithiation at the chosen cycling rate.

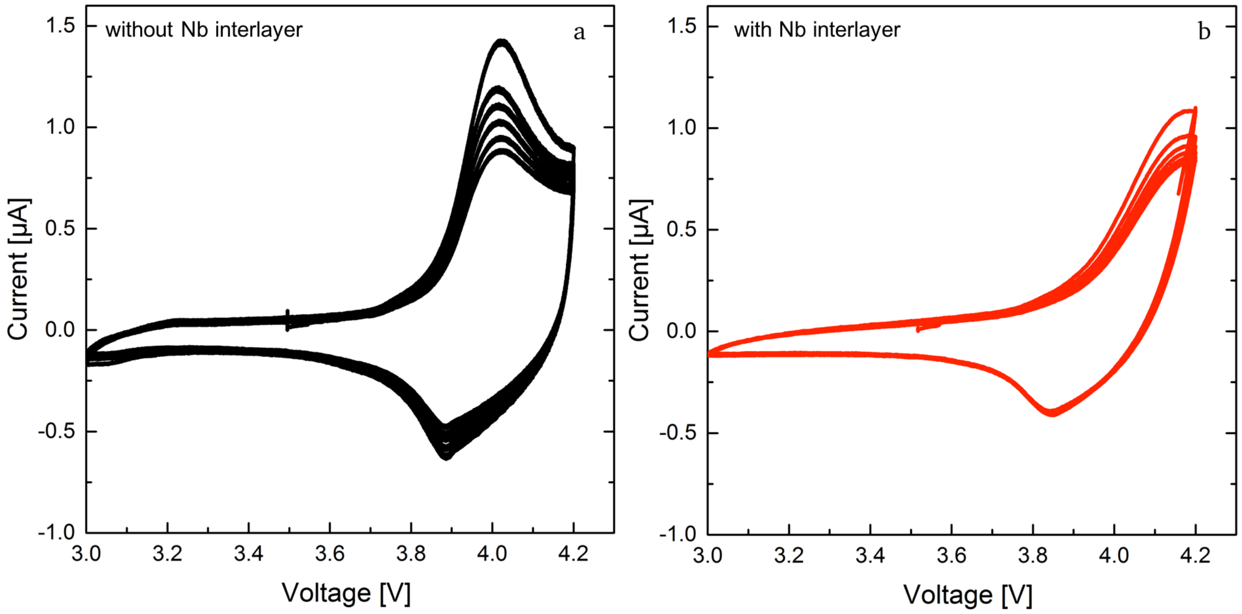

Figure 8-5: Cyclic voltammograms of LCO|LLZO|Li (a) and LCO|Nb|LLZO|Li (b) cells with a cycling rate of 0.1 mV s^{-1} at 25 °C in the potential range between 3 V and 4.2 V, obtained after cycling for 5 galvanostatic cycles.

The introduction of a Nb interlayer results in a reduction of the chemical interaction between $LiCoO_2$ and LLZO by in-situ formation of amorphous $LiNbO_3$ as the desired interphase between the cathode and solid electrolyte. According to literature this is achieved by annealing the Nb coated solid electrolyte at 600 °C for 2 hours under oxygen [101]. This procedure is not followed in this study, since annealing under an oxygen containing atmosphere is expected to alter the LLZO ceramics sintered using field assisted sintering and thereby influencing the electrochemical performance (see section 7.3), but it can be assumed that the LLZO|Nb interface undergoes a similar annealing step during LA-CVD, where it is heated up to 700 °C under an oxygen containing atmosphere. The possible in-situ formation of a $LiNbO_3$ interphase does not deliver the optimal composition and/or structure, which would explain the increase in overpotential of the cell with a Nb interlayer.

8.1.4 Microstructure

After cycling of the all-solid-state battery cell it is broken manually for imaging. Cross sectional scanning electron micrographs of the cathode and anode sides are shown in Figure 8-6. The thickness of the $LiCoO_2$ film is smaller than 1 μm, which is expected from the previous studies [103]. A good coverage of the LLZO pellet is achieved using the LA-CVD method for the cathode material and the melting method using a soldering iron for Li metal as the anode. Since imaging is performed after cycling the observed delamination near the LCO|LLZO interface is either due to cycling or due to the preparation of the pellet for imaging.

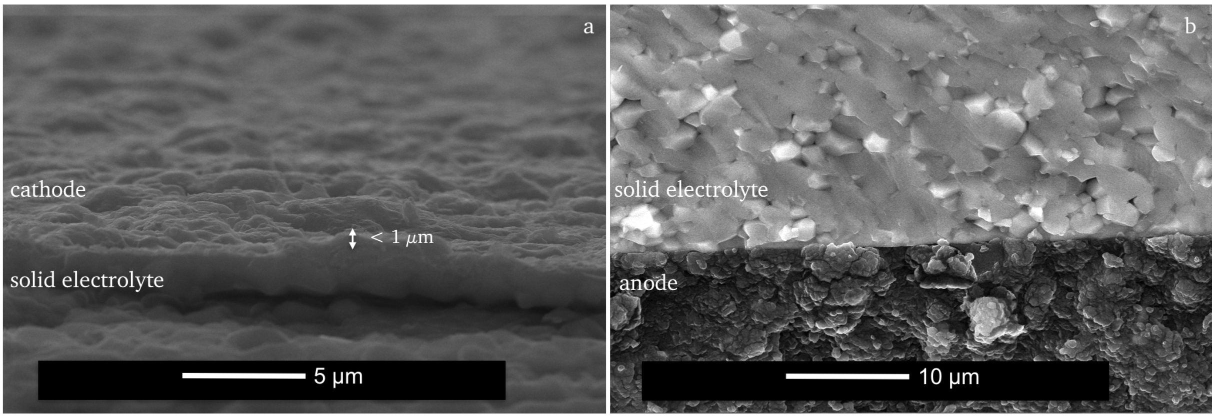

Figure 8-6: SEM cross sectional micrographs of the all-solid-state cell taken after cycling at cathode (a) and anode side (b).

An all-solid-state battery cell is successfully prepared combining LLZO bulk ceramic with a $LiCoO_2$ thin film cathode and a Li metal anode. A relatively high deposition temperature during the LA-CVD process (700 °C) allows for a good contact between the cathode and solid electrolyte, while the short deposition time (15 min) [103] and the small $LiCoO_2$ amount in contact with the LLZO ceramic limits the chemical interaction between LLZO and $LiCoO_2$, which is reported in reference [101] and presents a challenge for achieving a bulk all-solid-state cell.

8.2 Bulk composite cathode processing by FAST

On a quest to achieve a bulk full-solid-state Li-ion battery the biggest challenge is manufacturing an optimal interface between the cathode and the solid electrolyte, minimizing the chemical interaction between the respective components and optimizing the charge transfer resistance. Field assisted sintering is expected to overcome these challenges. Since the sintering process under the application of a direct current electric field allows for the use of lower temperatures (< 600 °C) than during conventional sintering techniques as well as during hot pressing, the chemical interaction between $LiCoO_2$ cathode material and $Li_{7-3x}La_3Zr_2Al_xO_{12}$ solid electrolyte could possibly be minimized. Additionally, the technique could allow for a good contact not only between the cathode and the solid electrolyte but also good contact between particles within the cathode independent of their chemical composition due to the simultaneous application of a direct current electric field and pressure. This can be advantageous when manufacturing a composite cathode material containing $Li_{7-3x}La_3Zr_2Al_xO_{12}$, $LiCoO_2$ and carbon black, leading to an increase in contact points between the solid electrolyte and the active cathode material not only on the surface of the ceramic pellet but also within the cathode.

The $Li_{7-3x}La_3Zr_2Al_xO_{12}$ ceramic, with $x = 0.22$ and 30 wt.% Li-excess during synthesis, used for this study is synthesized combining NSP and FAST, achieving a total ionic conductivity of 0.43 mS cm^{-1} and an activation energy of 0.35 eV, which is a suitable performance for the application in a bulk all-solid-state battery cell operated at room temperature.

8.2.1 Cathode processing

The composite cathode (CC) is processed using $LiCoO_2$ commercial powder (Sigma-Aldrich, 442704) as active material with a particle size between 2 μm and 15 μm, $Li_{7-3x}La_3Zr_2Al_xO_{12}$ calcined powder with an Al-content $x = 0.22$ and a Li-excess during synthesis of 30 wt.% and carbon black (Sigma-Aldrich, 699624) with a particle size <500 nm. $LiCoO_2$ and carbon black in a mass ratio of 5:1 are ball milled at 300 rpm for 10 min. To obtain $Li_{7-3x}La_3Zr_2Al_xO_{12}$ powder, the as-synthesized powder is calcined at 1000 °C for 1 hour under an Ar atmosphere. During calcination the initial mass of the as-synthesized powder decreases by approximately 20%, see section 5.1, leading to 520 mg of $Li_{7-3x}La_3Zr_2Al_xO_{12}$ powder, which is added to the LCO/carbon black mixture. The final mass ratio of the components of the composite electrode is 5:5:1 for LCO, $Li_{7-3x}La_3Zr_2Al_xO_{12}$ and carbon black. The composite electrode powder is ball milled using Retsch PM100CM planetary ball mill at 300 rpm for 20 min under an Ar atmosphere in a zirconia jar with a volume of 50 ml. The ball to powder mass ratio is approximately 28:1. The composite powder is then added on both sides of the sintered pellet to achieve a homogeneous electric field and temperature distribution to both sides of the symmetrical cell. After the first sintering step at 400 °C and 25 MPa for 10 min under vacuum (10^{-2} mbar), the graphite die is turned to effectively switch the direct current electric field for the second step where the sintering process is repeated. The switching of the electric field is of great importance, since previous experiments have shown that otherwise only one side of the electrolyte pellet has been attached to the composite electrode.

8.2.2 Phase composition

The X-ray diffraction patterns for the as-synthesized, calcined as well as the ceramic pellet measured on both sides are shown in Figure 8-7. The surface of the composite cathode is measured after the electrochemical characterization. The as-synthesized powder is mainly composed of $La_{0.5+\partial}Zr_{0.5-\partial}O_{1.75-\partial/2}$ and Li_2CO_3. During calcination at 1000 °C for 1 h under a flowing Ar atmosphere a phase transformation into the cubic garnet structure takes place with additional minor impurity phases of $La_2Zr_2O_7$ and Li_2ZrO_3. After sintering at 950 °C for 3 min at a pressure of 30 MPa under vacuum, the ceramic shows a mixture of cubic and distorted tetragonal structure with a higher microstrain and a larger unit cell volume than the cubic phase. The c/a ratio for the distorted phase is 0.986. The impurity phases of the calcined powder are also present in the sintered ceramic. The inset shows a photograph of the half-cell after removing one electrode layer by polishing. The blue discoloration of the solid electrolyte indicates a chemical reaction taking place during co-sintering already at 400 °C, which most probably involves the formation of a Co^{2+} containing compound. After performing electrochemical experiments, the surface of the composite cathode shows $LiCoO_2$ ($R\bar{3}m$) to be the main phase fraction. A preferred orientation model in (0 0 l)-direction is used for fitting the $LiCoO_2$ pattern with a parameter G of 0.703, which leads to a R_{wp} value of 4.551% compared to 5.678% without the preferred orientation model commonly found for $LiCoO_2$ films [105]. The goodness of fit (GOF) is calculated to 1.03. The phase fractions of the solid electrolyte, including the cubic garnet structure and a $La_2Zr_2O_7$ impurity phase, and the $LiCoO_2$ active material are in good agreement with the mass ratios used for the composite cathode. The details of the Rietveld refinement are shown in Table 8-2.

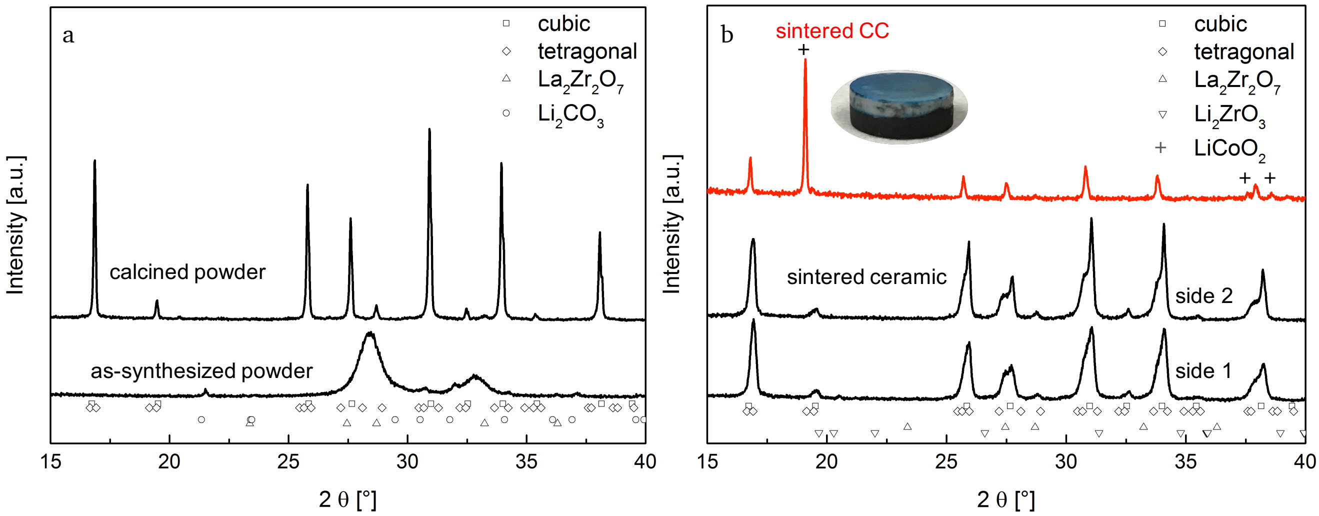

Figure 8-7: X-ray diffraction patterns of the as-synthesized and calcined powder at 1000 °C for 1 hour under Ar (a) and of the sintered ceramic measured on both sides of the pellet and of the sintered composite cathode, inlay shows a photograph of the half-cell (diameter approx. 7 mm) after removing one electrode (b). The symbols represent Bragg's positions of each phase present.

Table 8-2: Rietveld refinement data for calcined powder and sintered LLZO ceramic (electrolyte) and sintered composite cathode.

Sample	Phase	Phase fraction [wt.%]	Unit cell volume [Å^3]	Microstrain	c/a
Calcined powder	cubic garnet	95.83(24)	2187.997(58)	0.028(1)	1
	$La_2Zr_2O_7$	3.023(43)	1269.51(30)	0.07(3)	1
	Li_2ZrO_3	1.14(24)	-	-	-
Electrolyte	cubic garnet	41.28(21)	2176.29(24)	0.085(8)	1
	tetragonal g.	57.34(23)	2209.6(11)	0.331(13)	0.987
	$La_2Zr_2O_7$	0.891 (22)	1263.5(9)	0.085(8)	1
	Li_2ZrO_3	0.495(23)	-	-	-
Composite cathode	cubic garnet	46.91(75)	2218.98(37)	0.080(8)	1
	$La_2Zr_2O_7$	1.098(32)	1268.8(18)	0.080(8)	1
	$LiCoO_2$	51.99(77)	96.434(17)	0.05(2)	-

8.2.3 Cycling behavior

Galvanostatic cycling is carried out at a current of 12 μA, corresponding to a current density of approximately 31 μA cm^{-2}, between 3.2 V and 4.2 V vs. Li/Li$^+$. The result is shown in Figure 8-8. The first charging is complete within 32 seconds, while the whole cycling experiment is terminated within only 53 seconds. No discharge of the composite cathode is observed. The lack of cyclability is most probably due to the poor quality of the interface between the solid electrolyte and the composite cathode.

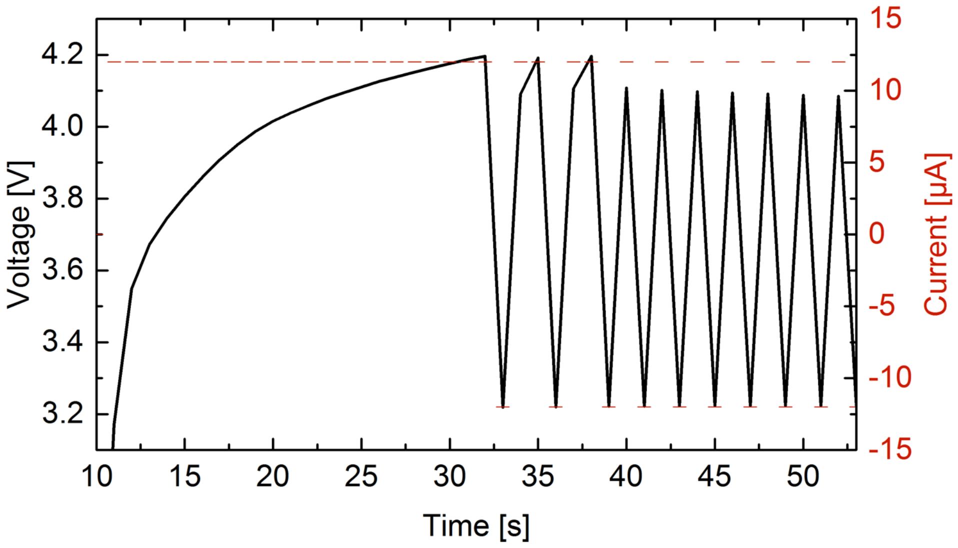

Figure 8-8: Galvanostatic cycling of CC|LLZO|Li cell at 12 µA in the potential range between 3.2 V and 4.2 V vs. Li/Li$^+$ for a total of 10 cycles at 25 °C.

To confirm the result from the galvanostatic cycling and to exclude high rate cycling, which might lead to poor cycling performance, cyclic voltammetry is carried out at a rate of 0.1 mV s^{-1} in the potential range between 3 V and 4.5 V vs. Li/Li$^+$. The resulting cyclic voltammograms are presented in Figure 8-9. Two oxidation peaks are observed in the first cycle at 3.7 V and 4.2 V vs. Li/Li$^+$, while no reduction processes are observed during discharge. Starting the second cycle the current drops drastically and the oxidation reactions are no longer observed. This result indicates that during the first charging step an irreversible oxidation reaction is taking place, which might be at the cathode-electrolyte interface or within the composite cathode. The subsequent cyclic voltammograms might represent the formation of a double layer during charging near the cathode-electrolyte interface due to the high interfacial resistance.

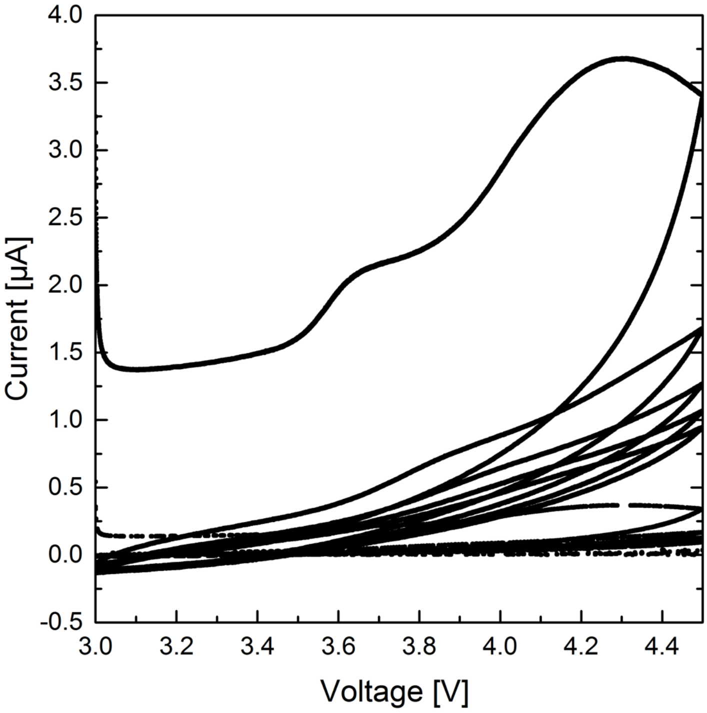

Figure 8-9: Cyclic voltammograms of CC|LLZO|Li cell obtained at a scan rate of 0.1 mV s^{-1} at 25 °C for 10 cycles in the potential range between 3 V and 4.5 V vs. Li/Li^{+}.

AC-impedance spectroscopy is performed before and after cycling of the CC|LLZO|Li cell. The corresponding Nyquist plots are compared to the plot for the ceramic electrolyte with two blocking Au-electrodes, Figure 8-10. The spectrum of the electrolyte with blocking electrodes is fitted using R(R CPE)(R CPE)CPE equivalent circuit, where R is the first intercept with the real axis, corresponding to the bulk resistance, the first (R CPE) segment represents the grain boundary contribution to the spectrum and the second (R CPE) segment is assigned to a surface layer between the electrolyte and the Au-electrodes, whereas the constant phase element CPE simulates the electrode blocking behavior. The plots for the full all-solid-state cell exhibit three separate semi-circles and they are fitted using R(R CPE)(R CPE)(R CPE)CPE equivalent circuit, where the first high frequency semi-circle is attributed to the grain boundary contribution of the solid electrolyte as it is in good agreement with the spectrum recorded with blocking electrodes. The second and the third semi-circles however correspond to the charge transfer between the solid electrolyte and the composite cathode on one side and the solid electrolyte and the Li anode on the other side. The blocking behavior observed, indicates the poor contact between the composite cathode and solid electrolyte. Comparing the spectra before and after discharge, the first semi-circle remains unchanged, which is expected for the grain boundary contribution, while both semi-circles with their maxima at the frequencies 25 kHz (electrode A) and 10 Hz (electrode B), respectively, show a higher resistance. For electrode A, the resistance increases from 0.45 kΩ (ASR = 178 Ω cm^2) to 0.50 kΩ, (ASR = 197 Ω cm^2) after cycling, while for electrode B it increases from 35 kΩ (ASR = 13.6 kΩ cm^2) to 155 kΩ (ASR = 61.2 kΩ cm^2). If correlated to previous experiments with symmetrical cells with Li electrodes, it is most probable that the semi-circle with the smaller resistance corresponds to the interface between the solid electrolyte and the Li anode, while the semi-circle marked electrode B represents the interface between the solid electrolyte and the composite electrode, with its partially blocking behavior due to the poor contact and the state of charge of the composite cathode, which is expected to be in a discharged state. The interfacial resistance for electrode A is approximately 5 times higher than previously reported for the LLZO|Li interfacial resistance reported in section 6.2.2, which might be due to the chemical interaction between the composite electrode and the solid electrolyte during co-sintering of the symmetrical cell with the composite electrodes on both sides of the ceramic electrolyte. Further details of the fit results of the impedance data are summarized in Table 8-3.

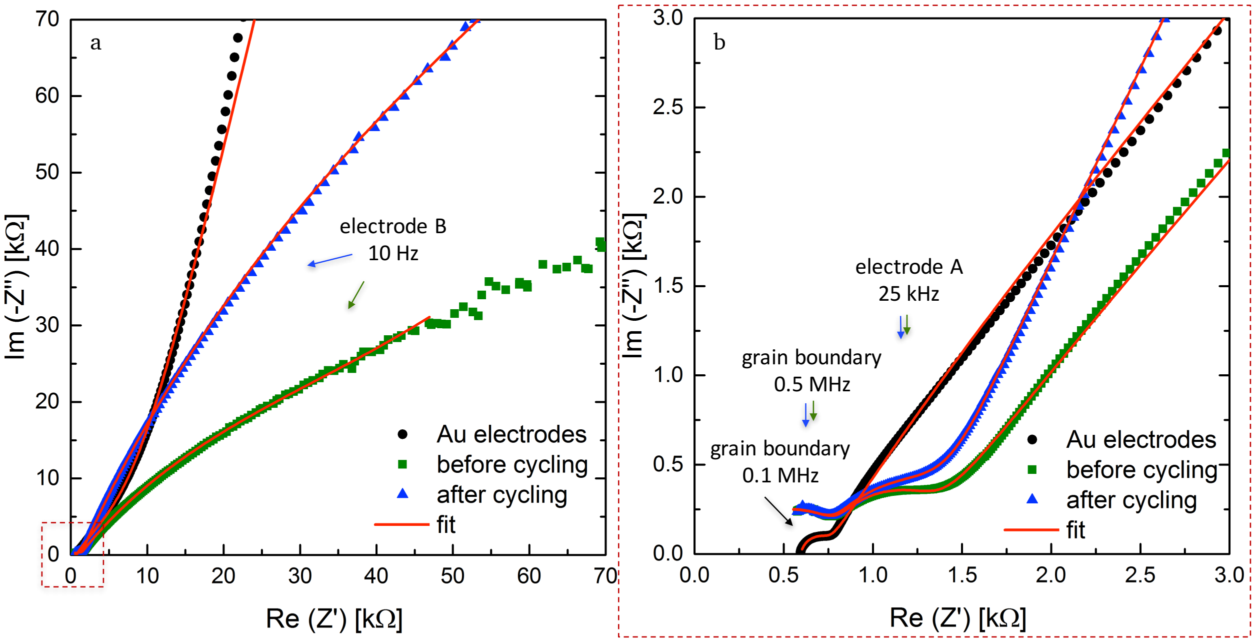

Figure 8-10: AC-impedance spectra and corresponding fits at 298 K with blocking Au-electrodes and full all-solid-state cell with a Li anode (electrode A) and a composite cathode (electrode B) before and after cycling, arrows point to the frequencies at the maxima of the semi-circles (a) and the magnification for the high frequency region (b).

Table 8-3: AC-IS fit results and goodness of fit χ^2 for the measurement of the solid electrolyte with Au-electrodes and the full composite cathode cell, before and after cycling. R: resistance, *Q* and *n*: CPE fit parameters and C: capacitance.

meas.	R_0 [kΩ]	R_1 [kΩ]	Q_1 [nF]	n_1 [-]	C_1 [nF]	R_2 [kΩ]	Q_2 [μF]	n_2 [-]	C_2 [μF]	R_3 [kΩ]	Q_3 [μF]	n_3 [-]	C_3 [μF]	χ^2 10^{-4}
Au el.	0.59	0.12	4.7	1	11	1.8	9.3	0.64	0.98	-	-	-	-	3
before cyc.	0.24	0.55	2.4	0.86	0.30	0.45	0.02	0.97	0.01	34.5	7.7	0.59	3.1	1
after cyc.	0.24	0.55	2.5	0.86	0.28	0.50	0.03	0.92	0.01	155	1.3	0.72	0.69	0.7

8.2.4 Microstructure

The micrographs of the solid electrolyte co-sintered with the composite electrode are shown in Figure 8-11. The microstructural investigation is carried out after cycling, at the cross-section of a manually broken pellet. The cathode composite layer exhibits a porous microstructure. On the cathode side hexagonal rods are observed, that correspond to the expected microstructure of $LiCoO_2$, which is textured in the (0 0 l)-direction. The formation of the textured structure presumably takes place at 400 °C during field assisted sintering, while the solid electrolyte fraction of the composite cathode does not experience observable changes at this low temperature. This leads to weak contacting between the active material and the solid electrolyte and therefore to great ramifications on the electrochemical performance of the composite cathode.

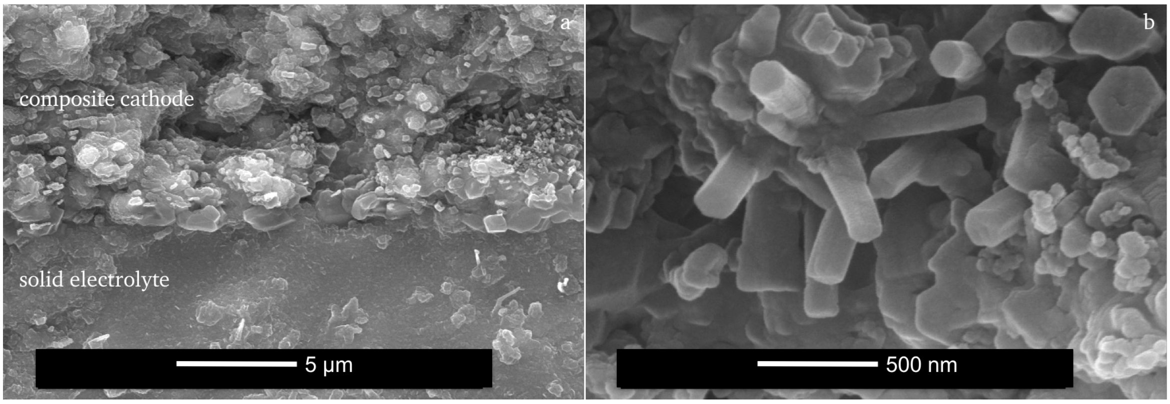

Figure 8-11: Cross-sectional micrographs of the composite cathode and LLZO solid electrolyte ceramic (a) and magnification of the interfacial region showing hexagonal rods (b).

As previously pointed out, the interfacial resistance between the solid electrolyte and the cathode is the biggest challenge facing the assembly of a bulk all-solid-state cell. To achieve a good contact a high temperature is crucial to ensure the sintering of the solid electrolyte pellet to the electrolyte fraction of the composite electrode. Higher temperatures cannot be employed using LCO powder, due to its chemical interaction with $Li_{7-3x}La_3Zr_2Al_xO_{12}$ and morphological instability. Other high voltage cathode materials, which have a better chemical stability in addition to allowing for a higher energy density need to be explored for the combination with the garnet solid electrolyte. The presence of carbon black for electronic conduction also poses a limitation on the processing temperature. As an electronically conducting additive metallic nanoparticles, e.g., silver, could be potentially used as a substitute for carbon black, but of course at a higher cost.

8.3 Slurry-based LCO cathode by conventional printing method

The conventionally used LCO cathode is a slurry-based cathode printed on the Al current collector. Besides the active LCO powder, the slurry also contains polyvinylidene fluoride (PVdF) as a binder, N-methyl-2-pyrrolidone (NMP) as a solvent and carbon black as an electronic conductor. The doctor blade technique is more advantageous for industrial application over the previously described methods and can be implemented in a roll to roll process. Therefore, the aim of this study is to manufacture a bulk Li-ion cell using a slurry-based cathode, $Li_{7-3x}La_3Zr_2Al_xO_{12}$ solid electrolyte and melted Li as an anode. As previously observed the quality of the interface between the solid electrolyte and the cathode is highly dependent on the processing temperature during cathode deposition or co-sintering. The slurry-based LCO cathode does not withstand high temperatures due to the presence of a binder and carbon black, hence a small amount of a 1M $LiPF_6$ solution (LP30, BASF) is utilized to obtain a good contact. The full cell is therefore not an all-solid-state cell, but a hybrid cell delivering some of its advantages compared to a conventional cell with liquid electrolyte and a separator. The first is the elimination of the contact between liquid electrolyte and Li anode, which is known to be the reason for increased dendrite formation leading to short circuiting of the conventional cell. The second advantage is the replacement of the separator with an ionically conductive ceramic, which has a high charge carrier selectivity and furthermore is electronically insulating. In addition, it shows a high thermal stability, which is an important requirement to ensure safety [108]. Optimization of the thickness of the solid electrolyte can lead to a decrease of the cell resistance and an increase of the energy density of the cell. Additionally, only a fraction of the liquid electrolyte is needed to ensure the contact between the solid electrolyte and the cathode layer. The $Li_{7-3x}La_3Zr_2Al_xO_{12}$ ceramic, with $x = 0.22$ and 30 wt.% Li-excess during synthesis, used for this study is synthesized combining NSP and FAST. The sintering process is carried out at 950 °C, under a pressure of 50 MPa under an Ar atmosphere, achieving a total ionic conductivity of 0.42 mS cm^{-1} and an activation energy of 0.37 eV. Compositional and microstructural characteristics are previously reported in section 7.2.2.

8.3.1 Cathode processing

The slurry-based cathode has a mass ratio of 8:1:1 of $LiCoO_2$ (Sigma-Aldrich), carbon black (Sigma-Aldrich, 699624) and PVdF (SOLEF). After weighing the powders of the active material and carbon black a solution composed of 10 wt.% of PVdF and 90 wt.% of NMP (BASF) is added to the powder mixture. An excess of NMP is added (approximately 30 wt.% of the active material) reducing the viscosity of the slurry. A high-performance dispersing instrument T25 digital Ultra-Turrax (IKA) is used in subsequent intervals of 5 min at 8000 rpm, a 2 min break, followed by 10 min stirring at 8000 rpm for the preparation of the slurry. In the following 5 min break NMP is added to the slurry ensuring optimal viscosity for homogeneous stirring. The stirring intervals are then repeated, followed by addition of NMP. The process is repeated three times. The total amount of NMP added during stirring is 3 times the mass of the active material. The slurry is then printed on an Al foil using a doctor blade technique with an approximate thickness of 120 μm. The electrode is then placed in an oven set to 40 °C for approximately 24 hours during which the evaporation of NMP takes place. After the drying process, the cathode with a diameter of 6 mm is formed using a puncher and transferred to a vacuum oven inside an Ar-filled glovebox and dried further at 100 °C for 12 hours.

The cathode printed on the Al current collector is placed in a Swagelok type connection and covered with $LiPF_6$ based liquid electrolyte. After ensuring a complete immersion of the cathode layer, excess liquid is removed. The ceramic pellet with a Li anode and Cu current collector already attached is placed on the liquid immersed cathode and the cell is firmly sealed. The roughness of the ceramic pellet surface towards the cathode is increased using polishing paper with a grit size of 600. This step is crucial to enhance cathode adhesion and liquid electrolyte penetration of the ceramic electrolyte surface. A reference cell is assembled using the slurry-based LCO cathode, the liquid electrolyte, a monolayer polypropylene separator membrane (Celgard), and a Li foil as an anode. The assembled cells are stored in a temperature cabinet for approximately 12 hours at 25 °C in order to ensure thermal and electrochemical equilibrium prior to cycling.

8.3.2 Cycling behavior

Cyclic voltammetry is performed between 3.2 V and 4.2 V vs. Li/Li$^+$ at a rate of 0.05 mV s^{-1}. The resulting voltammograms are shown in Figure 8-12. The reference cell composed of the slurry-based LCO cathode, $LiPF_6$ liquid electrolyte, a separator and a Li anode shows three oxidation peaks at 3.95 V, 4.1 V and 4.2 V. The first peak corresponds to the two-hexagonal phase region, while the next two peaks are attributed to a phase transition between the ordered and disordered Li-ion arrangement in the CoO_2 framework occurring around a composition $Li_{0.5}CoO_2$ [109]. All three oxidation reactions are reversible. The overpotential is approximately 50 mV. The maximum current achieved in the first cycle decreases in the following three cycles and seems to stabilize at the fifth cycle. During discharge a decrease in 3.6 V-plateau efficiency is observed for the reference cell, indicating an increase of the cell impedance during the first four cycles. On the other hand, the cell containing a solid electrolyte shows a good 3.6 V-plateau efficiency, which is stable throughout all five cycles. The oxidation peaks for this cell are not clearly separated and show a maximum current at 4.05 V, which is shifted to a 100 mV higher potential compared to the reference cell. The reduction peaks on the other hand are observed clearly in the first cycle, confirming reversible cycling with an overpotential of approximately 200 mV, which is four times higher than observed for the reference cell. Although the maximum current achieved in the first cycle is higher than for the reference cell, starting the second cycle continuous fading of the current is observed. It is evident that the kinetics in the cell containing a solid electrolyte are slower, when compared to the reference cell. Therefore, slower cycling rates and a higher cutoff potential might allow for more accurate detection of the occurring redox reactions.

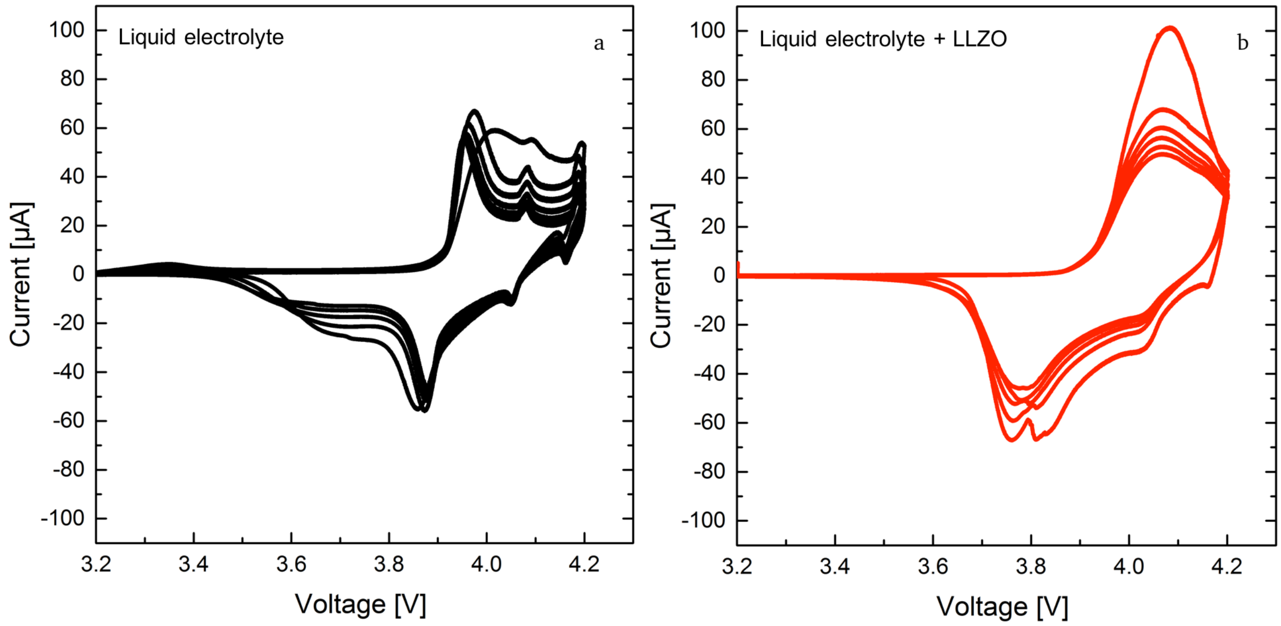

Figure 8-12: Cyclic voltammograms of LCO|$LiPF_6$|Li cell (a) and LCO|$LiPF_6$|LLZO|Li cell (b) performed at a scan rate of 0.05 mV s^{-1} at 25 °C for 5 cycles in the potential range between 3.2 V and 4.2 V vs. Li/Li$^+$.

As it is shown in Figure 8-13 galvanostatic cycling is performed for both cells using two currents, 15 μA and 21 μA, which correspond to a C/5 and a C/4 rate, respectively. The calculation considers the theoretical capacity expected for the voltage range from 3.2 V to 4.2 V vs. Li/Li$^+$ and the mass of the active material, LCO, leading to a theoretical discharge capacity of 100 mAh g^{-1}. These currents are chosen according to the previous experiments for symmetrical cells with Li electrodes, where cycling is expected to be stable. The first 15 cycles at the lower current show stable cycling for both cells. Stable cycling is observed after increasing the current for further 5 cycles for both cells. The current increase did not have significant ramifications on the reference cell and it is cycled for further 15 cycles, while the cell containing the solid electrolyte could not be cycled at the initial current. In total the reference cell could be cycled 35 cycles for 195 hours, while the cell with LLZO as a solid electrolyte could be cycled only 20 cycles for the duration of 120 hours. It has to be noted at this point that the Li anode of the hybrid cell, unlike the reference cell, has been previously cycled in a symmetrical cell configuration (see section 7.2.2.4), therefore, the failure of the cell after application of a higher current is most probably related to the degradation at the solid electrolyte-anode interface.

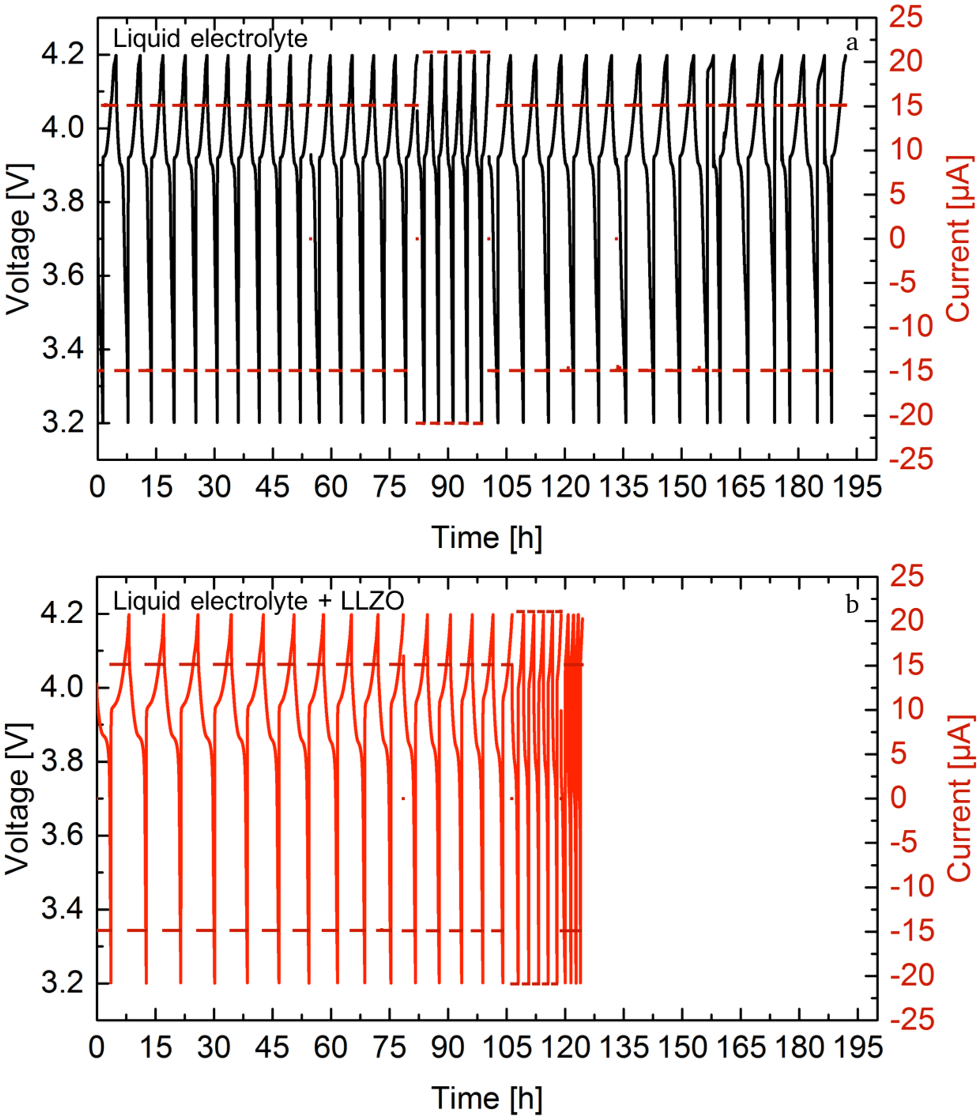

Figure 8-13: Galvanostatic cycling of the reference LCO|LiPF$_6$|Li cell (a) and the hybrid cell LCO|LiPF$_6$|LLZO|Li cell (b) at 15 µA and 21 µA in the potential range between 3.2 V and 4.2 V vs. Li/Li$^+$ at 25 °C.

The detailed features of the first galvanostatic charge and discharge cycle of both, the hybrid and the reference cell, are presented in Figure 8-14. The first discharge cycle of the galvanostatic cycling shows an internal resistance drop (IR drop) of 10 mV for the hybrid cell, while for the reference cell no IR drop is observed. The voltage drop corresponds to a resistance of 666 Ω, which is in the same range of the total resistance of the solid electrolyte. This resistance can be lowered by reducing the thickness of the solid electrolyte. Apart from the IR drop the hybrid cell shows a better performance than the reference cell concerning the previously mentioned 3.6 V-plateau efficiency, which is also evident from the galvanostatic measurements throughout the entire cycling time. Additionally, the discharge capacities for the first cycle from 4.2 V down to 3.2 V vs. Li/Li^+ are calculated to be 84 mAh g^{-1} and 58 mAh g^{-1} for the hybrid cell and the reference cell, respectively. These values indicate that the hybrid cell allows for the discharge of a larger amount of the active material on the cathode side. This might be related to the high surface roughness of the solid electrolyte and the higher, more uniform, pressure applied when using a ceramic electrolyte as opposed to the flexible separator as in the reference cell. The calculated Li amount which is cycled in two hours is $8.67 \cdot 10^{-7}$ mol and $1.67 \cdot 10^{-6}$ mol for the reference and hybrid cell, respectively. The discharge capacity continues fading for both cells reaching 97% and 93% during the second discharge for the hybrid and reference cell, respectively.

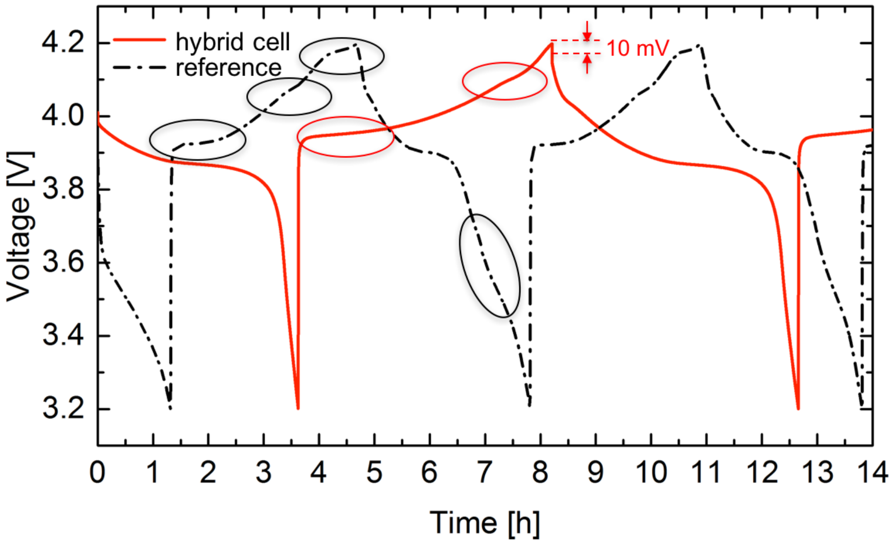

Figure 8-14: First cycles of the galvanostatic charge and discharge at 15 µA of the hybrid $LCO|LiPF_6|LLZO|Li$ cell and the reference $LCO|LiPF_6|Li$ cell, the voltage plateaus during the first charging step, as well as the 3.6 V-plateau during discharge for the reference cell are marked.

Great improvements of the bulk hybrid cell are needed, yet this result is proof that this cell design offers the possibility of reversible cycling. Additionally, it is shown that a charge transfer between $LiPF_6$ liquid electrolyte and LLZO ceramic electrolyte is possible, paving the way to a Li-ion battery that overcomes the safety issues and delivers the advantages of the integration of a solid electrolyte.

8.4 Conclusion and summary

Three approaches for battery design were presented in an attempt to overcome the high charge transfer resistance between the solid electrolyte and the cathode material, which remains the greatest challenge in the production of a full all-solid-state battery cell. The first approach where a thin film LCO cathode layer was deposited using LA-CVD at 700 °C results in stable cell performance, making it the first reported all-solid-state cell containing Al-doped LLZO as a solid electrolyte to be cycled for 30 galvanostatic and cyclic voltammetry (scan rate 0.1 mV s^{-1}) cycles at room temperature. The cathode properties were controlled through the deposition process leading to a dense cathode film with high purity insuring a high cathode performance. The deposition temperature is a crucial factor for achieving a good interfacial contact between the solid electrolyte and the thin cathode layer. The chemical interaction between the LCO active material and LLZO was not substantial, probably since the thin film cathode volume is limited.

In the second approach towards achieving a bulk all-solid-state cell the composite cathode containing LCO, LLZO and carbon black was produced using ball milling and a co-sintering process using FAST at 400 °C of a dense LLZO pellet sandwiched between the composite powder. Based on X-ray diffraction and electron microscopy results, the LCO particles contained in the composite cathode grew to form rods with a (0 0 l)-preferred orientation. The composite cathode material was, therefore, morphologically inhomogeneous in addition to its high porosity. Furthermore, the surface of the solid electrolyte pellet, after the removal of the LCO layer, showed a blue discoloration indicating a chemical interaction involving the formation of a Co^{2+} containing compound. The presented characteristics explain the poor cycling performance of the bulk all-solid-state cell. Further optimization is needed to achieve a homogeneous and dense composite cathode. This can only be achieved at high sintering temperatures, since the co-sintering of the active material and the solid electrolyte particles is required. Therefore, the presence of carbon black has to be eliminated and replaced by an electronically conductive oxide or silver particles [78]. In addition to the application of a high temperature to ensure a good contact between the composite cathode particles, a high temperature is also beneficial during co-sintering as it could reduce the interfacial resistance between the cathode and the solid electrolyte. A challenging aspect about the temperature optimization during co-sintering, especially using FAST, is the liquid phase formation of, e.g., Li_2CO_3, which would enhance sinterability but might lead to cracking or the formation of unwanted phases at the interface.

The third approach eliminates a solid-solid interface between the solid electrolyte and the slurry-based conventionally used LCO cathode by addition of a small amount of liquid electrolyte. The liquid electrolyte ensured good charge transfer between the rough surface of the solid electrolyte and the cathode, while it is completely separated from the Li anode, which is melted directly on the smooth solid electrolyte surface. With respect to the cycling performance, the cell containing the solid electrolyte showed superior discharge capacity and 3.6 V-plateau efficiency. On the other hand, after increasing the current during galvanostatic cycling the reference cell showed a longer cycling life. This is most probably due to failure of the Li anode-solid electrolyte interface, since it has been previously cycled as a symmetrical cell Li|LLZO|Li. Nevertheless, this novel approach is a proof of concept that the fabrication of a hybrid cell is a promising alternative to the existing cell designs, but it still requires further optimizations.

9 Concluding remarks and outlook

9.1 Concluding remarks

This work covers the complete processing line from the synthesis to the bulk battery cell integration of LLZO solid electrolyte. The most prominent findings during the course of this study that are crucial for further research are summarized as follows:

The starting point on the road to successful synthesis of LLZO was establishing NSP as a promising synthesis method. Although the as-synthesized powder is merely a precursor, which needed further heat treatment to achieve the desired LLZO phase, the synthesis method provides many advantages some of which are the high yield, scalability and the possibility of nanocrystalline powders that allow low temperatures and short times in subsequent processing steps.

The first method utilized to achieve LLZO ceramics was conventional sintering under air, in a sealed alumina boat. While the sealed boat has proven effective in minimizing the Li loss from the garnet structure, the densities of the pellets did not exceed 60% TD. The low density could be attributed mainly to the low temperature used for the sintering. The hollow spherical microstructure of the as-synthesized powder did not play a major role, since an additional ball milling step, which effectively broke the hollow spheres did not yield a higher density. Nevertheless, a pure cubic garnet structure was achieved with a conductivity value of 4.4 μS cm^{-1}, two orders of magnitude lower than values reported for fully dense cubic LLZO. To achieve higher densities several sintering methods were explored, e.g., two step sintering, hot pressing and field assisted sintering. The latter has proven the most effective and for its application a cubic garnet LLZO powder is needed as a starting material to reduce the sintering temperature and dwell time in order to minimize the Li loss from the garnet structure during sintering. The calcination of the as-synthesized powder was optimized and it was shown that the calcination atmosphere has a significant influence on the phase composition of the calcined powder due to its influence on the Li loss from the garnet structure. A flowing Ar atmosphere led to a composition containing the cubic and the tetragonal garnet structure with a higher Li occupancy, while calcination under static air yielded the cubic garnet structure alongside a Li-free impurity phase $La_2Zr_2O_7$. The Li loss was confirmed by ICP-OES measurements, which leads to the conclusion that in the case of calcination under air Li is lost in the form of volatile Li containing species, whereas in the case of calcination under Ar Li remains present in the solid state. Li might either occupy Li sites in the tetragonal garnet structure or be present in the form of Li_2O, which is not detectable using X-ray diffraction. The optimal calcination parameters were identified to be 900 °C for 1 h under flowing Ar atmosphere. Many factors influence these parameters, e.g., the actual temperature profile of the furnace, the quality of the zirconia crucible and more importantly the total amount of calcined powder. In the initial stage of this work it was possible to determine the Al^{3+} tetrahedral coordination, which proved that it resides on a Li 24d site with heterovalent substitution of 3 Li^+.

NSP and FAST were combined successfully to achieve dense LLZO ceramics with high densities above 93 %TD. In the initial stage of utilizing FAST the as-synthesized powders were calcined under static air achieving mainly a pure cubic structure at an Al doping level of $x = 0.17$. The powder was removed from the furnace at 300 °C to eliminate moisture adsorption and cooled further under an Ar atmosphere. At this stage the ceramics exhibited an ionic conductivity of 3.3 mS cm^{-1}, which is in good agreement with literature values and the characterization of symmetrical cells was made possible. Attaching Li electrodes to both sides of the ceramic pellet posed the next challenge. It was achieved by combining a heating plate to ensure the homogeneous heating of the pellet (approx. 180 °C) and a soldering iron used to melt the Li foil and spread it on the smooth pellet surface. This method led to ASR values comparable to the best reported literature values for pellets with a higher surface roughness. The best ASR reported in this work using this method was 30.7 Ω cm^2, which is amongst the best values reported to date for LLZO. While FAST gave the opportunity for a deeper understanding and thereby the possibility for further optimization of, e.g., the influence of the microstructure on the performance of LLZO, it also initiated new challenges due to the complicated sintering mechanisms taking place in a very short time (3 min) combining temperature, pressure and an electric field, whose influence on electronically insulating materials is still in need of further research. It was shown that after sintering a distorted tetragonal garnet phase with a higher microstrain was formed. At a later stage of this research it became clear that this distortion is dependent on the pressure used during sintering, the higher the pressure the higher the microstrain and the amount of the distorted phase. Additionally, a preferred orientation model had to be applied to adequately simulate the X-ray diffraction data, which showed the orientation of the long lattice parameter to be perpendicular to the surface of the pellet. A detailed mechanism was proposed to explain this finding, which correlates the distortion and its preferred orientation to the radial volume expansion of the ceramic specimen during the dwell time at the highest pressure. The complete release of the pressure at elevated temperatures during cool down and the inevitable residual radial pressure could act to reduce the lattice parameters parallel to the pellet surface and thereby elongation of the lattice parameters, which are perpendicular to the surface, especially in the grain portion near the grain boundary due to enhanced diffusion. It is important to note at this point that this effect might not be limited to this class of materials and that the influence of the pressure on the microstructure, i.e., microstrain has to be taken into account. For ionic conductors an increased microstrain correlated to a distortion of the unit cell may also influence the ion transport as it was shown for LLZO, where an enhancement of the ionic conductivity was proposed due to the presence of microstrain. A reduction of the microstrain by means of heat treatment did in fact reduce the electrochemical performance in the grain boundary region. The electrochemical performance was also reduced after a storage time of 10 months in an Ar filled glovebox, especially in the grain boundary region. X-ray diffraction measurement of the stored pellet showed a release of the microstrain and the elimination of the tetragonal distortion. The decay of electrochemical performance could have been due to the reduced microstrain or residual moisture in the glovebox leading to the formation of LiOH over a long period of time extracting charge carriers from the garnet structure. Heat treatment and storage of the solid electrolyte need to be performed very carefully bearing in mind their influence on the electrochemical performance. During electrode deposition moderate temperatures need to be used and the deposition time should be limited to a few minutes. All components of battery cells containing the moisture sensitive solid electrolyte need to be thoroughly dried before vacuum sealing the cell to ensure a stable performance of a long time period.

Not only does the microstrain seem to have an influence on the electrochemical performance of LLZO but also the grain size, which was varied using an additional ball milling step to both synthesis processes, using conventional sintering and field assisted sintering. For the first synthesis route, where the as-synthesized powder was ball milled a clear enhancement of the electrochemical performance was observed, which was attributed to the increase of the defect concentration during ball milling enhancing the Li-ion mobility. The second synthesis route yielding higher densities and overall higher electrochemical performance, on the other hand, a reduction of the grain size by ball milling the calcined powder led to a decay of the electrochemical performance. A large increase in grain boundary resistance was observed, which indicated that a reduction of the grain size from approximately 2.2 μm to 0.7 μm increased the amount of grain boundaries to a point where their resistance becomes larger than the bulk resistance, thereby reducing the total ionic conductivity. While this finding seems to contradict the enhancement of the ionic conductivity for the first synthesis route, it shows that the synthesis route has a substantial influence on the electrochemical performance of LLZO. Any comparisons between different synthesis routes concerning, e.g., the resulting grain size, have to be reconsidered. A different synthesis route results in a different nature, i.e., composition, structure and microstructure of the grain boundary of the respective ceramic leading to discrepancies in the grain boundary ionic conduction, which needs to be higher than the bulk conductivity to achieve a high electrochemical performance and a stable interface towards Li metal.

The integration of LLZO ceramics synthesized combining NSP and FAST in a battery cell was successful using a thin film LCO electrode deposited using LA-CVD resulting in an all-solid-state battery cell operational at room temperature, which is the first of its kind. Additionally, a slurry-based LCO cathode and a small amount of liquid electrolyte were used resulting in a hybrid battery cell that showed good performance at room temperature, while combining the advantages of an all-solid-state battery by eliminating the contact of the liquid electrolyte to the Li anode and ensuring a good contact to the cathode material and enhancing the charge transfer by introducing a small amount of liquid electrolyte in combination with a rough solid electrolyte surface.

9.2 Outlook

Despite the fact that LLZO is moisture sensitive and presents some challenges concerning its synthesis to achieve a high performance, the cubic modification of the solid electrolyte does exhibit high ionic conductivities at room temperature, which allow for a bulk battery integration. While synthesizing LLZO it is the main goal to further optimize the microstructure (density, microstrain and grain size) to achieve better electrochemical performance, especially to reduce the charge transfer resistance towards the electrodes.

A deeper understanding of the conduction mechanism and how the synthesis route influences the ionic mobility is of great importance. A high defect density or a high Li occupancy are parameters that need to be further characterized using neutron diffraction and possibly extensive ^{7}Li-NMR studies. Additionally, the presence of oxygen vacancies might also have an impact on the ionic mobility.

Apart from the optimization of the material properties, the all-solid-state cell design is in need for substantial development. An optimization of the electrolyte thickness is of great importance, which could be reduced down to 500 μm for the bulk ceramic. Additionally, the microstructure of the electrolyte surface could be altered to reduce interfacial resistance, e.g., a roughening of the surface on the cathode side. The same would be true for the Li anode side if a thin Li layer could be deposited on the rough pellet covering the complete surface.

The interfacial resistance on the cathode side can also be optimized by studying new composite cathodes including the solid electrolyte powder, a high voltage active material and a ceramic electronic conductor. This kind of composite cathodes would allow for co-sintering with the bulk solid electrolyte at high temperatures, that are needed for achieving a good contact.

Finally, in-situ cell characterization using, e.g., transmission electron microscopy and X-ray diffraction are needed to accurately monitor the cell reactions and identify the possible reasons for the deterioration of the electrochemical performance.

List of abbreviations

LCO	$LiCoO_2$
SEI	solid electrolyte interphase
HOMO	highest occupied molecular orbital
LUMO	lowest unoccupied molecular orbital
VB	valence band
CB	conduction band
IR	internal resistance
AC	alternating current
AC-IS	alternating current impedance spectroscopy
CPE	constant phase element
SEM	scanning electron microscopy
FIB	focused ion beam
HAADF STEM	annular dark field scanning transmission electron microscopy
EDXS	energy dispersive X-ray spectroscopy
ICP-OES	inductively coupled plasma optical emission spectrometry
DTA-TGA	differential thermal analysis and thermogravimetric analysis
MAS NMR	magic angle spinning nuclear magnetic resonance
XRD	X-ray diffraction
NSP	nebulized spray pyrolysis
FAST	field assisted sintering technology
SPS	spark plasma sintering
HP	hot pressing
LA-CVD	laser assisted chemical vapor deposition
TD	theoretical density
ASR	area specific resistance
LLZO	Al-doped $Li_7La_3Zr_2O_{12}$ ($Li_{7-3x}La_3Zr_2Al_xO_{12}$)
YSZ	yttrium stabilized zirconia
CC	composite cathode
GOF	goodness of fit
NMP	N-methyl-2-pyrrolidone
PVdF	polyvinylidene fluoride

List of symbols

p, q, r, s	the stoichiometric coefficients
A, B, C, D	chemical species
W_{max}	maximum possible electric energy
ΔG	change in Gibbs free energy
E	electromotive force
F	Farady constant
n	number of moles of electrons participating in the reaction
a	activity
a, b, c	lattice parameters
θ	diffraction angle
T	temperature
V_{oc}	open circuit voltage
$\mu_{\mathrm{a}}(\mathrm{Li})$	anode electrochemical potential
$\mu_{\mathrm{c}}(\mathrm{Li})$	cathode electrochemical potential
e	electron charge
E_g	band gap
E_a	activation energy
η_{dis}	polarization during discharge
η_{ch}	overpotential during charge
η_{act}	activation polarization
η_{ohm}	ohmic polarization
η_{conc}	concentration polarization
C_T	theoretical capacity
C_P	practical capacity
t	time
i	current
j_{corr}	corrected current density
ε_T	theoretical energy
ε_P	practical energy
P	power
g	site occupancy
R	gas constant
R	resistance
R_b	bulk resistance
R_{gb}	grain boundary resistance
Δ	observed difference in bulk resistance
ρ	electrical resistivity
σ	conductivity
C	capacitance
A	electrode area
A_t	theoretical electrode area
A_a	actual electrode area
d	distance between the electrodes
ε_r	relative permittivity
ε_0	electrical permittivity of vacuum
$V(t)$	voltage signal as a function of time
V_A	voltage amplitude

ω	radial frequency
f	frequency
f_c	critical relaxation frequncy
$I(t)$	current signal as a function of time
I_A	current amplitude
φ	phase shift between voltage and current
$Z_A, \lvert Z \rvert$	impedance magnitude
$\mathrm{Re}(Z')$	real impedance part
$\mathrm{Im}(Z'')$	imaginary impedance part
n	degree of deviation of the constant phase element from an ideal capacitance
Q	fit parameter of the constant phase element
τ	relaxation time constant
x	Al-doping level
χ^2	goodness of fit squared
R_{wp}	weighted profile R-factor
R_{exp}	expected R-factor
G	preferred orientation parameter
α	angle of intersection between two lattice planes
ε	microstrain
P_k	preferred orientation function

List of figures

List of tables

Curriculum Vitea

Education

01/2013 - present	PhD candidate at the Joint Research Laboratory Nanomaterials (Technische Universität Darmstadt, TUD and Karlsruhe Institute of Technology, KIT) Supervisor: Prof. Dr.-Ing. Horst Hahn
06/06/2012	Diploma thesis at TUD in collaboration with the Zentrum für Sonnenergie- und Wasserstoffforschung (ZSW), Stuttgart, Germany
10/2007 - 06/2012	Diplom in Material Science and Engineering at TUD, grade: good (1.9)
05/2007	High school graduation: Abitur, grade: good (1.7)
08/2003 - 05/2007	High school: Deutsche Schule der Borromäerinnen (DSB), Cairo, Egypt
08/1994 - 07/2003	Elementary and middle school of DSB, Cairo, Egypt

Work Experience

Research Scientist

01/2013 - present	Synthesis and characterization of solid electrolyte for Li-ion batteries (PhD work) Supervision of practical laboratory courses on a lambda probe for students Providing training on laboratory equipment (e.g. impedance spectroscopy using a cryostat, spark plasma sintering) Supervisor: Prof. Dr.-Ing. Horst Hahn Department: Joint Research Laboratory Nanomaterials (TUD/KIT), Darmstadt, Germany

Intern

02/2011 - 04/2011	Electrolytic deposition of nanowires. Gesellschaft für Schwerionenforschung (GSI), Darmstadt, Germany
07/2010 - 08/2010	In-situ characterization of shape-selected Pt catalyst synthesized using two different synthesis routes. (Fuel Cells) Supervisor: Prof. Dr. Christina Roth Department: Renewable Energies (TUD), Darmstadt, Germany

Research Assistant

05/2011 - 07/2011	Chemical vapor deposition of CdTe thin films at DAISY-Sol (Solar Cells) Department: Surface Science (TUD), Darmstadt, Germany
10/2009 - 01/2011	Synthesis of electrode materials for fuel cells and their preparation for electron microscopy. Department: Renewable Energies (TUD), Darmstadt, Germany

Honors and Awards

Poster award

2015	Outstanding poster award 20th International Conference on Solid State Ionics, Keystone, Colorado, USA

DAAD-scholarship

10/2007 - 09/2012	DAAD full scholarship for graduates of german schools abroad

Participation in math competitions

2002/03	Rheinland-Pfalz 1. Round, 3rd place
2003/04	Monoid competition, 2nd place

Participation in national sports competitions

2003 - 2007	High jump, long jump and 200 m sprint
2002 - 2007	Sailing (Optimist und Laser Radial)

List of publications

Peer-reviewed publications

M. Botros, R. Djenadic, O. Clemens, M. Möller, H. Hahn, Field assisted sintering of fine-grained $Li_{7-3x}La_3Zr_2Al_xO_{12}$ solid electrolyte and the influence of the microstructure on the electrochemical performance, Journal of Power Sources, 309 (2016) 108–115.

R. Djenadic, A. Sarkar, O. Clemens, C. Loho, M. Botros, V.S.K. Chakravadhanula, C. Kübel, S.S. Bhattacharya, A.S. Gandhi, H. Hahn, Multicomponent equiatomic rare earth oxides, Materials Research Letters, 5 (2016) 1–8.

R. Djenadic, M. Botros, H. Hahn, Is Li-doped $MgAl_2O_4$ a potential solid electrolyte for an all-spinel Li-ion battery?, Solid State Ionics. 287 (2016) 71–76.

R. Djenadic, M. Botros, C. Benel, O. Clemens, S. Indris, A. Choudhary, T. Bergfeldt, H. Hahn, Nebulized spray pyrolysis of Al-doped $Li_7La_3Zr_2O_{12}$ solid electrolyte for battery applications, Solid State Ionics, 263 (2014) 49–56.

T. Adler, M. Botros, W. Witte, D. Hariskos, R. Menner, M. Powalla, A Klein, Valence band offsets at $Cu(In,Ga)Se_2/Zn(O,S)$ interfaces, Physica Status Solidi a, 211 (2014) 1972-1980.

D. Dixon, J. Melke, M. Botros, J. Rathore, H. Ehrenberg, C. Roth, Increase of catalyst utilization in polymer electrolyte membrane fuel cells by shape-selected Pt nanoparticles, Int. J. Hydrogen Energy, 38 (2013) 13393–13398.

Proceedings

W. Witte, M. Powalla, D. Hariskos, A. Eicke, M. Botros et al., Chemical gradients in $Cu(In,Ga)(S,Se)_2$ thin-film solar cells: results of the Gracis Project.
27th European Photovoltaic Solar Energy Conference, Frankfurt, Germany

Conference talks

M. Botros, R. Djenadic, C. Loho, O. Clemens, H. Hahn, From synthesis to all-solid-state battery integration of $Li_{7-3x}La_3Zr_2Al_xO_{12}$ solid electrolyte. Bunsen-Kolloquium on Solid-State Batteries - From Fundamentals to Application 2016, Frankfurt, Germany

M. Botros, R. Djenadic, H. Hahn, Aluminum-doped $Li_7La_3Zr_2O_{12}$ as a solid electrolyte for lithium-ion batteries. Conference for Young Scientists in Ceramics - Students Meeting 2015, Novi Sad, Serbia

M. Botros, R. Djenadic, H. Hahn, Synthesis and characterization of Al-doped $Li_7La_3Zr_2O_{12}$ solid electrolyte for Li-ion batteries. Materials Research Society Spring Meeting 2014 (MRS), San Francisco, USA

M. Botros, R. Djenadic, H. Hahn, Characterization of Al-doped LLZO solid electrolyte synthesized using nebulized spray pyrolysis. Bunsen-Kolloquium on Solid-State Batteries - From Fundamentals to Application 2014, Frankfurt, Germany

M. Botros, R. Djenadic, H. Hahn, LLZO solid electrolyte for Li-ion batteries. Conference for Young Scientists in Ceramics - Students Meeting 2013, Novi Sad, Serbia

Posters

M. Botros, R. Djenadic, H. Hahn, Field assisted sintering of $Li_{7-3x}La_3Zr_2Al_xO_{12}$ solid electrolyte and the influence of the microstructure on the electrochemical performance. 18th International Meeting on Lithium Batteries 2016 (IMLB), Chicago, Illinois, USA

M. Botros, R. Djenadic, H. Hahn, Aluminum-doped $Li_7La_3Zr_2O_{12}$ - a promising candidate as a solid electrolyte for lithium-ion batteries. 20th International Conference on Solid State Ionics, Keystone, Colorado, USA (Outstanding Poster Award 2015)

M. Botros, R. Djenadic, H. Hahn, Electrochemical characterization of nano-scaled solid electrolyte for lithium-ion batteries. 556th WE-Heraeus-Seminar 2014, Bad Honnef, Germany

References

[1] I. Buchman, Batteries in a Portable World: A Handbook on Rechargeable Batteries for Non-Engineers (2001).

[2] T. Nagaura, K. Tozawa, Lithium ion rechargeable battery, Prog. Batter. Sol. Cells. 9 (1990) 209–217.

[3] J.B. Goodenough, K.-S.S. Park, The Li-ion rechargeable battery: A perspective, J. Am. Chem. Soc. 135 (2013) 1167–76.

[4] G.L. Soloveichik, Battery Technologies for Large-Scale Stationary Energy Storage, (2011) 503–529.

[5] R. Murugan, V. Thangadurai, W. Weppner, Fast lithium ion conduction in garnet-type $Li_7La_3Zr_2O_{12}$, Angew. Chem. Int. Ed. Engl. 46 (2007) 7778–81.

[6] J. Wolfenstine, J.L. Allen, J. Read, J. Sakamoto, Chemical stability of cubic $Li_7La_3Zr_2O_{12}$ with molten lithium at elevated temperature, J. Mater. Sci. 48 (2013) 5846–5851.

[7] D. Linden, T.B. Reddy, HANDBOOK OF BATTERIES, (2001).

[8] D. Deng, Li-ion batteries: basics, progress, and challenges, Energy Sci. Eng. 3 (2015) 385–418.

[9] M.S. Islam, C.A.J. Fisher, Lithium and sodium battery cathode materials: computational insights into voltage, diffusion and nanostructural properties, Chem. Soc. Rev. 43 (2014) 185–204.

[10] J.-K. Park, The Basic of Battery Chemistry, Princ. Appl. Lithium Second. Batter., Wiley-VCH Verlag GmbH & Co. KGaA (2012) 9–19.

[11] M.K. Aydinol, G. Ceder, First-Principles Prediction of Insertion Potentials in Li-Mn Oxides for Secondary Li Batteries, J. Electrochem. Soc. . 144 (1997) 3832–3835.

[12] J.N. Mrgudich, Conductivity of Silver Iodide Pellets for Solid-Electrolyte Batteries, J. Electrochem. Soc. 107 (1960) 475–479.

[13] K. Takada, Progress and prospective of solid-state lithium batteries, Acta Mater. 61 (2013) 759–770.

[14] K. Takada, Solid Electrolytes and Solid-State Batteries, 20008 (2016).

[15] K. Takada, N. Ohta, Recent Progress in Interfacial Nanoarchitectonics in Solid-State Batteries, (2015) 205–213.

[16] M.W. Yoshiyuki Inaguma, Chen Liquan, Mitsuru Itoh, Tetsurō Nakamura, Takashi Uchida, Hiromasa Ikuta, High ionic conductivity in lithium lanthanum titanate, 86 (1993) 689–693.

[17] D. Rettenwander, A. Welzl, L. Cheng, J. Fleig, M. Musso, E. Suard, M.M. Doe, G.J. Redhammer, G. Amthauer, Synthesis , Crystal Chemistry , and Electrochemical Properties of Polymorph via Substitution of Zr^{4+} by Mo^{6+}, 12 (2015).

[18] E.J. Cussen, T.W.S. Yip, G. Oneill, M.P. Ocallaghan, A comparison of the transport properties of lithium-stuffed garnets and the conventional phases $Li_3Ln_3Te_2O_{12}$, J. Solid State Chem. 184

(2011) 470–475.

[19] M. Nb, V. Thangadurai, H. Kaack, W.J.F. Weppner, Novel Fast Lithium Ion Conduction in Garnet-Type $Li_5La_3M_2O_{12}$, 40 (2003) 437–440.

[20] B.V. Thangadurai, W. Weppner, $Li_6ALa_2Ta_2O_{12}$ (A = Sr, Ba): Novel Garnet-Like Oxides for Fast Lithium Ion Conduction, 12 (2005) 107–112.

[21] K. Meier, T. Laino, A. Curioni, Solid-State Electrolytes: Revealing the Mechanisms of Li-Ion Conduction in Tetragonal and Cubic LLZO by First-Principles Calculations, J. Phys. Chem. C. 118 (2014) 6668−6679.

[22] J. Awaka, A. Takashima, K. Kataoka, N. Kijima, Y. Idemoto, J. Akimoto, Crystal Structure of Fast Lithium-ion-conducting Cubic $Li_7La_3Zr_2O_{12}$, Chem. Lett. 40 (2011) 60–62.

[23] C. a Geiger, E. Alekseev, B. Lazic, M. Fisch, T. Armbruster, R. Langner, M. Fechtelkord, N. Kim, T. Pettke, W. Weppner, Crystal chemistry and stability of “$Li_7La_3Zr_2O_{12}$” garnet: a fast lithium-ion conductor., Inorg. Chem. 50 (2011) 1089–97.

[24] J. Awaka, N. Kijima, H. Hayakawa, J. Akimoto, Synthesis and structure analysis of tetragonal $Li_7La_3Zr_2O_{12}$ with the garnet-related type structure, J. Solid State Chem. 182 (2009) 2046–2052.

[25] H. Xie, J.A. Alonso, Y. Li, M.T. Fern, J.B. Goodenough, Lithium Distribution in Aluminum-Free Cubic $Li_7La_3Zr_2O_{12}$, (2011) 3587–3589.

[26] P.P. Kumar, S. Yashonath, Ionic conduction in the solid state, 118 (2006) 135–154.

[27] J. Wolfenstine, E. Rangasamy, J.L. Allen, J. Sakamoto, High conductivity of dense tetragonal $Li_7La_3Zr_2O_{12}$, J. Power Sources. 208 (2012) 193–196.

[28] N. Bernstein, M.D. Johannes, K. Hoang, Origin of the structural phase transition in $Li_7La_3Zr_2O_{12}$, Phys. Rev. Lett. 109 (2012) 2–6.

[29] J.L. Allen, J. Wolfenstine, E. Rangasamy, J. Sakamoto, Effect of substitution (Ta , Al , Ga) on the conductivity of $Li_7La_3Zr_2O_{12}$, J. Power Sources. 206 (2012) 315–319.

[30] V.F. Lvovich, Fundamentals of Electrochemical Impedance Spectroscopy, in: Impedance Spectrosc., John Wiley & Sons, Inc., (2012) 1–21.

[31] J.T.S. Irvine, D.C. Sinclair, A.R. West, Electroceramics: Characterization by Impedance Spectroscopy, Adv. Mater. 2 (1990) 132–138.

[32] N. Aristov, A. Habekost, Cyclic Voltammetry - A Versatile Electrochemical Method Investigating Electron Transfer Processes, World J. Chem. Educ. Vol. 3 (2015) 115–119.

[33] V.S. Bagotsky, Electrochemical Research Techniques, in: Fundam. Electrochem. Second Ed., (2005) 191–215.

[34] H.A. Kramers, On the theory of X-ray absorption and of the continuous X-ray spectrum, Philos. Mag. 46 (1923) 836–871.

[35] R.A. Young, (Ed.), The Rietveld Method, (1993).

[36] B.H. Toby, R factors in Rietveld analysis: How good is good enough?, Powder Diffr. 21 (2006) 67–70.

[37] N.E. Motl, A.K.P. Mann, S.E. Skrabalak, Aerosol-assisted synthesis and assembly of nanoscale building blocks, J. Mater. Chem. A. 1 (2013) 5193.

[38] R. Djenadic, M. Botros, H. Hahn, Is Li-doped $MgAl_2O_4$ a potential solid electrolyte for an all-spinel Li-ion battery ?, Solid State Ionics. 287 (2016) 71–76.

[39] L. Cheng, E.J. Crumlin, W. Chen, R. Qiao, H. Hou, S. Franz Lux, V. Zorba, R. Russo, R. Kostecki, Z. Liu, The origin of high electrolyte – electrode interfacial resistances in lithium cells containing garnet type solid electrolytes, Phys. Chem. Chem. Phys. 16 (2014) 18294–18300.

[40] P. Boch, A. Leriche, Sintering and Microstructure of Ceramics, Ceram. Mater., ISTE (2010) 55–93.

[41] O. Guillon, J. Gonzalez-Julian, B. Dargatz, T. Kessel, G. Schierning, J. Räthel, M. Herrmann, Field-Assisted Sintering Technology/Spark Plasma Sintering: Mechanisms, Materials, and Technology Developments, Adv. Eng. Mater. 16 (2014) 830–849.

[42] M. Suárez, A. Fernández, J.L. Menéndez, R. Torrecillas, H.U. Kessel, J. Hennicke, R. Kirchner, T. Kessel, Challenges and Opportunities for Spark Plasma Sintering : A Key Technology for a New Generation of Materials, Sinter. Appl. (2013) 319.

[43] J. Räthel, M. Herrmann, W. Beckert, Temperature distribution for electrically conductive and non-conductive materials during Field Assisted Sintering (FAST), J. Eur. Ceram. Soc. 29 (2009) 1419–1425.

[44] R. Djenadic, M. Botros, C. Benel, O. Clemens, S. Indris, A. Choudhary, T. Bergfeldt, H. Hahn, Nebulized spray pyrolysis of Al-doped $Li_7La_3Zr_2O_{12}$ solid electrolyte for battery applications, Solid State Ionics. 263 (2014) 49–56.

[45] E. Rangasamy, J. Wolfenstine, J. Sakamoto, The role of Al and Li concentration on the formation of cubic garnet solid electrolyte of nominal composition $Li_7La_3Zr_2O_{12}$, Solid State Ionics. 206 (2012) 28–32.

[46] G.-W.W. Lee, J.H. Ryu, W. Han, K.H. Ahn, S.M. Oh, J. Heon, W. Han, K. Hyun, S.M. Oh, J.H. Ryu, W. Han, K.H. Ahn, S.M. Oh, Effect of slurry preparation process on electrochemical performances of $LiCoO_2$ composite electrode, J. Power Sources. 195 (2010) 6049–6054.

[47] H. Buschmann, J. Dölle, S. Berendts, A. Kuhn, P. Bottke, M. Wilkening, P. Heitjans, A. Senyshyn, H. Ehrenberg, A. Lotnyk, V. Duppel, L. Kienle, J. Janek, Structure and dynamics of the fast lithium ion conductor "$Li_7La_3Zr_2O_{12}$"., Phys. Chem. Chem. Phys. 13 (2011) 19378–92.

[48] F.D. Aude A. Hubaud, David J. Schroeder, Baris Key, Brian J. Ingram, and J.T.V. Vaughey, Low temperature stabilization of cubic $(Li_{7x}Al_{x/3})La_3Zr_2O_{12}$: role of aluminum during formation, J. Mater. Chem. A. (2013) 8813–8818.

[49] A. Düvel, A. Kuhn, L. Robben, M. Wilkening, P. Heitjans, Mechanosynthesis of Solid Electrolytes : Preparation , Characterization , and Li Ion Transport Properties of Garnet-Type Al-Doped $Li_7La_3Zr_2O_{12}$ Crystallizing with Cubic Symmetry, (2012).

[50] A.A. Raskovalov, E.A. Il, B.D. Antonov, Structure and transport properties of $Li_7La_3Zr_2A_{0.75x}Al_xO_{12}$ superionic solid electrolytes, J. Power Sources. 238 (2013) 48–52.

[51] I. Kokal, M. Somer, P.H.L. Notten, H.T. Hintzen, Sol–gel synthesis and lithium ion conductivity of $Li_7La_3Zr_2O_{12}$ with garnet-related type structure, Solid State Ionics. 185 (2011) 42–46.

[52] B.Y.R.D. Shannon, M. H, N.H. Baur, O.H. Gibbs, M. Eu, V. Cu, Revised Effective Ionic Radii and Systematic Studies of Interatomie Distances in Halides and Chaleogenides, (1976).

[53] Y. Jin, P.J. McGinn, Al-doped $Li_7La_3Zr_2O_{12}$ synthesized by a polymerized complex method, J. Power Sources. 196 (2011) 8683–8687.

[54] S. Kumazaki, Y. Iriyama, K. Kim, R. Murugan, K. Tanabe, K. Yamamoto, T. Hirayama, Z. Ogumi, Electrochemistry Communications High lithium ion conductive $Li_7La_3Zr_2O_{12}$ by inclusion of both Al and Si, Electrochem. Commun. 13 (2011) 509–512.

[55] M. Kotobuki, K. Kanamura, Y. Sato, T. Yoshida, Fabrication of all-solid-state lithium battery with lithium metal anode using, J. Power Sources. 196 (2011) 7750–7754.

[56] F. Lin, I.M. Markus, M.M. Doeff, H.L. Xin, Chemical and Structural Stability of Lithium-Ion Battery Electrode Materials under Electron Beam, 2 (2014) 1–6.

[57] Y. Zhang, F. Chen, R. Tu, Q. Shen, L. Zhang, Field assisted sintering of dense Al-substituted cubic phase $Li_7La_3Zr_2O_{12}$ solid electrolytes, J. Power Sources. 268 (2014) 960–964.

[58] R. Takano, K. Tadanaga, A. Hayashi, M. Tatsumisago, Low temperature synthesis of Al-doped $Li_7La_3Zr_2O_{12}$ solid electrolyte by a sol–gel process, Solid State Ionics. 255 (2014) 104–107.

[59] K. Tadanaga, R. Takano, T. Ichinose, S. Mori, A. Hayashi, M. Tatsumisago, Low temperature synthesis of highly ion conductive $Li_7La_3Zr_2O_{12}$–Li_3BO_3 composites, Electrochem. Commun. 33 (2013) 51–54.

[60] C. Suryanarayana, C.C. Koch, Nanocrystalline materials – Current research and future directions, (2000) 5–44.

[61] R. Chaim, M. Levin, A. Shlayer, C. Estournes, Open Archive Toulouse Archive Ouverte (OATAO) Sintering and densification of nanocrystalline ceramic oxide powders : a review, 107 (2008) 159–169.

[62] Y. Wang, W. Lai, Phase transition in lithium garnet oxide ionic conductors $Li_7La_3Zr_2O_{12}$: The role of Ta substitution and H_2O/CO_2 exposure, J. Power Sources. 275 (2015) 612–620.

[63] Z.F. Yow, Y.L. Oh, W. Gu, R.P. Rao, S. Adams, Effect of Li^+/H^+ exchange in water treated Ta-doped $Li_7La_3Zr_2O_{12}$, Solid State Ionics. 292 (2016) 122–129.

[64] M. Matsui, K. Takahashi, K. Sakamoto, A. Hirano, Y. Takeda, O. Yamamoto, N. Imanishi, Phase

stability of a garnet-type lithium ion conductor $Li_7La_3Zr_2O_{12}$, Dalt. Trans. 43 (2014) 1019–1024.

[65] S. Toda, K. Ishiguro, Y. Shimonishi, A. Hirano, Y. Takeda, O. Yamamoto, N. Imanishi, Low temperature cubic garnet-type CO_2-doped $Li_7La_3Zr_2O_{12}$, Solid State Ionics. 233 (2013) 102–106.

[66] a. N. Timoshevskii, M.G. Ktalkherman, V. a. Emel'kin, B. a. Pozdnyakov, a. P. Zamyatin, High-temperature decomposition of lithium carbonate at atmospheric pressure, High Temp. 46 (2008) 414–421.

[67] J.-M. Lee, T. Kim, S.-W. Baek, Y. Aihara, Y. Park, Y.-I. Kim, S.-G. Doo, High lithium ion conductivity of $Li_7La_3Zr_2O_{12}$ synthesized by solid state reaction, Solid State Ionics. 258 (2014) 13–17.

[68] M. Huang, T. Liu, Y. Deng, H. Geng, Y. Shen, Y. Lin, C.-W. Nan, Effect of sintering temperature on structure and ionic conductivity of $Li_{7-x}La_3Zr_2O_{12-0.5x}$ (x=0.5~0.7) ceramics, Solid State Ionics. 204–205 (2011) 41–45.

[69] M. Botros, R. Djenadic, O. Clemens, M. Matthias, H. Hahn, Field assisted sintering of fine-grained $Li_{7-3x}La_3Zr_2Al_xO_{12}$ solid electrolyte and the influence of the microstructure on the electrochemical performance, J. Power Sources. 309 (2016) 108–115.

[70] L. Cheng, W. Chen, M. Kunz, K.A. Persson, N. Tamura, G. Chen, M.M. Doeff, Effect of Surface Microstructure on Electrochemical Performance of Garnet Solid Electrolytes., ACS Appl. Mater. Interfaces. (2015).

[71] J. Sakamoto, E. Rangasamy, H. Kim, Y. Kim, J. Wolfenstine, Synthesis of nano-scale fast ion conducting cubic $Li_7La_3Zr_2O_{12}$, Nanotechnology. 24 (2013) 424005.

[72] W.C. Hamilton, Significance Tests on the Crystallographics R Factor, Acta Cryst. 18 (1965) 502–510.

[73] L. Ta, A. Logéat, T. Köhler, U. Eisele, B. Stiaszny, A. Harzer, M. Tovar, A. Senyshyn, H. Ehrenberg, B. Kozinsky, From order to disorder: The structure of lithium-conducting garnets $Li_{7-x}La_3Ta_xZr_{2-x}O_{12}$ (x=0–2), Solid State Ionics. 206 (2012) 33–38.

[74] J. Gonzalez-Julian, O. Guillon, Effect of Electric Field/Current on Liquid Phase Sintering, J. Am. Ceram. Soc. 98 (2015) 2018–2027.

[75] A. R. West, Basic Solid State Chemistry, 2nd ed., John Wiley & Sons Ltd: Chichester, 1999.

[76] L. Cheng, J.S. Park, H. Hou, V. Zorba, G. Chen, T. Richardson, J. Cabana, R. Russo, M. Doeff, Effect of microstructure and surface impurity segregation on the electrical and electrochemical properties of dense Al-substituted $Li_7La_3Zr_2O_{12}$, J. Mater. Chem. A. 2 (2014) 172.

[77] H. Buschmann, S. Berendts, B. Mogwitz, J. Janek, Lithium metal electrode kinetics and ionic conductivity of the solid lithium ion conductors "$Li_7La_3Zr_2O_{12}$" and $Li_{7-x}La_3Zr_{2-x}Ta_xO_{12}$ with garnet-type structure, J. Power Sources. 206 (2012) 236–244.

[78] S.-W. Baek, J.-M. Lee, T.Y. Kim, M.-S. Song, Y. Park, Garnet related lithium ion conductor

processed by spark plasma sintering for all solid state batteries, J. Power Sources. 249 (2014) 197–206.

[79] H. He, W. Weppner, All-solid-state thick-film battery, Ionics (Kiel). 7 (2001) 469–474.

[80] A. Sharafi, H.M. Meyer, J. Nanda, J. Wolfenstine, J. Sakamoto, A. Shara, H.M. Meyer, J. Nanda, J. Wolfenstine, J. Sakamoto, Characterizing the Li $Li_7La_3Zr_2O_{12}$ interface stability and kinetics as a function of temperature and current density, J. Power Sources. 302 (2016) 135–139.

[81] J. Janek, Oscillatory kinetics at solid/solid phase boundaries in ionic crystals, Solid State Ionics. 131 (2000) 129–142.

[82] N. Schichtel, C. Korte, D. Hesse, J. Janek, Elastic strain at interfaces and its influence on ionic conductivity in nanoscaled solid electrolyte thin films--theoretical considerations and experimental studies., Phys. Chem. Chem. Phys. 11 (2009) 3043–8.

[83] S. Filipovi, N. Obradovi, V.B. Pavlovi, M. Mitri, A. Đ, M. Kachlik, K. Maca, Effect of consolidation parameters on structural, microstructural and electrical properties of magnesium titanate ceramics, 42 (2016) 9887–9898.

[84] J. Weissmüller, J. Löffler, Martin Kleber, ATOMIC STRUCTURE OF NANOCRYSTALLINE METALS STUDIED BY DIFFRACTION TECHNIQUES AND EXAFS, NanoStruetured Mater. 6 (1995) 105–114.

[85] M. Wilkening, D. Bork, S. Indris, P. Heitjans, Diffusion in amorphous $LiNbO_3$ studied by ^{7}Li NMR - comparison with the nano- and microcrystalline material, Phys. Chem. Chem. Phys. 4 (2002) 3246–3251.

[86] C. Li, Y. Liu, J. He, K.S. Brinkman, Ga-substituted $Li_7La_3Zr_2O_{12}$: An investigation based on grain coarsening in garnet-type lithium ion conductors, J. Alloys Compd. 695 (2017) 3744–3752.

[87] S. Afyon, F. Krumeich, J.L.M. Rupp, A shortcut to garnet-type fast Li-ion conductors for all-solid state batteries, J. Mater. Chem. A. 3 (2015) 18636–18648.

[88] B. Xu, H. Duan, W. Xia, Y. Guo, H. Kang, H. Li, H. Liu, Multistep sintering to synthesize fast lithium garnets, J. Power Sources. 302 (2016) 291–297.

[89] L. La, T. Zr, K. Liu, J. Ma, C. Wang, Excess lithium salt functions more than compensating for lithium loss, J. Power Sources. 260 (2014) 109–114.

[90] T.B. Holland, U. Anselmi-Tamburini, D. V. Quach, T.B. Tran, A.K. Mukherjee, Local field strengths during early stage field assisted sintering (FAST) of dielectric materials, J. Eur. Ceram. Soc. 32 (2012) 3659–3666.

[91] M.M. Ahmad, Estimation of the concentration and mobility of mobile Li^+ in the cubic garnet-type $Li_7La_3Zr_2O_{12}$, RSC Adv. 5 (2015) 25824–25829.

[92] A. Kilmametov, R. Gröger, H. Hahn, T. Schimmel, S. Walheim, Bulk Density Measurements of Small Solid Objects Using Laser Confocal Microscopy, Adv. Mater. Technol. (2016) 1600115.

[93] D. Wang, G. Zhong, O. Dolotko, Y. Li, M.J. McDonald, J. Mi, R. Fu, Y. Yang, The synergistic effects of Al and Te on the structure and Li^+-mobility of garnet-type solid electrolytes, J. Mater. Chem. A. 2 (2014) 20271–20279.

[94] A. March, Mathematische Theorie der Regelung nach der Korngestalt bei affiner Deformation, Z. Krist. 81 (1932) 285–297.

[95] P. Bottke, D. Rettenwander, W. Schmidt, G. Amthauer, M. Wilkening, Ion Dynamics in Solid Electrolytes: NMR Reveals the Elementary Steps of Li^+ Hopping in the Garnet $Li_{6.5}La_3Zr_{1.75}Mo_{0.25}O_{12}$, Chem. Mater. 27 (2015) 6571–6582.

[96] A.S. Edelstein, R.C. Cammarata, Nanomaterials: Synthesis, Properties and Applications, (1998).

[97] M. Kubicek, A. Wachter-welzl, D. Rettenwander, R. Wagner, S. Berendts, R. Uecker, G. Amthauer, H. Hutter, J. Fleig, Oxygen Vacancies in Fast Lithium-Ion Conducting Garnets Oxygen Vacancies in Fast Lithium-Ion Conducting Garnets, (2017).

[98] M. Kotobuki, K. Kanamura, Y. Sato, K. Yamamoto, T. Yoshida, Electrochemical properties of $Li_7La_3Zr_2O_{12}$ solid electrolyte prepared in argon atmosphere, J. Power Sources. 199 (2012) 346–349.

[99] S. Ohta, T. Kobayashi, J. Seki, T. Asaoka, Electrochemical performance of an all-solid-state lithium ion battery with garnet-type oxide electrolyte, J. Power Sources. 202 (2012) 332–335.

[100] L.J. Miara, W.D. Richards, Y.E. Wang, G. Ceder, First-Principles Studies on Cation Dopants and Electrolyte|Cathode Interphases for Lithium Garnets, (2015).

[101] T. Kato, T. Hamanaka, K. Yamamoto, T. Hirayama, F. Sagane, M. Motoyama, Y. Iriyama, In-situ $Li_7La_3Zr_2O_{12}/LiCoO_2$ interface modification for advanced all-solid-state battery, J. Power Sources. 260 (2014) 292–298.

[102] F. Du, N. Zhao, Y. Li, C. Chen, Z. Liu, X. Guo, All solid state lithium batteries based on lamellar garnet-type ceramic electrolytes, J. Power Sources. 300 (2015) 24–28.

[103] C. Loho, A.J. Darbandi, R. Djenadic, O. Clemens, H. Hahn, CO_2-laser flash evaporation as novel CVD precursor delivery system for functional thin film growth, Chem. Vap. Depos. 20 (2014) 152–160.

[104] D. Vrankovic, L.M. Reinold, R. Riedel, M. Graczyk-zajac, Void-shell silicon/carbon/SiCN nanostructures: toward stable silicon-based electrodes, J. Mater. Sci. 51 (2016) 6051–6061.

[105] H. Xia, Y.S. Meng, L. Lu, G. Ceder, S. Alliance, Electrochemical behavior and Li Diffusion study of $LiCoO_2$ thin film electrodes prepared by PLD, Sci. Commons. (2010).

[106] M. Winterer, V. V. Srdic, R. Djenadic, A. Kompch, T.E. Weirich, Chemical vapor synthesis of nanocrystalline perovskites using laser flash evaporation of low volatility solid precursors, Rev. Sci. Instrum. 78 (2007).

[107] E. Antolini, $LiCoO_2$: formation, structure, lithium and oxygen nonstoichiometry, electrochemical

behaviour and transport properties, 170 (2004) 159–171.

[108] S.S. Zhang, A review on the separators of liquid electrolyte Li-ion batteries, J. Power Sources. 164 (2007) 351–364.

[109] J. Reimers, J. Dahn, Electrochemical and In Situ X-Ray Diffraction Studies of Lithium Intercalation in Li_xCoO_2, J. Electrochem. Soc. 139 (1992) 2091–2097.